Three-dimensional Integral Boundary Layer Method for Viscous Aerodynamic Analysis

Shun Zhang

B.S.E., Aerospace Engineering, University of Michigan (2015)
B.S.E., Mechanical Engineering, Shanghai Jiao Tong University (2015)
M.S., Aerospace Engineering, Massachusetts Institute of Technology (2018)

Submitted to the Department of Aeronautics and Astronautics in partial fulfillment
of the requirements for the degree of
Doctor of Philosophy in Computational Science and Engineering
at the
Massachusetts Institute of Technology
September 2022

Author .....
Department of Aeronautics and Astronautics
August 16, 2022

Certified by .....
Mark Drela
Terry J. Kohler Professor of Aeronautics and Astronautics, MIT
Thesis Supervisor/Thesis Committee Chair

Certified by .....
David L. Darmofal
Jerome C. Hunsaker Professor of Aeronautics and Astronautics, MIT
Thesis Committee Member

Certified by .....
Steven R. Allmaras
Research Engineer of Aeronautics and Astronautics, MIT
Thesis Committee Member

Certified by .....
David L. Rodriguez
Senior Research Scientist, NASA
Thesis Committee Member

Accepted by .....
Jonathan P. How
R. C. Maclaurin Professor of Aeronautics and Astronautics, MIT
Chair of Graduate Program Committee

Accepted by .....
Youssef Marzouk
Professor of Aeronautics and Astronautics, MIT
Co-director of Center for Computational Science and Engineering

Three-dimensional Integral Boundary Layer Method for Viscous Aerodynamic Analysis

by

Shun Zhang

Submitted to the Department of Aeronautics and Astronautics
on August 16, 2022, in partial fulfillment of the
requirements for the degree of
Doctor of Philosophy in Computational Science and Engineering

Abstract

Viscous aerodynamic analysis is crucial for aircraft design in terms of understanding key performance metrics such as drag. However, despite advances in computational fluid dynamics (CFD) in the past few decades, a physics-based three-dimensional (3D) viscous analysis suitable for aircraft preliminary design remains a challenge. To that end, the integral boundary layer (IBL) method is a promising candidate primarily for its superior computational efficiency and aerodynamic design insights, evidenced from its success in existing two-dimensional (2D) applications. This thesis aims to develop a reliable off-the-shelf three-dimensional (3D) IBL method through contributions in both the physical and numerical modeling aspects.

First, this thesis presents novel closure modeling strategies for 3D IBL and develops a new set of closure models, which were lacking in previous 3D IBL methods. Original 3D boundary layer data sets have been generated and form the basis for data-driven closure modeling in this work. New neural network regression models with embedded constraints are proposed for constructing 3D IBL closure and to help identify important parameters. Moreover, a model inversion formulation is devised for automated data-driven calibration of the turbulence shear stress transport model in the IBL context. Numerical studies demonstrate the effective boundary layer modeling by the proposed closure models through comparison against higher-fidelity reference solution and previous 3D IBL formulations.

Second, the proper stabilization scheme is explored for the numerical discretization of the 3D IBL equations. On the one hand, difficulties have been identified for a rigorous stabilization formulation guided by conventional characteristic analysis. On

the other hand, heuristically-defined numerical stabilization schemes are revealed to be ill-posed based on the numerical examples of this work. Instead, an intermediate fix to the numerical discretization is tailored for 3D IBL based on its underlying conservation principles. This fix is observed to produce well-behaved solution as in the numerical results throughout this thesis.

Finally, this work develops the capability of flow transition prediction that is missing from existing 3D IBL methods. Two ways of numerical treatment for free transition are proposed and compared in detail, namely, transition fitting versus transition capturing. With its advantageous implementation convenience, solution robustness and interface resolution, the transition capturing approach is demonstrated to be effective based on both 2D and 3D test cases, and hence is recommended for 3D IBL transition modeling.

Thesis Supervisor/Thesis Committee Chair: Mark Drela
Title: Terry J. Kohler Professor of Aeronautics and Astronautics, MIT

Thesis Committee Member: David L. Darmofal
Title: Jerome C. Hunsaker Professor of Aeronautics and Astronautics, MIT

Thesis Committee Member: Steven R. Allmaras
Title: Research Engineer of Aeronautics and Astronautics, MIT

Thesis Committee Member: David L. Rodriguez
Title: Senior Research Scientist, NASA

Thesis Reader: Krzysztof J. Fidkowski
Title: Professor of Aerospace Engineering, University of Michigan

Thesis Reader: Qiqi Wang
Title: Associate Professor of Aeronautics and Astronautics, MIT

Acknowledgments

I would never have been able to march this far in my PhD journey at MIT without all the people who helped and supported me. First and foremost, I want to thank my advisors and mentors. As the Chinese saying goes, "once a mentor, forever a parent". Indeed, I feel like the luckiest and happiest adopted academic child.

I am deeply grateful to Prof. Mark Drela for your advising over the years. It is truly a blessing to have such an accessible and supportive advisor. For all that I could achieve in my PhD journey, it is because I stand on the shoulders of giants like yourself. Learning from you feels like drinking from a fire hose and I enjoy every single moment of that. Thank you for being the role model that I always look up to and strive to be.

I want to thank Prof. David Darmofal for bringing me into MIT and for your engagement with my advising and research. Having been both your advisee and teaching assistant, I know for a fact that every piece of your advice/feedback is a true gift, behind which is the thought, care and rigor you devote to advising and teaching.

I am thankful to Dr. Steven Allmaras for all your help and support, from supervising my Master's thesis to serving on my PhD thesis committee. You have always been very thorough and helpful in answering my questions, and the physical distance from coast to coast has never discounted your engagement.

I also thank Dr. David Rodriguez for graciously joining my thesis committee. I very much appreciate your engagement with my research by going out of your way to attend my research meetings every week. The thoughtful questions your ask and ideas you share are instrumental in helping me correct course and make progress.

I owe very much to Prof. Krzysztof Fidkowski for being a very engaged and

responsive thesis reader, and also for bringing me into my current academic family and the world of numerical methods and CFD. I always cherish the fond memories at your research group back in Michigan.

I am also grateful to Prof. Qiqi Wang for your engagement with my PhD study throughout the thesis proposal and the thesis defense. You insightful questions always inspire me to think more deeply and thoroughly about the work on IBL.

My research would not have been possible without contributions of everyone from the Solution Adaptive Numerical Simulator (SANS) team. I am in particular grateful to Dr. Marshall Galbraith for leading the code development and for tirelessly helping with my questions and providing feedback. I also would like to thank my fellow labmates (past and present): Arthur, Ben, Carmen, Chris, Cory, Hugh, Phil, Savithru and Yixuan. Thank you all very much for the teamwork to make SANS great and for the friendship and support throughout the time we shared at MIT.

I owe tremendously to my family. Thank you Mom and Dad for raising me to be what I am proud to be. Now that I have become a parent myself, I have come to appreciate all the more those untold suffering and sacrifice you made just for me over the many years. I also want to thank my parents-in-law for raising my wife to be as awesome as she is and for welcoming me into their family. I am deeply indebted to my wife Yu for her unwavering support and unconditional love through my ups and downs. I could not ask for a better partner for life. I also would love to thank my daughter Sophia for making full-time daddy a rewarding job, so much that I will probably never retire.

The financial support from the National Aeronautics and Space Administration (NASA) award NNX15AU41A, with Michael Aftosmis as the technical monitor, is greatly appreciated

Table of Contents

List of Figures

List of Tables

Chapter 1

Introduction

This thesis focuses on the development of a three-dimensional (3D) integral boundary layer (IBL) method for viscous aerodynamic analysis. The introduction begins with the motivation for IBL methods and related previous work and then summarizes the main contributions and the organization of the thesis.

1.1 Motivation for Integral Boundary Layer

Aerodynamics significantly drives the performance and constraints of flight vehicles and miscellaneous aero-mechanical systems. The IBL method is a desirable viscous aerodynamic analysis tool for the unparalleled computational efficiency and the valuable design insights.

Take for example the arduous development process for modern flight vehicles, which is fraught with compromises between performance, cost and schedule. A clean-sheet commercial aircraft development program, such as the Airbus A350 model, can span roughly a decade from initiation to certification [7]. An important contributing

factor to this dilemma is the fact that most critical design decisions are fixed at a rather early stage. In particular, as a crucial design driver, the aerodynamic design is often frozen by the end of the preliminary design stage [8]. However, only a disproportionally small fraction of the overall resources are available thus far, as illustrated in Figure 1-1. Hence, the overall process would likely be significantly accelerated and improved if better analysis tools were made available as early as possible, which is of particular interest to this thesis.

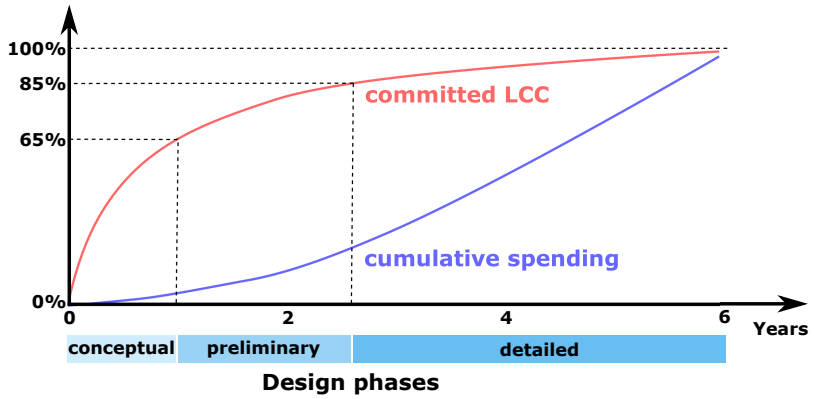

Figure 1-1: Imbalance between committed life-cycle cost (LCC) and cumulative spending across different stages of aircraft design. (Adapted from Refs. [1, 2])

Modern aerodynamic analysis increasingly relies on computational methods to complement or reduce conventional wind tunnel experiments and flight testing. Computational fluid dynamics (CFD) algorithms based on solving the Reynolds-averaged Navier-Stokes (RANS) equations are usually the only available tool for analyzing fully 3D viscous aerodynamic flow over aircraft. However, obtaining 3D RANS solutions often requires considerable computational resources, typically involving hours or even days of runtime on a multi-processor computing cluster and non-trivial user efforts such as mesh generation which is traditionally time-consuming and labor-intensive. These barriers often prove too high to be acceptable for preliminary design, where

numerous iterations need to be made to explore the design space.

The rapid computational speed is a primary advantage of the IBL method over RANS. IBL modeling is based on the viscous-inviscid interaction (VII) principle, as illustrated in Figure 1-2, which decomposes the real flow of viscous nature into an equivalent inviscid flow (EIF) and a defect region (e.g. boundary layer). Instead of modeling all of the real flow using RANS methods, VII methods solve for the inviscid flow and the defect in a coupled manner. Inviscid solutions using, for example, full-potential or Euler solvers can be orders-of-magnitude faster than RANS-based viscous solutions as shown in Table 1.1. As for the defect region, it is highly localized in high-Reynolds-number flows which are of primary interest in aircraft aerodynamics. In this case, the viscous effects can be effectively modeled using the IBL equations, a significant simplification of the underlying Navier-Stokes equations. The IBL model only adds fractional computational cost on top of the inviscid solution due to the reduced topological dimension, and hence leads to the overall efficiency of the VII method.

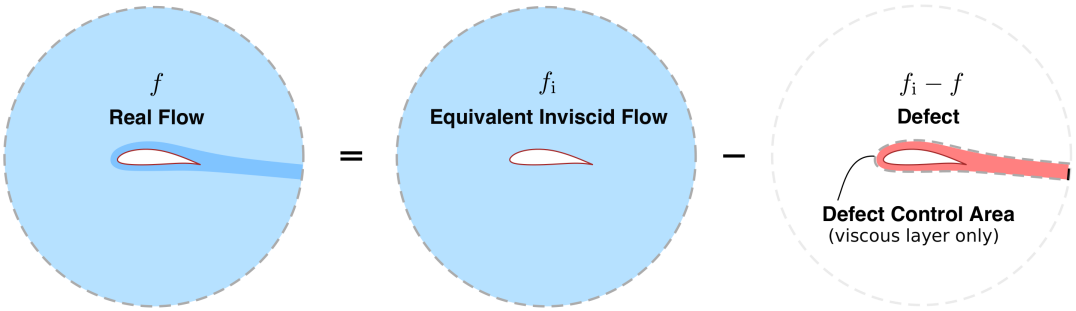

Figure 1-2: Domain decomposition of flow field in viscous-inviscid interaction

Moreover, while the RANS solutions can characterize flows with 3D details, such seemingly rich information is often unwieldy to visualize and interpret in practice. Hence, surface pressure and skin friction tend to be the focus when interrogating

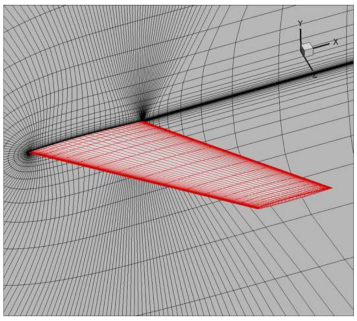

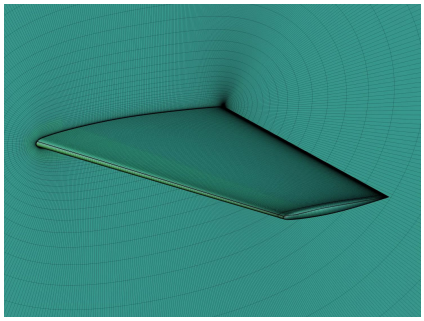

Method	Full-potential [9]	RANS [6]
Grid cell count	$\sim$ 200,000	$\sim$ 8,000,000
CPU time	$\sim$ 18 seconds	$\sim$ 28 hours
Hardware	single-core laptop	120-processor cluster

Table 1.1: Computational cost comparison between representative 3D full-potential (left) and RANS (right) solution methods. Sample computational grids for the M6 wing, courtesy of Refs. [5] (left) and [6] (right)

RANS results. To glean further insights into the drag-producing loss mechanisms from the development of the boundary layer and wake, RANS solutions need to be post-processed to obtain quantities such as the momentum defect thicknesses θ_{ij} $(i, j \in \{1, 2\})$ and kinetic energy dissipation rate $\mathcal{D}$ summarized in Equations (A.11) and (A.12), which are directly related to the overall viscous drag, viewed from force and energy perspectives, respectively. Besides, $\mathcal{D}$ is a convenient and unambiguous measure to track energy dissipation, which produces profile drag, and fits well into the power balance analysis of aerodynamic flows [10]. Although the post-processing of thickness integrals (such as θ and $\mathcal{D}$) can be tedious and complicated for RANS, they are directly characterized in the IBL equations (see Equations (2.1) to (2.4)) and readily computed from the IBL solution, which can then be easily utilized in design.

1.2 Previous Work

In the past several decades, two-dimensional (2D) viscous aerodynamic design and analysis has in fact benefited tremendously from the coupled IBL methods for its rapid computational speed. For example, XFOIL is able to compute an entire drag polar for an airfoil within a few seconds [11] and achieve comparable or even better solution accuracy than RANS solvers, especially in cases with flow transition [12]. Moreover, for fluid-structural interacting problems, the aerostructural coupling is more conveniently realized using a displacement body model in IBL [13], in contrast to mesh movement algorithms required for RANS methods [14].

Quasi-2D IBL methods have also been developed, such as Boeing's proprietary TRANAIR code (coupling a 3D full-potential solver with quasi-2D IBL) [15, 16, 17]. TRANAIR was reported to be a dominant CFD tool within Boeing [16], and to offer two to four orders of magnitude faster speed with more reliable grid convergence in contrast to its RANS counterpart [17]. However, the underlying assumptions of weak 3D effects are only strictly applicable to cases such as high aspect-ratio wings and axisymmetric bodies. Hence, quasi-2D IBL methods fall short on fully 3D flow features that frequently appear on general aircraft configurations such as wing-fuselage joints.

Early developments of the 3D IBL method in the 1970s and 1980s [18, 19, 20, 21] were formulated in surface curvilinear coordinates and thus are not readily applicable to complex 3D geometries. These difficulties were later addressed by finite-element formulations of the IBL equations [22, 23]. The subsequent development of a four-equation 3D IBL formulation by Drela [3] captures additional crossflow modes and maintains rotational invariance.

Despite the aforementioned progress, some critical questions still remain to be

addressed before the 3D IBL method is ready for aerodynamic design in practice. First, existing 3D IBL closure models are mostly carried over from established 2D closures and then combined with simple heuristic 3D assumptions, which limits the reliability of the overall IBL method in terms of both accuracy and robustness. Second, flow transition modeling has not been studied in any detail in previous 3D IBL methods, but remains a challenging yet important problem in terms of physical modeling and numerical treatment. Last but not least, although numerical discretization such as finite element and finite volume methods are suitable for 3D IBL on general geometries, the robustness of the numerical solution has received little attention in previous studies. Better understanding of numerical stabilization for the IBL equations is likely necessary for robust solution in the presence of complex scenarios involving, for example, boundary layer separation and free transition.

1.3 Thesis Contributions and Outline

The advantages of the IBL formulation and its successes in 2D and quasi-2D applications motivate the work in this thesis to close the technical gaps among existing 3D IBL methods. The major thesis contributions are summarized as follows.

1. This thesis presents novel strategies for 3D IBL closure modeling and develops a new and complete set of closure models. As part of this study, original boundary layer data sets have been generated from the numerical solution of 3D differential boundary layer equations and RANS equations, which marks a unique data-driven modeling effort for the 3D IBL closure. Regression-based IBL closure models are formulated for the first time based on neural network models that are customized to embed physical constraints and facilitate variable selection. Also new to the IBL context, a model inversion formulation

is proposed and trialed for automated data-driven calibration of the turbulent shear stress transport model.

2. This thesis also contributes by investigating the proper numerical stabilization for the discontinuous Galerkin (DG) finite element method (FEM) of the IBL equations. Although finite element discretization of the 3D IBL equations has appeared in previous studies, its stability has not been examined closely or stress-tested. In fact, numerical studies in this work are the first to reveal that heuristic numerical flux schemes for DG FEM lead to ill-posed numerical solutions in the presence of boundary layer separation and transition. Despite difficulties of devising the numerical flux based on 3D IBL characteristic analysis, an intermediate modification on stabilization is proposed and is able to produce well-behaved numerical solutions.

3. Another contribution of this thesis is the exploration and proposal of a suitable numerical treatment of flow transition for 3D IBL. While the capability of 3D transition prediction was lacking in previous 3D IBL methods, this thesis proposes and compares two ways of numerical treatment for transition: *fitting* and *capturing*. Based on a first-of-its-kind comparison between both methods, transition capturing is demonstrated to be more favorable and effective and thus recommended for transition modeling in the 3D IBL method.

This thesis is organized to first present the 3D IBL formulation along with viscous-inviscid interaction in Chapter 2. Chapter 3 describes the IBL closure problem and associated modeling approaches. Next, the finite element numerical discretization scheme and necessary modification for IBL are discussed in Chapter 4. Chapter 5 presents the proposed flow transition capturing method in comparison to the alter-

native transition fitting approach. Finally, Chapter 6 concludes with a summary and areas for future work.

Chapter 2

Integral Boundary Layer Formulation

This chapter summarizes the key elements of a 3D IBL model, including its governing equations and boundary conditions and the fully-simultaneous viscous-inviscid interaction scheme.

2.1 Governing Equations

A four-equation 3D IBL formulation is adopted in this work, following the development by Drela [3]. This thesis summarizes the main theoretical elements, while Appendix A provides a more detailed exposition including nomenclature and derivation.

The following equations are derived from mass and momentum conservation laws, under the thin shear layer and first-order boundary layer approximations. They apply to most high-Reynolds-number aerodynamic flows with at most relatively shallow

separations for which the thin shear layer approximations remain valid.

$$\frac{\partial m}{\partial t} + \widetilde{\nabla} \cdot \mathbf{M} - \rho_{\mathrm{e}}\, \mathbf{q}_{\mathrm{e}} \cdot \hat{\mathbf{n}}_{\mathrm{w}} = 0 \tag{2.1}$$

$$\frac{\partial \mathbf{M}}{\partial t} - \mathbf{q}_{\mathrm{e}} \frac{\partial m}{\partial t} + \widetilde{\nabla} \cdot \overline{\overline{\mathbf{P}}} + \mathbf{M} \cdot \widetilde{\nabla} \mathbf{q}_{\mathrm{e}} - \boldsymbol{\tau}_{\mathrm{w}} = \mathbf{0} \tag{2.2}$$

$$\frac{\partial e}{\partial t} - \rho_{\mathrm{e}} \mathbf{Q} \cdot \frac{\partial \mathbf{q}_{\mathrm{e}}}{\partial t} - q_{\mathrm{e}}^2 \frac{\partial m}{\partial t} + \widetilde{\nabla} \cdot \mathbf{K} + \mathbf{D} \cdot \widetilde{\nabla} \left(q_{\mathrm{e}}^2\right) - 2\,\mathcal{D} = 0 \tag{2.3}$$

$$\begin{aligned} &\frac{\partial k^{\circ}}{\partial t} + \frac{e}{q_{\mathrm{e}}^2} \left(\mathbf{q}_{\mathrm{e}} \times \frac{\partial \mathbf{q}_{\mathrm{e}}}{\partial t} \right) \cdot \hat{\mathbf{n}} - \rho_{\mathrm{e}} \mathbf{Q} \times \frac{\partial \mathbf{q}_{\mathrm{e}}}{\partial t} \cdot \hat{\mathbf{n}} - 2\rho_{\mathrm{e}} \mathbf{Q}^{\circ} \cdot \frac{\partial \mathbf{q}_{\mathrm{e}}}{\partial t} + \widetilde{\nabla} \cdot \mathbf{K}^{\circ} \\ &+ \frac{\mathbf{E}}{q_{\mathrm{e}}^2} \cdot \left(\mathbf{q}_{\mathrm{e}} \times \widetilde{\nabla} \mathbf{q}_{\mathrm{e}} \right) \cdot \hat{\mathbf{n}} - \frac{1}{2} \rho_{\mathrm{e}} \mathbf{Q} \times \widetilde{\nabla} (q_{\mathrm{e}}^2) \cdot \hat{\mathbf{n}} - \rho_{\mathrm{e}} \mathbf{Q}^{\circ} \cdot \widetilde{\nabla} (q_{\mathrm{e}}^2) + \mathcal{D}^{\times} + 2\mathcal{D}^{\circ} = 0 \end{aligned} \tag{2.4}$$

Appendix A provides detailed derivation and related definitions. Equations (2.1) to (2.4) are the mass, momentum, kinetic energy and lateral curvature equations respectively, involving the following quantities that characterize the boundary layer.

$$\begin{aligned} m, \mathbf{M}, \overline{\overline{\mathbf{P}}}, k, \mathbf{K}, \mathbf{Q}, \mathbf{D}, e, \mathbf{E}, k^{\circ}, \mathbf{K}^{\circ}, \mathbf{Q}^{\circ} \qquad & \text{integral defects} \\ \boldsymbol{\tau}_{\mathrm{w}} \qquad & \text{wall shear stress vector} \\ \mathcal{D}, \mathcal{D}^{\times}, \mathcal{D}^{\circ} \qquad & \text{dissipation integrals} \end{aligned} \tag{2.5}$$

The modeling of these quantities constitutes the IBL closure problem and plays a crucial role in the overall IBL method. Chapter 3 discusses the closure models in greater detail.

Equations (2.1) to (2.4) are defined on a topologically 2D manifold (i.e. a surface within the 3D space) on which the shear layer develops. This surface is uniquely identified by a surface normal unit vector field $\hat{\mathbf{n}}$, which is aligned with the boundary layer thickness coordinate. For example, one convenient choice as adopted in this

thesis is the aerodynamic surface (e.g. of a wing) as illustrated in Figure 2-1, in which case $\hat{\mathbf{n}}$ coincides with the commonly-used outward-pointing wall-normal unit vector $\hat{\mathbf{n}}_\mathrm{w}$. Alternatively, the field $\hat{\mathbf{n}}$ can deviate from the solid surface to model, for example, geometric perturbation or fairing, although this option has not been implemented in this work. The unit vectors $\{\hat{\mathbf{e}}_1, \hat{\mathbf{e}}_2, \hat{\mathbf{n}}\}$ form a local Cartesian basis. The surface-tangent vectors $\hat{\mathbf{e}}_1$ and $\hat{\mathbf{e}}_2$ are intended to resolve the vector momentum equation (2.2) into two in-plane scalar components and their construction in the finite element discretization scheme is discussed in Chapter 4. It is worth distinguishing $\{\hat{\mathbf{e}}_1, \hat{\mathbf{e}}_2\}$, which can be arbitrarily chosen, from the streamwise-crossflow basis $\{\hat{\mathbf{s}}_1, \hat{\mathbf{s}}_2\}$ which are uniquely defined based on the equivalent inviscid flow as in Equation (A.7). The in-surface gradient and divergence operators are denoted by $\widetilde{\nabla}()$ and $\widetilde{\nabla} \cdot ()$ respectively. The velocity $\mathbf{q}_\mathrm{e}$ (of magnitude q_e) and density ρ_e at the notional boundary layer edge are governed by the inviscid flow model through viscous-inviscid interaction.

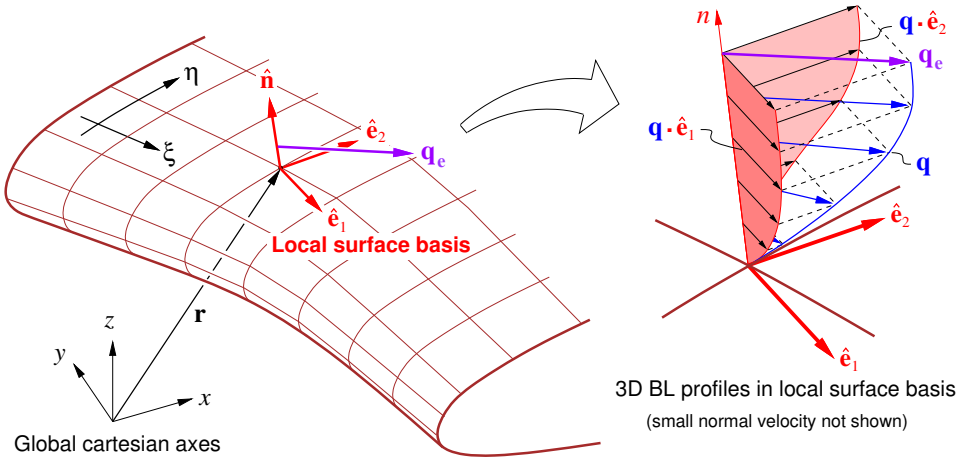

Figure 2-1: Example wing surface geometry, local Cartesian basis $\{\hat{\mathbf{e}}_1, \hat{\mathbf{e}}_2, \hat{\mathbf{n}}\}$ and 3D boundary layer velocity profile. Reproduced from Ref. [3] with permission.

The mass equation (2.1) relates the wall transpiration mass flux $\rho_\mathrm{e}\, \mathbf{q}_\mathrm{e} \cdot \hat{\mathbf{n}}_\mathrm{w}$ to the

viscous effects (specifically, defect quantities m and $\mathbf{M}$ defined in Appendix A) and serves as a boundary condition to the inviscid flow.

Collectively, the momentum, kinetic energy and lateral curvature equations (i.e. Equations (2.2), (2.3) and (2.4)) constitute the four-equation 3D IBL governing equations. The momentum equation consists of two independent in-surface scalar components, while its surface-normal component is discarded in accordance with the first-order boundary layer approximation. It is worth noting that Equations (2.2) and (2.3) form the basis of the three-equation 3D IBL formulation of earlier work such as in Ref. [22, 24]. Equation (2.4) was introduced by Drela with the aim of enriching the 3D boundary layer crossflow representation in a rotation-invariant manner [3].

The primary variables for the 3D IBL equations are denoted by $\mathcal{Q}_{\text{IBL}}$. The choice of $\mathcal{Q}_{\text{IBL}}$ is not unique, but, as a rule of thumb, should consist of independent variables that collectively provide an expressive characterization of the boundary layer. This work chooses the definition as

$$\mathcal{Q}_{\text{IBL}} \equiv \{\delta_1^*, \delta_2^*, \theta_{11}, \theta_{12}\} \tag{2.6}$$

which are thickness integrals (defined in Equation (A.11)) characterizing streamwise and crossflow boundary layer profiles as well as their coupling (as in θ_{12}). The utility of this choice is corroborated by the effective IBL closure models discussed in Chapter 3.

In this work, the IBL equations are further augmented with the e^N envelope method for modeling flow transition (see Chapter 5) and the "lag" equation for modeling turbulent shear stress transport (see Section 3.4). These models introduce additional variables, i.e. $\tilde{n}$ and $\mathcal{G}$ respectively.

2.2 Boundary Conditions

The following IBL boundary conditions are considered in this work.

2.2.1 Inflow

At the inflow boundary, the full IBL solution is specified based on Dirichlet boundary data (denoted by the subscript BC) .

$$\begin{aligned} \delta_1^* &= (\delta_1^*)_{\mathrm{BC}} \\ \delta_2^* &= (\delta_2^*)_{\mathrm{BC}} \\ \theta_{11} &= (\theta_{11})_{\mathrm{BC}} \\ \theta_{12} &= (\theta_{12})_{\mathrm{BC}} \end{aligned} \tag{2.7}$$

This boundary condition assumes that all the characteristics enter into the computational domain. One example is the inlet boundary for a flat plate.

2.2.2 Outflow

At the outflow boundary, no boundary condition is specified which amounts to assuming that all the characteristics exit from the computational domain. Examples include the outflow boundary of a flat plate or a wake.

2.2.3 Slip Sidewall

For a slip sidewall, the flow tangency condition needs to be satisfied, i.e.

$$\mathbf{q} \cdot \hat{\mathbf{t}} = 0 \tag{2.8}$$

where the unit vector $\hat{\mathbf{t}}$ is orthogonal to the sidewall and tangent to the IBL manifold. As a corollary, the inviscid flow should also satisfy flow tangency $\mathbf{q}_e \cdot \hat{\mathbf{t}} = 0$. Then, the following Dirichlet boundary conditions follow from the closure definition in Section A.3,

$$\begin{aligned} \delta_2^* &= 0 \\ \theta_{12} &= 0 \end{aligned} \tag{2.9}$$

which corresponds to a vanishing boundary layer crossflow at the sidewall. For a straight slip sidewall, this boundary condition is equivalent to that for a symmetry plane. A sample use case of this boundary condition is the centerline of a standalone half wing.

For a curved sidewall, the boundary condition (2.9) is not well-posed as discussed in Appendix D. The main reason is that both the IBL equations and the differential boundary layer equations might lack mechanisms for driving the crossflow to zero at the sidewall. In contrast, the full Navier-Stokes equations remain well-posed since they retain the terms (for example, in-plane diffusion) discarded based on the thin shear layer assumption. The curved slip sidewall boundary condition is mainly for academic curiosity rather than of significant interest for practical aerodynamic applications.

2.2.4 Comments on Characteristics

The inflow, outflow and straight slip sidewall boundary conditions have been verified to produce well-behaved numerical solution in all the test cases presented in this thesis. On the other hand, the proper number and type of IBL boundary conditions should ideally be determined based on the analysis of characteristics (into or

out of the computational domain). However, such analysis is analytically difficult and practically unwieldy due to various complications including the form of the IBL equations, the underlying IBL closure and viscous-inviscid interaction. Appendix C presents more details on the characteristic analysis, including the difficulties associated with it.

2.3 Viscous-inviscid Interaction

A viscous-inviscid interaction (VII) scheme is also necessary for utilizing the IBL method. One conspicuous reason is that the IBL equations require a definition of the edge velocity field $\mathbf{q}_e$ which should come from a model of the external inviscid flow field. Lock and Williams presented a comprehensive discussion of the VII theory and a summary of VII schemes, ranging from weak coupling by one-way interaction to strong coupling by simultaneous viscous-inviscid solution [25].

In addition, the IBL equations (with adequate closure) are subject to the so-called Goldstein Separation Singularity [26, 13]. That is, if a prescribed edge velocity field $\mathbf{q}_e$ drives the flow to separation, the IBL equations become ill-defined in the sense that the solution no longer exists, or at best is no longer unique. As a symptom of this issue, the Jacobian $\partial\mathcal{R}_{\mathrm{IBL}}/\partial Q_{\mathrm{IBL}}$ in Equation (2.14) becomes singular. In consequence, unless the viscous-inviscid solution is strongly coupled so that $\mathbf{q}_e$ can be modified by the shear layer, the VII schemes are either incapable of or not robust for practical aerodynamic analysis involving boundary layer separation.

Hence, a strong coupling approach as presented in Ref. [27] is adopted here, which also allows for coupling with different inviscid flow solvers. Table 2.1 summarizes components of the overall VII formulation, for the example of IBL coupled with an incompressible potential flow model.

Table 2.1: List of abbreviations, variables, residuals and governing equations in the coupled global system

Abbreviation	Unknown Q	Residual $\mathcal{R}$	Governing Equation(s)
IBL	$\mathcal{Q}_{\text{IBL}}, \tilde{n}, \mathcal{G}$	IBL	(2.2), (2.3), (2.4), (5.1), (3.16)
inv	Φ	Inviscid	(2.10)
auxi	Λ	Auxiliary inviscid	(2.11)
auxv	$\mathbf{q}_{\text{e}}$	Auxiliary viscous	(2.12)

The governing equation for incompressible potential flow is

$$\nabla^2 \Phi = 0 \qquad \text{subject to} \qquad (\rho_{\text{i}}\, \mathbf{q}_{\text{i}})_{\text{w}} \cdot \hat{\mathbf{n}}_{\text{w}} = \Lambda \;\; \text{(boundary condition)} \tag{2.10}$$

where Φ is the velocity potential and the flow velocity is $\mathbf{q}_{\text{i}} = \nabla\Phi$. The source term Λ in the *wall transpiration* boundary condition models the viscous displacement effect, geometry deformation or wall blowing/suction. The corresponding numerical solution of 3D inviscid flow can be obtained using a potential flow solver on a volume grid or a panel method.

Viscous-inviscid coupling is realized through the following additional auxiliary equations defined on the IBL manifold,

$$\Lambda - \widetilde{\nabla} \cdot \mathbf{M} = 0 \tag{2.11}$$

$$\mathbf{q}_{\text{e}} - \mathbf{q}_{\text{i}} = 0 \tag{2.12}$$

where Λ and $\mathbf{q}_{\text{e}}$ are the corresponding auxiliary variables. The mass defect flux $\mathbf{M}$ (defined in Equation (A.9)) depends the IBL solution and the auxiliary variable $\mathbf{q}_{\text{e}}$. The auxiliary variables Λ and $\mathbf{q}_{\text{e}}$ are discretized using finite elements of appropriate

orders (i.e. commensurate with the discretization of viscous and inviscid equations) and the discrete auxiliary equations are essentially L_2-projections.

2.3.1 Global Newton Solution Method

The VII formulation results in the following global coupled system of equations,

$$\boldsymbol{\mathcal{R}}(\boldsymbol{Q}) = \boldsymbol{0}, \qquad \boldsymbol{\mathcal{R}} \equiv \begin{pmatrix} \mathcal{R}_{\text{auxv}}(Q_{\text{auxv}}, Q_{\text{inv}}) \\ \mathcal{R}_{\text{auxi}}(Q_{\text{auxv}}, Q_{\text{auxi}}, Q_{\text{IBL}}) \\ \mathcal{R}_{\text{IBL}}(Q_{\text{auxv}}, Q_{\text{IBL}}) \\ \mathcal{R}_{\text{inv}}(Q_{\text{auxi}}, Q_{\text{inv}}) \end{pmatrix}, \qquad \boldsymbol{Q} \equiv \begin{pmatrix} Q_{\text{auxv}} \\ Q_{\text{auxi}} \\ Q_{\text{IBL}} \\ Q_{\text{inv}} \end{pmatrix} \tag{2.13}$$

where $\boldsymbol{\mathcal{R}}$ and $\boldsymbol{Q}$ denote the global residual and solution respectively, with their components summarized in Table 2.1. The viscous-inviscid interaction is manifested in the structure of the Jacobian of the global residual,

$$\left[\frac{\partial \boldsymbol{\mathcal{R}}}{\partial \boldsymbol{Q}}\right] = \begin{pmatrix} \left[\frac{\partial \mathcal{R}_{\text{auxv}}}{\partial Q_{\text{auxv}}}\right] & 0 & 0 & \left[\frac{\partial \mathcal{R}_{\text{auxv}}}{\partial Q_{\text{inv}}}\right] \\ \left[\frac{\partial \mathcal{R}_{\text{auxi}}}{\partial Q_{\text{auxv}}}\right] & \left[\frac{\partial \mathcal{R}_{\text{auxi}}}{\partial Q_{\text{auxi}}}\right] & \left[\frac{\partial \mathcal{R}_{\text{auxi}}}{\partial Q_{\text{IBL}}}\right] & 0 \\ \left[\frac{\partial \mathcal{R}_{\text{IBL}}}{\partial Q_{\text{auxv}}}\right] & 0 & \left[\frac{\partial \mathcal{R}_{\text{IBL}}}{\partial Q_{\text{IBL}}}\right] & 0 \\ 0 & \left[\frac{\partial \mathcal{R}_{\text{inv}}}{\partial Q_{\text{auxi}}}\right] & 0 & \left[\frac{\partial \mathcal{R}_{\text{inv}}}{\partial Q_{\text{inv}}}\right] \end{pmatrix} \tag{2.14}$$

where the two off-diagonal sub-matrices $\partial \mathcal{R}_{\text{inv}}/\partial Q_{\text{IBL}}$ and $\partial \mathcal{R}_{\text{IBL}}/\partial Q_{\text{inv}}$ vanish by design to avoid intrusive interdependence between viscous and inviscid solvers.

To achieve strong viscous-inviscid coupling, the global coupled solution is solved

simultaneously using a Newton method. The n-th Newton solution update is,

$$\boldsymbol{\mathcal{R}}(\boldsymbol{Q}^n) + \left[\frac{\partial \boldsymbol{\mathcal{R}}}{\partial \boldsymbol{Q}}\right]^n \Delta \boldsymbol{Q}^n = \boldsymbol{0} \tag{2.15}$$

$$\boldsymbol{Q}^{n+1} = \boldsymbol{Q}^n + \beta\, \Delta \boldsymbol{Q}^n \tag{2.16}$$

Equation (2.15) can be solved by a direct or iterative linear solver depending on factors such as the size, sparsity pattern and conditioning of the linear system. Also, the residual and solution ordering in Equation (2.13) determine the sparsity pattern in the global Jacobian in Equation (2.14) and can be optimized for memory and computation efficiency of the linear solution, depending on the characteristics of the inviscid and auxiliary equations. For example, the sub-matrix $\partial \mathcal{R}_{\text{inv}}/\partial Q_{\text{inv}}$ is dense for a classic panel method but sparse for a potential or Euler solver. The relaxation factor β controls the step size of the solution update. An initial solution guess $\boldsymbol{Q}^0$ is provided for the Newton update to start with.

Nonlinear solution robustness is enhanced using a line-search algorithm and pseudo-transient continuation (PTC) [28]. The line search adapts the step size β to avoid solutions that violate physical validity or increase residuals (beyond some tolerance). The PTC method introduces a time derivative (hence the name of pseudo-transient) and solves the artificially unsteady problem until the solution converges to a steady state.

It is worth noting that these nonlinear solution enhancement techniques cannot be applied if a transition fitting approach is adopted to model flow transition. Instead, the nonlinear solution resorts to an under-relaxed Newton method which compromises robustness and efficiency in general. This is a primary reason for pursuing the transition capturing method rather than fitting, as discussed in Chapter 5.

Chapter 3

Integral Boundary Layer Closure

This chapter formulates the IBL closure problem, reviews existing closure models and describes new strategies for closure construction, including neural network regression models and an automated model calibration method for turbulence stress transport in the IBL context.

To complete the 3D IBL governing equations requires closure models that map independent parameters (collectively denoted by $\boldsymbol{v}$) to closure quantities (collectively denoted by $\mathcal{F}$) that completely define the thickness variables and coefficients in Equations (A.11) and (A.12) and thereby quantities in Equation (A.9). The following map $\boldsymbol{v} \mapsto \mathcal{F}(\boldsymbol{v})$ is an example that provides closure to the 3D IBL equations.

$$\begin{aligned} \boldsymbol{v} &\equiv (\mathbf{q}_\mathrm{e}, \rho_\mathrm{e}, \mu_\mathrm{e}, \mathcal{Q}_\mathrm{IBL}) \\ \mathcal{F}(\boldsymbol{v}) &\equiv \{\theta_{11}, H_0, H_1, H_2, H_{k_1}, H_{k_2}, H_{10}, H_{20}, H_{12}, H_{21}, H_{22}, \\ &\qquad H_0^*, H_1^*, H_2^*, H_{d_1}, H_{d_2}, H_0^\circ, H_1^\circ, H_2^\circ, c_{f_1}, c_{f_2}, c_\mathcal{D}, c_\mathcal{D}^\times, c_\mathcal{D}^\circ\} \end{aligned} \tag{3.1}$$

where $\mathcal{Q}_\mathrm{IBL}$ denotes the primary IBL variables such as defined in Equation (2.6) and is four-dimensional (i.e. $\mathcal{Q}_\mathrm{IBL} \in \mathbb{R}^4$) for a four-equation 3D IBL formulation. It worth

noting that the parametrization $\boldsymbol{v}$ in Equation (3.1) only serves as an example, but the final form of parametrization is determined based on variable selection discussed in Section 3.3.

The IBL closure modeling involves the following two main tasks and is elaborated in the ensuing sections.

1. Variable selection: identify a suitable parametrization, i.e. $\boldsymbol{v}$ (including $\mathcal{Q}_{\text{IBL}}$)
2. Closure modeling: identify a suitable mapping $\boldsymbol{v} \mapsto \mathcal{F}(\boldsymbol{v})$

3.1 Existing 3D IBL Closure

Existing 3D IBL closure models require significant improvement to be useful in practice. For example, the four-equation IBL formulation of Drela adopts a *profile-based approach* [3], where the normalized velocity profiles $U(\eta; \boldsymbol{v}), W(\eta; \boldsymbol{v})$ (illustrated in Figure A-3) are assumed to be functions parametrized by a handful of parameters $\boldsymbol{v}$. The task of closure construction becomes learning the profile parametrization operator that maps shape parameters $\boldsymbol{v}$ to profile functions $U(\cdot; \boldsymbol{v}), W(\cdot; \boldsymbol{v})$. Existing profile families are heuristically constructed, usually based on polynomials. In consequence, these assumed parametrized functions can miss some realistic profile modes while introducing non-physical ones. A more methodical way to construct these profile families is to leverage 3D boundary layer data and carry out *operator learning* using tools such as DeepONet [29] and Neural Implicit Flow [30] (an even more general framework). These data-driven approaches are widely applicable but are potentially too complicated and costly (in terms of both training and inference) for the IBL closure.

Moreover, since only the velocity profiles are parametrized, the calculation of the

integrals in Equations (A.11) and (A.12) requires computation-intensive numerical quadrature. The numerous evaluations of those integrals on the fly (for example, at each quadrature point of a finite element method) required for the IBL solution incurs a prohibitively high computational cost and is subject to inaccurate quadrature rules (particularly for turbulent profiles with an exponential behavior in the log layer).

An alternative closure strategy is to employ a *regression-based approach* that constructs a regression model $\mathcal{F}(\boldsymbol{v})$. Here, the task of multivariate regression modeling is simpler than the operator learning problem for profile-based closure. Also, the computation of $\mathcal{F}(\boldsymbol{v})$ sidesteps the need of numerically integrating profile quantities and hence can be computationally efficient if the model itself is not too complicated. For example, correlation relations have been developed for 2D IBL models and widely used in examples such as XFOIL [11] and MSES [31]. Nishida extended these existing 2D correlations to a three-equation 3D IBL formulation with primary variables $\mathcal{Q}_{\text{IBL}} \equiv \{\delta_1^*, \delta_2^*, \theta_{11}\}$ that require much fewer non-trivial closure models than Equation (3.1) [22]. However, instead of carrying out comprehensive regression based on 3D boundary layer data, heuristic assumptions were made to define and derive crossflow-related closure models (i.e. $\left\{H_{12},\, H_{21},\, H_{22},\, H_2^*,\, c_{f_2}\right\}$). Hence, these closure relations therein introduce only limited 3D enrichment and are susceptible to crossflow misrepresentation.

Figure 3-1 compares the profile-based and the regression-based closure strategies. In favor of its efficient computation and convenient construction, this work sets out to develop regression-based IBL closure models based on 3D boundary layer data.

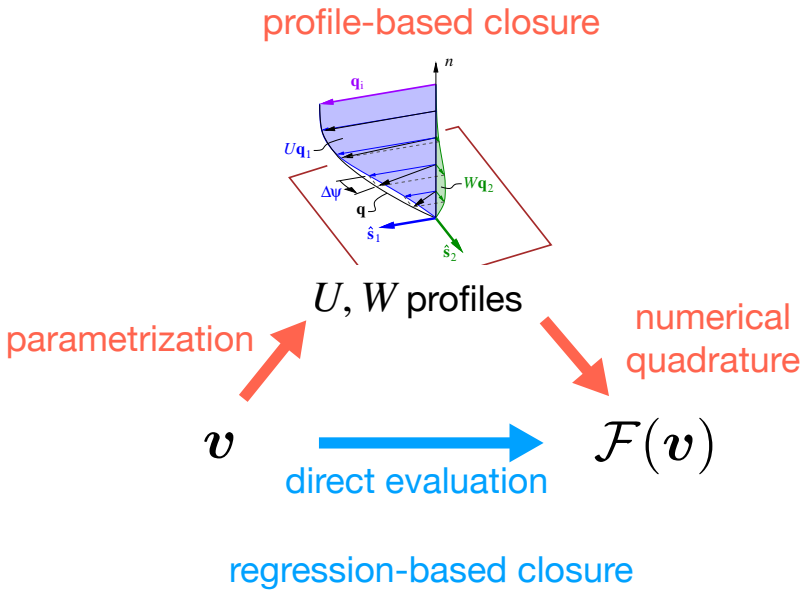

Figure 3-1: Comparison between profile-based closure and regression-based closure

3.2 Three-dimensional Boundary Layer Data Set

Data is the basis for regression-based closure modeling. In this work, extensive 3D boundary layer data are generated from numerical simulations of higher fidelity than IBL. A suite of cases of 3D boundary layers involving crossflow and separation phenomena are carried out. For example, one set of cases includes boundary layers developing on a flat plate under a spatially-varying pressure gradient (both favorable and adverse) induced by a torpedo-shaped [3] or a sphere-shaped body over the flat plate. These cases are parametrized by the shape and location of the body to produce various data of boundary layer profiles with 3D features, as detailed in Sections 3.5.2 and B.3.

The laminar boundary layer data are generated from a finite-difference solver of 3D differential boundary layer equations developed by Drela [32]. Such a solution is numerically exact (up to discretization errors) for laminar boundary layers modeled

with thin shear layer approximations. To produce 3D turbulent data, a Reynolds-averaged Navier Stokes solver with a Spalart-Allmaras turbulence model (RANS-SA) is used [28]. The total sample size is about 15,000 and 78,000 for laminar and turbulent data respectively. Each sample corresponds to an instance of an entire boundary layer profile.

The choice of data source here is intended to conveniently generate a meaningfully large data set and cover various 3D boundary layer features. On the other hand, numerical solution of even higher fidelity (such as LES and DNS) and experimental data are potential alternative sources that are more accurate, but are not considered in this work due to their limited quantity, high acquisition cost, and, in some cases, incomplete description of the closure quantities listed in Equation (3.1).

3.3 Neural Network Regression Model

The closure model $\mathcal{F}(\boldsymbol{v})$ is constructed by defining a suitable set of low-dimensional input variables $\boldsymbol{v}$ and obtaining the function $\mathcal{F}$ of a higher-dimensional co-domain via a regression algorithm. This task is mathematically a *dimension reduction* problem. To this end, generic fully data-driven algorithms can be applied. For example, an autoencoder neural network method can be used to discover low-dimensional latent variables while providing the low-to-high-dimension mapping via its decoder component (see Chapter 14 of Ref. [33]). However, fully data-driven methods tend to require large amounts of data, more than what is typically available in a physical modeling setting. Also, the identified low-dimensional space is, if at all, hardly interpretable from a physics perspective.

Hence, the need of physical interpretability motivates the use of physics-grounded domain knowledge. In fact, the same principle motivates the choice of IBL primary

variables $\mathcal{Q}_{\text{IBL}}$ in Equation (2.6). The dimensional parameters in Equation (3.1) are then non-dimensionalized to provide the following unit-invariant parametrization

$$\boldsymbol{v} \equiv (H_1, H_2, H_{12}, Re_{\theta_{11}}) \tag{3.2}$$

where $Re_{\theta_{11}}$ the Reynolds-number based on θ_{11} and the shape factors H result form normalization by θ_{11} as defined in Equation (A.15). The input $\boldsymbol{v}$ can be further augmented with Mach number M_{e} to account for compressibility effects. This extension would require more compressible boundary layer data and is left to future work.

Given that θ_{11} is chosen as an IBL variable and the simplification by the identities and approximations in Equations (A.13), (A.16) and (A.17), closure relations remaining to be constructed reduce from Equation (3.1) to the following non-dimensionalized quantities.

$$\left(H_{22}, H_1^*, H_2^*, H_{d_1}, H_{d_2}, H_0^\circ, H_1^\circ, H_2^\circ, c_{f_1}, c_{f_2}, c_{\mathcal{D}}, c_{\mathcal{D}}^\circ\right)$$

In this work, the closure mapping $\boldsymbol{v} \mapsto \mathcal{F}(\boldsymbol{v})$ is represented with fully-connected feed-forward neural networks (FNN), primarily motivated by the expressiveness and convenience for multivariate regression. While fundamentals of neural networks are well covered in existing literature such as Ref. [33], we focus on specific aspects that are most relevant to IBL closure modeling.

A dedicated FNN model is fitted for each individual component of the vector $\mathcal{F}$, as opposed to having all output components sharing the same neural network, in order to maximize fitting accuracy. Each neural network has two hidden layers with the same width as the respective input. For example, the input before variable selection is given in Equation (3.2). After variable selection, the input definition follows the

functional forms given in the lists (3.6) and (3.7). The choice of neural network configuration is driven by trial-and-error hyperparameter tuning. Also, a parsimonious model as such is intentionally pursued for fast computation and to avoid overfitting, as opposed to very deep and wide neural networks. Computational efficiency is an important consideration here because closure models need to be frequently evaluated and differentiated (using automatic differentiation) in the overall IBL method, e.g. for computing the IBL equation residual $\mathcal{R}_{\text{IBL}}$ and Jacobian $\partial\mathcal{R}_{\text{IBL}}/\partial Q_{\text{IBL}}$ in Equation (2.13). The hyperbolic tangent activation function is adopted mainly to obtain differentiable closure relations, a desired property for the Newton method used to solve the overall nonlinear system of equations (see Section 2.3.1).

Standard practices for neural network training are adopted, including data standardization and a 80-20 data split (i.e. 80% for training and 20% for validation). Additional L_2 and L_1 regularization (with a modest weighting factor of 10^{-5} for each) on the weights and biases are introduced in training the final trimmed functional forms in the lists (3.6) and (3.7), although they are not necessary in the variable selection because the primary goal therein is to identify important parameters.. The training is carried out using the ADAM optimizer with a learning rate of 10^{-3}. The training and selection of the neural network models are implemented using TensorFlow [34].

3.3.1 Variable Selection

It is worth noting that the full parametrization defined in Equation (3.2) is not directly used in closure construction because not all the variables are equally effective in parametrizing the closure relations. In order to identify important parameters and obtain parsimonious models, a *variable selection* procedure is carried out to find the lowest-dimensional yet effective input parametrization. While a wide variety of

variable selection methods exist [35], this work draws on inspiration from Refs. [36, 37, 38] and adopts a sparsity regularization approach that naturally applies to the neural network models herein.

To introduce this sparsity-regularized variable selection method, a generic FNN model denoted by $h : \boldsymbol{v} \mapsto h(\boldsymbol{v})$ is considered. It can be viewed as a composition of two function components g and a such that $h \equiv g \circ a$. Here, g encapsulates the composite mapping from the first layer of hidden states to the final output. That is, it involves the activation functions of the first layer, all the ensuing hidden layers, and the output layer. The function a represents the affine transformation from the input $\boldsymbol{v}$ to the first layer of hidden states, with weights W and bias $\mathbf{b}$ as follows.

$$a(\boldsymbol{v}) \equiv W\boldsymbol{v} + \mathbf{b} \equiv \begin{bmatrix} | & | & \\ \boldsymbol{w}_1 & \boldsymbol{w}_2 & \cdots \\ | & | & \end{bmatrix} \begin{bmatrix} v_1 \\ v_2 \\ \vdots \end{bmatrix} + \begin{bmatrix} b_1 \\ b_2 \\ \vdots \end{bmatrix} \tag{3.3}$$

The column vector $\boldsymbol{w}_i$ encodes the influence of the input component v_i to the ensuing layers and hence the final output. All the components v_i have been normalized using the standard scaler presented in Section B.2 and thus have a similar order of magnitude. Hence, the magnitude (in terms of L_2 norm) of $\boldsymbol{w}_i$ provides a comparative measure of significance for v_i. For example, if $\|\boldsymbol{w}_i\|_2$ vanishes, it means that v_i does not affect the final output at all.

In training the FNN model, the following sparse-input regularization term is added to the conventional mean-square-error (MSE) loss,

$$\gamma \sum_{i=1}^{d} \|\boldsymbol{w}_i\|_2 \tag{3.4}$$

where d is the input dimension (i.e. the dimension of $\boldsymbol{v}$) and γ is a tunable parameter to balance sparsity regularization and least-squares fit. The effect of the added regularization term is to reduce the number of significant variables and hence promote sparsity in the input. In practice, there is no need to optimize γ. Instead, a series of γ values are trialed to verify if certain variables are consistently deemed important. The less important variables are discarded from the final parametrization.

Take the following initial functional form of turbulent boundary layer closure for example.

$$H_2^\circ(H_1, H_2, H_{12}, \log_{10}(Re_{\theta_{11}})) \tag{3.5}$$

The relative magnitudes of weights $\boldsymbol{w}_i$ of a trained neural network model are summarized in Table 3.1, and imply a small influence on H_2° due to the Reynolds number $Re_{\theta_{11}}$. Hence, the functional form is further simplified to $H_2^\circ(H_1, H_2, H_{12})$.

Input component	H_1	H_2	H_{12}	$\log_{10}(Re_{\theta_{11}})$
$\dfrac{\lVert \boldsymbol{w}_i \rVert_2}{\max_i \lVert \boldsymbol{w}_i \rVert_2}$	0.446	1.00	0.492	0.0275

Table 3.1: Magnitude of input influence weight vectors. ($\log_{10}(Re_{\theta_{11}})$ is used in practice as an input variable since $Re_{\theta_{11}}$ spans a few orders of magnitude.)

Based on the aforementioned variable selection process, the final closure model is parametrized with the selected subset of input variables and trained again to obtain

its eventual form, resulting in the following functional dependence,

$$
\begin{array}{lll}
H_{22}\left(H_1, H_2, H_{12}\right) & H_1^*(H_1) & H_2^*(H_2, H_{12}) \\
H_{d_1}(H_2) & H_{d_2}\left(H_1, H_2, H_{12}\right) & \\
H_0^\circ(H_2, H_{12}) & H_1^\circ(H_2, H_{12}) & H_2^\circ\left(H_1, H_2, H_{12}\right) \quad \text{(laminar)} \\
Re_{\theta_{11}} c_{f_1}(H_1) & Re_{\theta_{11}} c_{f_2}\left(H_1, H_2, H_{12}\right) & \\
Re_{\theta_{11}} c_{\mathcal{D}}(H_1) & Re_{\theta_{11}} c_{\mathcal{D}}^\circ\left(H_1, H_2, H_{12}\right) &
\end{array}
\tag{3.6}
$$

$$
\begin{array}{lll}
H_{22}\left(H_1, H_2, H_{12}\right) & H_1^*(H_1, Re_{\theta_{11}}) & H_2^*(H_2, H_{12}) \\
H_{d_1}(H_2, H_{12}) & H_{d_2}(H_2, H_{12}) & \\
H_0^\circ(H_2, H_{12}) & H_1^\circ(H_2, H_{12}) & H_2^\circ\left(H_1, H_2, H_{12}\right) \quad \text{(turbulent)} \\
c_{f_1}(H_1, H_2, Re_{\theta_{11}}) & c_{f_2}(H_1, H_{12}, Re_{\theta_{11}}) & \\
c_{\mathcal{D}}\left(Re_{\theta_{11}}, H_1, H_2, H_{12}, c_\tau\right) & c_{\mathcal{D}}^\circ\left(H_2, H_{12}, Re_{\theta_{11}}, c_{\mathcal{D}}\right) &
\end{array}
\tag{3.7}
$$

where the turbulent dissipation relation $c_{\mathcal{D}}$ is re-calibrated from the 2D baseline formulation in Equation (3.17) and discussed in detail in Section 3.4.

It is worth noting that, for laminar flows, $\left\{c_{f_1}, c_{f_2}, c_{\mathcal{D}}, c_{\mathcal{D}}^\circ\right\}$ are multiplied with $Re_{\theta_{11}}$ to form the target output functions because the resulting products are independent of the Reynolds number and thereby simplify the closure. In contrast, the turbulent counterparts have a nontrivial dependence on the Reynolds number and hence include $Re_{\theta_{11}}$ as an input parameter.

3.3.2 Constraints Embedding

Certain constraints also need to be imposed on the closure relations. First, by closure definitions in Equations (A.11) and (A.12), two crossflow velocity profiles that are

symmetric with respect to each other (i.e. $W(n)$ and $-W(n)$) should satisfy the following relations.

$$H_{22}, H_1^*, H_{d_2}, H_2^\circ, c_{f_1}, c_{\mathcal{D}} \quad \text{symmetric (same value)} \tag{3.8}$$

$$H_2, H_{12}, H_2^*, H_{d_1}, H_0^\circ, H_1^\circ, c_{f_2}, c_{\mathcal{D}}^\circ \quad \text{anti-symmetric (opposite value)} \tag{3.9}$$

These closure quantities need to be symmetric or anti-symmetric with respect to H_2 and/or H_{12} which are among the input parameters. Second, 2D boundary layer profiles (i.e. without any crossflow) have $H_2 = H_{12} = 0$ and other closure quantities analytically known a priori, such as $H_2^* \equiv 0$. Hence, the invariant relations like $H_2^*(H_2 = 0, H_{12} = 0) \equiv 0$ should ideally be encoded in the closure model. Also, a useful property for the newly developed 3D closure relations is to match existing 2D closure in the case of a 2D boundary layer. These constraints are not automatically satisfied by the plain neural network model, which thus needs modification to incorporate that prior knowledge either weakly or exactly [39].

Learning solely from data is a common way to impose constraints "softly". It simply relies on minimizing the least-squares fitting error in hope that the constraints encoded in the data are reflected in the learned model. However, such an expectation is never fully met in practice due to, for example, noise in the data and imperfect optimization in the training. Besides, the demand for sample size is often impractically high compared to what is available in the context of physical modeling. Hence, the constraints are only enforced weakly rather than being satisfied exactly.

As an alternative, the neural network model in this work is manipulated to embed relevant constraints in an exact manner. In terms of enforcing the symmetry constraint in neural networks, another attempt has appeared in Ref. [40], albeit in a univariate context with a more complicated formulation. Let functions $f : \mathbb{R}^d \to \mathbb{R}$

and $h : \mathbb{R}^d \to \mathbb{R}$ denote the target closure and a generic FNN model respectively, for the input parameter $\boldsymbol{v} \in \mathbb{R}^d$. The proposed closure is composed of FNN models in the following forms,

$$f(\boldsymbol{v}) \equiv h(\boldsymbol{v}) + h(\overline{\boldsymbol{v}}) \qquad \Rightarrow f(\boldsymbol{v}) \equiv f(\overline{\boldsymbol{v}}) \qquad \text{(symmetry)} \tag{3.10}$$

$$f(\boldsymbol{v}) \equiv h(\boldsymbol{v}) - h(\overline{\boldsymbol{v}}) \qquad \Rightarrow f(\boldsymbol{v}) \equiv -f(\overline{\boldsymbol{v}}) \qquad \text{(anti-symmetry)} \tag{3.11}$$

where $\overline{\boldsymbol{v}}$ is the an input vector that is identical to $\boldsymbol{v}$ except for having opposite values for the subset of crossflow-related components. For example, $\overline{\boldsymbol{v}} = (H_1, -H_2, -H_{12})$ for $\boldsymbol{v} = (H_1, H_2, H_{12})$. By construction, the function f automatically satisfies symmetry or anti-symmetry constraints, as in the following examples,

$$H_{22}(H_1, H_2, H_{12}) \equiv H_{22}(H_1, -H_2, -H_{12}) \qquad \text{(symmetry)} \tag{3.12}$$

$$c_{f_2}(H_1, H_{12}, Re_{\theta_{11}}) \equiv -c_{f_2}(H_1, -H_{12}, Re_{\theta_{11}}) \qquad \text{(anti-symmetry)} \tag{3.13}$$

The same idea of customizing function representation is also be applied to construct 3D closure that encompasses existing 2D closure relations (denoted by $f_{2\mathrm{D}}$) as follows,

$$f(\boldsymbol{v}) \equiv f_{2\mathrm{D}}(\boldsymbol{v}) + h(\boldsymbol{v}) - h(\boldsymbol{v}_{2\mathrm{D}}) \qquad \Rightarrow \qquad f(\boldsymbol{v}_{2\mathrm{D}}) \equiv f_{2\mathrm{D}}(\boldsymbol{v}_{2\mathrm{D}}) \tag{3.14}$$

where $\boldsymbol{v}_{2\mathrm{D}}$ refers to a 2D flow state, e.g. $(H_1, H_2, H_{12})_{2\mathrm{D}} \equiv (H_1, 0, 0)$. Another condition of zero intercept is also of interest, for example, $H_{22}(H_1, H_2 = 0, H_{12} = 0) \equiv 0$. This condition is enforced using the following functional form,

$$f(\boldsymbol{v}) \equiv h(\boldsymbol{v}) - h(\boldsymbol{v}_{2\mathrm{D}}) \qquad \Rightarrow \qquad f(\boldsymbol{v}_{2\mathrm{D}}) \equiv 0 \tag{3.15}$$

The final closure models are documented in Appendix B.2, which are embedded with applicable constraints given in Equations (3.12), (3.13), (3.14) and (3.15) .

3.4 Turbulence Model Calibration by Inversion

Turbulent shear stress transport is modeled with the following "lag" equation,

$$\begin{aligned}\frac{\partial \mathcal{G}}{\partial t} + \mathbf{q}_{\mathrm{e}} \cdot \widetilde{\nabla} \mathcal{G} - \frac{q_{\mathrm{e}}}{2\,\widetilde{\delta}} \left[5.6 \left((c_\tau)_{\mathrm{eq}}^{1/2} - {c_\tau}^{1/2} \right)\right] \\ - \frac{q_{\mathrm{e}}}{B_{\mathrm{eq}} \delta_1^*} \left[\frac{c_{f_1}}{2} - \left(\frac{H_1 - 1}{A_{\mathrm{eq}} K_{\mathrm{dl}} H_1} \right)^2 \right] + \widetilde{\nabla} \cdot \mathbf{q}_{\mathrm{e}} = 0\end{aligned} \tag{3.16}$$

and the variable $\mathcal{G} \equiv \ln({c_\tau}^{1/2})$ feeds into the IBL equations via the dissipation formula.

$$(c_{\mathcal{D}})_{\mathrm{2D}} = \frac{c_{f_1}}{2} U_S + c_\tau \left(1 - U_S\right) \tag{3.17}$$

Details of the model parameters and closure are given in Appendix A. The lag equation and the dissipation formula were originally developed for 2D IBL methods and need to be re-calibrated using the current 3D RANS data.

The interaction between the turbulent shear stress model and the IBL equations is diagrammed in Figure 3-2. The IBL equations receive information solely through the energy dissipation rate characterized by $c_{\mathcal{D}}$. Motivated by this feedback structure, this work focuses on revising the 2D dissipation relation in Equation (3.17) by introducing a *model correction factor* β in the following form.

$$c_{\mathcal{D}} = \beta \, (c_{\mathcal{D}})_{\mathrm{2D}} = \beta \left[\frac{c_{f_1}}{2} U_S + c_\tau \left(1 - U_S\right) \right] \tag{3.18}$$

The correction factor β is calibrated by *inversion* and then modeled as an additional closure relation.

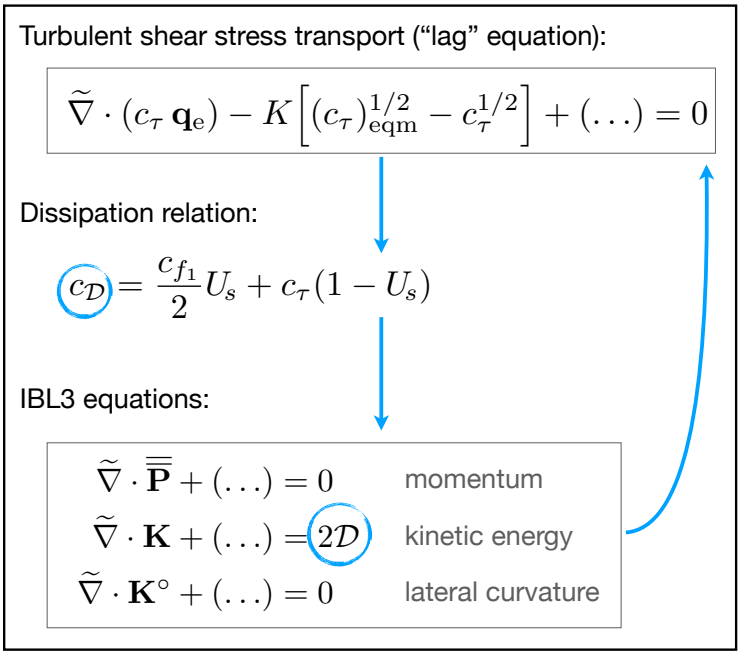

Figure 3-2: Two-way coupling structure between the 3D IBL (IBL3) equations and the lag equation through the dissipation relation

The inversion step solves an inverse problem where the function $\beta : (x, y, z) \mapsto \beta(x, y, z)$ is optimized to minimize the $c_{\mathcal{D}}$ prediction error as measured against the reference value $(c_{\mathcal{D}})_{\text{data}}$ obtained from RANS solution. The corresponding mathematical statement is as follows,

$$\arg\min_{\beta} \|c_{\mathcal{D}}(\beta) - (c_{\mathcal{D}})_{\text{data}}\| \qquad \text{subject to} \qquad \{\text{3D IBL, lag}\} \text{ equations} \tag{3.19}$$

where the norm does not need to be defined explicitly since the optimal solution is obtained analytically by the following shortcut.

To solve the optimization problem (3.19) for a given case, the RANS reference

solution $(c_{\mathcal{D}})_{\text{data}}$ is prescribed for the 3D IBL equations by setting $c_{\mathcal{D}} = (c_{\mathcal{D}})_{\text{data}}$ rather than using the lag equation and the dissipation relation. Hence, an optimality condition for the problem (3.19) is attained by construction. In doing so, the coupling between the IBL equations and the lag equation becomes one-way; that is, the lag equation and the variable c_τ do not affect the IBL solution $\mathcal{Q}_{\text{IBL}}$, but $\mathcal{Q}_{\text{IBL}}$ drives the solution c_τ through the lag equation. Computed based on such solution $\mathcal{Q}_{\text{IBL}}$ and c_τ, the model correction factor chosen as $\beta \equiv (c_{\mathcal{D}})_{\text{data}}/(c_{\mathcal{D}})_{\text{2D}}$ proves to be an optimal solution to the problem (3.19). This strategy requires only a single numerical solution of the 3D IBL equations along with the lag equation.

A data set of analytically optimal solution β can be obtained by carrying out the aforementioned procedure for all the RANS samples and then employed to construct another closure relation in the functional form of

$$(H_1, H_2, H_{12}, Re_{\theta_{11}}, c_\tau) \mapsto \beta$$

using the neural network regression model discussed in Section 3.3.

3.4.1 Rationale for Inversion Formulation

It is worth noting the rationale underpinning the model inversion formulation proposed in Section 3.4. First of all, the optimization statement forms the conceptual basis of the generic class of model calibration and parameter estimation problems, albeit instantiated in the IBL terms. The traditional approach is to adjust β by trial and error, effectively carrying out a manual and heuristic optimization procedure until time and resources run out. This strategy was used in calibrating the dissipation formula and lag equation parameters in the development of MSES [31] and XFOIL [11, 41]. More recently, the inversion problem (3.19) has been solved numer-

ically to calibrate RANS turbulence and transition models by minimizing errors in, respectively, the predicted lift coefficient or flow transition location measured against experimental data [42, 43].

However, the PDE-constrained optimization problem is expensive and complicated to solve using iterative optimization algorithms. The main reason is that numerous iterations are required to attain optimality (albeit approximately and often locally in practice) and each iteration requires solving the PDE. Hence, the inversion technique in this work stands out as a more efficient and convenient alternative, enabled primarily by the judicious choice of model correction formulation in Equation (3.18) and the problem-specific coupling structure between the IBL and lag equations. If the model correction factor β were introduced to the lag equation instead (as an additive or multiplicative parameter), then a more complicated numerical optimization procedure would be necessary, similar to Refs. [42, 43].

Another important consideration in formulating the inversion problem for model calibration is the choice of the objective function for the problem (3.19). The current method does not attempt to match higher-level derived output quantities such as lift and drag coefficients. Otherwise, the optimization problem is potentially ill-posed in the sense that it risks unnecessarily or fortuitously compensating for errors due to other components of the overall IBL method, for example, different closure relations and numerical discretization etc., which are not associated with the specific turbulence model to be calibrated.

3.5 Numerical Results

The section presents a series of numerical results to demonstrate the effectiveness of the closure models described in this chapter. The proposed closure has been

incorporated in the four-equation 3D IBL formulation (see Chapter 2) discretized using a discontinuous Galerkin (DG) finite element method (see Chapter 4).

3.5.1 Three-equation vs. Four-equation 3D IBL Formulation

The first test case compares the three-equation and the four-equation variants of 3D IBL formulation, and thereby demonstrates the expected advantage of the four-equation formulation (including its closure) for characterizing 3D boundary layer profiles with crossflow crossover. To the best knowledge of the author, this work is the first to substantiate such a comparison with concrete numerical examples.

This case examines boundary layer flow on a flat plate. A manufactured edge velocity field $\mathbf{q}_\mathrm{e}$ is prescribed for the boundary layer and defined as follows,

$$\mathbf{q}_\mathrm{e}(x, y) = V_\infty \left[x\, \hat{\mathbf{x}} + \alpha\, (y - 0.05)(y - 1)\, \hat{\mathbf{y}} \right] \tag{3.20}$$

where the computational domain is defined for $(x, y) \in [0.05, 1] \times [0.05, 1]$ (with non-dimensional coordinates (x, y)), V_∞ is a velocity scale and $\alpha > 0$ is a tunable parameter. The velocity field $\mathbf{q}_\mathrm{e}$ is irrotational in order to model inviscid flow. Although it is not incompressible, it does not affect the investigation into the IBL solution behavior. Figure 3-3 illustrates this manufactured flow field. It features a peak in flow speed q_e at the y-centerline across which the gradient $\widetilde{\nabla} q_\mathrm{e}$ switches direction. The intention is to induce crossover crossflow profiles in the boundary layer flow.

For the given $\mathbf{q}_\mathrm{e}$ field, the following IBL boundary conditions are well-posed and adopted.

- $x_\mathrm{min} = 0.05$: inflow (based on Blasius boundary layer states)

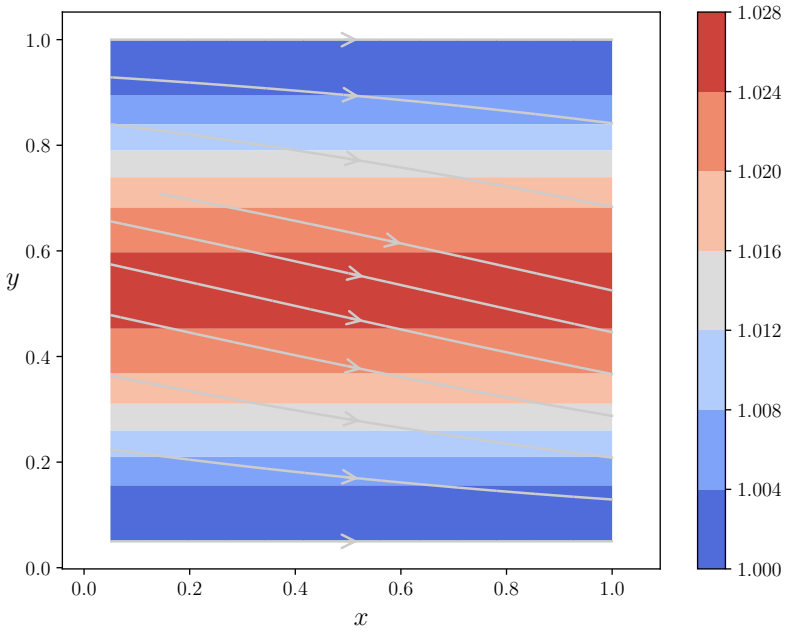

Figure 3-3: Manufactured flow field in Equation (3.20) for $\alpha = 1$: $\mathbf{q}_e$ streamlines and normalized flow speed q_e/V_∞ contour.

- $x_{\max} = 1$: outflow (based on domain interior states)
- $y_{\min} = 0.05$ and $y_{\max} = 1$: (straight) slip sidewall (i.e. $\delta_2^* = 0$ and $\theta_{12} = 0$)

The solution to the 3D differential boundary layer equations is obtained from the numerical solver DBL3 [32] and serves as a reference. Figure 3-4 illustrates a sample DBL3 result for laminar boundary layer and highlights an example of crossover crossflow profile.

Figures 3-5 and 3-6 compare the three-equation [22] and four-equation 3D IBL methods respectively to the DBL3 reference for the case of $\alpha = 0.5$. The four-equation 3D IBL result matches DBL3 very well, whereas the three-equation IBL3 result deviates noticeably from the other two methods (especially near the $x_{\max}$

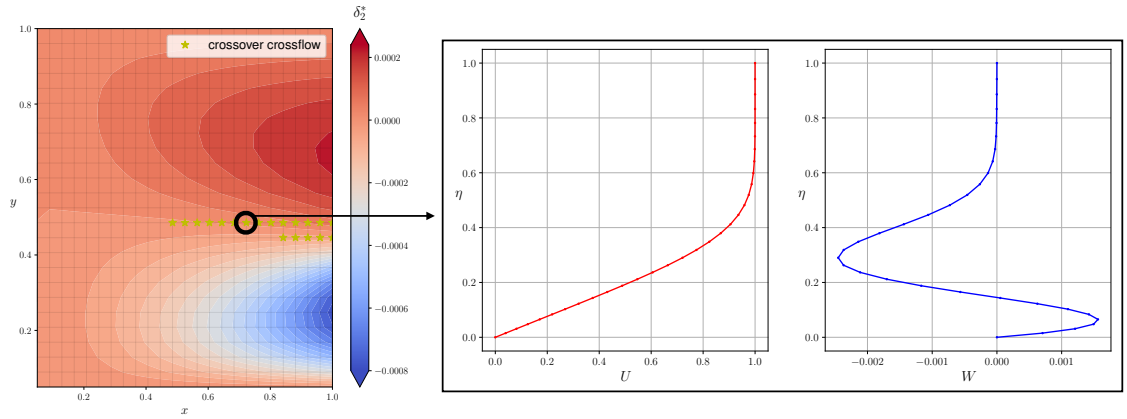

Figure 3-4: Case $\alpha = 1.0$: DBL3 result δ_2^* (left) and a sample boundary layer profile with crossover crossflow W (right)

boundary). As the crossflow crossover is intensified by increasing to $\alpha = 1.0$, the close match is maintained between the four-equation 3D IBL and DBL3 results, as shown in Figure 3-7. In contrast, the three-equation 3D IBL solution is no longer attainable in practice despite various attempts such as employing a more robust pseudo-transient nonlinear solver. This implies that the four-equation 3D IBL formulation with the proposed closure in this work outperforms its three-equation predecessor in terms of characterizing crossflow crossover. This favorable performance benefits from the additional lateral curvature equation and the fourth independent boundary layer variable θ_{12} which together provide a richer characterization of crossflow compared to the three-equation formulation with only a single crossflow-related primary variable δ_2^*.

3.5.2 3D Laminar Boundary Layer

The test case of 3D laminar boundary layer flow over a flat plate under spatially-varying pressure distribution from Ref. [3] is adopted here. The case setup is illus-

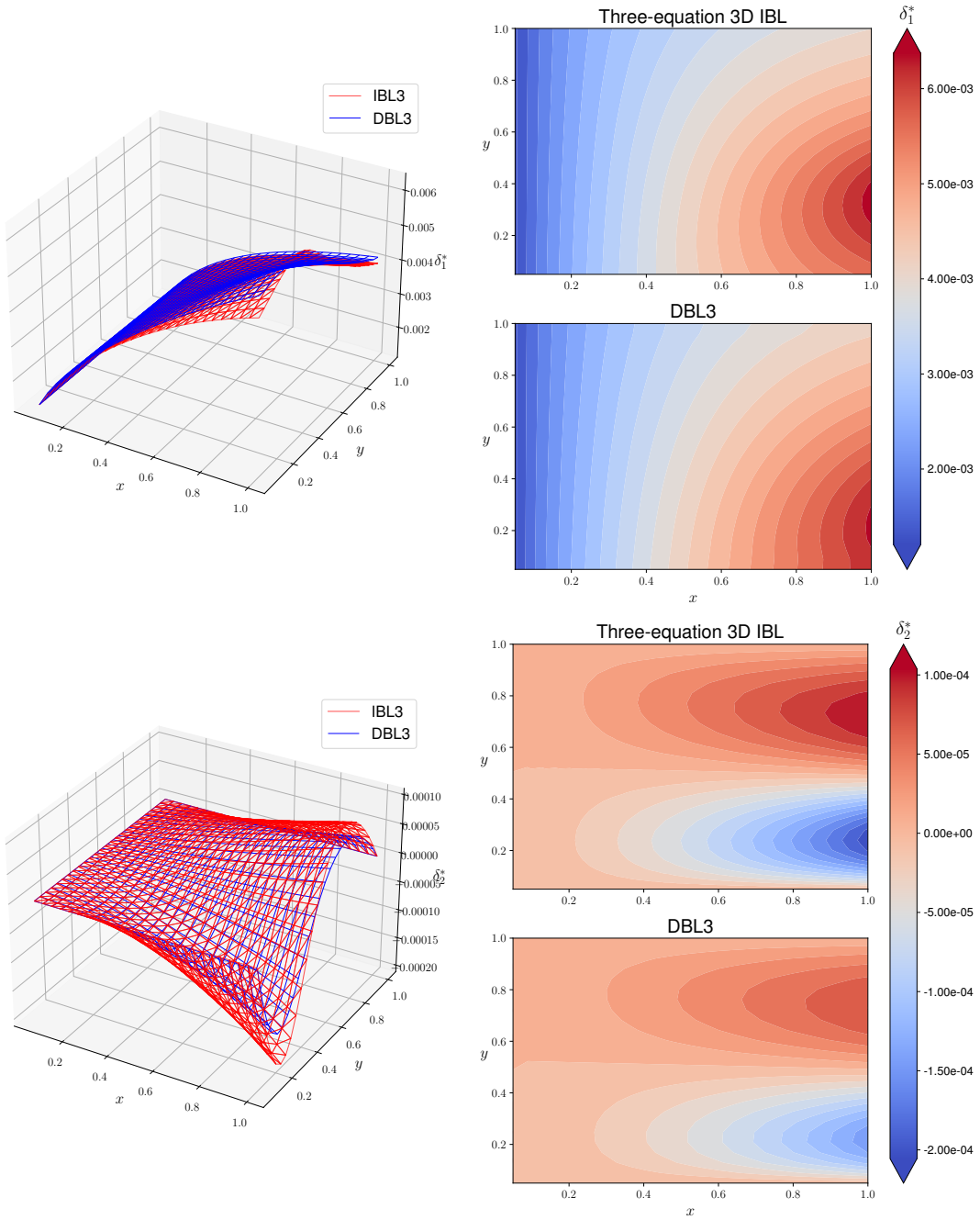

Figure 3-5: Case $\alpha = 0.5$: comparison between three-equation 3D IBL and DBL3

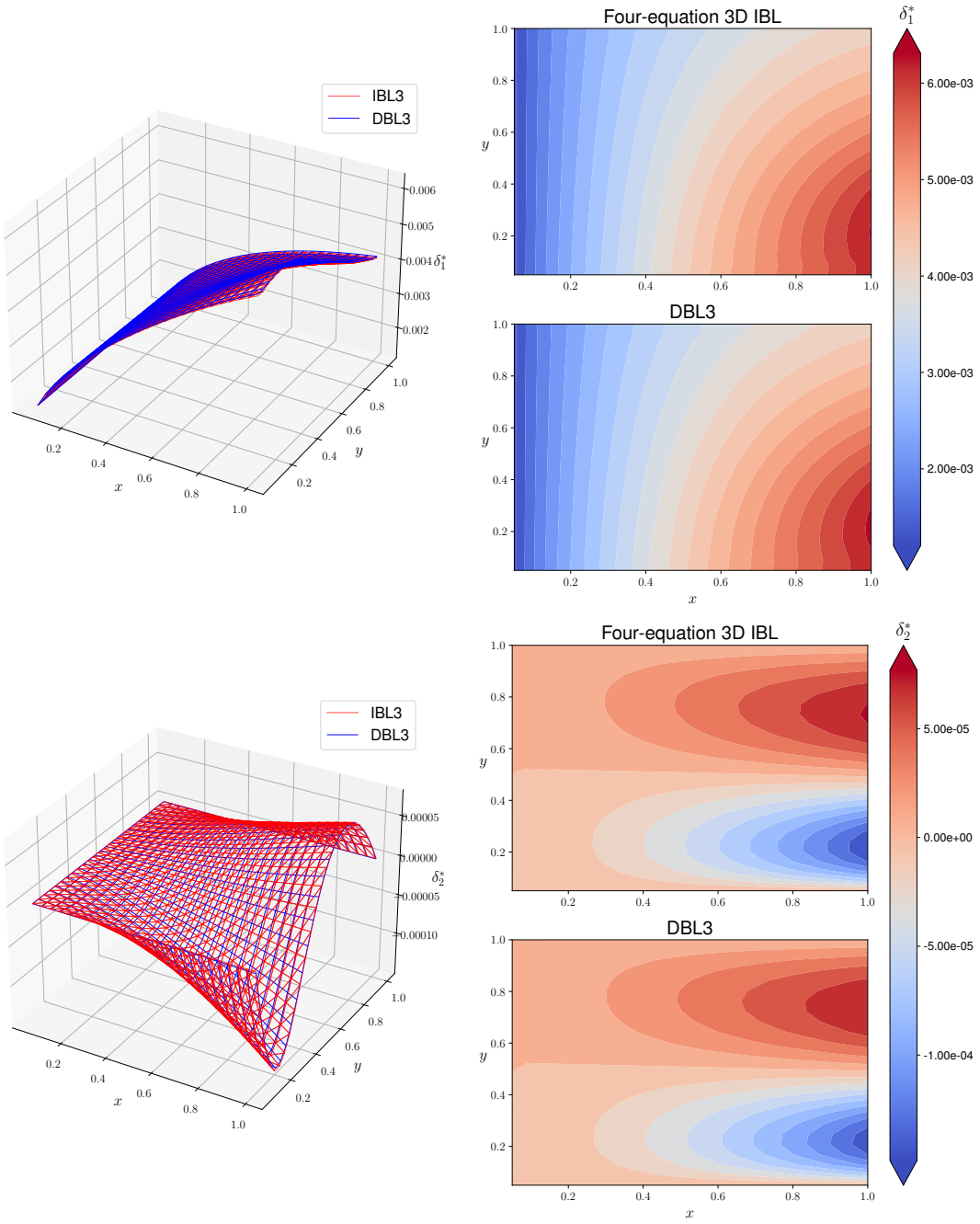

Figure 3-6: Case $\alpha = 0.5$: comparison between four-equation 3D IBL and DBL3

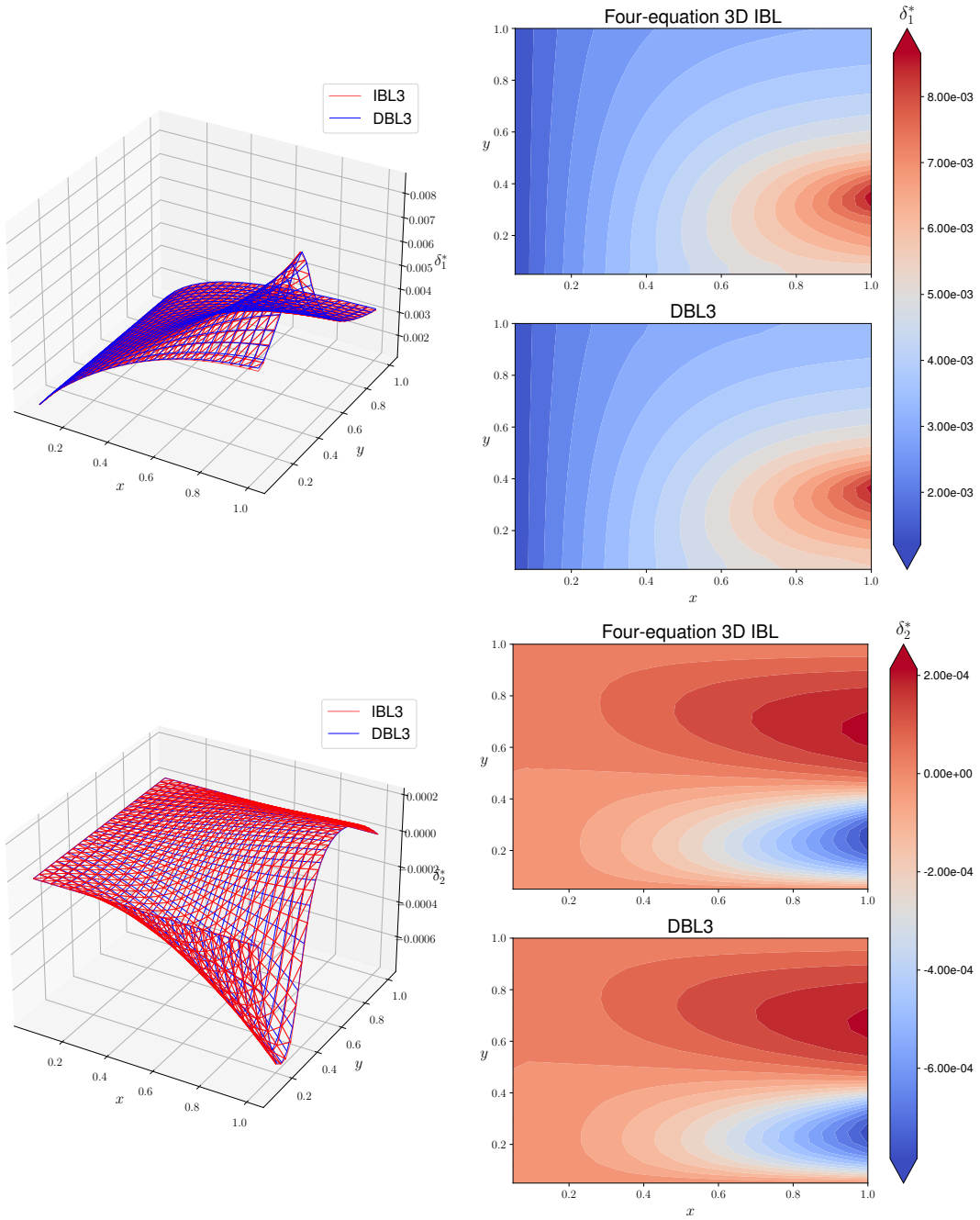

Figure 3-7: Case $\alpha = 1.0$: comparison between four-equation 3D IBL and DBL3

trated in Figure 3-8. The computational domain under consideration is the square patch of $[0.05, 1] \times [0.05, 1]$ the xy-plane rotated clockwise about the z-axis for 45 degrees so that one diagonal is aligned with the x-axis, as shown in Figure 3-9. The boundary layer develops on the flat plate with the leading edge at $x = 0$ and Dirichlet boundary conditions prescribed at the inflow edges based on the Blasius boundary layer solution (initiating from the leading edge). The Reynolds number based on unit plate length is 10^5. The torpedo-shaped body over the flat plate governs the pressure variation on the plate and thereby induces the 3D boundary layer behavior. The body is modeled by a point source parametrized by its center coordinates (x_c, y_c, z_c) and strength Σ.

A configuration is tested with the following set of parameters

$$(x_c, y_c, z_c) = (0.54446, 0, 0.12), \quad \Sigma/q_\infty = 0.02$$

which features significant pressure gradient in the crossflow direction as shown in Figure 3-9. This test configuration is not included in the training data set listed as follows.

- $(x_c, y_c, z_c) = (0.5, 0, 0.5), \quad \Sigma/q_\infty = 0.5$
- $(x_c, y_c, z_c) = (0.95, 0, 0.5), \quad \Sigma/q_\infty = 0.5$
- $(x_c, y_c, z_c) = (0.2, 0, 0.35), \quad \Sigma/q_\infty = 0.2$
- $(x_c, y_c, z_c) = (1.3, 0, 0.25), \quad \Sigma/q_\infty = 0.1$
- $(x_c, y_c, z_c) = (0.75, 0, 0.2), \quad \Sigma/q_\infty = 0.05$
- $(x_c, y_c, z_c) = (0.75, 0, 0.1), \quad \Sigma/q_\infty = 0.01$

The 3D IBL (IBL3) solution is compared against 3D differential boundary layer (DBL3) results as a reference. Figure 3-10 demonstrates a good match in the streamwise momentum thickness θ_{11} between IBL and DBL3, which is critical in achieving consistent drag prediction.

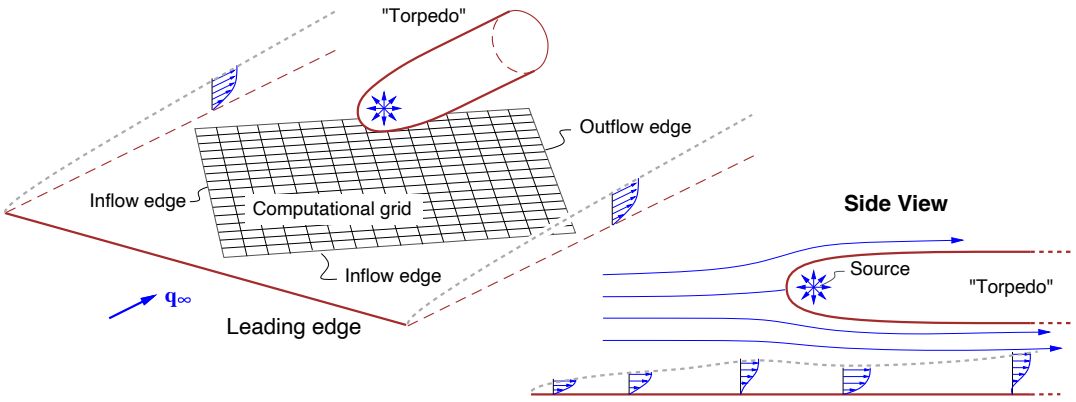

Figure 3-8: Test case setup: 3D laminar boundary layer developing under spatially-varying pressure distribution induced by a torpedo-shaped body on the flat plate. Reproduced with permission from Ref. [3]

3.5.3 Re-calibrated Turbulent Dissipation Relation

The turbulent boundary layer over a flat plate under zero pressure gradient is examined here. The Reynolds number per unit plate length is 10^6. Figure 3-11 compares the dissipation coefficient $c_{\mathcal{D}}$ predicted using the baseline 2D formulation and the revised version resulting from model inversion and neural network closure model. The revision demonstrates a good match with the reference RANS solution and a significant improvement compared to the baseline $c_{\mathcal{D}}$ model.

The model inversion approach herein is promising for calibrating the turbulence model based on a given set of reference data. On the other hand, it is worth noting that the model calibrated this way should not be expected to overcome the inherent

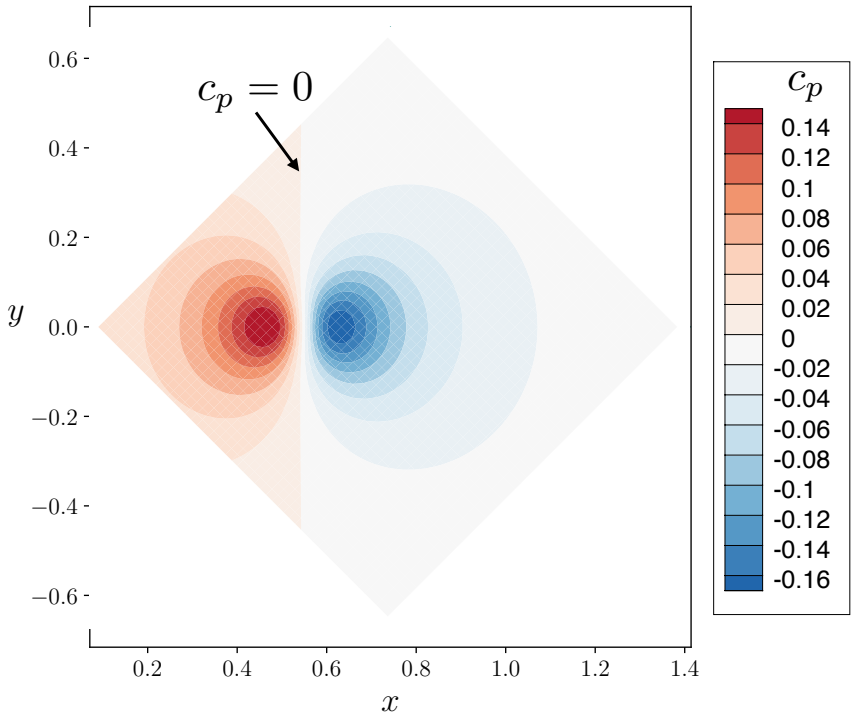

Figure 3-9: Pressure coefficient c_p distribution induced by the torpedo-shaped body over the flat plate surface. Freestream velocity is along the positive x direction.

limitations of the underlying reference data. That is, the best data-driven model is no better than the data-generating reference model in terms of physical fidelity. For example, since the RANS-SA model assumes isotropic turbulent shear stress and its solution is used as reference data for calibrating the IBL dissipation relation, the resulting IBL turbulence model does not generalize beyond that isotropy assumption. In this case, the main advantage of the IBL model with calibrated turbulent shear stress transport lies in its prospect of achieving predictive accuracy comparable to the RANS model at only a fraction of the computational cost. Also, the use of higher-fidelity reference data will potentially further improve the modeling capability of the calibrated IBL turbulence model.

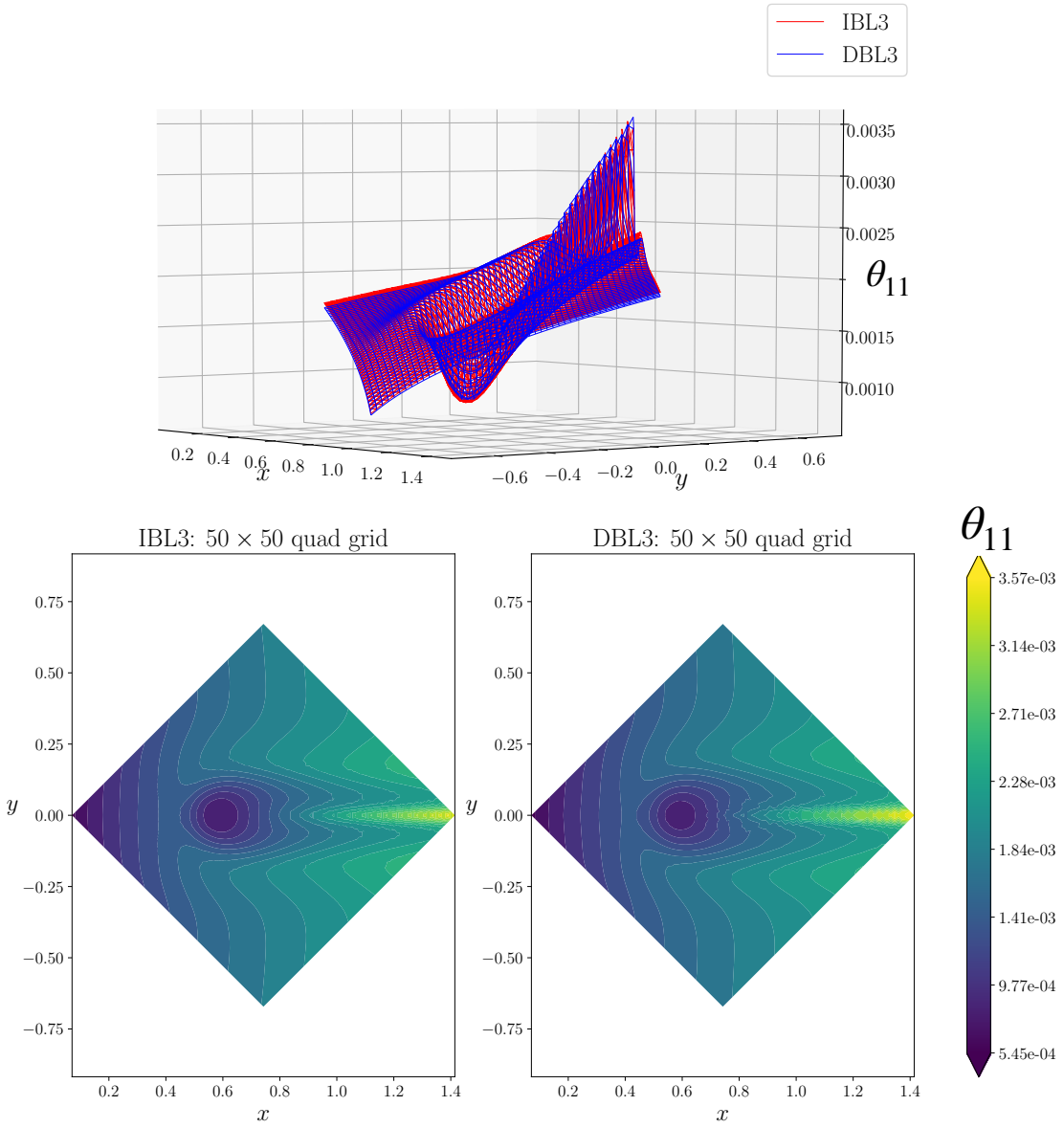

Figure 3-10: Comparison of streamwise momentum thickness θ_{11} obtained by 3D IBL (IBL3) and 3D differential boundary layer solution (DBL3).

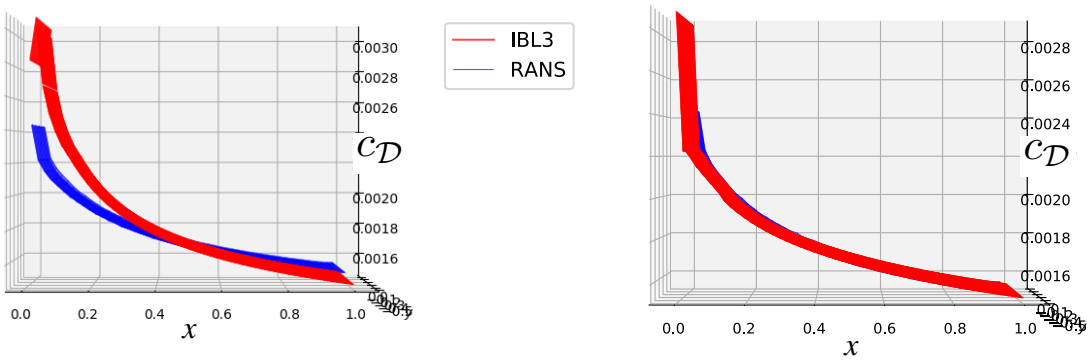

(a) $c_{\mathcal{D}}$

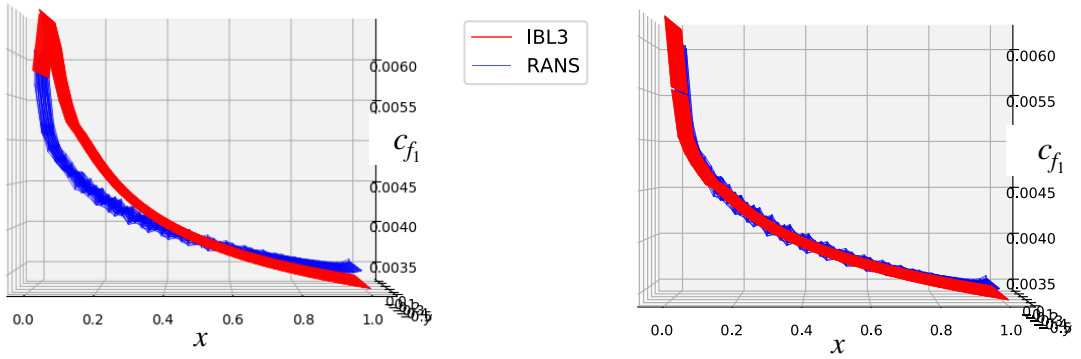

(b) c_{f_1}

Figure 3-11: Comparison between baseline (Equation (3.17)) and re-calibrated (Equation (3.18)) dissipation relations for $c_{\mathcal{D}}$. Results of $c_{\mathcal{D}}$ and c_{f_1} are shown. The RANS-SA solution serves as a reference.

Chapter 4

Finite Element Discretization

This chapter introduces the numerical discretization of the 3D IBL equations using a discontinuous Galerkin (DG) finite element scheme. Numerical studies conducted in this work have revealed that the DG formulation with heuristically-defined numerical flux schemes does not provide sufficient stabilization and thus leads to ill-behaved numerical solutions in some difficult-to-solve test cases. On the other hand, a rigorous characteristic analysis is not readily available for the IBL equations. Hence, this thesis proposes an intermediate stabilization method inspired by the momentum conservation law and tailored for IBL, which is able to regularize the numerical solution.

4.1 Discontinuous Galerkin Formulation

This section summarizes the key elements of the DG finite element discretization for 3D IBL. The computational domain identified with the open set $\Omega \subset \mathbb{R}^3$ in a topologically-2D manifold/surface is discretized into a triangulation $\mathcal{T}_h$ composed of

disjoint open finite elements K such that

$$\overline{\Omega} = \bigcup_{K \in \mathcal{T}_h} \overline{K} \tag{4.1}$$

The DG finite element solution space is

$$\mathcal{V}_h \equiv \left\{ v_h \in L^2(\Omega) : v_h|_K \in \mathcal{P}^p(K),\ \forall K \in \mathcal{T}_h \right\} \tag{4.2}$$

where $\mathcal{P}^p(K)$ denotes the function space restricted to the element K and comprised of polynomials in the elemental reference coordinates (ξ, ζ) of a degree up to p. Let $\{\mathcal{W}_j\}\,(j = 1, 2, \ldots)$ be a complete set of basis functions of $\mathcal{V}_h$ that are locally supported on individual finite elements and discontinuous across element boundaries. The DG approximation of the primary unknowns $\boldsymbol{v}$ is

$$\boldsymbol{v}_h|_K\,(\xi, \zeta) = \sum_j \boldsymbol{v}_{h,j}\,\mathcal{W}_j(\xi, \zeta) \qquad \forall K \in \mathcal{T}_h \tag{4.3}$$

where (ξ, ζ) are the element reference coordinates. Similar to the solution discretization, the surface geometry is discretized and represented as

$$\mathbf{r}_h|_K\,(\xi, \zeta) = \sum_j \mathbf{r}_{h,j}\,\mathcal{W}_j(\xi, \zeta) \qquad \forall K \in \mathcal{T}_h \tag{4.4}$$

A local Cartesian basis $\{\hat{\mathbf{e}}_1, \hat{\mathbf{e}}_2, \hat{\mathbf{n}}_\mathrm{w}\}$ is constructed as follows

$$\hat{\mathbf{e}}_1 \equiv \frac{\dfrac{\partial \mathbf{r}_h}{\partial \xi}}{\left\| \dfrac{\partial \mathbf{r}_h}{\partial \xi} \right\|}, \qquad \hat{\mathbf{n}}_\mathrm{w} \equiv \frac{\dfrac{\partial \mathbf{r}_h}{\partial \xi} \times \dfrac{\partial \mathbf{r}_h}{\partial \zeta}}{\left\| \dfrac{\partial \mathbf{r}_h}{\partial \xi} \times \dfrac{\partial \mathbf{r}_h}{\partial \zeta} \right\|}, \qquad \hat{\mathbf{e}}_2 \equiv \hat{\mathbf{n}}_\mathrm{w} \times \hat{\mathbf{e}}_1 \tag{4.5}$$

with $\{\hat{\mathbf{e}}_1, \hat{\mathbf{e}}_2\}$ and $\hat{\mathbf{n}}_\mathrm{w}$ being, respectively, tangent and orthogonal to the surface. In the current work, $\{\hat{\mathbf{e}}_1, \hat{\mathbf{e}}_2\}$ are used to resolve the vector momentum equation (2.2) into two in-plane components, and the normal vector $\hat{\mathbf{n}}$ of the IBL manifold coincides with $\hat{\mathbf{n}}_\mathrm{w}$.

Each scalar component of the governing equations (i.e. Equations (2.2), (2.3), (2.4), (5.1), (3.16)) can be cast into a generic form of a first-order PDE,

$$\widetilde{\nabla} \cdot \mathbf{F} + S = 0 \tag{4.6}$$

the combination of which forms a nonlinear system of equations often known as *balance laws* [44] or hyperbolic conservation laws with source terms [45]. The flux is defined as

$$\mathbf{F} \in \left\{ \hat{\mathbf{e}}_1 \cdot \overline{\overline{\mathbf{P}}},\ \hat{\mathbf{e}}_2 \cdot \overline{\overline{\mathbf{P}}},\ \mathbf{K},\ \mathbf{K}^\circ,\ \tilde{n}\,\mathbf{q}_\mathrm{e},\ \mathcal{G}\,\mathbf{q}_\mathrm{e} \right\} \tag{4.7}$$

and S denotes the source term. The source terms are not restated explicitly here for conciseness since their exact definitions can be trivially deduced based on the governing equations and the flux definitions. The corresponding DG weighted residual of each scalar equation (4.6) and the corresponding discrete equation are defined as

$$\mathcal{R}(\boldsymbol{v}_h, \mathcal{W}) \equiv \sum_{K \in \mathcal{T}_h} \iint_K \left(\mathcal{W}\, S - \widetilde{\nabla}\mathcal{W} \cdot \mathbf{F} \right) \mathrm{d}A + \sum_{\partial K \in \partial \mathcal{T}_h} \oint_{\partial K} \mathcal{W}\, \hat{\mathbf{t}} \cdot \widehat{\mathbf{F}}\, \mathrm{d}\ell \tag{4.8}$$

$$\mathcal{R} = 0 \qquad \forall \mathcal{W} \in \mathcal{V}_h \tag{4.9}$$

where $\partial\mathcal{T}_h$ denotes the set of all the element boundaries ∂K and $\hat{\mathbf{t}}$ is the outward-pointing unit tangent vector of the element K that is orthogonal to the boundary ∂K as depicted in Figure A-2.

The numerical flux $\widehat{\mathbf{F}}$ in Equation (4.8) adds complications for the (vectorial)

momentum equation since it involves the local basis vectors $\{\hat{\mathbf{e}}_1, \hat{\mathbf{e}}_2\}$. The associated treatment is discussed Section 4.2. Moreover, the numerical flux $\widehat{\mathbf{F}}$ needs to be formulated to preserve applicable conservation laws, maintain numerical accuracy and provide numerical stabilization. This may appear as a straightforward task given a wealth of numerical methods developed for solving nonlinear systems of hyperbolic conservation laws (with source terms) [44, 45] that provide recipes for $\widehat{\mathbf{F}}$. However, designing a proper numerical flux for the 3D IBL equations turns out to be non-trivial, as discussed in Sections 4.3 and 4.4.

4.2 Local Surface-tangent Basis Treatment

The IBL momentum equation is resolved in the surface-tangent basis $\{\hat{\mathbf{e}}_1, \hat{\mathbf{e}}_2\}$ to produce two in-plane components, the corresponding flux of which depends on the surface-tangent vector $\hat{\mathbf{e}}_i$ $(i = 1, 2)$ as in Equation (4.7) and takes a functional form of $\mathbf{F}(\boldsymbol{v}; \hat{\mathbf{e}}_i) \equiv \hat{\mathbf{e}}_i \cdot \overline{\overline{\mathbf{P}}}(\boldsymbol{v})$. It may be tempting to define the numerical flux in the form of $\widehat{\mathbf{F}}(\boldsymbol{v}_L, \boldsymbol{v}_R; \hat{\mathbf{e}}_{i,L}, \hat{\mathbf{e}}_{i,R})\big|_\epsilon$ which involves both the unknowns $\boldsymbol{v}$ and the basis vector $\hat{\mathbf{e}}_i$ of the left and right elements. However, this treatment is inconsistent with the underlying equation because, as illustrated in Figure 4-1, basis vectors $\hat{\mathbf{e}}_{i,L}$ and $\hat{\mathbf{e}}_{i,R}$ are local to their respective elements and thus generally independent of each other.

To shed light on how to handle the local basis vectors properly, it is worth examining the discrete equation associated with a specific element K, that is,

$$\mathcal{R}_K \equiv \iint_K \Big(\mathcal{W}\, S - \widetilde{\nabla}\mathcal{W} \cdot \mathbf{F} \Big)\, \mathrm{d}A + \oint_{\partial K} \mathcal{W}\, \hat{\mathbf{t}} \cdot \widehat{\mathbf{F}}\, \mathrm{d}\ell = 0 \qquad \forall \mathcal{W} \in \mathcal{V}_{h,K} \tag{4.10}$$

To ensure a consistent discretization, the local basis vectors $\{\hat{\mathbf{e}}_i\}$ need to be chosen in accordance with the element K. In the integral over the element K, the source

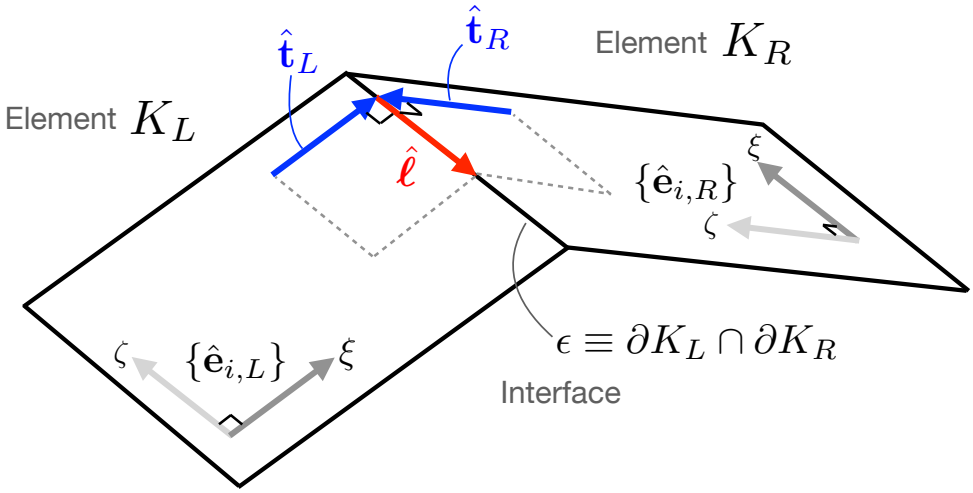

Figure 4-1: Sample configuration of two adjacent elements (K_L and K_R) and their interface ϵ: surface-tangent basis $\{\hat{\mathbf{e}}_i\}$, outward-pointing unit normal vector $\hat{\mathbf{t}}$ (tangent to the element and orthogonal to the interface), and interface unit tangent vector $\hat{\boldsymbol{\ell}}$, element reference coordinates (ξ, ζ)

and flux terms use the local basis vectors constructed as in Equation (4.5). In the integral over the element interface ϵ, the normal flux $\hat{\mathbf{t}} \cdot \widehat{\mathbf{F}}$ is defined separately for the two neighboring elements as

$$\begin{aligned} &\text{For } \mathcal{R}_{K_L}, \text{ use } \hat{\mathbf{t}}_L \text{ and } \widehat{\mathbf{F}}(\boldsymbol{v}_L, \boldsymbol{v}_R;\ \hat{\mathbf{e}}_{i,L}, \hat{\mathbf{e}}_{i,L\to R}) \\ &\text{For } \mathcal{R}_{K_R}, \text{ use } \hat{\mathbf{t}}_R \text{ and } \widehat{\mathbf{F}}(\boldsymbol{v}_L, \boldsymbol{v}_R;\ \hat{\mathbf{e}}_{i,R\to L}, \hat{\mathbf{e}}_{i,R}) \end{aligned} \tag{4.11}$$

where the modified basis vectors $\hat{\mathbf{e}}_{i,L\to R}$ and $\hat{\mathbf{e}}_{i,R\to L}$ are defined as

$$\begin{aligned} \hat{\mathbf{e}}_{i,L\to R} &\equiv \left(\hat{\mathbf{e}}_{i,L} \cdot \hat{\boldsymbol{\ell}}\right) \hat{\boldsymbol{\ell}} + \left(\hat{\mathbf{e}}_{i,L} \cdot \hat{\mathbf{t}}_L\right) (-\hat{\mathbf{t}}_R) \\ \hat{\mathbf{e}}_{i,R\to L} &\equiv \left(\hat{\mathbf{e}}_{i,R} \cdot \hat{\boldsymbol{\ell}}\right) \hat{\boldsymbol{\ell}} + \left(\hat{\mathbf{e}}_{i,R} \cdot \hat{\mathbf{t}}_R\right) (-\hat{\mathbf{t}}_L) \end{aligned} \tag{4.12}$$

The modified basis vector $\hat{\mathbf{e}}_{i,L\to R}$ (or $\hat{\mathbf{e}}_{i,R\to L}$) is simply the rotation of $\hat{\mathbf{e}}_{i,L}$ (or $\hat{\mathbf{e}}_{i,L}$) about the element interface direction $\hat{\boldsymbol{\ell}}$ into the tangent space of the neighboring

element K_R (or K_L). The local basis vector treatment in Equations (4.11) and (4.12) achieves a consistent discretization in that the associated discretization error vanishes in the limit of infinitely refined geometry discretization $\mathbf{r}_h$ or the case of a planar geometry.

4.3 Numerical Flux Challenges

The typical point of departure for devising a numerical flux $\widehat{\mathbf{F}}$ is a characteristic analysis of the governing equations. In classic examples such as the Euler equations and the shallow water equations, an analytical solution to the associated eigenvalue problem is available and forms the basis of the corresponding approximate or exact Riemann solver.

However, such characteristic analysis for the 3D IBL equations is, if not impossible, very difficult, as discussed in detail in Appendix C. In summary, one reason is that the 3D IBL equations (2.2) to (2.4) are, strictly speaking, not physical conservation laws, but are derived by algebraically manipulating mass and momentum conservation principles. Hence, the notion of conservative variables and fluxes is not unambiguously defined based on physics. Besides the ambiguity with the conservation laws, an analytical solution of the 3D IBL eigenvalue problem is not readily available since it would depend on both the form of the equations and the IBL closure models. The viscous-inviscid interaction scheme further complicates the IBL characteristic analysis because the inviscid flow formulation may not be hyperbolic (for example, the elliptic governing equation for incompressible potential flow) even if the IBL equations are purely hyperbolic.

On the other hand, some heuristic options of numerical flux seem plausible at first glance. A simple recipe is a fully upwinded flux based on the edge velocity $\mathbf{q}_e$

as follows.

$$\begin{aligned}
\left(\hat{\mathbf{t}}\cdot\widehat{\mathbf{F}}\right)_{\partial K_L} &\equiv \begin{cases} \hat{\mathbf{t}}_L\cdot\mathbf{F}(\boldsymbol{v}_L;\,\hat{\mathbf{e}}_{i,L}), & \left(\mathbf{q}_{\mathrm{e}}\cdot\hat{\mathbf{t}}\right)\big|_{\partial K_L}\geq 0 \\ \hat{\mathbf{t}}_R\cdot\mathbf{F}(\boldsymbol{v}_R;\,\hat{\mathbf{e}}_{i,L\to R})\,, & \text{otherwise} \end{cases} \\
\left(\hat{\mathbf{t}}\cdot\widehat{\mathbf{F}}\right)_{\partial K_R} &\equiv \begin{cases} \hat{\mathbf{t}}_L\cdot\mathbf{F}(\boldsymbol{v}_L;\,\hat{\mathbf{e}}_{i,R\to L}), & \left(\mathbf{q}_{\mathrm{e}}\cdot\hat{\mathbf{t}}\right)\big|_{\partial K_L}\geq 0 \\ \hat{\mathbf{t}}_R\cdot\mathbf{F}(\boldsymbol{v}_R;\,\hat{\mathbf{e}}_{i,R})\,, & \text{otherwise} \end{cases}
\end{aligned} \tag{4.13}$$

where $\hat{\mathbf{t}}\big|_{\partial K}$ is a unit normal vector of ∂K pointing away from K and $\hat{\mathbf{t}}\cdot\mathbf{F}$ is evaluated separately for ∂K_L and ∂K_R like in Equation (4.11). This amounts to assuming all the characteristics are in the direction of $\mathbf{q}_{\mathrm{e}}$.

Another example is a local Lax-Friedrichs flux,

$$\begin{aligned}
\left(\hat{\mathbf{t}}\cdot\widehat{\mathbf{F}}\right)_{\partial K_L} \equiv& \frac{1}{2}\left[\hat{\mathbf{t}}_L\cdot\mathbf{F}(\boldsymbol{v}_L;\,\hat{\mathbf{e}}_{i,L})+\hat{\mathbf{t}}_R\cdot\mathbf{F}(\boldsymbol{v}_R;\,\hat{\mathbf{e}}_{i,L\to R})\right] \\
&+\frac{1}{2}\alpha\left[u(\boldsymbol{v}_L;\,\hat{\mathbf{e}}_{i,L})-u(\boldsymbol{v}_R;\,\hat{\mathbf{e}}_{i,L\to R})\right] \\
\left(\hat{\mathbf{t}}\cdot\widehat{\mathbf{F}}\right)_{\partial K_R} \equiv& \frac{1}{2}\left[\hat{\mathbf{t}}_L\cdot\mathbf{F}(\boldsymbol{v}_L;\,\hat{\mathbf{e}}_{i,R\to L})+\hat{\mathbf{t}}_R\cdot\mathbf{F}(\boldsymbol{v}_R;\,\hat{\mathbf{e}}_{i,R})\right] \\
&+\frac{1}{2}\alpha\left[u(\boldsymbol{v}_L;\,\hat{\mathbf{e}}_{i,R\to L})-u(\boldsymbol{v}_R;\,\hat{\mathbf{e}}_{i,R})\right]
\end{aligned} \tag{4.14}$$

where the dissipation coefficient α and conservative variable u are heuristically defined as,

$$\alpha=\max(|\mathbf{q}_{\mathrm{e}}\cdot\hat{\mathbf{t}}|_{\partial K_L},|\mathbf{q}_{\mathrm{e}}\cdot\hat{\mathbf{t}}|_{\partial K_R}),\qquad u\in\{\mathbf{M}\cdot\hat{\mathbf{e}}_1,\ \mathbf{M}\cdot\hat{\mathbf{e}}_2,\ e,\ k^{\circ},\ \tilde{n},\ \mathcal{G}\} \tag{4.15}$$

The conservative variables are chosen by examining the time derivatives of viscous-solution-dependent quantities in Equations (2.2) to (2.4). The formulation in Equa-

tion (4.15) assumes that $|\mathbf{q}_e \cdot \hat{\mathbf{t}}|$ is a reasonably tight upper bound of the IBL characteristic speed and u is the conserved quantities for the IBL equations.

The heuristic assumptions of the fully upwinded flux (4.14) and the Lax-Friedrichs flux (4.15) cannot not be verified for lack of rigorous characteristic analysis. In numerical experiments, they performed reasonably for 2D attached boundary layers as in Refs. [46, 4]. However, neither flux choice is sufficiently stable as revealed in test cases involving boundary layer separation and transition [47].

Figure 4-2 illustrates some examples of ill-behaved numerical solution. For a case of flow over an Eppler 387 airfoil with flow transition triggered by a separation bubble on the upper surface, the fully upwinded flux (4.13) results in excessive jumps in the displacement thickness δ_1^* at finite element interfaces for strongly-coupled viscous-inviscid solution. In another case of an FX67-K-170 sailplane airfoil, small but intense separation bubbles appear on both the upper and lower surfaces. The viscous-inviscid solution is solved for in a fully coupled manner. In this case, the Lax-Friedrichs flux (4.14) leads to noticeable oscillations in δ_1^* (plotted) and θ_{11} for x/c in range of 0.5 to 0.8.

4.4 Tailored Discretization for 3D IBL Equations

4.4.1 Flux Correction

An intermediate fix to the numerical anomalies illustrated in Figure 4-2 is identified by investigating the underlying conservation of the IBL momentum equation (2.2). Based on the derivation given in Section A.4.2, the momentum conservation law in

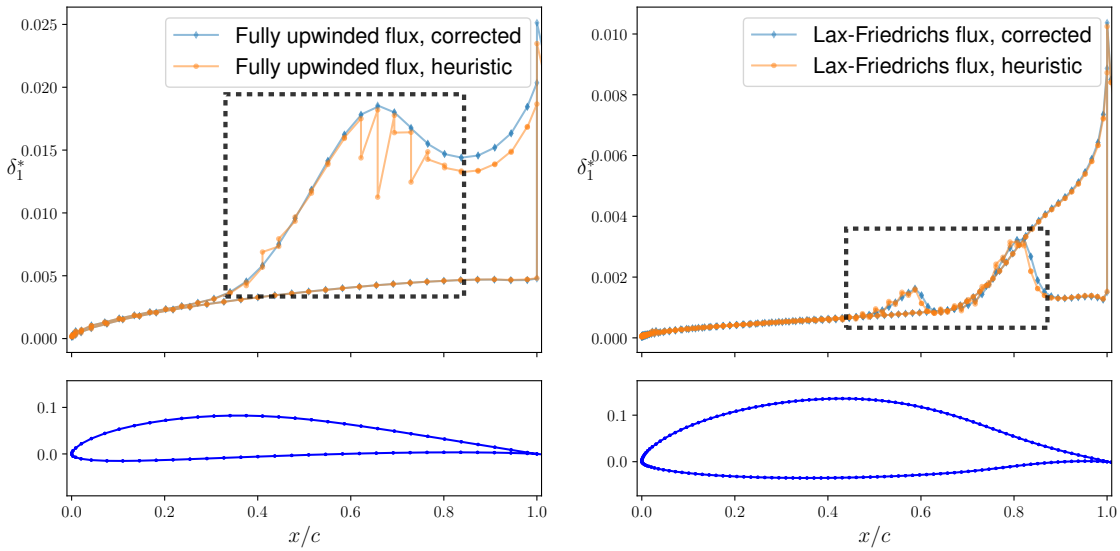

Figure 4-2: Left: Eppler 387, $Re = 10^5, \alpha = 4°$. Right: FX67-K-170, $\alpha = 4.156°, Re = 2 \times 10^6$. Numerical results shown for heuristic flux definitions (oscillatory behavior highlighted in dark-dashed boxes) in comparison to corrected ones (well-behaved) presented in Section 4.4.1.

an integral defect form is

$$\oint_{\partial\Omega} \left(\overline{\overline{\mathbf{P}}} + \mathbf{q}_\mathrm{e} \otimes \mathbf{M}\right) \cdot \hat{\mathbf{t}} \, \mathrm{d}\ell + \iint_{\Omega} \left[\frac{\partial \mathbf{M}}{\partial t} - \mathbf{q}_\mathrm{e} \left(\rho_\mathrm{e} \, \mathbf{q}_\mathrm{e} \cdot \hat{\mathbf{n}}_\mathrm{w}\right) - \boldsymbol{\tau}_\mathrm{w}\right] \mathrm{d}A = 0 \qquad \forall \Omega \quad (4.16)$$

from which Equation (2.2) is derived by applying the divergence theorem and substituting the wall transpiration term $\rho_\mathrm{e} \, \mathbf{q}_\mathrm{e} \cdot \hat{\mathbf{n}}_\mathrm{w}$ using Equation (2.1). The integral defect conservation equation (4.16) implies that, in lieu of $\overline{\overline{\mathbf{P}}}$, the momentum flux defect $\overline{\overline{\mathbf{J}}} \equiv \overline{\overline{\mathbf{P}}} + \mathbf{q}_\mathrm{e} \otimes \mathbf{M}$ is a more suitable conservative flux and thus upwinded in the numerical flux definition. To reflect the underlying conservative flux, Equation (2.2) is rewritten in an alternative form,

$$\frac{\partial \mathbf{p}}{\partial t} + m \frac{\partial \mathbf{q}_\mathrm{e}}{\partial t} + \widetilde{\nabla} \cdot \overline{\overline{\mathbf{J}}} - \left(\widetilde{\nabla} \cdot \mathbf{M}\right) \mathbf{q}_\mathrm{e} - \boldsymbol{\tau}_\mathrm{w} = \mathbf{0} \quad (4.17)$$

The corresponding DG weighted residual is

$$\begin{aligned} \mathcal{R} \equiv \sum_{K \in \mathcal{T}_h} \iint_K \mathcal{W} \left[- \operatorname{tr}\left(\overline{\overline{\mathbf{J}}}^T \cdot \left(\widetilde{\nabla} \hat{\mathbf{e}}\right)\right) - \left(\widetilde{\nabla} \cdot \mathbf{M}\right) \mathbf{q}_\mathrm{e} \cdot \hat{\mathbf{e}} - \boldsymbol{\tau}_\mathrm{w} \cdot \hat{\mathbf{e}} \right] \mathrm{d}A \\ + \sum_{K \in \mathcal{T}_h} \iint_K - \widetilde{\nabla} \mathcal{W} \cdot \left(\hat{\mathbf{e}} \cdot \overline{\overline{\mathbf{J}}}\right) \mathrm{d}A + \sum_{\partial K \in \partial \mathcal{T}_h} \oint_{\partial K} \mathcal{W} \, \hat{\mathbf{t}} \cdot \widehat{\mathbf{F}}_J \, \mathrm{d}\ell \end{aligned} \quad (4.18)$$

In contrast to Equation (4.14), the flux for the momentum equation becomes $\mathbf{F} \equiv \hat{\mathbf{e}} \cdot \overline{\overline{\mathbf{J}}}$. In this case, the numerical flux $\widehat{\mathbf{F}}_J$ of the Lax-Friedrichs type is

$$\begin{aligned}
\left(\hat{\mathbf{t}} \cdot \widehat{\mathbf{F}}_J\right)_{\partial K_L} \equiv & \frac{1}{2}\left[\hat{\mathbf{e}}_{i,L} \cdot \overline{\overline{\mathbf{J}}} \cdot \hat{\mathbf{t}}_L + \hat{\mathbf{e}}_{i,L\to R} \cdot \overline{\overline{\mathbf{J}}} \cdot \hat{\mathbf{t}}_R\right] \\
& + \frac{1}{2}\alpha\left[u(\boldsymbol{v}_L;\, \hat{\mathbf{e}}_{i,L}) - u(\boldsymbol{v}_R;\, \hat{\mathbf{e}}_{i,L\to R})\right] \\
\left(\hat{\mathbf{t}} \cdot \widehat{\mathbf{F}}_J\right)_{\partial K_R} \equiv & \frac{1}{2}\left[\hat{\mathbf{e}}_{i,R\to L} \cdot \overline{\overline{\mathbf{J}}} \cdot \hat{\mathbf{t}}_L + \hat{\mathbf{e}}_{i,R} \cdot \overline{\overline{\mathbf{J}}} \cdot \hat{\mathbf{t}}_R\right] \\
& + \frac{1}{2}\alpha\left[u(\boldsymbol{v}_L;\, \hat{\mathbf{e}}_{i,R\to L}) - u(\boldsymbol{v}_R;\, \hat{\mathbf{e}}_{i,R})\right]
\end{aligned} \tag{4.19}$$

This modified discretization scheme turns out to fix the interface jump or oscillation in the 2D IBL solution as shown in Figure 4-2.

It is worth noting that, based on the conclusion of Ref. [48], the discretization (4.18) is not dual consistent due to the term $\widetilde{\nabla} \cdot \mathbf{M}$ that involves first derivatives of the solution variable, specifically $\widetilde{\nabla}\delta_1^*$ and $\widetilde{\nabla}\delta_2^*$ in this case. Although not crucial in the current discussion, dual consistency potentially plays an important role if an adjoint formulation for IBL is pursued in the future (for design optimization or mesh adaptation purposes) and can be recovered by introducing lifting operators [48].

Motivated by the fix achieved with the discretization (4.18) and (4.19), and carrying out integration by parts on the term involving $\widetilde{\nabla} \cdot \mathbf{M}$, the following alternative weighted residual is derived,

$$\begin{aligned}
\mathcal{R} \equiv & \sum_{K\in\mathcal{T}_h} \iint_K \left\{\mathcal{W}\left[-\operatorname{tr}\left(\overline{\overline{\mathbf{P}}}^{\,T} \cdot \left(\widetilde{\nabla}\hat{\mathbf{e}}\right)\right) + \hat{\mathbf{e}} \cdot \left(\widetilde{\nabla}\mathbf{q}_\mathrm{e}\right) \cdot \mathbf{M} - \boldsymbol{\tau}_\mathrm{w} \cdot \hat{\mathbf{e}}\right] - \widetilde{\nabla}\mathcal{W} \cdot (\hat{\mathbf{e}} \cdot \overline{\overline{\mathbf{P}}})\right\} \mathrm{d}A \\
& + \sum_{\partial K\in\partial\mathcal{T}_h} \oint_{\partial K} \mathcal{W}\,\hat{\mathbf{t}} \cdot \Big[\widehat{\mathbf{F}}_P + \underbrace{(\widehat{\mathbf{F}}_J - \widehat{\mathbf{F}}_P - \mathbf{M} \otimes \mathbf{q}_\mathrm{e} \cdot \hat{\mathbf{e}})}_{\text{flux correction}}\Big] \mathrm{d}\ell
\end{aligned} \tag{4.20}$$

where $\widehat{\mathbf{F}}_P$ is the numerical flux counterpart for $\hat{\mathbf{e}} \cdot \overline{\overline{\mathbf{P}}}$ as defined in Equation (4.14). In

contrast to the standard DG discretization (4.8), the discretization (4.20) effectively introduces a correction to the numerical flux based on momentum conservation. Similar to the scheme in (4.18) and (4.19), it also fixes the aforementioned ill-behaved numerical solution. Moreover, the source term does not involve any derivative of the primary unknown variables $\mathcal{Q}_{\text{IBL}}$.

4.4.2 Dissipation Coefficient

The dissipation coefficient α also needs modification for 3D IBL. In the formulation (4.15), α vanishes when $\mathbf{q}_{\text{e}}$ is orthogonal to $\hat{\mathbf{t}}$, which essentially assumes that none of the characteristics have any component along $\hat{\mathbf{t}}$ in this case. However, the actual boundary layer velocity profile may still have a nonzero crossflow component (i.e. $\mathbf{q} \cdot \hat{\mathbf{t}} \neq 0$). Hence, information can still propagate in the direction of $\hat{\mathbf{t}}$ or $-\hat{\mathbf{t}}$. Based on this qualitative argument, the dissipation coefficient α for 3D IBL is chosen to be

$$\alpha = \max((q_{\text{e}})_{\partial K_L}, (q_{\text{e}})_{\partial K_R}) \tag{4.21}$$

so that it does not lead to zero numerical dissipation when $\mathbf{q}_{\text{e}} \cdot \hat{\mathbf{t}} = 0$ unless upon flow stagnation (i.e. $q_{\text{e}} = 0$). For 2D IBL, Equations (4.15) and (4.21) are essentially the same because $\mathbf{q}_{\text{e}}$ and $\hat{\mathbf{t}}$ are approximately co-linear. In numerical studies of this work, the q_{e}-based dissipation coefficient is observed to be more robust than the one based on $\mathbf{q}_{\text{e}} \cdot \hat{\mathbf{t}}$ as illustrated in Figure 4-3.

On the other hand, there is no empirical evidence that the choice in Equation (4.21) is excessively dissipative. In fact, a numerical experiment as illustrated in Figure 4-4 indicates that the q_{e}-based dissipation coefficient is able to preserve the sharp jump in δ_1^* propagated from the Dirichlet boundary condition at the inlet

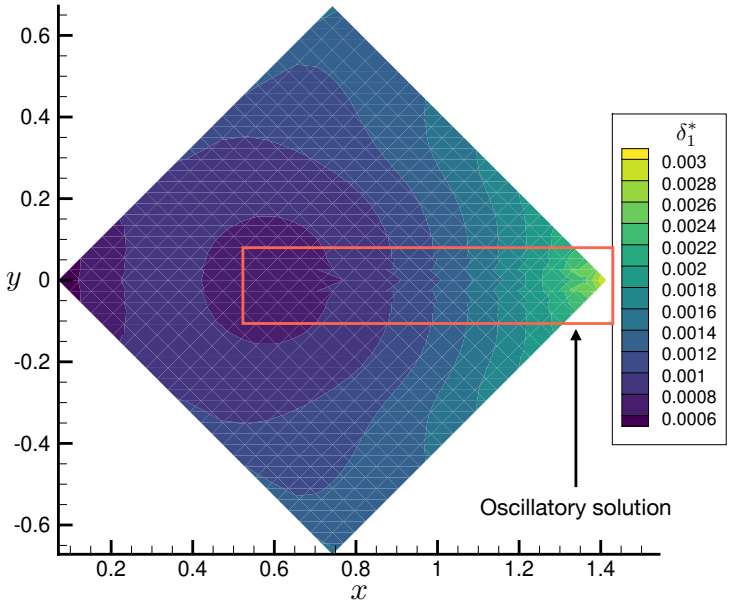

(a) $|\mathbf{q}_e \cdot \hat{\mathbf{t}}|$-based dissipation coefficient α as in Equation (4.15)

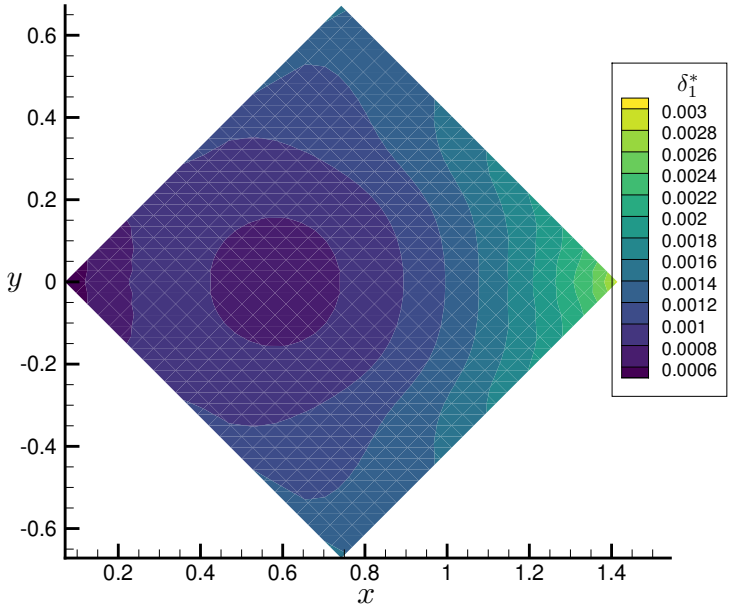

(b) q_e-based dissipation coefficient α as in Equation (4.21)

Figure 4-3: Comparison of dissipation coefficients on a sample torpedo case from Figure 3-8. Oscillatory solution near the center $\mathbf{q}_e$ streamline (i.e. $y = 0$) is observed and highlighted for the $|\mathbf{q}_e \cdot \hat{\mathbf{t}}|$-based α definition. Edges of triangular elements are colored in gray and some coincide with the center streamline where $\mathbf{q}_e \cdot \hat{\mathbf{t}} = 0$.

$x = 0$ prescribed as follows.

$$\delta_1^*(y) = 1.72080\, R(y)\, \delta_{\mathrm{FS}}(y), \quad \theta_{11}(y) = 0.66412\, R(y)\, \delta_{\mathrm{FS}}(y), \quad \delta_2^* = \theta_{12} = 0 \tag{4.22}$$

$$\delta_{\mathrm{FS}}(y) = \sqrt{\frac{\nu_\infty}{q_\infty}}\, (x + 0.05)^{1/2}\, |_{x=0}, \quad R(y) = d_1 + \frac{d_2 - d_1}{1 + \exp(-8(y - y_c)/d)}$$

$$\nu_\infty = 10^5,\ q_\infty = 1,\ d_1 = 1,\ d_2 = 10,\ y_c = 0.5,\ d = 0.1$$

It is worth noting that, currently, without the help of a rigorous characteristic analysis, the flux correction and the choice of the dissipation coefficient presented in Section 4.4 are ad-hoc fixes to the discretization issues encountered in numerical studies, and there is still potential room for improvement in future work.

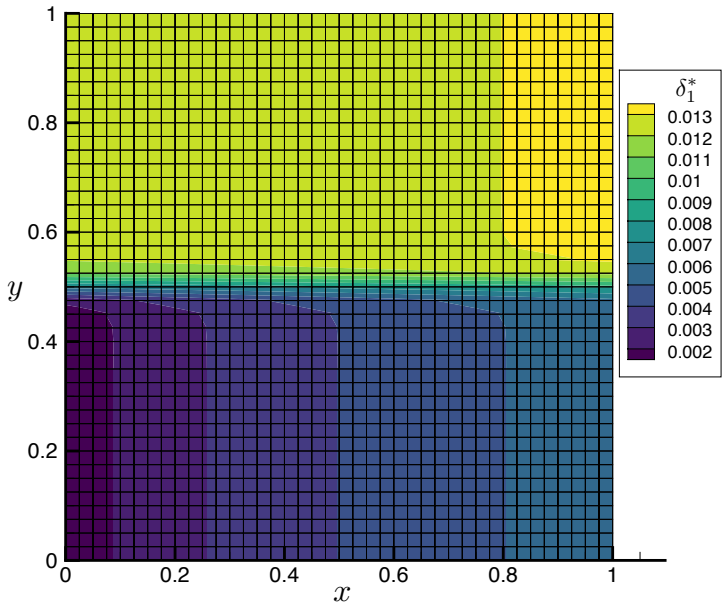

(a) $|\mathbf{q}_e \cdot \hat{\mathbf{t}}|$-based dissipation coefficient α as in Equation (4.15)

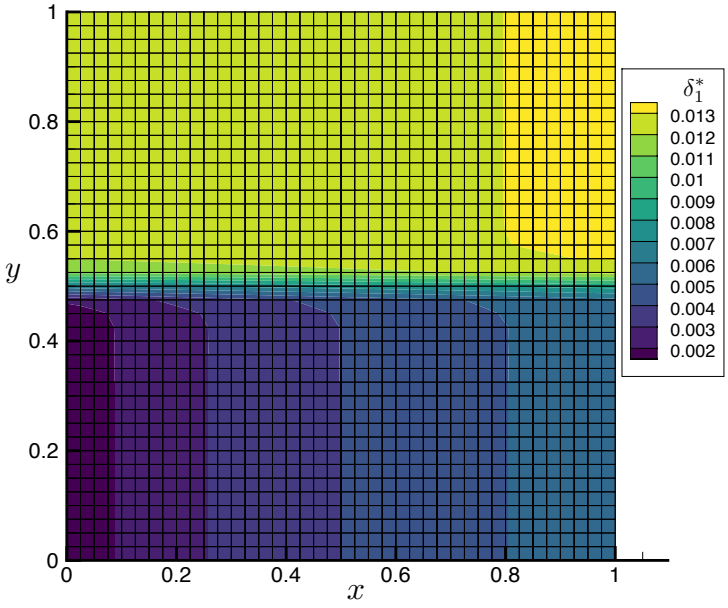

(b) q_e-based dissipation coefficient α as in Equation (4.21)

Figure 4-4: Comparison of dissipation coefficients for maintaining the resolution of solution jump propagated from the inlet boundary $x = 0$. A constant $\mathbf{q}_e$ is prescribed in the x-direction. Quadrilateral grids are indicated by dark lines.

Chapter 5

Numerical Modeling of Flow Transition

This chapter first provides an overview of the flow transition modeling problem, and then discusses and compares two ways of numerical treatment for flow transition in an IBL method: transition fitting versus capturing. The proposed transition capturing method is shown to be more favorable and its effectiveness is demonstrated on both 2D and 3D test cases.

5.1 Flow Transition Modeling Overview

5.1.1 Literature Survey

Prediction of laminar-to-turbulent flow transition plays an important role in aircraft aerodynamic analysis, particularly in applications involving natural laminar flow and flow control [49].

However, transition prediction is significantly underserved in conventional RANS-

based CFD algorithms which tend to focus on modeling fully turbulent flows. A key challenge is the tension that compatibility with RANS CFD methods requires local formulation but existing transition models are mostly based on boundary layer theories that need non-local quantities such as thickness integrals defined in Equation (A.11).

A number of recent research efforts have emerged to augment RANS CFD methods with transition modeling capability. One approach is to couple two established components: one for RANS solution and the other for transition prediction [50, 51, 52, 53]. The transition modeling module is typically based on solving the boundary layer equations and the boundary layer stability problem. The boundary layer solution is subject to the Goldstein Separation Singularity problem (discussed in Section 2.3), and, when combined with RANS solution through the loose iterative coupling, will take a toll on the overall solution robustness. Moreover, the implementation of RANS-transition coupling tends to be formidably complex and tedious.

Another avenue for modeling transition is to endow existing RANS solvers with additional governing equation(s). Notable examples in this category include the γ-Re_{θ_t} transport equation of Langtry and Menter [54] which is purely based on correlation, and the amplification factor transport equation of Coder [55, 56] motivated by the linear stability theory and the e^N envelope method. These baseline models have also been extended to incorporate additional transition mechanisms such as crossflow instability [57, 58]. However, the development of these methods is still at a relatively nascent stage with plenty of to-be-resolved practical issues including solution robustness, grid dependence, over-sensitivity to turbulence model, and boundary conditions (according to the first AIAA Transition Modeling Workshop [59]).

In contrast to RANS, the IBL method offers a more convenient framework for

transition modeling mainly because it is naturally compatible with established transition models which are mostly based on boundary layer stability theories. For example, 2D IBL methods such as XFOIL and MSES are able to predict transition through the e^N envelope method. However, 3D transition prediction with IBL has seldom been studied. This work focuses on closing this gap by examining and developing a suitable numerical treatment of 3D transition.

5.1.2 Physical Modeling

In this thesis, the e^N envelope method is adopted as the physical model of transition for its convenience and demonstrated effectiveness in 2D and 3D applications [31, 11, 50].

The e^N envelope method here is based on the linear flow stability theory and captures the streamwise-mode natural transition by monitoring the growth of Tollmien-Schlichting (TS) waves. Figure 5-1 illustrates the notional evolution of flows undergoing transition within a boundary layer. The maximum magnitude of TS waves is characterized by the magnitude q' of the velocity fluctuation $\mathbf{q}'$ from the Reynolds decomposition and relates to the small Reynolds stress in the laminar regime.

In the e^N envelope method, the evolution of the amplification factor $\tilde{n} \equiv \ln(q'/q'_0)$ (i.e. the exponential growth factor of q' from some an initial value q'_0) is modeled by a transport equation,

$$\frac{\partial \tilde{n}}{\partial t} + \mathbf{q}_\mathrm{e} \cdot \widetilde{\nabla} \tilde{n} - \frac{q_\mathrm{e}}{\theta_{11}} f_\mathrm{TS} = 0 \tag{5.1}$$

The forcing function f_TS governs the growth rate of $\tilde{n}$ and is defined using a correlation relation, for example, in the form of $f_\mathrm{TS}(H_1, Re_{\theta_{11}})$ as detailed in Ref. [4] and

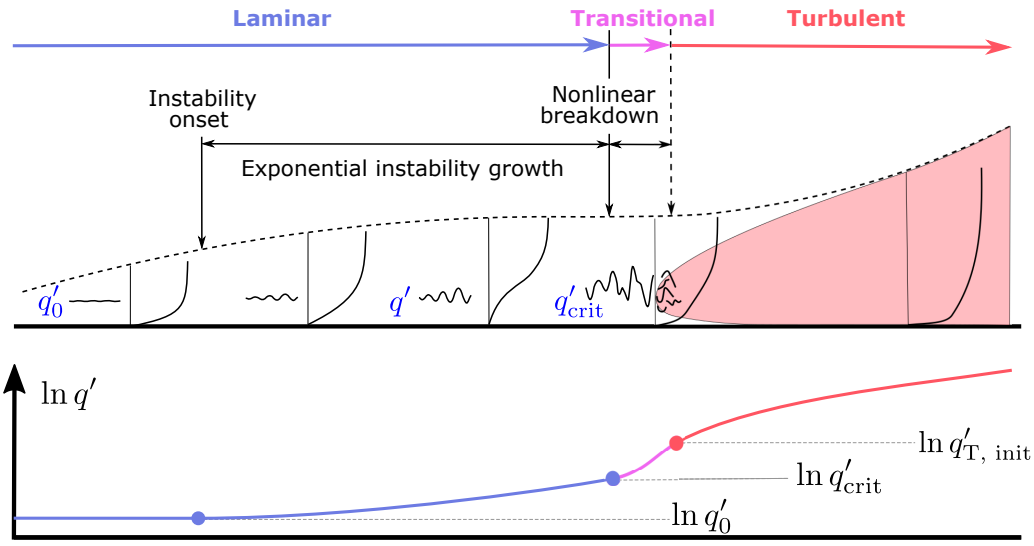

Figure 5-1: Laminar-to-turbulent flow transition in a generic boundary layer (top) and the corresponding evolution of the Reynolds velocity fluctuation q' in the natural logarithmic scale (bottom). (The size of the transitional flow region is exaggerated in this figure, but flow transition is assumed to occur instantaneously, corresponding to effectively a step jump of the magenta curve.) Reproduced from Ref. [4] with permission.

restated in Appendix B.4. The transition criterion is defined as follows

$$\tilde{n} < \tilde{n}_{\text{crit}} \rightarrow \text{laminar}, \qquad \tilde{n} \geq \tilde{n}_{\text{crit}} \rightarrow \text{turbulent} \tag{5.2}$$

where the critical threshold $\tilde{n}_{\text{crit}}$ identifies the division between laminar and turbulent flows.

To extend the e^N envelope method for 3D flow physics, the crossflow transition mechanism needs to be accounted for. Although the associated physical modeling is beyond the scope of this thesis, it is worth noting a prospective strategy owing to Sturdza and Kroo [60, 61].

One approach used in that work is to define an additional amplification factor

$\tilde{n}_{\text{CF}}$ to track the crossflow wave growth and a dedicated transport equation,

$$\frac{\partial \tilde{n}_{\text{CF}}}{\partial t} + \mathbf{q}_{\text{e}} \cdot \widetilde{\nabla} \tilde{n}_{\text{CF}} - \frac{q_{\text{e}}}{\theta_{11}} f_{\text{CF}} = 0 \tag{5.3}$$

where the forcing function f_{CF} characterizes the corresponding growth rate of crossflow perturbation. For example, Sturdza developed a regression model f_{CF} based on data of numerical solution to the crossflow linear stability problem [60] for supersonic flows and its parametrization likely can be substituted by the set of parameters as in Equation (3.2).

Assuming that the TS and crossflow waves are independent, which is plausible in the linear stability context (i.e. with small perturbations), a 3D transition criterion can be formulated as follows,

$$\tilde{n} < \tilde{n}_{\text{crit}} \text{ and } \tilde{n}_{\text{CF}} < \tilde{n}_{\text{crit,CF}} \rightarrow \text{laminar}, \qquad \text{Otherwise} \rightarrow \text{turbulent} \tag{5.4}$$

where a crossflow transition threshold $\tilde{n}_{\text{crit,CF}}$ is introduced. The potential interaction between the TS and crossflow transition modes requires further research and insight into its physical mechanisms. If it is deemed to be important, such interaction may be modeled by coupling the amplification factor equations (5.1) and (5.3), and/or modifying the transition criterion (5.4).

5.1.3 Numerical Treatment

The numerical treatment of flow transition is also nontrivial, in particular for its extension from 2D to 3D. This section summarizes the challenges and potential solution before proposing two methods of numerical treatment in the ensuing sections.

Figure 5-2 illustrates a sample IBL problem setup for airfoil aerodynamic anal-

ysis. A salient feature introduced by flow transition is the transition front Γ_{tr} that separates the laminar and turbulent sub-domains. It is reminiscent of interfacial problems in other physical context, such as crack propagation in fracture mechanics, shocks in gas dynamics and gas-liquid interaction in multiphase flows.

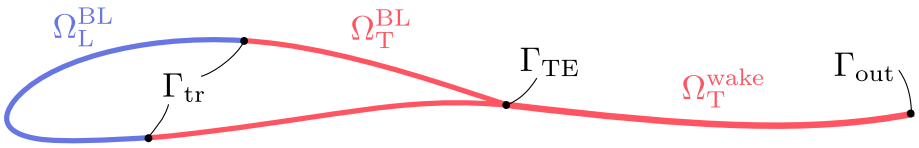

Figure 5-2: A sample configuration for airfoil aerodynamic analysis with flow transition. Subscript "L" and blue color denote "laminar"; subscript "T" and red color denote "turbulent". Ω refers to a sub-domain ("BL" for boundary layer and "wake" is literal) and Γ stands for an interface or boundary ("tr" for transition, "TE" for trailing edge, and "out" for outflow). Reproduced from Ref. [4] with permission.

IBL transition modeling also adds special challenges. First, across the transition front Γ_{tr}, the laminar and turbulent sub-domains employ different physical models because laminar and turbulent closure relations are used in respective sub-domains. The laminar part is additionally modeled with the amplification factor growth equation (5.1), whereas the turbulent part requires modeling turbulent shear stress transport using the lag equation (3.16). Additional matching conditions also need to be imposed at the interface, including mass and momentum conservation and the turbulent onset of c_τ as in Equation (B.16). Second, the transition front Γ_{tr} is tightly coupled with the IBL solution. Specifically, the variable $\tilde{n}$ identifies the transition front via the criterion (5.2) and the Γ_{tr} location drives the IBL solution reciprocally.

There are mainly two numerical methods for handling flow transition, distinguished by the way they represent the interface (i.e. the transition front): *transition fitting* and *transition capturing*. Transition fitting identifies the interface explicitly by parametrization of the corresponding point (in 2D) or curve (in 3D), whereas

transition capturing tracks the interface implicitly based on the transition criterion $\tilde{n} = \tilde{n}_{\text{crit}}$. The numerical treatment has a direct bearing on the accuracy, robustness, efficiency and complexity of the overall numerical solution. Sections 5.2 and 5.3 propose and compare both numerical schemes for transition respectively.

5.2 Transition Fitting

A transition fitting approach based on a cut-cell finite element formulation is presented in this section, while the development of this method was originally proposed and documented in Ref. [4].

The pursuit of this approach was primarily motivated by the fact that established 2D IBL methods such as MSES and XFOIL adopt a transition fitting approach albeit in a finite difference discretization setting [31, 11]. The explicit representation of the transition front and sub-grid numerical treatment allows for resolving sharp discontinuities across that interface even on coarse grids.

However, the 2D development of the transition fitting approach in this work has revealed some key disadvantages. The 2D implementation is already quite complex and the 3D extension will be even worse considering the more complicated interface topology (i.e. a curve in 3D versus a point in 2D). Also, the nonlinear solution robustness is compromised by the use of an under-relaxed Newton solver, whereas enhancement techniques such as line search and pseudo-transient continuation (PTC) as discussed in Section 2.3.1 are no longer applicable in this case.

Those drawbacks will be clear from the following method description and through the comparison to a more favorable transition capturing approach in Section 5.3. Although the transition fitting approach is not adopted and recommended in this thesis, its 2D formulation is still presented for contrast and completeness.

5.2.1 Cut-cell Formulation

The transition fitting approach (in its 2D formulation) of this work features a cut-cell treatment of the DG finite element discretization to enable sub-cell resolution of the transition front interface.

The overall IBL model (including governing equations and solution variables) is first decomposed into components based on their domains of definition: the laminar sub-domain (denoted by subscript "L"), the turbulent sub-domain (denoted by subscript "T"), and the entire domain (without any subscript). Such decomposition is summarized in Table 5.1.

Table 5.1: IBL model components categorized based on domain of definition

Equation Form	Variable	Governing Equation
(5.5)	$\tilde{n}$	(5.1)
(5.6)	$(\mathcal{Q}_{\mathrm{IBL}})_{\mathrm{L}}$	(2.2), (2.3) with laminar closure
(5.7)	$(\mathcal{Q}_{\mathrm{IBL}})_{\mathrm{T}}, \mathcal{G}$	(2.2), (2.3), (3.16) with turbulent closure

The generic forms of equations are

$$\widetilde{\nabla} \cdot \mathbf{F}(\boldsymbol{v}) + S(\boldsymbol{v}) = 0 \qquad \text{in} \quad \Omega \tag{5.5}$$

$$\widetilde{\nabla} \cdot \mathbf{F}_{\mathrm{L}}(\boldsymbol{v}_{\mathrm{L}}) + S_{\mathrm{L}}(\boldsymbol{v}_{\mathrm{L}}) = 0 \qquad \text{in} \quad \Omega_{\mathrm{L}} \tag{5.6}$$

$$\widetilde{\nabla} \cdot \mathbf{F}_{\mathrm{T}}(\boldsymbol{v}_{\mathrm{T}}) + S_{\mathrm{T}}(\boldsymbol{v}_{\mathrm{T}}) = 0 \qquad \text{in} \quad \Omega_{\mathrm{T}} \tag{5.7}$$

The transition front Γ_{tr} is identified by the level set $\tilde{n} = \tilde{n}_{\mathrm{crit}}$, and each front is a simply a point in a 2D setting. In the current implementation, the location of Γ_{tr} is explicitly parametrized by the linear interpolation of variable $\tilde{n}$ on the finite element(s) where transition occurs (hence the solution dependence). Such

parametrization assumes linear finite elements, whereas higher-order solution discretization makes it more difficult to identify the level set. For 3D IBL, the transition front topology becomes a curve in general and consequently will be more complicated to parametrize.

A cut-cell treatment is applied based on the parametrization of Γ_{tr} as illustrated in Figure 5-3. Specifically, each finite element K_{tr} on which transition occurs is divided into two sub-elements: K_{L} (laminar) and K_{T} (turbulent); that is,

$$\overline{K}_{\text{tr}} = \overline{K}_{\text{L}} \cup \overline{K}_{\text{T}}, \qquad K_{\text{L}} \cap K_{\text{T}} = \emptyset, \qquad \Gamma_{\text{tr},K} \equiv \overline{K}_{\text{L}} \cap \overline{K}_{\text{T}} \subset \Gamma_{\text{tr}} \tag{5.8}$$

where $\Gamma_{\text{tr},K}$ denotes the part of the transition front Γ_{tr} on the element $\overline{K}_{\text{tr}}$. The basis functions for finite element discretization are also shown in Figure 5-3 for both a regular element and cut-cell sub-elements.

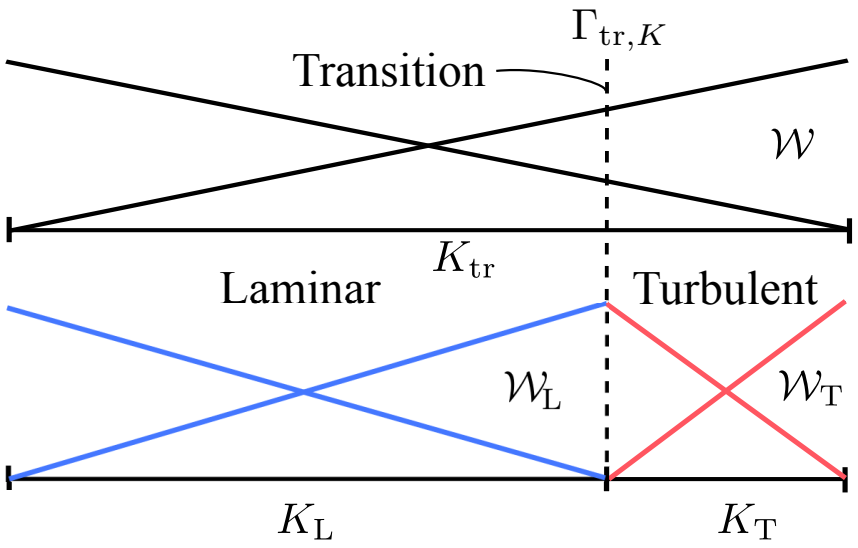

Figure 5-3: A regular finite element K_{tr} with basis $\mathcal{W}$ (top), and a cut-cell element divided into laminar and turbulent parts K_{L} and K_{T} with locally supported and enriched bases $\mathcal{W}_{\text{L}}$ and $\mathcal{W}_{\text{T}}$ respectively (bottom). A linear Lagrange polynomial basis is shown as an example.

Equations (5.5), (5.6) and (5.7) are discretized differently. Only the amplification factor $\tilde{n}$ and its governing transport equation (5.1) are defined across the entire domain. It follows the generic form of equation (5.5) and is discretized using the plain DG discretization (4.8) with the original approximate solution space $\mathcal{V}_h$. The source term S there of Equation (5.1) is extended to the turbulent region Ω_{T} as

$$S = \begin{cases} S_{\Gamma_{\mathrm{tr},K}} & \equiv -\tilde{n}\,\widetilde{\nabla}\cdot\mathbf{q}_{\mathrm{e}} - \dfrac{q_{\mathrm{e}}}{\theta_{11}} f_{\mathrm{TS}} \quad \text{on } K_{\mathrm{T}} \subset K_{\mathrm{tr}} \\ S_{\mathrm{T}} & \equiv -\tilde{n}\,\widetilde{\nabla}\cdot\mathbf{q}_{\mathrm{e}} - \dfrac{q_{\mathrm{e}}}{\theta_{11}} f_{\mathrm{TS,T}} \quad \text{on } K \subset \Omega_{\mathrm{T}} \end{cases} \tag{5.9}$$

where $S_{\Gamma_{\mathrm{tr},K}}$ is evaluated at $\Gamma_{\mathrm{tr},K}$. The turbulent growth rate $f_{\mathrm{TS,T}}$ is chosen to be constant and positive as in Equation (B.10) to ensure the growth $\tilde{n}$ in the fully turbulent elements and avoid fictitious re-laminarization. Despite the extension of the amplification equation, the growth of $\tilde{n}$ remains largely unaltered in the laminar region and in the vicinity of the transition front.

Next, for the generic form (5.6), the original DG discretization (4.8) still applies to the set of finite elements K that are in the interior of the laminar region Ω_{L} (i.e. $K \in \mathcal{T}_h$ and $K \subset \Omega_{\mathrm{L}}$), but the cut-cell modification is introduced to the laminar part of each transitional element K_{tr}.

$$\boldsymbol{v}_{\mathrm{L},h}(\xi) = \begin{cases} \displaystyle\sum_j \boldsymbol{v}_{\mathrm{L},h,j}\,\mathcal{W}_{\mathrm{L},j}(\xi) & \text{on } K_{\mathrm{L}} \\ \displaystyle\sum_j \boldsymbol{v}_{\mathrm{L},h,j}\,\mathcal{W}_j(\xi) & \text{on } K \text{ without transition} \end{cases} \tag{5.10}$$

On a sub-element K_{L}, the standard DG elemental residual originally associated with

the element K_{tr} is replaced by

$$\begin{aligned} 0 &= \mathcal{R}(\boldsymbol{v}_{\text{L},h}, \mathcal{W}_{\text{L}}) \qquad \forall \mathcal{W}_{\text{L}} \in \mathcal{P}^p(K_{\text{L}}) \\ &\equiv \sum_{\Gamma_{\text{tr},K}} \mathcal{W}_{\text{L}}\, \hat{\mathbf{t}} \cdot \mathbf{F}_{\text{L}}(\boldsymbol{v}_{\text{L},h}) + \sum_{\partial K_{\text{L}} \backslash \Gamma_{\text{tr},K}} \mathcal{W}_{\text{L}}\, \hat{\mathbf{t}} \cdot \widehat{\mathbf{F}}_{\text{L}}(\boldsymbol{v}_{\text{L},h}) \\ &\quad + \int_{K_{\text{L}}} \Big(\mathcal{W}_{\text{L}}\, S_{\text{L}}(\boldsymbol{v}_{\text{L},h}) - \widetilde{\nabla} \mathcal{W}_{\text{L}} \cdot \mathbf{F}_{\text{L}}(\boldsymbol{v}_{\text{L},h}) \Big)\, \mathrm{d}\ell \end{aligned} \tag{5.11}$$

The $\Gamma_{\text{tr},K}$ interface is assumed to correspond to laminar outflow, for which an outflow boundary condition (as in Section 2.2.2) is applied.

The turbulent-only equation (5.7) is discretized in a similar manner as the aforementioned laminar-only counterpart, and stated as follows.

$$\begin{aligned} 0 &= \mathcal{R}(\boldsymbol{v}_{\text{T},h}, \mathcal{W}_{\text{T}}) \qquad \forall \mathcal{W}_{\text{T}} \in \mathcal{P}^p(K_{\text{T}}) \\ &\equiv \sum_{\Gamma_{\text{tr},K}} \mathcal{W}_{\text{T}}\, F_{\text{tr},K} + \sum_{\partial K_{\text{T}} \backslash \Gamma_{\text{tr},K}} \mathcal{W}_{\text{T}}\, \hat{\mathbf{t}} \cdot \widehat{\mathbf{F}}_{\text{T}}(\boldsymbol{v}_{\text{T},h}) \\ &\quad + \int_{K_{\text{T}}} \Big(\mathcal{W}_{\text{T}}\, S_{\text{T}}(\boldsymbol{v}_{\text{T},h}) - \widetilde{\nabla} \mathcal{W}_{\text{T}} \cdot \mathbf{F}_{\text{T}}(\boldsymbol{v}_{\text{T},h}) \Big)\, \mathrm{d}\ell \end{aligned} \tag{5.12}$$

A free (flux) variable $F_{\text{tr},K}$ is introduced for each turbulent-only equation on all the sub-elements K_{T}, and serves as a Lagrange multiplier for imposing the inflow boundary conditions of the sub-element K_{T}, with Dirichlet data of $\{\delta_1^*, \theta_{11}, c_\tau\}$ based on the laminar outflow at the transition front and a c_τ closure relation at turbulent onset.

It is worth emphasizing that, on a sub-element K_{L} (or K_{T}), the cut-cell basis $\mathcal{W}_{\text{L}}$ (or $\mathcal{W}_{\text{T}}$) is used in lieu of $\mathcal{W}$ to define both the weighted residual in Equation (5.11) and discrete solution in Equation 5.10 in order to achieve a well-conditioned system of equations, specifically, in terms of the condition number of its linearization which

is identified by the Jacobian $\partial \mathcal{R}_{\mathrm{IBL}} / \partial Q_{\mathrm{IBL}}$ of Equation (2.14).

Also, it is fortunate that the condition number is independent of the aspect ratio for the sub-elements (i.e. $\max(|K_{\mathrm{L}}|/|K_{\mathrm{T}}|, |K_{\mathrm{T}}|/|K_{\mathrm{L}}|)$), as confirmed by numerical experiments in this work. Established theories (see Section 5.2 of Ref. [62]) also support this observation for finite element discretization of first-order PDEs generally. In contrast, the discretization of second-order PDEs leads to a condition number that scales with the aspect ratio and is ill-conditioned when two sub-elements have drastically different sizes (see Chapter 5 of Ref. [63]), unless the equations are formulated as a system of first-order PDEs and discretized using a mixed method [62]).

A major complication associated with the cut-cell treatment is the need to enrich DOFs of a standard finite element K to two sub-elements K_{L} and K_{T}, similarly to enriched/extended finite element methods [64]. Transition fitting is further complicated by the fact that such DOF enrichment is solution-dependent. That is, the definition of discrete equations (as well as the numerical quadrature for evaluating weighted residuals) and solution (as in Equations (5.10), (5.11), and (5.12)) depends on the transition front Γ_{tr} and thereby is determined by the IBL solution itself. Ref. [4] provides a sample implementation strategy resorting to dummy equations and variables. However, the implementation is significantly complex and tedious, and will be even more so for the extension to 3D.

5.2.2 Under-relaxed Newton Solver

The cut-cell treatment also complicates the Newton method presented in Section 2.3.1 for solving the global nonlinear system of equations.

First, an exact Newton method requires the calculation of the following Jacobian

$$\frac{\mathrm{d}\mathcal{R}_{\mathrm{IBL}}}{\mathrm{d}Q_{\mathrm{IBL}}} = \frac{\partial \mathcal{R}_{\mathrm{IBL}}}{\partial Q_{\mathrm{IBL}}} + \frac{\partial \mathcal{R}_{\mathrm{IBL}}}{\partial X_{\mathrm{tr}}} \frac{\mathrm{d}X_{\mathrm{tr}}}{\mathrm{d}Q_{\mathrm{IBL}}} \tag{5.13}$$

Compared to standard finite element discretization without cut-cell treatment, it introduces the second term involving the solution-dependent interface parametrization X_{tr} through the chain rule of differentiation and thereby adds to the implementation complexity.

Moreover, some techniques for enhancing nonlinear solution robustness are no longer applicable. The line-search algorithm is contingent on the smoothness of the equation residual, but the cut-cell definition of equations and solution generally changes between Newton iterations. For example, at the n-th Newton iteration as illustrated in Figures 5-4a and 5-4b, the solution Q^n and its plain Newton update Q^{n+1} can refer to different transition locations and hence disparate cut-cell configurations. Meanwhile, residuals $\mathcal{R}^n$ and $\mathcal{R}^{n+1}$ are defined differently as well, and thus are no longer comparable for the sake of line search.

As a remedy, the overall transition fitting has to resort to an under-relaxed Newton method. A sample algorithm originally from Ref. [4] is described by Algorithm 1 and illustrated in Figure 5-4. However, the under-relaxation unfortunately compromises nonlinear solution robustness, which is another reason for not pursuing the cut-cell transition fitting approach.

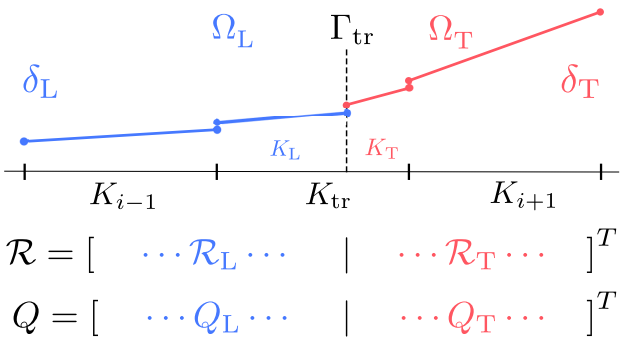

(a) Initial solution Q^n

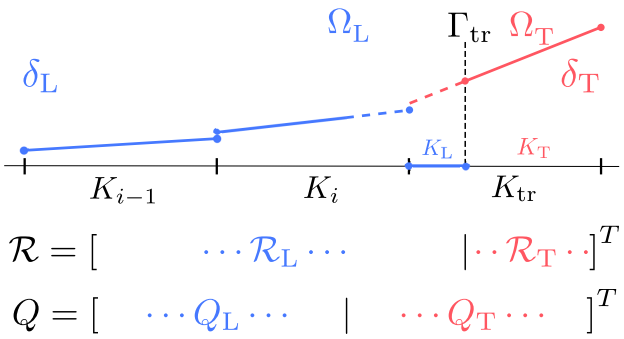

(b) Solution $\widetilde{Q}^{n+1}$ results from a Newton update that assumes it is defined in the same manner as Q^n. However, based on the updated solution $\widetilde{Q}^{n+1}$, the transition front Γ_{tr} has moved and the residual definition changes accordingly.

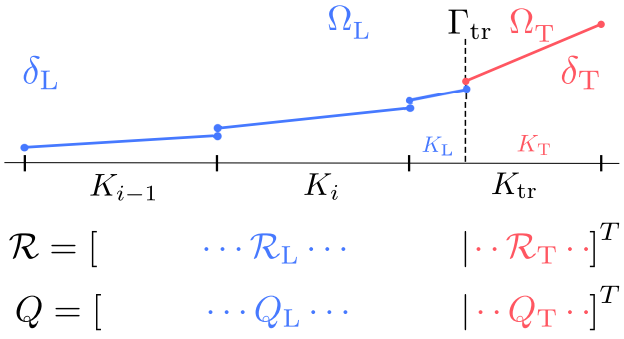

(c) Re-conditioned solution Q^{n+1} is obtained by solving a forced-transition problem with a fixed transition location Γ_{tr} based on $\widetilde{Q}^{n+1}$

Figure 5-4: Schematic of solution and residual evolution in an under-relaxed Newton iteration for transition fitting. The linear DG finite element representation of a nominal solution δ is illustrated here as an example.

Algorithm 1: Under-relaxed Newton solution method for transition fitting

Initialize: Initial solution guess $\boldsymbol{Q}^0$, relaxation factor $\beta = 1$, Newton iteration $n = 0$, maximum iteration $n_{\max}$

while *Solution* $\boldsymbol{Q}^n$ *is not converged and* $n \leq n_{max}$ **do**

- Solve Equation (2.15) of the free-transition problem for $\Delta\boldsymbol{Q}^n$.
- **Under-relax** the plain Newton solution update (2.16):
  $\widetilde{\boldsymbol{Q}}^{n+1} = \boldsymbol{Q}^n + \beta\,\Delta\boldsymbol{Q}^n$
- **if** *Solution* $\widetilde{\boldsymbol{Q}}^{n+1}$ *converges* **then**
  - Set $\boldsymbol{Q}^{n+1} = \widetilde{\boldsymbol{Q}}^{n+1}$.
  - Exit the while loop.
- **else**
  - Identify the transition front Γ_{tr}^{n+1} based on $\widetilde{\boldsymbol{Q}}^{n+1}$.
  - Solve the forced transition problem with fixed Γ_{tr}^{n+1} using the line-search Newton method and the initial solution guess $\widetilde{\boldsymbol{Q}}^{n+1}$.
  - **Re-conditioning**: Set $\boldsymbol{Q}^{n+1} = \widetilde{\boldsymbol{Q}}^{n+1}$.
- **end**
- Increment n by 1.

end

Return solution $\boldsymbol{Q}$, if it is converged.

5.3 Transition Capturing

A transition capturing method is proposed in this thesis to sidestep the aforementioned difficulties of implementation and robustness for transition fitting. It has also turned out to provide satisfactory accuracy and tolerance of coarse grids, on par with traditional transition fitting methods. The 2D formulation was originally presented

in Ref. [47]. The 3D extension is demonstrated to be convenient and effective in this thesis through its implementation and associated 3D numerical results.

5.3.1 Transition Capturing versus Transition Fitting

Before detailing the transition capturing formulation, it is worth comparing it with transition fitting. Figure 5-5 illustrates the differences by examining the DG finite element solution representation.

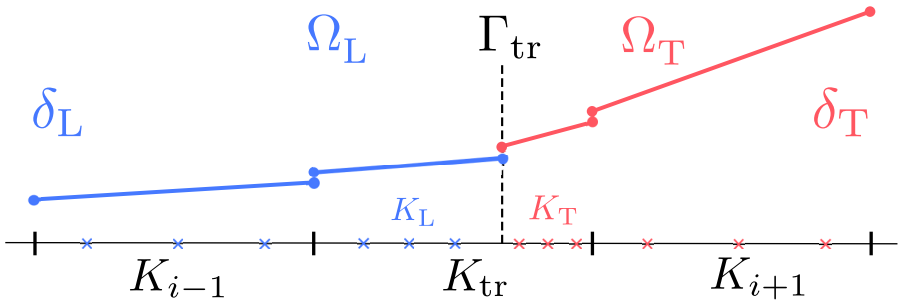

(a) Transition fitting (based on a cut-cell method)

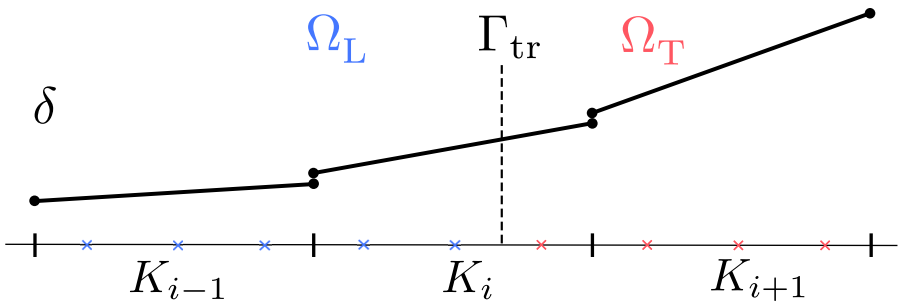

(b) Transition capturing

Figure 5-5: DG finite element solution representation (of a nominal variable δ) for transition fitting and capturing methods. A linear Lagrange polynomial basis is considered here. Cross symbols indicate numerical quadrature points for evaluating weighted residuals. Blue and red colors refer to laminar and turbulent respectively.

For transition fitting via the cut-cell finite element method, the transition front Γ_{tr}

is explicitly identified and parametrized, based on which the numerical discretization is modified. The transitional element K_{tr} is split into two sub-elements, and enriched with additional DOFs as well as numerical quadrature points. The governing equations are discretized on respective sub-elements, with matching conditions enforced at the transition front interface.

In contrast, for transition capturing, the solution representation and equation discretization requires no modification from the DG formulation presented in Chapter 4. The transition front Γ_{tr} is represented implicitly. That is, instead of specifying its exact location (e.g. via parametrization of the spatial coordinates (x, y, z)), the method only needs to know if a given location is laminar or turbulent (for example, by comparing $\tilde{n}$ and $\tilde{n}_{\text{crit}}$). As shown in Figure 5-5b, such implicit identification of Γ_{tr} happens at each numerical quadrature point of finite elements.

The simplicity of the transition capturing method stands out in comparison to transition fitting, especially for 3D IBL. Numerical results of the proposed method also demonstrate its competitive accuracy. Hence, the transition capturing method in this work is recommended for the numerical treatment of flow transition in 3D IBL.

5.3.2 Intermittency-based Blending Formulation

The transition capturing method is formulated by modifying the governing equations instead of changing the numerical discretization. The flux $\mathbf{F}$ and the source S terms in Equation (4.6) are defined as

$$\mathbf{F}(\boldsymbol{v}) = (1-\gamma)\,\mathbf{F}_{\text{L}}(\boldsymbol{v}) + \gamma\,\mathbf{F}_{\text{T}}(\boldsymbol{v}), \qquad S(\boldsymbol{v}) = (1-\gamma)\,S_{\text{L}}(\boldsymbol{v}) + \gamma\,S_{\text{T}}(\boldsymbol{v}) \tag{5.14}$$

where the subscripts "L" and "T" indicate laminar and turbulent components, evaluated with respective closure relations. An *intermittency factor* γ is introduced to linearly combine laminar and turbulent contributions, such that the values $\gamma = 0$ and $\gamma = 1$ correspond to fully-laminar and fully-turbulent shear layers respectively.

The intermittency factor γ is defined as

$$\gamma(\tilde{n}) = \begin{cases} 0, & f \in (-\infty, -1] \\ \frac{1}{2}\left[1 + \sin\left(\frac{\pi f}{2}\right)\right], & f \in (-1, 1) \\ 1, & f \in [1, +\infty) \end{cases}, \qquad f \equiv \frac{\tilde{n} - \tilde{n}_{\text{crit}}}{\Delta\tilde{n}} \tag{5.15}$$

so that γ varies smoothly and monotonically from 0 to 1 as $\tilde{n}$ increases from 0 and surpasses $\tilde{n}_{\text{crit}}$, which is consistent with the transition criterion (5.2). The smooth ramp function avoids introducing any $\mathcal{C}^0$-discontinuity to the governing equations which otherwise would be difficult for the numerical discretization scheme to resolve.

The parameter $\Delta\tilde{n}$ is defined as

$$\Delta\tilde{n} \equiv \Delta s \, \frac{\mathbf{q}_{\text{e}} \cdot \widetilde{\nabla}\tilde{n}}{q_{\text{e}}} \approx \Delta s \, \frac{f_{\text{TS}}}{\theta_{11}} \tag{5.16}$$

where the approximation follows from Equation (5.1) and is exact in the steady-state case. The $\Delta\tilde{n}$ definition is intended to achieve a transition length scale Δs, which is chosen to be twice the local grid element length scale that is fixed a priori [47]. For simplicity, the growth rate function f_{TS} is approximated using the constant value defined for the turbulent regime as in Equation (B.10).

The intermittency-based blending formulation in Equation (5.14) is applied to Equations (2.2), (2.3), (2.4), (5.1) and (3.16). Equation (5.1) is extended to the turbulent regime by introducing a positive constant growth rate as in Equation (B.10).

Equation (3.16) is also extended to the laminar region by modifying the source term so that the solution c_τ closely tracks the turbulent onset c_τ closure, of which the detailed formulation is presented in Appendix B.5.

It is worth noting that the numerical intermittency factor γ in this work is solely a numerical artifact intended to facilitate the transition capturing. In a different context, the concept of intermittency may refer to the physical phenomena of the intermittent switch between laminar and turbulent flow states. However, that physical modeling warrants a dedicated separate discussion and is beyond the scope of this thesis.

5.4 Numerical Results

Motivated by its evident advantages in comparison to transition fitting, the transition capturing method is recommended and adopted in the following 2D and 3D numerical studies to demonstrate its effectiveness.

5.4.1 2D Transitional Flow over Eppler 387 Airfoil

The first test case involves incompressible flow over the Eppler 387 airfoil at angle of attack $\alpha = 4^\circ$ and chord-based Reynolds number $Re = 10^5$. It features a separation bubble and ensuing flow transition on the suction side (i.e. upper surface). A sample configuration is illustrated in Figure 5-6, where the wake geometry and mesh are generated from XFOIL based on the inviscid flow velocity field. For all the numerical results of this and the following test cases, the SANS-IBL method uses a polynomial order $p = 1$ and the Lax-Friedrichs numerical flux for the DG discretization with the modification in Equation (4.20). The weighted integrals in the DG weak form

are integrated using a three-point Gauss-Legendre quadrature rule for computational efficiency, while higher-order quadrature that was trialed (namely, a seven-point and a twenty-point rule) had negligible impact on the solution.

Figure 5-6: Sample grid of Eppler 387 airfoil test case $\alpha = 4°$ (64 and 14 elements on the airfoil and the wake respectively)

Figure 5-7 illustrates a close match between numerical results of SANS-IBL and XFOIL. The comparison also includes a 3D axisymmetric IBL formulation MTFLOW [65], which adopts a captured transition approach for free transition modeling. The MTFLOW results are obtained from a ring wing geometry with a radius-to-chord ratio of 100 in order to produce approximately 2D flows at any airfoil cross section. In view of the difference in far-field boundary conditions, the angle of attack in MTFLOW is adjusted to match XFOIL's lift coefficient. Compared to XFOIL and SANS-IBL as shown in Figure 5-7, the pressure gradient at reattachment after the separation bubble is less steep in MTFLOW and implies a coarser transition resolution. This is mainly attributed to the fact that MTFLOW imposes a constant shear stress level $(c_\tau)_{\mathrm{T,init}}$ at the turbulence onset, which tends to be much smaller than a solution-dependent $(c_\tau)_{\mathrm{T,init}}$ closure. On the other hand, enforcing the interface condition of $(c_\tau)_{\mathrm{T,init}}$ in MTFLOW is nontrivial because the the amplification factor growth and the lag equations are solved as a single equation with a shared variable $\mathcal{G}$ (similar to the transition capturing treatment of Ref. [4]).

That difficulty is overcome by the current captured transition treatment of SANS-IBL. The intermittency factor γ of SANS-IBL as shown in Figure 5-8 illustrates a transitional region, identified by $0 < \gamma < 1$, that spans only a handful of (e.g. three)

elements, and achieves a comparable transition resolution as XFOIL. Also, it provides sufficient numerical regularization for the otherwise discontinuous IBL equations at flow transition that are not readily amenable to the nonlinear solver. In addition, by defining the transition length scale Δs to be proportional to a representative grid element size, the resolution of the transition region is further sharpened with mesh refinement.

5.4.2 Drag Polar of FK67-K-170 Airfoil

A second stress test is carried out for the FX67-K-170 sailplane airfoil at Reynolds number 2×10^6. For angle of attack $\alpha = 4.156°$, the incompressible flow over the FX67-K-170 airfoil features small yet intense separation bubbles and correspondingly induced flow transition. Such characteristics need to be well resolved in order to predict the drag accurately and are thus quite demanding for the numerical method. Figure 5-9 shows sample numerical results of SANS-IBL that match the XFOIL results closely.

At the same flow condition, a grid refinement study is also conducted for both SANS-IBL and XFOIL, the results of which are shown in Figure 5-10. The study reveals noticeable oscillation in the drag coefficient computed from XFOIL as its mean trend line converges gradually with grid refinement. This observation is consistent with the findings reported in Ref. [11] and the issue is attributed to the fitted transition treatment based on a cut-cell method. Although the exact solution to the IBL equations remains invariant, the cut cell configuration changes from grid to grid (as it is refined) in order to numerically track the transition front, and turns out to have a strong bearing on the resulting viscous solution. Such grid sensitivity often requires excessive grid resolution to provide reliably converged solutions. In

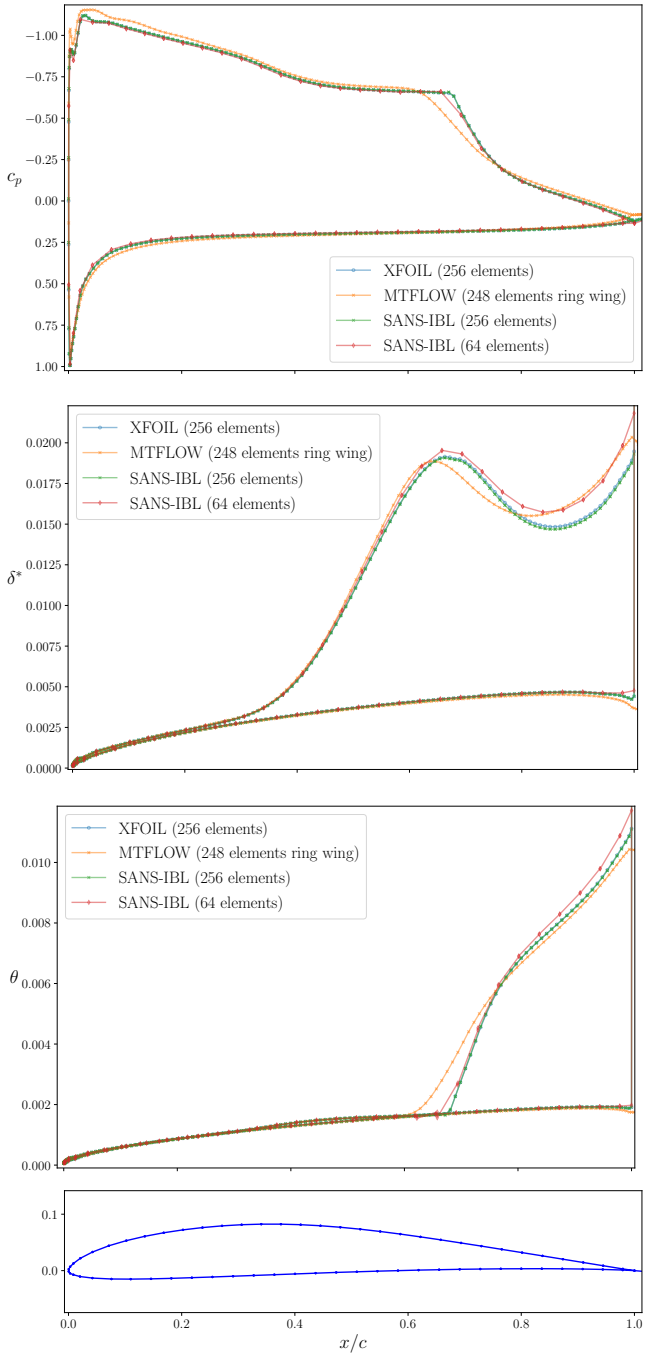

Figure 5-7: Eppler 387, $\alpha = 4°, Re = 10^5$: pressure coefficient c_p (upper left), displacement thickness δ^* (upper right) and momentum thickness θ (lower center)

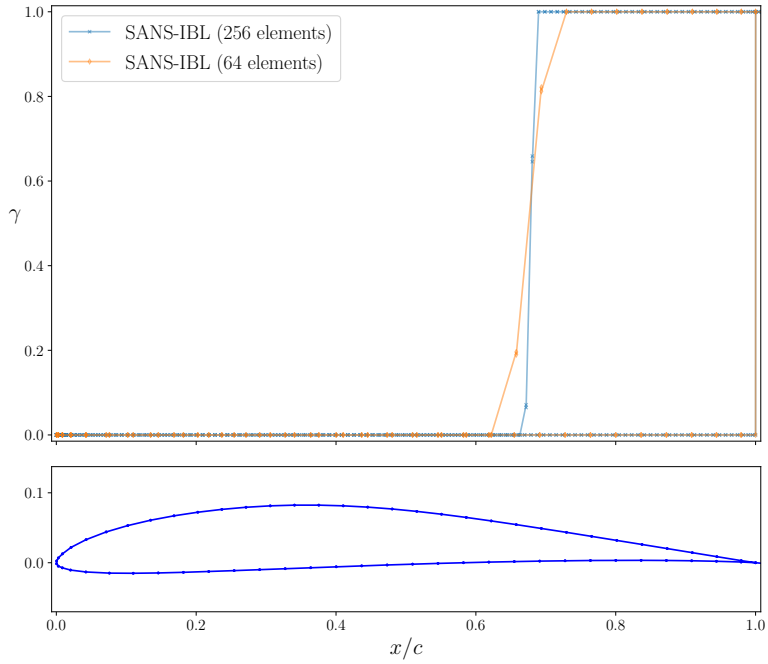

Figure 5-8: Intermittency factor γ of SANS-IBL solution for different mesh resolutions

contrast, the SANS-IBL method with a captured transition treatment demonstrates an unambiguous trend of grid convergence in its numerical solution as illustrated in Figure 5-10, which is more favorable.

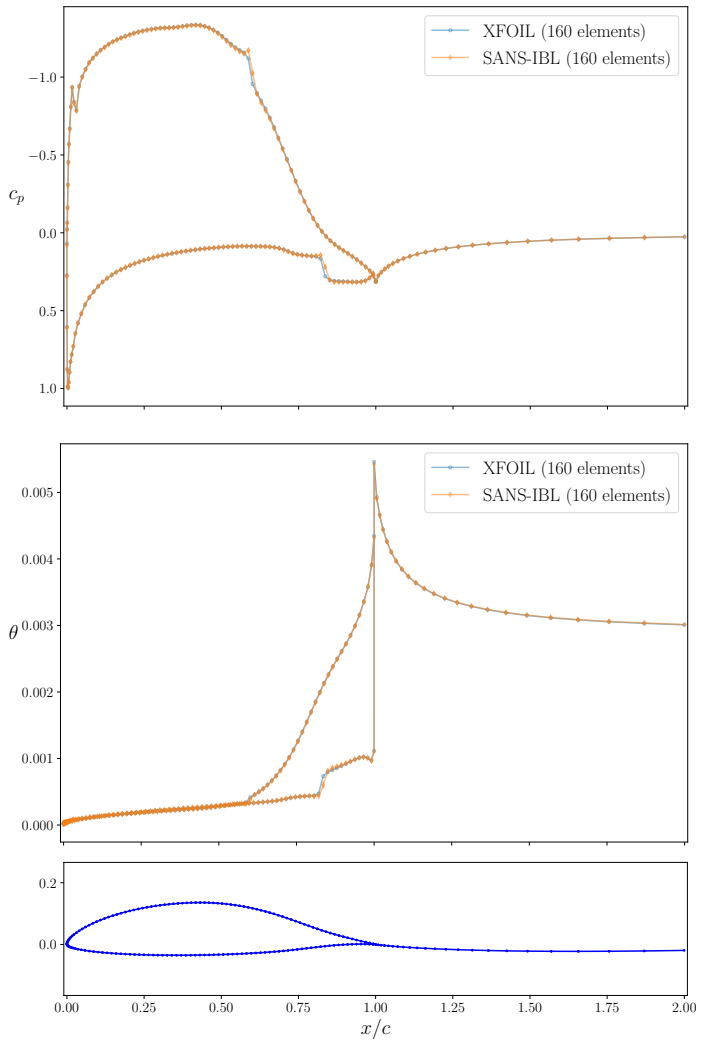

Figure 5-9: FX67-K-170, $\alpha = 4.156°, Re = 2 \times 10^6$: pressure coefficient c_p (left) and momentum thickness θ (right)

Figure 5-11 shows the drag polars at $Re = 2 \times 10^6$ computed from SANS-IBL and XFOIL on three different grids (with respectively 160, 240 and 320 elements

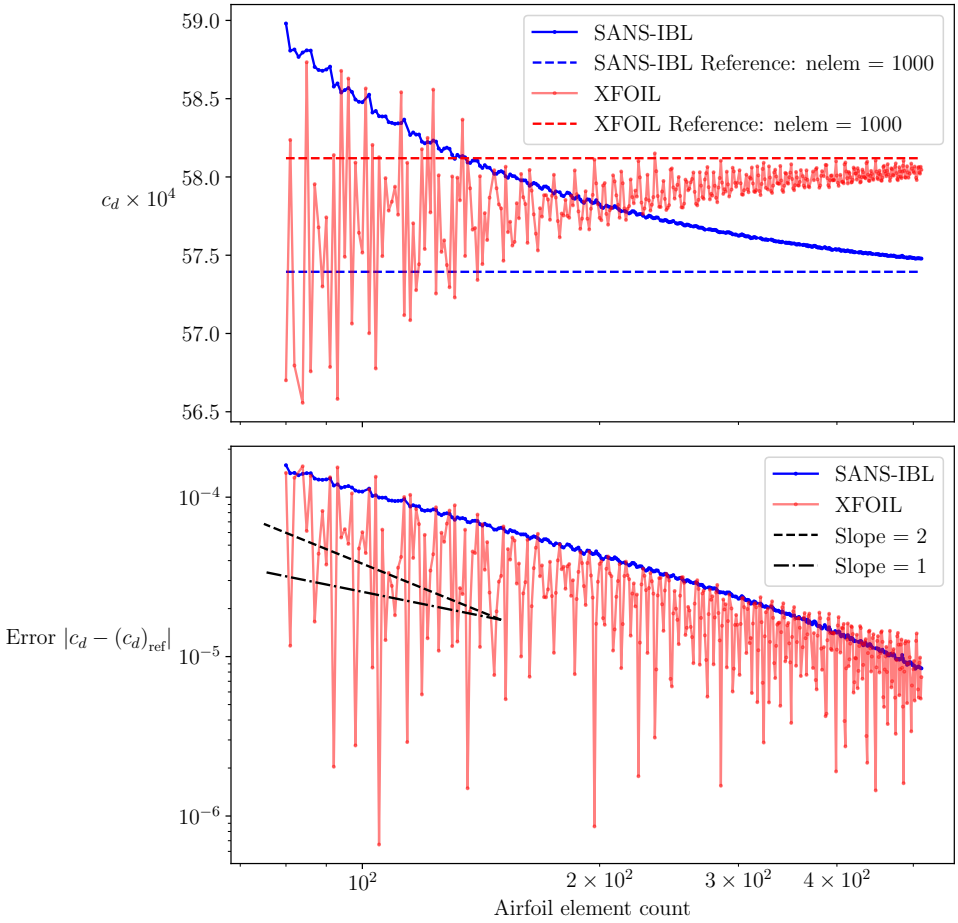

Figure 5-10: Grid convergence of drag coefficient c_d.

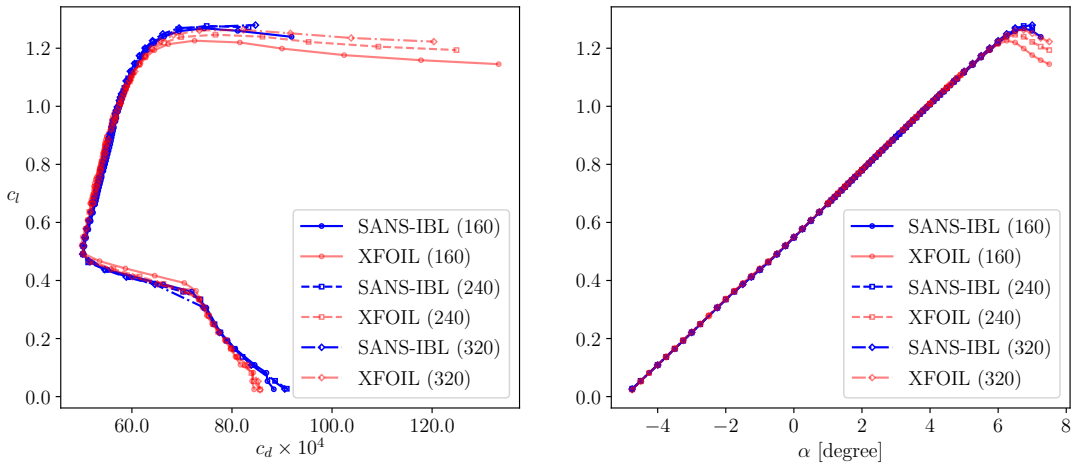

Figure 5-11: Drag polar for FX67-K-170 airfoil at $Re = 2 \times 10^6$ for different grid refinement levels. (Airfoil element count indicated in parentheses)

on the airfoil surface). The comparison demonstrates an overall reasonable agreement between SANS-IBL and XFOIL. It is also worth noting that, as highlighted in Figure 5-12, the drag polar computed from XFOIL appears more ragged than SANS-IBL as the angle of attack traverses the range of $0° < \alpha < 5°$. For this range of α, the separation bubbles are strong and the corresponding transition front moves across nodes on a given fixed grid. The resulting wavy behavior in the drag polar is another manifestation of the solution sensitivity to the underlying cut-cell fitted transition treatment. Such behavior will lead to unreliable derivative calculations, e.g. $\partial(c_d)/\partial\alpha$ and $\partial(c_d)/\partial(c_l)$, and hence is not desirable, for example, in the context of design optimization. In comparison, that problem is sidestepped in the SANS-IBL method which is able to compute a smooth drag polar.

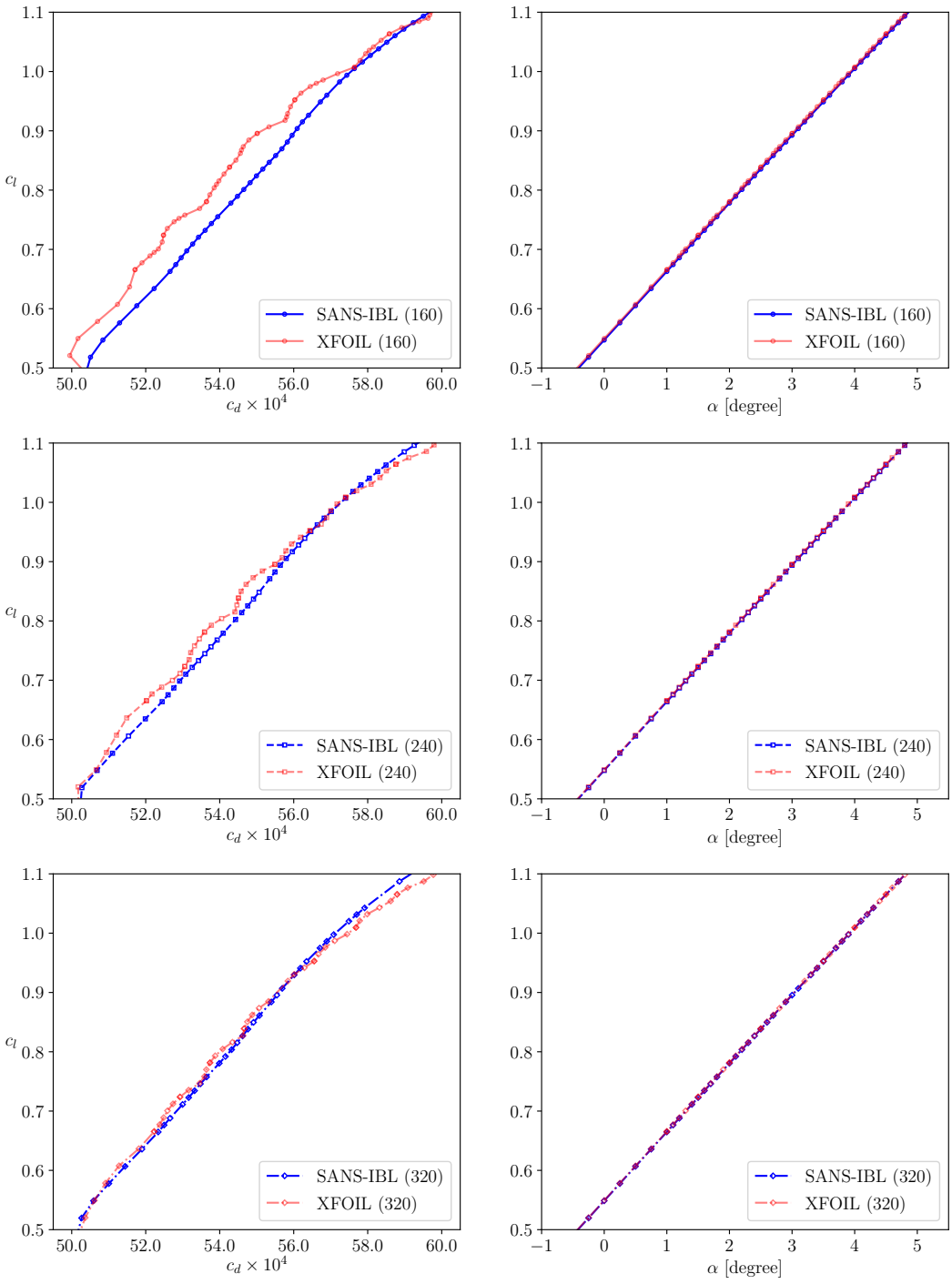

Figure 5-12: Close-up views of drag polar for FX67-K-170 airfoil at $Re = 2 \times 10^6$ for different grid refinement levels. (Airfoil element count indicated in parentheses)

5.4.3 3D Transitional Boundary Layer on Flat Plate under a Sphere

The final test case is intended to demonstrate the transition capturing capability for 3D problems with free transition. In addition, it illustrates the integrated 3D IBL solution with strong viscous-inviscid interaction, laminar and turbulent closure and flow separation.

The case is for 3D boundary layer developing on a flat plate under a sphere body. Its setup resembles the case illustrated in Figure 3-8, except that the torpedo-shaped body modeled by a point source is replaced by a sphere body modeled as a doublet with the following parameters.

$$(x_c, y_c, z_c) = (0.75, 0, 0.25) \qquad \text{(center coordinates)}$$

$$\mu = 0.005\, q_\infty \qquad \text{(doublet strength)}$$

The Reynolds number based on unit plate length is 10^6. A computational grid consisting of 50×50 uniformly distributed quadrilateral elements is used, as shown in Figure 5-13. The following three flow scenarios are investigated.

- **Scenario 1**: Full laminar boundary layer with $\tilde{n}_{\text{crit}} = +\infty$. Flow transition is deliberately ruled out. Flow becomes severely separated.

- **Scenario 2**: Transitional boundary layer with $\tilde{n}_{\text{crit}} = 9.0$. Free transition is induced by a separation bubble.

- **Scenario 3**: Transitional boundary layer with $\tilde{n}_{\text{crit}} = 3.0$. Compared to Scenario 2, the lower $\tilde{n}_{\text{crit}}$ threshold here corresponds to a stronger tendency to trigger flow transition. Free transition occurs prematurely without flow sepa-

ration.

Figure 5-13 illustrates the spatially-varying pressure distribution on the flat plate based on the coupled 3D IBL solution. The dominating pattern is governed by the presence of the sphere body above the flat plate, while variation between the three flow scenarios stems from different boundary layer behavior and the associated viscous effects through tight viscous-inviscid coupling. As it develops on the flat plate, the boundary layer undergoes both favorable and adverse pressure gradients in an alternating fashion.

Figure 5-14 shows the behavior of the $\tilde{n}$ solution and the corresponding intermittency factor γ. In Scenario 1, flow transition is effectively delayed indefinitely so that the boundary layer remains fully laminar, although $\tilde{n}$ still grows following the amplification factor equation (5.1). Scenarios 2 and 3 result into two different transition front topologies corresponding to flow transition triggered at different thresholds $\tilde{n}_{\text{crit}}$. As transition occurs, the intermittency factor γ displays smooth blending/ramp-up from the laminar regime to the turbulent one. It is clear that the current transition capturing method for 3D IBL is able to resolve a generally curved transition front.

Other aspects of the boundary layer behavior are illustrated in Figures 5-15 and 5-16. The negative value of streamwise skin friction coefficient c_{f_1} and the streamwise shape factor $H_1 > 4.0$ (approximately) both identify the downstream flow separation in the fully laminar boundary layer of Scenario 1 and the separation bubble that triggers the flow transition in Scenario 2. The separation is also visualized in Figure 5-13 based on the wall-limiting streamlines $\boldsymbol{\tau}_{\text{w}}$ that reverse direction and pile up near $(x, y) = (0.9, 0)$. As the boundary layer undergoes transition in Scenario 2 and 3, all of θ_{11}, c_{f_1} and $c_{\mathcal{D}}$ values increase significantly from the laminar regime to the

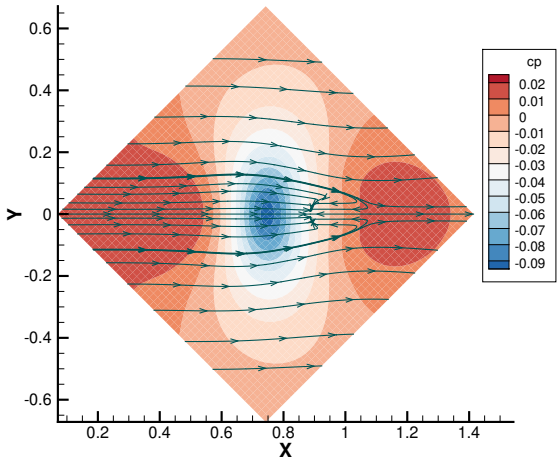

(a) Scenario 1: fully laminar $\tilde{n}_{\text{crit}} = +\infty$

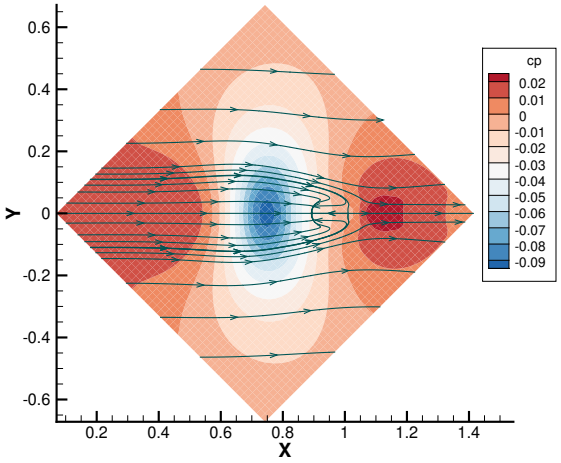

(b) Scenario 2: free transition $\tilde{n}_{\text{crit}} = 9.0$

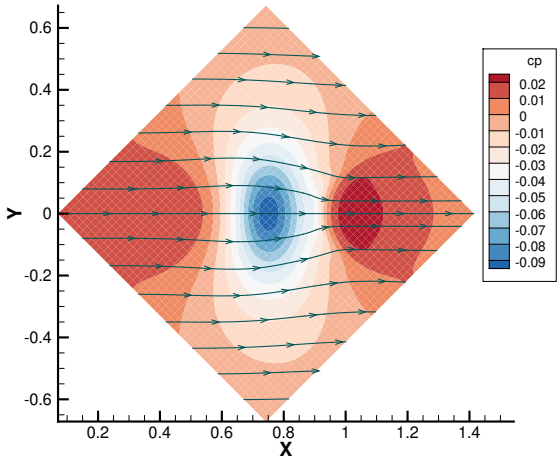

(c) Scenario 3: free transition $\tilde{n}_{\text{crit}} = 3.0$

Figure 5-13: 3D Transitional boundary layers on flat plate under a sphere: pressure coefficient c_p distribution (colored contour) and wall-limiting streamlines $\boldsymbol{\tau}_{\text{w}}$ (analogous to a surface oil flow visualization)

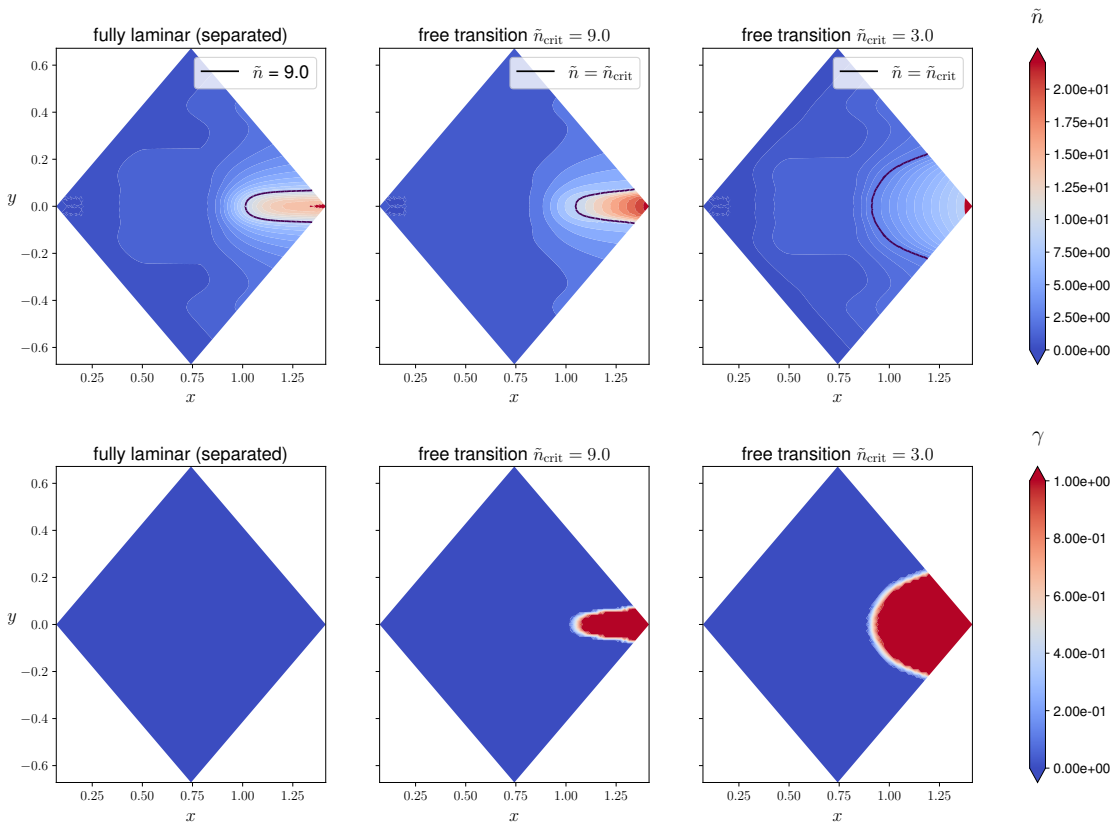

Figure 5-14: 3D Transitional boundary layers on flat plate under a sphere: amplification factor $\tilde{n}$ (top) and intermittency γ (bottom)

turbulent regime, corresponding to a much higher level of drag-producing dissipation. Another observation is that crossflow phenomena are milder for turbulent boundary layers than for laminar ones, as indicated by the magnitude of crossflow shape factor H_2.

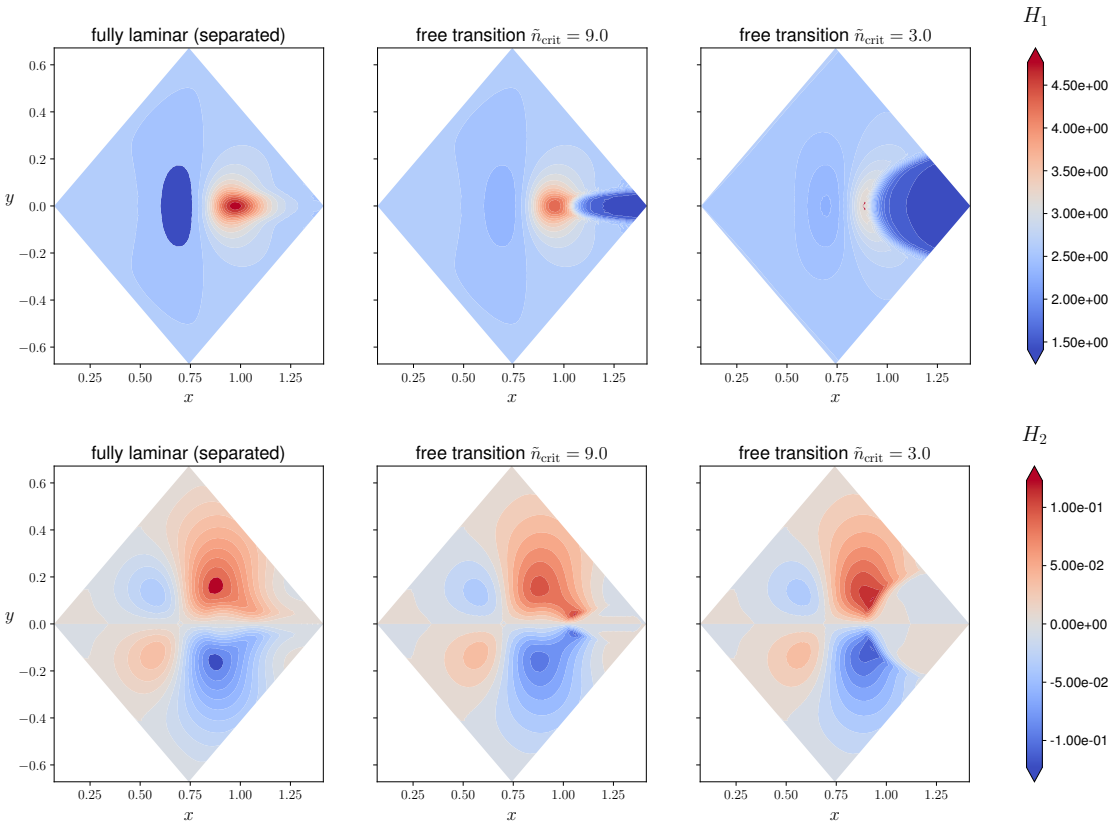

Figure 5-15: 3D Transitional boundary layers on flat plate under a sphere: streamwise shape factor H_1 (top) and crossflow shape factor H_2 (bottom)

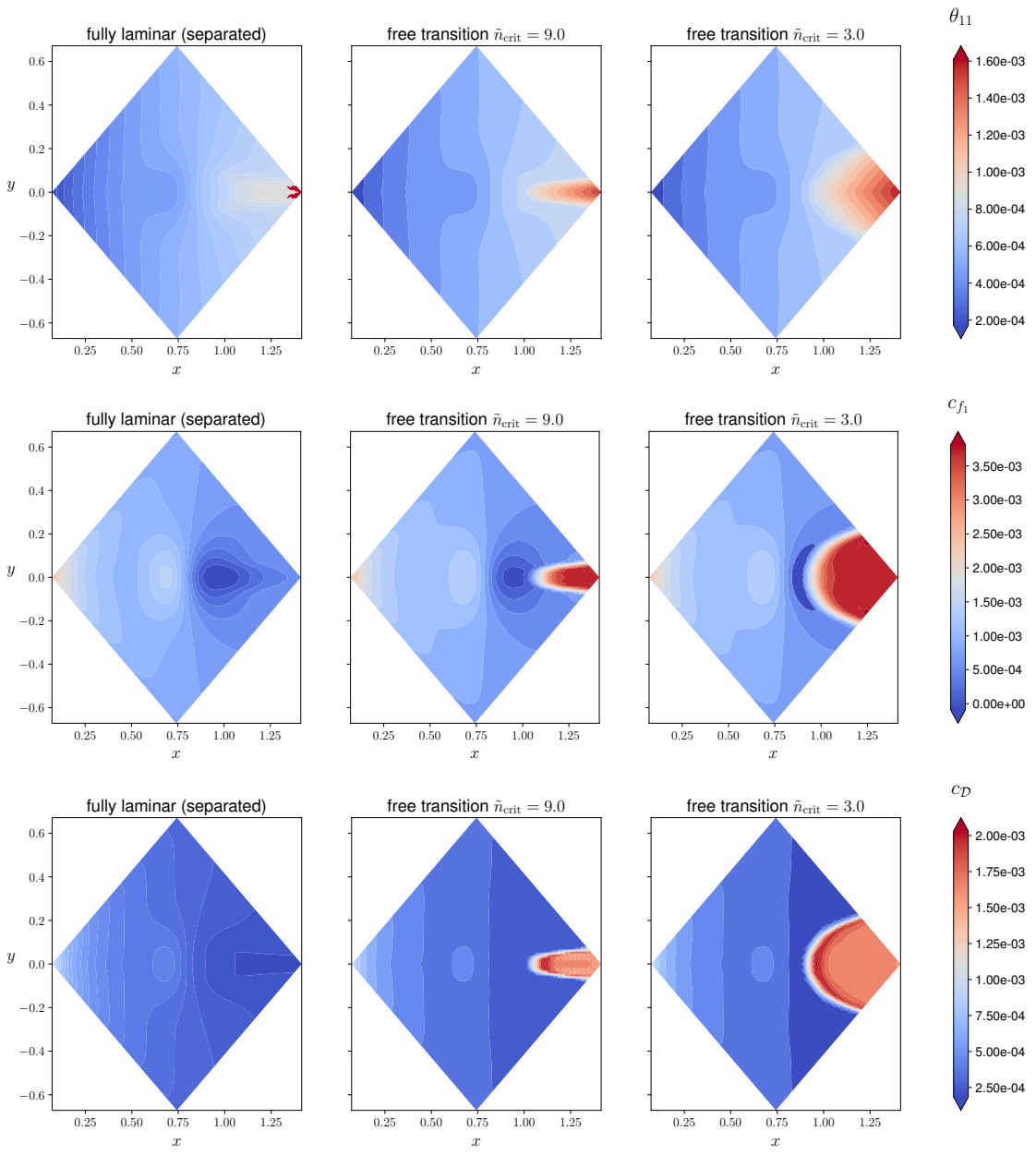

Figure 5-16: 3D Transitional boundary layers on flat plate under a sphere: streamwise momentum defect thickness θ_{11} (top), streamwise skin friction coefficient c_{f_1} (middle), and dissipation coefficient $c_{\mathcal{D}}$ (bottom)

Chapter 6

Conclusions and Future Work

This thesis concludes with a summary of the main contributions and potential avenues for future research. The following list highlights a number of thesis contributions.

1. This thesis presents novel strategies and results of 3D IBL closure modeling. In contrast to previous studies that formulate the 3D IBL closure simply based on heuristic assumption, this thesis takes a data-driven modeling approach and has generated original 3D boundary layer data sets from higher-fidelity numerical solutions. Based on these data, neural network regression models are adopted for the first time to build the IBL closure. In addition to leveraging their convenience and expressiveness for multivariate regression, the neural network models are also customized to encode physical constraints and to facilitate variable selection. Moreover, a model inversion method is proposed for automated data-driven calibration of the turbulent shear stress transport model in the IBL context. Numerical results have demonstrated the effectiveness of the overall four-equation 3D IBL equipped with newly developed closure, evidenced from

the richer crossflow characterization as compared to previous three-equation formulation and a great match with the reference numerical solution.

2. A second thesis contribution is to investigate the proper numerical stabilization of the DG FEM for the IBL equations. Although the finite element discretization of the 3D IBL equations is not new, its stability has not been examined with stress tests. In fact, numerical studies in this work are the first to reveal that heuristic numerical flux schemes for DG FEM lead to ill-posed numerical solution in the presence of boundary layer separation and transition. On the other hand, difficulties have been identified regarding the 3D IBL characteristic analysis and its application to devising a numerical flux for DG FEM. As an intermediate remedy, a modified stabilization scheme motivated by the underlying momentum conservation law is proposed and is observed to have produced well-behaved numerical solution as shown in the results throughout this thesis.

3. This thesis also develops transition prediction capability for 3D IBL methods. A suitable numerical treatment of 3D free flow transition is recommended based on a comparison between two main strategies. The development starts with an implementation of the transition fitting approach which is popular among existing 2D IBL methods. However, the transition fitting method based on cut-cell finite elements developed in this thesis has revealed its disadvantages including complex implementation and compromised robustness. This observation motivates the proposal of a new transition capturing approach based on an implicit transition front representation using the concept of numerical intermittency. This transition capturing method is demonstrated to perform well in 2D and 3D transition prediction, and hence deemed suitable for transition

modeling in the 3D IBL model.

This work has also identified opportunities for improvement and extension in potential future research summarized as follows.

1. **IBL Closure Refinement**. The 3D IBL closure developed in work has been demonstrated to be quite effective in modeling 3D boundary layers, thanks to the newly-generated data sets and the data-driven closure modeling approach. Using the same closure modeling methodology, the closure models can continue to be improved as the size of the data sets becomes larger. Also, data from even higher-fidelity sources than DBL3 and RANS are expected to further improve the physical modeling capability of 3D IBL. For example, numerical results from Large Eddy Simulation (LES) and Direct Numerical Simulation (DNS) are potential candidates, although they are not available in this work due to high acquisition costs.

   Closure for the turbulent wake can also be studied in more detail. Currently, it is not distinguished from the turbulent boundary layer closure except for the vanishing skin friction, in the same way the turbulent wake is treated in 2D IBL methods. However, behavior of a 3D turbulent wake can be further examined and confirmed against wake data

2. **Application to 3D Geometries**. Although the numerical results in this work demonstrate the effective modeling of 3D boundary layer flow physics by the proposed IBL method, only a flat plate geometry is considered. To exploit the full benefits of 3D IBL modeling for viscous aerodynamic analysis in practice, it remains to be applied to general 3D configurations such as aircraft wing and wing-body geometries. This extension requires mainly implementation efforts

involving geometry generation, meshing and development of inviscid solvers (for example, a 3D potential flow solver or a panel method). These efforts are tangential to the main thesis contributions and hence have not been pursued in the current work.

Another challenge arising from the general 3D configurations is juncture flow where boundary layers developing on separate surfaces interact. For example, this scenario can appear at a 90°-corner of the wing-fuselage joint. At such a corner, the thin shear layer assumption underlying the IBL model breaks down because the in-plane diffusion of one wall is actually wall-normal diffusion to the neighboring wall and thus no longer negligible. Therefore an additional physical model or closure is likely necessary for such juncture flow to maintain proper conservation principles, while practical workarounds such as adding geometric fairing is proposed in Appendix E.

3. **Computational Efficiency Gain**. While the IBL modeling is already computationally more efficient compared to DBL or RANS models thanks to the thickness-integral model reduction, the implementation of the 3D IBL method can be further optimized to achieve the most efficiency gain. First, the linear solver (for computing the Newton solution update as discussed in Section 2.3.1) can be improved. The numerical studies in this work mostly adopt a direct linear solver since the problem size is modest and the associated demand for computation time and memory is easily satisfied by a laptop, which is a strength of the overall IBL method. On the other hand, an iterative solver such as GMRES is likely more appropriate if the problem size gets larger and if the inviscid solver (for example, potential or Euler solvers) results in a conducive sparsity pattern of the global Jacobian (in contrast to the dense Jacobian blocks result-

ing from IBL coupling with a panel method). Further investigation into the associated preconditioner and equation ordering may also offer potential gain in performance.

Second, a parallel implementation of the coupled IBL method will enable simulation at a much larger scale and using much less wall-clock time, although the current numerical studies are run in serial without much issues thanks to their modest size. To run the coupled 3D IBL method in parallel may involve some challenges, such as the proper domain decomposition strategy when the inviscid solver involves a volume grid whereas the IBL formulation (as well as auxiliary equations for viscous-inviscid coupling) resides on the volume's boundary, i.e. a surface grid.

Finally, a different variant of the finite element discretization may be adopted to provide better efficiency than the DG formulation in this work. The generic continuous Galerkin (CG) formulation adopted by Nishida [22] and Drela [3] is more efficient in terms of the computational cost per degree of freedom (DOF) to achieve the same level of numerical accuracy [66], but its numerical stabilization needs to be examined more closely. Another prospective candidate is the Variational Multiscale with Discontinuous subscales (VMSD) variant of CG scheme developed by Huang [66], which can draw on the same numerical stabilization developed for DG in this work while offering much better DOF efficiency.

4. **Physical Modeling of 3D Flow Transition**. This thesis focuses on the numerical treatment of 3D free flow transition, whereas the physical modeling of 3D flow transition mechanisms remains to be investigated. The primary additional mode of transition to be characterized is the crossflow instability.

Section 5.1 points to some existing literature on crossflow transition modeling and briefly states a prospective formulation for incorporating crossflow transition into the current e^N envelope method. Another avenue for improving the current transition model based on linear stability is to utilize a nonlocal or nonlinear stability theory such as the parabolized stability equation.

5. **Improved Numerical Stabilization**. The numerical discretization of 3D IBL still leaves room for improvement. As discussed in Chapter 4, the current work has identified difficulties with the characteristic analysis of the 3D IBL equations and resorts to an ad hoc numerical flux formulation to address ill-behaved numerical solution. However, a more rigorous stability analysis and formulation of numerical stabilization remains to be desired. Improvement on that front will likely further boost the robustness of the numerical discretization scheme for 3D IBL.

6. **Aerostructural Coupling and Design Optimization**. The 3D IBL method can be further coupled with a structural mechanics solver to conduct aeroelastic analysis, by extending the viscous-inviscid coupling scheme in Section 2.3. For example, the combination of the 3D IBL method, a full-potential solver [67] and a hybrid shell model [68] forms a suite of medium-fidelity aerostructural analysis tools suitable for aircraft preliminary design. The significant speedup compared to RANS also makes IBL an attractive method for design optimization involving viscous aerodynamic analysis. To that end, an adjoint formulation of the IBL equations is worth pursuing, which will be useful for design sensitivity studies and gradient-based optimization. The implementation of the IBL adjoint can build on the existing automatic-differentiation-assisted sensitivity calculation for the Newton nonlinear solution method in Section 2.3.1.

Appendix A

3D IBL Formulation and Derivation

For completeness, this appendix restates details of the 3D IBL formulation and derivation previously covered in Ref. [3, 27, 4, 47].

A.1 Equivalent Inviscid Flow

Equivalent Inviscid Flow (EIF) includes the outer potential flow and its continuation into the viscous layer, shown in Figure A-1 for a flat and curved wall surface.

The EIF is assumed to be irrotational (i.e. $\nabla \times \mathbf{q}_\mathrm{i} = \mathbf{0}$), and to match the real flow outside the viscous layers (i.e. $\mathbf{q}_\mathrm{i} = \mathbf{q}$ for $n > n_\mathrm{e}$). In general it is not tangent to the surface, $(\mathbf{q}_\mathrm{i} \cdot \hat{\mathbf{n}})_\mathrm{w} \neq 0$ (i.e. a nonzero wall transpiration effect that reflects the presence of a viscous layer). For a curved wall, the EIF velocity variation across the viscous layer is $|\mathbf{q}_{\mathrm{i_e}} - \mathbf{q}_{\mathrm{i_w}}| = \mathcal{O}\{\kappa(n_\mathrm{e} - n_\mathrm{w})|\mathbf{q}_{\mathrm{i_e}}|\}$. For the case of small curvature κ as in thin shear layer approximations, $\mathbf{q}_\mathrm{i}$ and hence the pressure p_i are constant across the thickness of the viscous layer.

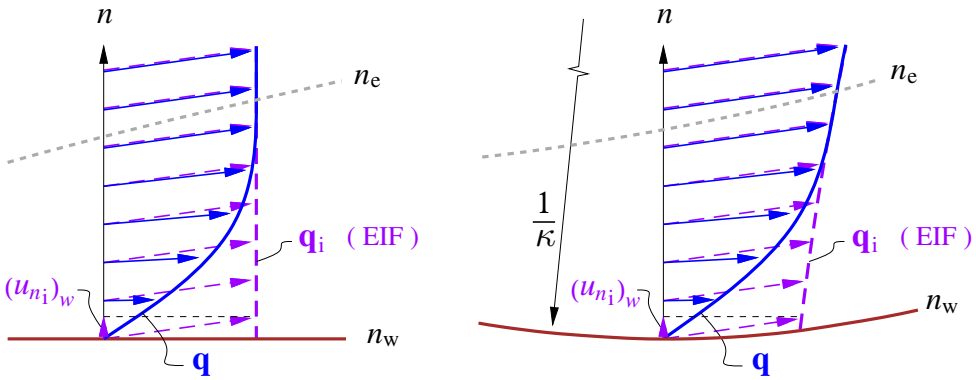

Figure A-1: Real viscous flow and Equivalent Inviscid Flow (EIF) profiles across boundary layers on flat and curved (with curvature κ)walls. Reproduced from Ref. [3] with permission.

A.2 Defect Control Volume

In addition to the EIF, the defect control volume (DCV) constitutes the other component of the viscous-inviscid zonal decomposition as depicted in Figure 1-2. By definition, viscous effects are modeled solely in the DCV, which is hence the focus of in the development of the IBL formulation.

The size of the DCV is much smaller than the overall domain (spanned by the real flow or the EIF) based on the thin shear layer assumptions that

$$\frac{\mathrm{d}\delta}{\mathrm{d}s} \ll 1, \qquad \kappa\,\delta \ll 1 \tag{A.1}$$

where δ is the notional thickness of the boundary layer, s denotes the streamwise coordinate (along the EIF velocity at the wall) and κ stands for the curvature of the aerodynamic surface as illustrated Figure A-1. The thin shear layer assumptions generally apply to high-Reynolds-number aerodynamic flows (with up to moderate separation) over surfaces of small curvature.

The DCV is decomposed into finite elements (DCVE), each of which spans the

viscous layer and covers some portion of the shear layer surface as shown in Figure A-2. The $n = 0$ reference surface inside the DCVE is denoted by $\widetilde{\text{DCVE}}$, which can be placed arbitrarily inside the shear layer and is chosen to be the solid surface (i.e. $n_\text{w} \neq 0$) with $\hat{\mathbf{n}} = \hat{\mathbf{n}}_\text{w}$ in this work.

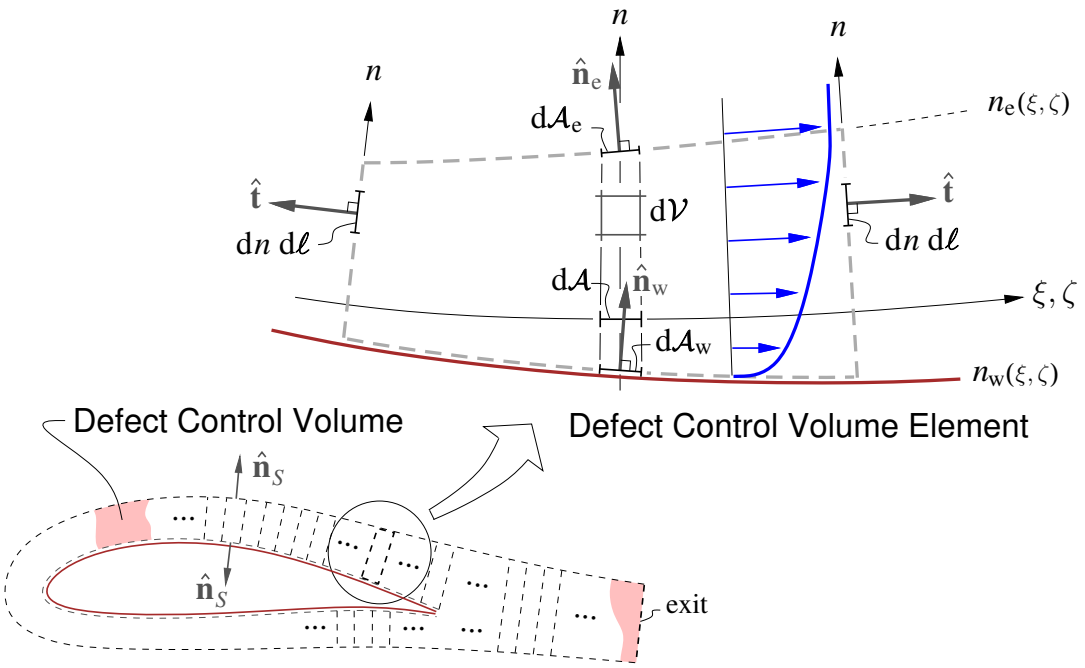

Figure A-2: DCV partitioned into DCV elements. Reproduced from Ref. [3] with permission.

The length, area, and volume differentials over the DCVE can be formed while accounting for the curvature of the element. For example, the area and volume differentials shown in Figure A-2 are given by

$$\begin{aligned} d\mathcal{A}_\text{e} &= (1 - \kappa\, n_\text{e})\, d\mathcal{A} \\ d\mathcal{V} &= (1 - \kappa\, n)\, dn\, d\mathcal{A} \end{aligned}$$

where $d\mathcal{A}$ is the area element on the $n = 0$ surface. Based on the small curvature

assumption in (A.1), the curvature terms are negligible, resulting in the following approximations of area and volume differentials.

$$\begin{aligned}
\hat{\mathbf{n}}_S \,\mathrm{d}\mathcal{S} = &\quad \hat{\mathbf{n}}_\mathrm{e} \,\mathrm{d}\mathcal{A}_\mathrm{e} \approx \quad \hat{\mathbf{n}}_\mathrm{e} \,\mathrm{d}\mathcal{A} && \text{(edge)} \\
\hat{\mathbf{n}}_S \,\mathrm{d}\mathcal{S} = &-\hat{\mathbf{n}}_\mathrm{w} \,\mathrm{d}\mathcal{A}_\mathrm{w} \approx -\hat{\mathbf{n}}_\mathrm{w} \,\mathrm{d}\mathcal{A} && \text{(wall)} \\
\hat{\mathbf{n}}_S \,\mathrm{d}\mathcal{S} \approx &\ \hat{\mathbf{t}} \,\mathrm{d}n \,\mathrm{d}\ell && \text{(perimeter surface)} \\
\mathrm{d}\mathcal{V} \approx &\ \mathrm{d}n \,\mathrm{d}\mathcal{A} && \text{(volume)}
\end{aligned}$$

where $\hat{\mathbf{t}}$ is the unit vector tangent to the $n = 0$ reference surface and the length coordinate ℓ runs around the volume perimeter at the reference surface.

The following relation is then derived to facilitate the derivation of the IBL governing equations.

$$\begin{aligned}
\iint_{\mathrm{DCVE}} \nabla \cdot \mathbf{f} \,\mathrm{d}\mathcal{V} &= \iint_{\widetilde{\mathrm{DCVE}}} \left(\mathbf{f}_\mathrm{e} \cdot \hat{\mathbf{n}}_\mathrm{e} - \mathbf{f}_\mathrm{w} \cdot \hat{\mathbf{n}}_\mathrm{w}\right) \mathrm{d}\mathcal{A} + \oint_{\partial\widetilde{\mathrm{DCVE}}} \mathbf{F} \cdot \hat{\mathbf{t}} \,\mathrm{d}\ell \\
&= \iint_{\widetilde{\mathrm{DCVE}}} \left(\mathbf{f}_\mathrm{e} \cdot \hat{\mathbf{n}}_\mathrm{e} - \mathbf{f}_\mathrm{w} \cdot \hat{\mathbf{n}}_\mathrm{w} + \widetilde{\nabla} \cdot \mathbf{F}\right) \mathrm{d}\mathcal{A}
\end{aligned} \tag{A.2}$$

$$\mathbf{F} \equiv \int_{n_\mathrm{w}}^{n_\mathrm{e}} \mathbf{f} \,\mathrm{d}n \tag{A.3}$$

The area integrals in the numerical implementation is evaluated in the form

$$\iint_{\widetilde{\mathrm{DCVE}}} (\cdot) \,\mathrm{d}\mathcal{A} = \iint (\cdot) J \,\mathrm{d}\xi \,\mathrm{d}\zeta \tag{A.4}$$

$$J = \left(\frac{\partial \mathbf{r}}{\partial \xi} \times \frac{\partial \mathbf{r}}{\partial \zeta}\right) \cdot \hat{\mathbf{n}} \tag{A.5}$$

where ξ, ζ are the element reference coordinates.

A.3 Closure Definition

This section presents the definitions and computation of the various quantities in the list (2.5) that are needed for 3D IBL closure. A generic boundary layer profile is illustrated in Figure A-3. Neglecting the normal velocity component along $\hat{\mathbf{n}}$ in consistency with thin shear layer approximations, the shear layer velocity profile is approximated with only planar components as follows,

$$\mathbf{q}(n) \approx \widetilde{\mathbf{q}}(n) \equiv U\,\mathbf{q}_1 \;+\; W\mathbf{q}_2 \qquad \text{where} \qquad \mathbf{q}_1 \equiv q_{\mathrm{i}}\,\hat{\mathbf{s}}_1, \quad \mathbf{q}_2 \equiv q_{\mathrm{i}}\,\hat{\mathbf{s}}_2 \tag{A.6}$$

where $U(n)$ and $W(n)$ are the q_{i}-normalized *streamwise* and *crossflow* velocity profiles, associated with basis vectors $\hat{\mathbf{s}}_1$ and $\hat{\mathbf{s}}_2$ respectively defined as follows,

$$\hat{\mathbf{s}}_1 \equiv \frac{\mathbf{q}_{\mathrm{i}}}{q_{\mathrm{i}}}, \qquad \hat{\mathbf{s}}_2 \equiv \frac{\hat{\mathbf{n}} \times \hat{\mathbf{s}}_1}{\|\hat{\mathbf{n}} \times \hat{\mathbf{s}}_1\|} \tag{A.7}$$

The subscripts "1" and "2" denote streamwise and crossflow directions respectively. The lateral angle deviation profile $\Delta\psi$ is defined directly from velocity profiles U and W.

$$\Delta\psi(n) \;=\; \psi - \psi_{\mathrm{i}} \;=\; \arctan\frac{W}{U} \tag{A.8}$$

It is worth noting that the absolute lateral angle ψ or ψ_{i} depends on the axis used but only the change or difference in lateral angle is of interest in this study, such as in $\Delta\psi$, $\partial\psi_{\mathrm{i}}/\partial t$ or $\widetilde{\nabla}\psi_{\mathrm{i}}$.

For a given shear layer profile, various closure quantities are defined and then computed in terms of thickness variables and coefficients as follows,

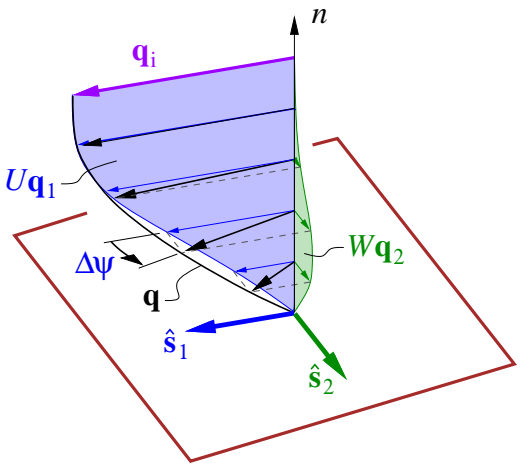

Figure A-3: Streamwise and crossflow velocity profiles of a boundary layer. We note that the convention adopted here is that $\{\hat{\mathbf{s}}_1, \hat{\mathbf{s}}_2, \hat{\mathbf{n}}\}$ form a right-hand system, which differs from Ref. [3] and results in only notational differences in the definition of some crossflow-related closure quantities. Reproduced from Ref. [3] with permission.

$$
\begin{aligned}
m &\equiv \int (\rho_{\mathrm{i}} - \rho)\,\mathrm{d}n && = \rho_{\mathrm{e}}\,\delta_0^* && \text{mass defect}\\
\mathbf{M} &\equiv \int (\rho_{\mathrm{i}}\,\mathbf{q}_{\mathrm{i}} - \rho\,\mathbf{q})\,\mathrm{d}n && = \rho_{\mathrm{e}}\,(\delta_1^*\,\mathbf{q}_1 + \delta_2^*\,\mathbf{q}_2) && \text{mass flux defect}\\
\mathbf{p} &\equiv \int \rho\,(\mathbf{q}_{\mathrm{i}} - \mathbf{q})\,\mathrm{d}n && = \mathbf{M} - m\,\mathbf{q}_{\mathrm{i}} && \text{momentum defect}\\
\overline{\overline{\mathbf{P}}} &\equiv \int \rho\,(\mathbf{q}_{\mathrm{i}} - \mathbf{q}) \otimes \mathbf{q}\,\mathrm{d}n && = \sum_{j=1}^{2}\sum_{k=1}^{2} \rho_{\mathrm{e}}\,\theta_{jk}\,\mathbf{q}_j \otimes \mathbf{q}_k && \text{momentum defect flux (tensor)}\\
k &\equiv \int \left(q_{\mathrm{i}}^2 - q^2\right)\rho\,\mathrm{d}n && = \rho_{\mathrm{e}}\,q_{\mathrm{e}}^2\,\theta_0^* && \text{kinetic energy defect}\\
\mathbf{K} &\equiv \int \rho\,(q_{\mathrm{i}}^2 - q^2)\,\mathbf{q}\,\mathrm{d}n && = \rho_{\mathrm{e}}\,q_{\mathrm{e}}^2\,(\theta_1^*\,\mathbf{q}_1 + \theta_2^*\,\mathbf{q}_2) && \text{kinetic energy defect flux}\\
\mathbf{Q} &\equiv \int (\mathbf{q}_{\mathrm{i}} - \mathbf{q})\,\mathrm{d}n && = \delta_1'\,\mathbf{q}_1 + \delta_2'\,\mathbf{q}_2 && \text{velocity defect}\\
\mathbf{D} &\equiv \int (\rho_{\mathrm{i}} - \rho)\,\mathbf{q}\,\mathrm{d}n && \approx \mathbf{M} - \rho_{\mathrm{e}}\,\mathbf{Q} && \text{density defect flux}\\
e &\equiv \int \left(\rho_{\mathrm{i}} q_{\mathrm{i}}^2 - \rho q^2\right)\,\mathrm{d}n && = k + m\,q_{\mathrm{e}}^2 && \text{total kinetic energy defect}\\
\mathbf{E} &\equiv \int (\rho_{\mathrm{i}}\,q_{\mathrm{i}}^2\,\mathbf{q}_{\mathrm{i}} - \rho\,q^2\,\mathbf{q})\,\mathrm{d}n && = \mathbf{K} + q_{\mathrm{e}}^2\,\mathbf{M} && \text{total kinetic energy flux defect}\\
k^\circ &\equiv \int (\psi_{\mathrm{i}} - \psi)\,\rho q^2\,\mathrm{d}n && = \rho_{\mathrm{e}}\,q_{\mathrm{e}}^2\,\theta_0^\circ && \text{curvature defect}\\
\mathbf{K}^\circ &\equiv \int (\psi_{\mathrm{i}} - \psi)\rho\,q^2\,\mathbf{q}\,\mathrm{d}n && = \rho_{\mathrm{e}}\,q_{\mathrm{e}}^2\,(\theta_1^\circ\,\mathbf{q}_1 + \theta_2^\circ\,\mathbf{q}_2) && \text{curvature defect flux}\\
\mathbf{Q}^\circ &\equiv \int (\psi_{\mathrm{i}} - \psi)\mathbf{q}\,\mathrm{d}n && = \delta_1^\circ\,\mathbf{q}_1 + \delta_2^\circ\,\mathbf{q}_2 && \text{defect curvature volume flux}\\
\boldsymbol{\tau}_{\mathrm{w}} &\equiv \overline{\overline{\boldsymbol{\tau}}} \cdot \hat{\mathbf{n}}_{\mathrm{w}} && = \frac{1}{2}\rho_{\mathrm{e}}\,q_{\mathrm{e}}\left(c_{f_1}\,\mathbf{q}_1 + c_{f_2}\,\mathbf{q}_2\right) && \text{wall shear stress}\\
\mathcal{D} &\equiv \int \left(\overline{\overline{\boldsymbol{\tau}}} \cdot \nabla\right) \cdot \mathbf{q}\,\mathrm{d}n && = \rho_{\mathrm{e}}\,q_{\mathrm{e}}^3\,c_{\mathcal{D}} && \text{dissipation integral}\\
\mathcal{D}^\times &\equiv \int \left(\overline{\overline{\boldsymbol{\tau}}} \cdot \nabla\right) \times \mathbf{q} \cdot \hat{\mathbf{n}}\,\mathrm{d}n && = \rho_{\mathrm{e}}\,q_{\mathrm{e}}^3\,c_{\mathcal{D}}^\times && \text{shear-anisotropy work integral}\\
\mathcal{D}^\circ &\equiv \int \left(\overline{\overline{\boldsymbol{\tau}}} \cdot \nabla\right) \cdot [(\psi_{\mathrm{i}} - \psi)\mathbf{q}]\,\mathrm{d}n && = \rho_{\mathrm{e}}\,q_{\mathrm{e}}^3\,c_{\mathcal{D}}^\circ && \text{lateral work integral}
\end{aligned}
\tag{A.9}
$$

The integration here is understood to be carried across the shear layer thickness. Based on the first-order boundary layer theory adopted in the current formulation, the inviscid velocity $\mathbf{q}_\mathrm{i}$ is constant through the boundary layer thickness and thus equal to the edge velocity $\mathbf{q}_\mathrm{e}$. The density defect flux $\mathbf{D}$ vanishes for incompressible viscous flows. We note that $\mathcal{D}^\circ$ is defined differently from Ref. [3], specifically in the sign of $\pm(\psi_\mathrm{i} - \psi)$, but this difference is only a matter of notation choice.

Under the thin shear layer assumptions, the dissipation integrals are approximated as,

$$\begin{aligned}
\mathcal{D} &\equiv \int \left(\overline{\overline{\boldsymbol{\tau}}} \cdot \nabla\right) \cdot \mathbf{q} \, \mathrm{d}n &&\approx \int \boldsymbol{\tau} \cdot \frac{\partial \mathbf{q}}{\partial n} \, \mathrm{d}n \\
\mathcal{D}^\times &\equiv \int \left(\overline{\overline{\boldsymbol{\tau}}} \cdot \nabla\right) \times \mathbf{q} \cdot \hat{\mathbf{n}} \, \mathrm{d}n &&\approx \int \boldsymbol{\tau} \times \frac{\partial \mathbf{q}}{\partial n} \cdot \hat{\mathbf{n}} \, \mathrm{d}n \\
\mathcal{D}^\circ &\equiv \int \left(\overline{\overline{\boldsymbol{\tau}}} \cdot \nabla\right) \cdot [(\psi_\mathrm{i} - \psi)\mathbf{q}] \, \mathrm{d}n &&\approx \int \boldsymbol{\tau} \cdot \frac{\partial \left[(\psi_\mathrm{i} - \psi)\mathbf{q}\right]}{\partial n} \, \mathrm{d}n
\end{aligned} \tag{A.10}$$

By definition, $\mathcal{D}^\times$ is identically zero for laminar flows and turbulent flows with isotropic shear stress.

The thickness variables and coefficients are defined as follows.

$$
\begin{aligned}
\delta_0^* &\equiv \delta \int \left(1 - R\right) \, \mathrm{d}\eta \\
\delta_1^* &\equiv \delta \int \left(1 - RU\right) \, \mathrm{d}\eta \\
\delta_2^* &\equiv \delta \int \left(0 - RW\right) \, \mathrm{d}\eta \\
\delta_1' &\equiv \delta \int \left(1 - U\right) \, \mathrm{d}\eta \\
\delta_2' &\equiv \delta \int \left(0 - W\right) \, \mathrm{d}\eta \\
\theta_{10} &\equiv \delta \int \left(1 - U\right) R \, \mathrm{d}\eta \\
\theta_{20} &\equiv \delta \int \left(0 - W\right) R \, \mathrm{d}\eta \\
\theta_{11} &\equiv \delta \int \left(1 - U\right) RU \, \mathrm{d}\eta \\
\theta_{12} &\equiv \delta \int \left(1 - U\right) RW \, \mathrm{d}\eta
\end{aligned}
\qquad
\begin{aligned}
\theta_{21} &\equiv \delta \int \left(0 - W\right) RU \, \mathrm{d}\eta \\
\theta_{22} &\equiv \delta \int \left(0 - W\right) RW \, \mathrm{d}\eta \\
\theta_0^* &\equiv \delta \int \left(1 - Q^2\right) R \, \mathrm{d}\eta \\
\theta_1^* &\equiv \delta \int \left(1 - Q^2\right) RU \, \mathrm{d}\eta \\
\theta_2^* &\equiv \delta \int \left(1 - Q^2\right) RW \, \mathrm{d}\eta \\
\delta_1^\circ &\equiv \delta \int -\Delta\psi \, U \, \mathrm{d}\eta \\
\delta_2^\circ &\equiv \delta \int -\Delta\psi \, W \, \mathrm{d}\eta \\
\theta_0^\circ &\equiv \delta \int -\Delta\psi \, Q^2 \, R \, \mathrm{d}\eta \\
\theta_1^\circ &\equiv \delta \int -\Delta\psi \, Q^2 \, RU \, \mathrm{d}\eta \\
\theta_2^\circ &\equiv \delta \int -\Delta\psi \, Q^2 \, RW \, \mathrm{d}\eta
\end{aligned}
\tag{A.11}
$$

$$
\begin{aligned}
c_{f_1} &= 2S_{(0)} \\
c_{f_2} &= 2T_{(0)}
\end{aligned}
\qquad
\begin{aligned}
c_{\mathcal{D}} &= \int \left(S \tfrac{\mathrm{d}U}{\mathrm{d}\eta} + T \tfrac{\mathrm{d}W}{\mathrm{d}\eta} \right) \mathrm{d}\eta \\
c_{\mathcal{D}}^\times &= \int \left(S \tfrac{\mathrm{d}W}{\mathrm{d}\eta} - T \tfrac{\mathrm{d}U}{\mathrm{d}\eta} \right) \mathrm{d}\eta \\
c_{\mathcal{D}}^\circ &= \int \left(S \tfrac{\mathrm{d}(-\Delta\psi U)}{\mathrm{d}\eta} + T \tfrac{\mathrm{d}(-\Delta\psi W)}{\mathrm{d}\eta} \right) \mathrm{d}\eta
\end{aligned}
\tag{A.12}
$$

where δ is a boundary layer thickness scale (which is a primary unknown variable that is solved for in Ref. [3] but its role is only notional in the closure models to be developed in this work).

It is worth noting that the following identity holds for laminar shear layers and turbulent flows with isotropic shear stress, such as the RANS-SA model used to

generate the turbulent boundary layer data set of this thesis.

$$c_{\mathcal{D}}^{\times} \equiv 0 \tag{A.13}$$

Other non-dimensional quantities are defined as follows, namely, thickness coordinate η, density profile R, streamwise and crossflow stress profiles S, T and Reynolds number Re_δ.

$$\begin{gathered} \eta \equiv \frac{n}{\delta}, \qquad R(n) \equiv \frac{\rho(n)}{\rho_{\mathrm{e}}} \\ S(n) \equiv \frac{1}{Re_\delta}\frac{\mu(n)}{\mu_{\mathrm{e}}}\frac{\mathrm{d}U}{\mathrm{d}\eta}, \qquad T(n) \equiv \frac{1}{Re_\delta}\frac{\mu(n)}{\mu_{\mathrm{e}}}\frac{\mathrm{d}W}{\mathrm{d}\eta}, \qquad Re_\delta \equiv \frac{\rho_{\mathrm{e}} q_{\mathrm{e}} \delta}{\mu_{\mathrm{e}}} \end{gathered} \tag{A.14}$$

For incompressible flow, the definitions are simplified to $R(n) \equiv 1$ and $\mu(n) \equiv \mu_{\mathrm{e}}$.

The thickness variables in Equation (A.11) are normalized by the streamwise momentum thickness θ_{11} (i.e. a conventional choice of thickness scale) to define the following non-dimensional boundary layer shape factors.

$$\begin{array}{lll} H_0 \equiv \delta_0^*/\theta_{11} & H_{12} \equiv \theta_{12}/\theta_{11} & H_{d_1} \equiv \delta_1^\circ/\theta_{11} \\ H_1 \equiv \delta_1^*/\theta_{11} & H_{21} \equiv \theta_{21}/\theta_{11} & H_{d_2} \equiv \delta_2^\circ/\theta_{11} \\ H_2 \equiv \delta_2^*/\theta_{11} & H_{22} \equiv \theta_{22}/\theta_{11} & H_0^\circ \equiv \theta_0^\circ/\theta_{11} \\ H_{k_1} \equiv \delta_1'/\theta_{11} & H_0^* \equiv \theta_0^*/\theta_{11} & H_1^\circ \equiv \theta_1^\circ/\theta_{11} \\ H_{k_2} \equiv \delta_2'/\theta_{11} & H_1^* \equiv \theta_1^*/\theta_{11} & H_2^\circ \equiv \theta_2^\circ/\theta_{11} \\ H_{10} \equiv \theta_{10}/\theta_{11} & H_2^* \equiv \theta_2^*/\theta_{11} & \\ H_{20} \equiv \theta_{20}/\theta_{11} & & \end{array} \tag{A.15}$$

The definitions of thickness variables and shape factors lead to the following identi-

ties.

$$H_{10} \equiv H_1 - H_0, \quad H_{20} \equiv H_2, \quad H_{21} \equiv H_{12} + H_2, \quad H_0^* \equiv -H_0 + H_1 + 1 + H_{22} \tag{A.16}$$

In addition, the following approximations hold for incompressible flows.

$$H_0 \equiv 0, \qquad H_{k_1} \equiv H_1, \qquad H_{k_2} \equiv H_2, \tag{A.17}$$

A.4 Integral Defect Equation Derivation

The 3D IBL equations derive from the mass and momentum conservation laws as follows.

$$\frac{\partial \rho}{\partial t} + \nabla \cdot (\rho\, \mathbf{q}) = 0 \qquad \text{(mass)} \tag{A.18}$$

$$\frac{\partial (\rho\, \mathbf{q})}{\partial t} + \nabla \cdot (\rho\, \mathbf{q} \otimes \mathbf{q}) + \nabla \cdot \left(p\, \bar{\bar{\mathbf{I}}} - \bar{\bar{\boldsymbol{\tau}}} \right) = \mathbf{0} \qquad \text{(momentum)} \tag{A.19}$$

Forming $\{2\mathbf{q} \cdot [\text{Equation (A.19)}] - q^2\, [\text{Equation (A.18)}]\}$ gives the following kinetic energy equation.

$$\begin{aligned}
&2\, \mathbf{q} \cdot \left\{ \frac{\partial (\rho\, \mathbf{q})}{\partial t} + \nabla \cdot (\rho\, \mathbf{q} \otimes \mathbf{q}) + \nabla \cdot \left(p\, \bar{\bar{\mathbf{I}}} - \bar{\bar{\boldsymbol{\tau}}} \right) \right\} - q^2 \left[\frac{\partial \rho}{\partial t} + \nabla \cdot (\rho\, \mathbf{q}) \right] \\
&= 2\, \mathbf{q} \cdot \left\{ \mathbf{q} \frac{\partial \rho}{\partial t} + \rho \frac{\partial \mathbf{q}}{\partial t} + \rho\, \mathbf{q} \cdot \nabla \mathbf{q} + [\nabla \cdot (\rho\, \mathbf{q})]\, \mathbf{q} + \nabla \cdot \left(p\, \bar{\bar{\mathbf{I}}} - \bar{\bar{\boldsymbol{\tau}}} \right) \right\} \\
&\qquad - q^2 \left[\frac{\partial \rho}{\partial t} + \nabla \cdot (\rho\, \mathbf{q}) \right] \\
&= q^2 \frac{\partial \rho}{\partial t} + \rho \frac{\partial q^2}{\partial t} + \rho\, \mathbf{q} \cdot \nabla \left(q^2 \right) + q^2\, \nabla \cdot (\rho\, \mathbf{q}) + 2\, \mathbf{q} \cdot \left[\nabla \cdot \left(p\, \bar{\bar{\mathbf{I}}} - \bar{\bar{\boldsymbol{\tau}}} \right) \right] \\
&= \frac{\partial (\rho\, q^2)}{\partial t} + \nabla \cdot \left(\rho\, q^2\, \mathbf{q} \right) + 2\, \mathbf{q} \cdot \left[\nabla \cdot \left(p\, \bar{\bar{\mathbf{I}}} - \bar{\bar{\boldsymbol{\tau}}} \right) \right] = 0 \qquad \text{(kinetic energy)}
\end{aligned} \tag{A.20}$$

Moreover, forming $\{\mathbf{q} \times [\text{Equation (A.19)}] \cdot \hat{\mathbf{n}} + \psi\,[\text{Equation (A.20)}]\}$ gives the following lateral curvature equation.

$$
\begin{aligned}
&\mathbf{q} \times \left\{ \frac{\partial (\rho\,\mathbf{q})}{\partial t} + \nabla \cdot (\rho\,\mathbf{q} \otimes \mathbf{q}) + \nabla \cdot \left(p\,\bar{\bar{\mathbf{I}}} - \bar{\bar{\boldsymbol{\tau}}} \right) \right\} \cdot \hat{\mathbf{n}} \\
&\qquad + \psi \left\{ \frac{\partial (\rho\,q^2)}{\partial t} + \nabla \cdot \left(\rho\,q^2\,\mathbf{q} \right) + 2\,\mathbf{q} \cdot \left[\nabla \cdot \left(p\,\bar{\bar{\mathbf{I}}} - \bar{\bar{\boldsymbol{\tau}}} \right) \right] \right\} \\
&= \mathbf{q} \times \left\{ \mathbf{q}\,\frac{\partial \rho}{\partial t} + \rho\,\frac{\partial \mathbf{q}}{\partial t} + \rho\,\mathbf{q} \cdot \nabla \mathbf{q} + [\nabla \cdot (\rho\,\mathbf{q})]\,\mathbf{q} + \nabla \cdot \left(p\,\bar{\bar{\mathbf{I}}} - \bar{\bar{\boldsymbol{\tau}}} \right) \right\} \cdot \hat{\mathbf{n}} \\
&\qquad + \psi \left\{ \frac{\partial (\rho\,q^2)}{\partial t} + \nabla \cdot \left(\rho\,q^2\,\mathbf{q} \right) + 2\,\mathbf{q} \cdot \left[\nabla \cdot \left(p\,\bar{\bar{\mathbf{I}}} - \bar{\bar{\boldsymbol{\tau}}} \right) \right] \right\} \\
&= \frac{\partial (\rho q^2 \psi)}{\partial t} + \nabla \cdot \left(\rho q^2 \psi\,\mathbf{q} \right) + \mathbf{q} \times \left[\nabla \cdot \left(p\,\bar{\bar{\mathbf{I}}} - \bar{\bar{\boldsymbol{\tau}}} \right) \right] \cdot \hat{\mathbf{n}} + 2\,\psi\,\mathbf{q} \left[\nabla \cdot \left(p\,\bar{\bar{\mathbf{I}}} - \bar{\bar{\boldsymbol{\tau}}} \right) \right] \\
&= 0 \qquad \text{(lateral curvature)}
\end{aligned}
\tag{A.21}
$$

Note that the differential equations (A.18) to (A.21) also apply to the EIF with a zero deviatoric stress tensor $\bar{\bar{\boldsymbol{\tau}}}_{\mathrm{i}}$. Subtracting the viscous equation from the EIF equation and integrating over a DCVE element result in the following form,

$$
\iiint_{\mathrm{DCVE}} \left[(\text{Residual})_{\mathrm{EIF}} - (\text{Residual}) \right] \mathrm{d}\mathcal{V} = 0 \tag{A.22}
$$

This general form is the point of departure for deriving the 3D IBL formulation and is applied separately to the mass, momentum, kinetic energy and lateral curvature equations in the following sections.

A.4.1 Mass

The goal is to derive a governing equation in terms of integral defect quantities. First, the form (A.22) is applied to the mass equation (A.18), while invoking the

thin layer approximations (A.1), Equation (A.2) and the integral defect definitions in Section A.3. This procedure is carried out as follows,

$$\begin{aligned}
0 &= \iiint_{\mathrm{DCVE}} \frac{\partial\left(\rho_{\mathrm{i}} - \rho\right)}{\partial t} + \nabla \cdot \left(\rho_{\mathrm{i}}\,\mathbf{q}_{\mathrm{i}} - \rho\,\mathbf{q}\right) \mathrm{d}\mathcal{V} \\
&= \iint_{\widetilde{\mathrm{DCVE}}} \left\{ \frac{\partial}{\partial t} \left[\int_{n_{\mathrm{w}}}^{n_{\mathrm{e}}} \left(\rho_{\mathrm{i}} - \rho\right) \mathrm{d}n \right] \right\} \mathrm{d}\mathcal{A} \\
&\quad + \iint_{\widetilde{\mathrm{DCVE}}} \left\{ \widetilde{\nabla} \cdot \left[\int_{n_{\mathrm{w}}}^{n_{\mathrm{e}}} \left(\rho_{\mathrm{i}}\,\mathbf{q}_{\mathrm{i}} - \rho\,\mathbf{q}\right) \mathrm{d}n \right] - \left(\rho_{\mathrm{i}}\,\mathbf{q}_{\mathrm{i}} - \rho\,\mathbf{q}\right)_{\mathrm{w}} \cdot \hat{\mathbf{n}}_{\mathrm{w}} \right\} \mathrm{d}\mathcal{A} \\
&= \iint_{\widetilde{\mathrm{DCVE}}} \left\{ \frac{\partial m}{\partial t} + \widetilde{\nabla} \cdot \mathbf{M} - \left(\rho_{\mathrm{i}}\,\mathbf{q}_{\mathrm{i}} - \rho\,\mathbf{q}\right)_{\mathrm{w}} \cdot \hat{\mathbf{n}}_{\mathrm{w}} \right\} \mathrm{d}\mathcal{A}
\end{aligned} \tag{A.23}$$

where the definitions (A.9) of integral defects $(m, \mathbf{M})$ are used. Note that the partial differentiation with respect to time (i.e. $\partial(\cdot)/\partial t$) is interchanged with the integral along n using the Leibniz rule of integration assuming that $\partial(n_{\mathrm{e}} - n_{\mathrm{w}})/\partial t = 0$. The fact that (A.23) holds for any arbitrary $\widetilde{\mathrm{DCVE}}$ leads to other following partial differential equation.

$$\frac{\partial m}{\partial t} + \widetilde{\nabla} \cdot \mathbf{M} - \left(\rho_{\mathrm{i}}\,\mathbf{q}_{\mathrm{i}} - \rho\,\mathbf{q}\right)_{\mathrm{w}} \cdot \hat{\mathbf{n}}_{\mathrm{w}} = 0 \tag{A.24}$$

In general, a nonzero flux $\left(\rho\,\mathbf{q}\right)_{\mathrm{w}}$ can be used to model blowing and suction of the viscous flow through the wall. However, in the scope of this thesis, a no-slip wall boundary condition $\mathbf{q}_{\mathrm{w}} = \mathbf{0}$ is assumed for the viscous flow. Then, the equation (A.24) simplifies to

$$\frac{\partial m}{\partial t} + \widetilde{\nabla} \cdot \mathbf{M} - \left(\rho_{\mathrm{i}}\,\mathbf{q}_{\mathrm{i}}\right)_{\mathrm{w}} \cdot \hat{\mathbf{n}}_{\mathrm{w}} = 0 \tag{A.25}$$

In viscous-inviscid interaction, the equation (A.25) is called a wall transpiration condition and sets the mass flux at the wall or wake cut for the inviscid flow (i.e. EIF) equations, typically as a modification to the flow-tangency boundary condition.

Note that m and $\partial m/\partial t$ may be omitted even for compressible unsteady flows since their magnitudes are likely to be negligible [69].

A.4.2 Momentum

As with the mass equation, a similar derivation is performed for momentum. Applying the form (A.22) to the momentum equation (A.19) gives

$$\mathbf{0} = \iiint_{\mathrm{DCVE}} \left[\frac{\partial \left(\rho_{\mathrm{i}} \, \mathbf{q}_{\mathrm{i}} - \rho \, \mathbf{q} \right)}{\partial t} + \nabla \cdot \left(\rho_{\mathrm{i}} \, \mathbf{q}_{\mathrm{i}} \otimes \mathbf{q}_{\mathrm{i}} - \rho \, \mathbf{q} \otimes \mathbf{q} \right) + \nabla \cdot \left(\left(p_{\mathrm{i}} - p \right) \bar{\bar{\mathbf{I}}} + \bar{\bar{\boldsymbol{\tau}}} \right) \right] \mathrm{d}\mathcal{V} \tag{A.26}$$

The three terms on the right-hand side of (A.26) are transformed separately as follows. The first term becomes

$$\begin{aligned} \iiint_{\mathrm{DCVE}} \frac{\partial \left(\rho_{\mathrm{i}} \, \mathbf{q}_{\mathrm{i}} - \rho \, \mathbf{q} \right)}{\partial t} \, \mathrm{d}\mathcal{V} &= \iint_{\widetilde{\mathrm{DCVE}}} \frac{\partial}{\partial t} \left[\int_{n_{\mathrm{w}}}^{n_{\mathrm{e}}} \left(\rho_{\mathrm{i}} \, \mathbf{q}_{\mathrm{i}} - \rho \, \mathbf{q} \right) \, \mathrm{d}n \right] \mathrm{d}\mathcal{A} \\ &= \iint_{\widetilde{\mathrm{DCVE}}} \frac{\partial \mathbf{M}}{\partial t} \, \mathrm{d}\mathcal{A} \\ &= \iint_{\widetilde{\mathrm{DCVE}}} \frac{\partial \left(\mathbf{p} + m \, \mathbf{q}_{\mathrm{i}} \right)}{\partial t} \, \mathrm{d}\mathcal{A} \\ &= \iint_{\widetilde{\mathrm{DCVE}}} \left(\frac{\partial \mathbf{p}}{\partial t} + \frac{\partial m}{\partial t} \mathbf{q}_{\mathrm{i}} + m \frac{\partial \mathbf{q}_{\mathrm{i}}}{\partial t} \right) \mathrm{d}\mathcal{A} \end{aligned} \tag{A.27}$$

The second term on the right-hand side of (A.26) becomes

$$
\begin{aligned}
&\iiint_{\mathrm{DCVE}} \nabla \cdot (\rho_{\mathrm{i}}\, \mathbf{q}_{\mathrm{i}} \otimes \mathbf{q}_{\mathrm{i}} - \rho\, \mathbf{q} \otimes \mathbf{q})\, \mathrm{d}\mathcal{V} \qquad \text{(A.28)}\\
&= \iiint_{\mathrm{DCVE}} \nabla \cdot [\rho\, (\mathbf{q}_{\mathrm{i}} - \mathbf{q}) \otimes \mathbf{q} + \mathbf{q}_{\mathrm{i}} \otimes (\rho_{\mathrm{i}}\, \mathbf{q}_{\mathrm{i}} - \rho\, \mathbf{q})]\, \mathrm{d}\mathcal{V}\\
&= \iint_{\widetilde{\mathrm{DCVE}}} \widetilde{\nabla} \cdot \left\{ \left[\int_{n_{\mathrm{w}}}^{n_{\mathrm{e}}} \rho\, (\mathbf{q}_{\mathrm{i}} - \mathbf{q}) \otimes \mathbf{q}\, \mathrm{d}n \right] - [\rho\, (\mathbf{q}_{\mathrm{i}} - \mathbf{q}) \otimes \mathbf{q}]_{\mathrm{w}} \cdot \hat{\mathbf{n}}_{\mathrm{w}} \right\} \mathrm{d}\mathcal{A}\\
&\quad + \iint_{\widetilde{\mathrm{DCVE}}} \widetilde{\nabla} \cdot \left\{ \left[\int_{n_{\mathrm{w}}}^{n_{\mathrm{e}}} \mathbf{q}_{\mathrm{i}} \otimes (\rho_{\mathrm{i}}\, \mathbf{q}_{\mathrm{i}} - \rho\, \mathbf{q})\, \mathrm{d}n \right] - [\mathbf{q}_{\mathrm{i}} \otimes (\rho_{\mathrm{i}}\, \mathbf{q}_{\mathrm{i}} - \rho\, \mathbf{q})]_{\mathrm{w}} \cdot \hat{\mathbf{n}}_{\mathrm{w}} \right\} \mathrm{d}\mathcal{A}\\
&= \iint_{\widetilde{\mathrm{DCVE}}} \left[\widetilde{\nabla} \cdot \overline{\overline{\mathbf{P}}} + \widetilde{\nabla} \cdot (\mathbf{q}_{\mathrm{i}} \otimes \mathbf{M}) - \mathbf{q}_{\mathrm{i}} \left(\frac{\partial m}{\partial t} + \widetilde{\nabla} \cdot \mathbf{M} \right) \right] \mathrm{d}\mathcal{A}\\
&= \iint_{\widetilde{\mathrm{DCVE}}} \left[\widetilde{\nabla} \cdot \overline{\overline{\mathbf{P}}} + \left(\widetilde{\nabla} \mathbf{q}_{\mathrm{i}} \right) \cdot \mathbf{M} + \left(\widetilde{\nabla} \cdot \mathbf{M} \right) \mathbf{q}_{\mathrm{i}} - \mathbf{q}_{\mathrm{i}} \left(\frac{\partial m}{\partial t} + \widetilde{\nabla} \cdot \mathbf{M} \right) \right] \mathrm{d}\mathcal{A}\\
&= \iint_{\widetilde{\mathrm{DCVE}}} \left[\widetilde{\nabla} \cdot \overline{\overline{\mathbf{P}}} + \left(\widetilde{\nabla} \mathbf{q}_{\mathrm{i}} \right) \cdot \mathbf{M} - \frac{\partial m}{\partial t} \mathbf{q}_{\mathrm{i}} \right] \mathrm{d}\mathcal{A} \qquad \text{(A.29)}
\end{aligned}
$$

where the definitions (A.9) of integral defects $(m, \mathbf{M}, \overline{\overline{\mathbf{P}}})$ are used. The no-slip wall condition ($\mathbf{q}_{\mathrm{w}} = \mathbf{0}$) nullifies the following flux,

$$
[\rho\, (\mathbf{q}_{\mathrm{i}} - \mathbf{q}) \otimes \mathbf{q}]_{\mathrm{w}} \cdot \hat{\mathbf{n}}_{\mathrm{w}} = [\rho\, (\mathbf{q}_{\mathrm{i}} - \mathbf{q})]_{\mathrm{w}}\, (\mathbf{q}_{\mathrm{w}} \cdot \hat{\mathbf{n}}_{\mathrm{w}}) = 0 \qquad \text{(A.30)}
$$

Also, the mass defect equation (A.24) gives the following substitution,

$$
[\mathbf{q}_{\mathrm{i}} \otimes (\rho_{\mathrm{i}}\, \mathbf{q}_{\mathrm{i}} - \rho\, \mathbf{q})]_{\mathrm{w}} \cdot \hat{\mathbf{n}}_{\mathrm{w}} = \mathbf{q}_{\mathrm{i}}\, [(\rho_{\mathrm{i}}\, \mathbf{q}_{\mathrm{i}} - \rho\, \mathbf{q})_{\mathrm{w}} \cdot \hat{\mathbf{n}}_{\mathrm{w}}] = \mathbf{q}_{\mathrm{i}} \left(\frac{\partial m}{\partial t} + \widetilde{\nabla} \cdot \mathbf{M} \right) \qquad \text{(A.31)}
$$

The third right-hand-side term of (A.26) becomes

$$\begin{aligned}
&\iiint_{\mathrm{DCVE}} \left\{ \nabla \cdot \left[(p_\mathrm{i} - p)\, \bar{\bar{\mathbf{I}}} + \bar{\bar{\boldsymbol{\tau}}} \right] \right\} \, \mathrm{d}\mathcal{V} \\
&= \iint_{\widetilde{\mathrm{DCVE}}} \left\{ \widetilde{\nabla} \cdot \left\{ \left[\int_{n_\mathrm{w}}^{n_\mathrm{e}} (p_\mathrm{i} - p)\, \bar{\bar{\mathbf{I}}} \, \mathrm{d}n \right] - \left[(p_\mathrm{i} - p)\, \bar{\bar{\mathbf{I}}} \right]_\mathrm{w} \cdot \hat{\mathbf{n}}_\mathrm{w} \right\} + \int_{n_\mathrm{w}}^{n_\mathrm{e}} \frac{\partial \boldsymbol{\tau}}{\partial n} \, \mathrm{d}n \right\} \mathrm{d}\mathcal{A} \\
&= \iint_{\widetilde{\mathrm{DCVE}}} \left[\widetilde{\nabla} \cdot (\Pi\, \bar{\bar{\mathbf{I}}}) - (p_\mathrm{i} - p)_\mathrm{w}\, \hat{\mathbf{n}}_\mathrm{w} + \left(\bar{\bar{\boldsymbol{\tau}}}_\mathrm{e} \cdot \hat{\mathbf{n}}_\mathrm{e} - \bar{\bar{\boldsymbol{\tau}}}_\mathrm{w} \cdot \hat{\mathbf{n}}_\mathrm{w} \right) \right] \, \mathrm{d}\mathcal{A} \\
&= \iint_{\widetilde{\mathrm{DCVE}}} \left(\widetilde{\nabla}\, \Pi - (p_\mathrm{i} - p)_\mathrm{w}\, \hat{\mathbf{n}}_\mathrm{w} - \boldsymbol{\tau}_\mathrm{w} \right) \, \mathrm{d}\mathcal{A}
\end{aligned} \tag{A.32}$$

where the definition (A.9) of Π is used. The viscous stress tensor vanishes at the edge of the viscous layer (i.e. $\bar{\bar{\boldsymbol{\tau}}}_\mathrm{e} = \bar{\bar{\mathbf{0}}}$). The viscous traction on the wall is defined and approximated as

$$\boldsymbol{\tau}_\mathrm{w} \equiv \bar{\bar{\boldsymbol{\tau}}}_\mathrm{w} \cdot \hat{\mathbf{n}}_\mathrm{w} \approx \bar{\bar{\boldsymbol{\tau}}}_\mathrm{w} \cdot \hat{\mathbf{n}} \tag{A.33}$$

Substituting (A.27), (A.29) and (A.32) into (A.26) gives

$$\begin{aligned}
\mathbf{0} &= \iiint_{\mathrm{DCVE}} \left[\frac{\partial \left(\rho_\mathrm{i}\, \mathbf{q}_\mathrm{i} - \rho\, \mathbf{q} \right)}{\partial t} + \nabla \cdot \left(\rho_\mathrm{i}\, \mathbf{q}_\mathrm{i} \otimes \mathbf{q}_\mathrm{i} - \rho\, \mathbf{q} \otimes \mathbf{q} \right) + \nabla \cdot \left((p_\mathrm{i} - p)\, \bar{\bar{\mathbf{I}}} + \bar{\bar{\boldsymbol{\tau}}} \right) \right] \, \mathrm{d}\mathcal{V} \\
&= \iint_{\widetilde{\mathrm{DCVE}}} \left[\frac{\partial \mathbf{p}}{\partial t} + m \frac{\partial \mathbf{q}_\mathrm{i}}{\partial t} + \widetilde{\nabla} \cdot \bar{\bar{\mathbf{P}}} + \left(\widetilde{\nabla} \mathbf{q}_\mathrm{i} \right) \cdot \mathbf{M} + \widetilde{\nabla}\, \Pi - (p_\mathrm{i} - p)_\mathrm{w}\, \hat{\mathbf{n}}_\mathrm{w} - \boldsymbol{\tau}_\mathrm{w} \right] \, \mathrm{d}\mathcal{A}
\end{aligned} \tag{A.34}$$

Since (A.34) holds for any $\widetilde{\mathrm{DCVE}}$, it follows that

$$\frac{\partial \mathbf{p}}{\partial t} + m \frac{\partial \mathbf{q}_\mathrm{i}}{\partial t} + \widetilde{\nabla} \cdot \bar{\bar{\mathbf{P}}} + \left(\widetilde{\nabla} \mathbf{q}_\mathrm{i} \right) \cdot \mathbf{M} + \widetilde{\nabla}\, \Pi - (p_\mathrm{i} - p)_\mathrm{w}\, \hat{\mathbf{n}}_\mathrm{w} - \boldsymbol{\tau}_\mathrm{w} = \mathbf{0} \tag{A.35}$$

Using the first-order thin shear layer approximations that $p_\mathrm{i} - p \approx 0$ and $\Pi \approx 0$, the equation (A.35) then simplifies to the following integral defect equation for

momentum,

$$\frac{\partial \mathbf{p}}{\partial t} + m\frac{\partial \mathbf{q}_\mathrm{i}}{\partial t} + \widetilde{\nabla} \cdot \overline{\overline{\mathbf{P}}} + \mathbf{M} \cdot \widetilde{\nabla}\mathbf{q}_\mathrm{i} - \boldsymbol{\tau}_\mathrm{w} = \mathbf{0} \tag{A.36}$$

Note that Equation (A.36) is a vector equation but only has components that are tangent to the $\widetilde{\mathrm{DCVE}}$ as a result of the thin shear layer approximations.

A.4.3 Kinetic Energy

Similarly, for the kinetic energy equation (A.20), the form (A.22) is applied again,

$$\begin{aligned} 0 = &\iiint_{\mathrm{DCVE}} \left[\frac{\partial \left(\rho_\mathrm{i}\, q_\mathrm{i}^2 - \rho\, q^2 \right)}{\partial t} + \nabla \cdot \left(\rho_\mathrm{i}\, q_\mathrm{i}^2\, \mathbf{q}_\mathrm{i} - \rho\, q^2\, \mathbf{q} \right) \right] \mathrm{d}\mathcal{V} \\ &+ \iiint_{\mathrm{DCVE}} \left[2 \left(\mathbf{q}_\mathrm{i} \cdot \nabla p_\mathrm{i} - \mathbf{q} \cdot \nabla p \right) + 2\mathbf{q} \cdot \left(\nabla \cdot \overline{\overline{\boldsymbol{\tau}}} \right) \right] \mathrm{d}\mathcal{V} \end{aligned} \tag{A.37}$$

The terms on the right-hand side of (A.37) are transformed separately as follows. The first term becomes

$$\begin{aligned} \iiint_{\mathrm{DCVE}} \frac{\partial \left(\rho_\mathrm{i}\, q_\mathrm{i}^2 - \rho\, q^2 \right)}{\partial t} \mathrm{d}\mathcal{V} &= \iint_{\widetilde{\mathrm{DCVE}}} \frac{\partial}{\partial t} \left[\int_{n_\mathrm{w}}^{n_\mathrm{e}} \left(\rho_\mathrm{i}\, q_\mathrm{i}^2 - \rho\, q^2 \right) \mathrm{d}n \right] \mathrm{d}\mathcal{A} \\ &= \iint_{\widetilde{\mathrm{DCVE}}} \frac{\partial}{\partial t} \left\{ \int_{n_\mathrm{w}}^{n_\mathrm{e}} \left[\rho \left(q_\mathrm{i}^2 - q^2 \right) + \left(\rho_\mathrm{i} - \rho \right) q_\mathrm{i}^2 \right] \mathrm{d}n \right\} \mathrm{d}\mathcal{A} \\ &= \iint_{\widetilde{\mathrm{DCVE}}} \frac{\partial \left(k + m\, q_\mathrm{i}^2 \right)}{\partial t} \mathrm{d}\mathcal{A} \end{aligned} \tag{A.38}$$

where the definitions (A.9) of integral defects (k, m) are used.

The second term on the right-hand side of (A.37) becomes

$$
\begin{aligned}
&\iiint_{\mathrm{DCVE}} \left[\nabla \cdot \left(\rho_{\mathrm{i}}\, q_{\mathrm{i}}^2\, \mathbf{q}_{\mathrm{i}} - \rho\, q^2\, \mathbf{q}\right)\right] \mathrm{d}\mathcal{V} \\
&= \iiint_{\mathrm{DCVE}} \nabla \cdot \left[\rho\left(q_{\mathrm{i}}^2 - q^2\right)\mathbf{q} + q_{\mathrm{i}}^2\left(\rho_{\mathrm{i}}\,\mathbf{q}_{\mathrm{i}} - \rho\,\mathbf{q}\right)\right] \mathrm{d}\mathcal{V} \\
&= \iint_{\widetilde{\mathrm{DCVE}}} \left\{\widetilde{\nabla} \cdot \left[\int_{n_{\mathrm{w}}}^{n_{\mathrm{e}}} \rho\left(q_{\mathrm{i}}^2 - q^2\right)\mathbf{q}\,\mathrm{d}n\right] - \left[\rho\left(q_{\mathrm{i}}^2 - q^2\right)\mathbf{q}\right]_{\mathrm{w}} \cdot \hat{\mathbf{n}}_{\mathrm{w}}\right\} \mathrm{d}\mathcal{A} \\
&\quad + \iint_{\widetilde{\mathrm{DCVE}}} \left\{\widetilde{\nabla} \cdot \left[\int_{n_{\mathrm{w}}}^{n_{\mathrm{e}}} q_{\mathrm{i}}^2\left(\rho_{\mathrm{i}}\,\mathbf{q}_{\mathrm{i}} - \rho\,\mathbf{q}\right)\mathrm{d}n\right] - \left[q_{\mathrm{i}}^2\left(\rho_{\mathrm{i}}\,\mathbf{q}_{\mathrm{i}} - \rho\,\mathbf{q}\right)\right]_{\mathrm{w}} \cdot \hat{\mathbf{n}}_{\mathrm{w}}\right\} \mathrm{d}\mathcal{A} \\
&= \iint_{\widetilde{\mathrm{DCVE}}} \left[\widetilde{\nabla} \cdot \mathbf{K} + \widetilde{\nabla} \cdot \left(q_{\mathrm{i}}^2\,\mathbf{M}\right) - q_{\mathrm{i}}^2 \left(\frac{\partial m}{\partial t} + \widetilde{\nabla} \cdot \mathbf{M}\right)\right] \mathrm{d}\mathcal{A} \\
&= \iint_{\widetilde{\mathrm{DCVE}}} \left[\widetilde{\nabla} \cdot \mathbf{K} + \mathbf{M} \cdot \widetilde{\nabla}\left(q_{\mathrm{i}}^2\right) - q_{\mathrm{i}}^2\,\frac{\partial m}{\partial t}\right] \mathrm{d}\mathcal{A}
\end{aligned}
\tag{A.39}
$$

where the definitions (A.9) of integral defects $(\mathbf{K}, \mathbf{M})$ are used. The no-slip wall condition $(\mathbf{q}_{\mathrm{w}} = \mathbf{0})$ results in the following relation,

$$
\left[\rho\left(q_{\mathrm{i}}^2 - q^2\right)\mathbf{q}\right]_{\mathrm{w}} \cdot \hat{\mathbf{n}}_{\mathrm{w}} = \left[\rho(q_{\mathrm{i}}^2 - q^2)\right]_{\mathrm{w}} \left(\mathbf{q}_{\mathrm{w}} \cdot \hat{\mathbf{n}}_{\mathrm{w}}\right) = 0 \tag{A.40}
$$

and the mass defect equation (A.24) gives the following substitution,

$$
\left[q_{\mathrm{i}}^2\left(\rho_{\mathrm{i}}\,\mathbf{q}_{\mathrm{i}} - \rho\,\mathbf{q}\right)\right]_{\mathrm{w}} \cdot \hat{\mathbf{n}}_{\mathrm{w}} = q_{\mathrm{i}}^2\left[\left(\rho_{\mathrm{i}}\,\mathbf{q}_{\mathrm{i}} - \rho\,\mathbf{q}\right)_{\mathrm{w}} \cdot \hat{\mathbf{n}}_{\mathrm{w}}\right] = q_{\mathrm{i}}^2 \left(\frac{\partial m}{\partial t} + \widetilde{\nabla} \cdot \mathbf{M}\right) \tag{A.41}
$$

The following identity is also applied,

$$
\widetilde{\nabla} \cdot \left(q_{\mathrm{i}}^2\,\mathbf{M}\right) \equiv q_{\mathrm{i}}^2\,\widetilde{\nabla} \cdot \mathbf{M} + \mathbf{M} \cdot \widetilde{\nabla}\left(q_{\mathrm{i}}^2\right) \tag{A.42}
$$

The rest of terms in (A.37) becomes

$$
\begin{aligned}
&\iiint_{\mathrm{DCVE}} \left[2\left(\mathbf{q}_{\mathrm{i}} \cdot \nabla p_{\mathrm{i}} - \mathbf{q} \cdot \nabla p\right) + 2\mathbf{q} \cdot \left(\nabla \cdot \overline{\overline{\boldsymbol{\tau}}}\right)\right] \mathrm{d}\mathcal{V} \\
&= \iint_{\widetilde{\mathrm{DCVE}}} \left\{ 2 \int_{n_{\mathrm{w}}}^{n_{\mathrm{e}}} \left[\left(\mathbf{q}_{\mathrm{i}} - \mathbf{q}\right) \cdot \nabla p_{\mathrm{i}} + \mathbf{q} \cdot \nabla (p_{\mathrm{i}} - p)\right] \mathrm{d}n \right\} \mathrm{d}\mathcal{A} \\
&\quad + \iiint_{\mathrm{DCVE}} 2\left[\nabla \cdot \left(\overline{\overline{\boldsymbol{\tau}}} \cdot \mathbf{q}\right) - \mathrm{tr}\left(\overline{\overline{\boldsymbol{\tau}}} \cdot (\nabla \mathbf{q})\right)\right] \mathrm{d}\mathcal{V} \\
&= \iint_{\widetilde{\mathrm{DCVE}}} 2\left[\mathbf{Q} \cdot \widetilde{\nabla} p_{\mathrm{i}} - \left(\overline{\overline{\boldsymbol{\tau}}} \cdot \mathbf{q}\right)_{\mathrm{w}} \cdot \hat{\mathbf{n}}_{\mathrm{w}} - \int_{n_{\mathrm{w}}}^{n_{\mathrm{e}}} \left(\boldsymbol{\tau} \cdot \frac{\partial \mathbf{q}}{\partial n}\right) \mathrm{d}n\right] \mathrm{d}\mathcal{A} \\
&= \iint_{\widetilde{\mathrm{DCVE}}} 2\left[\mathbf{Q} \cdot \widetilde{\nabla} p_{\mathrm{i}} - \mathcal{D}\right] \mathrm{d}\mathcal{A}
\end{aligned}
\tag{A.43}
$$

where definition (A.9) of $\mathbf{Q}$ and the expression (A.10) of $\mathcal{D}$ are applied. The thin shear layer approximation implies that $\nabla(p_{\mathrm{i}} - p) \approx \mathbf{0}$ and $\nabla p_{\mathrm{i}} \approx \widetilde{\nabla} p_{\mathrm{i}}$ is constant across the thickness of the viscous layer. The symmetry of the viscous stress tensor $\overline{\overline{\boldsymbol{\tau}}}$ (i.e. $\overline{\overline{\boldsymbol{\tau}}} = \overline{\overline{\boldsymbol{\tau}}}^{T}$) is used. The divergence theorem is applied to transform the following term,

$$
\begin{aligned}
\iiint_{\mathrm{DCVE}} \left[\nabla \cdot \left(\overline{\overline{\boldsymbol{\tau}}} \cdot \mathbf{q}\right)\right] \mathrm{d}\mathcal{V} &= \sum_{\partial \mathrm{D}\widetilde{\mathrm{DC}}\mathrm{A}} \int_{n_{\mathrm{w}}}^{n_{\mathrm{e}}} \left(\overline{\overline{\boldsymbol{\tau}}} \cdot \mathbf{q}\right) \cdot \hat{\mathbf{t}} \, \mathrm{d}n \\
&\quad + \iint_{\widetilde{\mathrm{DCVE}}} \left[\left(\overline{\overline{\boldsymbol{\tau}}} \cdot \mathbf{q}\right)_{\mathrm{e}} \cdot \hat{\mathbf{n}}_{\mathrm{e}} - \left(\overline{\overline{\boldsymbol{\tau}}} \cdot \mathbf{q}\right)_{\mathrm{w}} \cdot \hat{\mathbf{n}}_{\mathrm{w}}\right] \mathrm{d}\mathcal{A} \\
&= 0
\end{aligned}
\tag{A.44}
$$

where $\left(\overline{\overline{\boldsymbol{\tau}}} \cdot \mathbf{q}\right) \cdot \hat{\mathbf{t}} \approx 0$ according to the thin shear layer assumption ($\overline{\overline{\boldsymbol{\tau}}} \cdot \mathbf{q}$ only has a component along $\hat{\mathbf{n}}_{\mathrm{s}}$ ($\approx \hat{\mathbf{n}}$) and is thus approximately orthogonal to $\hat{\mathbf{t}}$). The edge quantity $\left(\overline{\overline{\boldsymbol{\tau}}} \cdot \mathbf{q}\right)_{\mathrm{e}} \cdot \hat{\mathbf{n}}_{\mathrm{e}}$ is dropped since $\overline{\overline{\boldsymbol{\tau}}}_{\mathrm{e}} = \overline{\overline{\mathbf{0}}}$. The wall term $\left(\overline{\overline{\boldsymbol{\tau}}} \cdot \mathbf{q}\right)_{\mathrm{w}} \cdot \hat{\mathbf{n}}_{\mathrm{w}}$ vanishes given the no-slip wall boundary condition ($\mathbf{q}_{\mathrm{w}} = \mathbf{0}$).

Substituting (A.38), (A.39) and (A.43) into (A.37) gives

$$
\begin{aligned}
0 &= \iiint_{\mathrm{DCVE}} \left[\frac{\partial \left(\rho_{\mathrm{i}} \, q_{\mathrm{i}}^2 - \rho \, q^2 \right)}{\partial t} + \nabla \cdot \left(\rho_{\mathrm{i}} \, q_{\mathrm{i}}^2 \, \mathbf{q}_{\mathrm{i}} - \rho \, q^2 \, \mathbf{q} \right) \right] \mathrm{d}\mathcal{V} \\
&\quad + \iiint_{\mathrm{DCVE}} \left[2 \left(\mathbf{q}_{\mathrm{i}} \cdot \nabla p_{\mathrm{i}} - \mathbf{q} \cdot \nabla p \right) + 2 \mathbf{q} \cdot \left(\nabla \cdot \overline{\overline{\boldsymbol{\tau}}} \right) \right] \mathrm{d}\mathcal{V} \\
&= \iint_{\widetilde{\mathrm{DCVE}}} \left[\frac{\partial \left(k + m \, q_{\mathrm{i}}^2 \right)}{\partial t} + \widetilde{\nabla} \cdot \mathbf{K} + \mathbf{M} \cdot \widetilde{\nabla} \left(q_{\mathrm{i}}^2 \right) - q_{\mathrm{i}}^2 \, \frac{\partial m}{\partial t} + 2 \, \mathbf{Q} \cdot \widetilde{\nabla} p_{\mathrm{i}} - 2 \, \mathcal{D} \right] \mathrm{d}\mathcal{A} \\
&= \iint_{\widetilde{\mathrm{DCVE}}} \left[\frac{\partial k}{\partial t} + m \, \frac{\partial \left(q_{\mathrm{i}}^2 \right)}{\partial t} + \widetilde{\nabla} \cdot \mathbf{K} + \mathbf{D} \cdot \widetilde{\nabla} \left(q_{\mathrm{i}}^2 \right) - 2 \, \mathcal{D} \right] \mathrm{d}\mathcal{A}
\end{aligned}
\tag{A.45}
$$

where the terms involving $\mathbf{M}$ and $\mathbf{Q}$ are combined into $\mathbf{D}$ using Equation (A.9). The following relation is derived from the momentum equation of the EIF,

$$
\nabla p_{\mathrm{i}} = -\frac{1}{2} \, \rho_{\mathrm{i}} \nabla \left(q_{\mathrm{i}}^2 \right) - \rho_{\mathrm{i}} \frac{\partial \mathbf{q}_{\mathrm{i}}}{\partial t} \tag{A.46}
$$

The gradient term is further expanded as

$$
\frac{1}{2} \, \nabla \left(q_{\mathrm{i}}^2 \right) = \frac{1}{2} \, \nabla \left(\mathbf{q}_{\mathrm{i}} \cdot \mathbf{q}_{\mathrm{i}} \right) = \mathbf{q}_{\mathrm{i}} \cdot \left(\nabla \mathbf{q}_{\mathrm{i}} \right) = \left(\nabla \mathbf{q}_{\mathrm{i}} \right) \cdot \mathbf{q}_{\mathrm{i}} = \left(\mathbf{q}_{\mathrm{i}} \cdot \nabla \right) \mathbf{q}_{\mathrm{i}} \tag{A.47}
$$

using the irrotationality of the EIF (i.e. $\nabla \times \mathbf{q} = \mathbf{0}$).

Since (A.45) holds for any $\widetilde{\mathrm{DCVE}}$, it follows that

$$
\frac{\partial k}{\partial t} + m \, \frac{\partial \left(q_{\mathrm{i}}^2 \right)}{\partial t} + \widetilde{\nabla} \cdot \mathbf{K} + \mathbf{D} \cdot \widetilde{\nabla} \left(q_{\mathrm{i}}^2 \right) - 2 \, \mathcal{D} = 0 \tag{A.48}
$$

which is the integral defect equation for kinetic energy.

A.4.4 Lateral Curvature

Similarly, for the lateral curvature equation (A.21), forming

$$([\text{Equation (A.21)}]_{\text{EIF}} - [\text{Equation (A.21)}]) - \psi_{\text{i}} \left\{ [\text{Equation (A.20)}]_{\text{EIF}} - [\text{Equation (A.20)}] \right\}$$

and then applying the form (A.22) gives

$$\frac{\partial(\rho q^2 \psi)}{\partial t} + \nabla \cdot \left(\rho q^2 \psi \, \mathbf{q}\right) + \mathbf{q} \times \left[\nabla \cdot \left(p \, \bar{\bar{\mathbf{I}}} - \bar{\bar{\boldsymbol{\tau}}}\right)\right] \cdot \hat{\mathbf{n}} + 2 \, \psi \, \mathbf{q} \left[\nabla \cdot \left(p \, \bar{\bar{\mathbf{I}}} - \bar{\bar{\boldsymbol{\tau}}}\right)\right] \quad \text{(A.49)}$$

for which applying the form (A.22) leads to

$$\begin{aligned}
0 = & \iiint_{\text{DCVE}} \left[\frac{\partial \left(\rho_{\text{i}} \, q_{\text{i}}^2 \psi_{\text{i}} - \rho \, q^2 \psi\right)}{\partial t} + \nabla \cdot \left(\rho_{\text{i}} \, q_{\text{i}}^2 \, \psi_{\text{i}} \, \mathbf{q}_{\text{i}} - \rho \, q^2 \psi \, \mathbf{q}\right) \right] \, \mathrm{d}\mathcal{V} \\
& + \iiint_{\text{DCVE}} \left[(\mathbf{q}_{\text{i}} \times \nabla p_{\text{i}}) \cdot \hat{\mathbf{n}} - (\mathbf{q} \times \nabla p) \cdot \hat{\mathbf{n}} + \mathbf{q} \times \left(\nabla \cdot \bar{\bar{\boldsymbol{\tau}}}\right) \cdot \hat{\mathbf{n}} \right] \, \mathrm{d}\mathcal{V} \\
& + \iiint_{\text{DCVE}} \left[2 \, \psi_{\text{i}} \, \mathbf{q}_{\text{i}} \cdot \nabla p_{\text{i}} - 2 \, \psi \, \mathbf{q} \cdot \nabla p + 2 \, \psi \, \mathbf{q} \cdot \left(\nabla \cdot \bar{\bar{\boldsymbol{\tau}}}\right) \right] \, \mathrm{d}\mathcal{V} \\
& + \iiint_{\text{DCVE}} -\psi_{\text{i}} \left\{ \frac{\partial \left(\rho_{\text{i}} \, q_{\text{i}}^2 - \rho \, q^2\right)}{\partial t} + \nabla \cdot \left(\rho_{\text{i}} \, q_{\text{i}}^2 \, \mathbf{q}_{\text{i}} - \rho \, q^2 \, \mathbf{q}\right) \right\} \, \mathrm{d}\mathcal{V} \\
& + \iiint_{\text{DCVE}} -\psi_{\text{i}} \left[2 \, \mathbf{q}_{\text{i}} \cdot \nabla p_{\text{i}} - 2 \, \mathbf{q} \cdot \nabla p + 2 \, \mathbf{q} \cdot \left(\nabla \cdot \bar{\bar{\boldsymbol{\tau}}}\right) \right] \, \mathrm{d}\mathcal{V} \\
= & \iiint_{\text{DCVE}} \left[\frac{\partial \left(\psi_{\text{i}} - \psi\right)}{\partial t} \rho q^2 + \left(\rho_{\text{i}} \, q_{\text{i}}^2 - \rho \, q^2\right) \frac{\partial \psi_{\text{i}}}{\partial t} \right] \, \mathrm{d}\mathcal{V} \\
& + \iiint_{\text{DCVE}} \left\{ \nabla \cdot \left[(\psi_{\text{i}} - \psi) \rho q^2 \mathbf{q} \right] + \left(\rho_{\text{i}} q_{\text{i}}^2 \mathbf{q}_{\text{i}} - \rho q^2 \mathbf{q}\right) \cdot \nabla \psi_{\text{i}} \right\} \, \mathrm{d}\mathcal{V} \\
& + \iiint_{\text{DCVE}} \left[(\mathbf{q}_{\text{i}} \times \nabla p_{\text{i}}) \cdot \hat{\mathbf{n}} - (\mathbf{q} \times \nabla p) \cdot \hat{\mathbf{n}} + \mathbf{q} \times \left(\nabla \cdot \bar{\bar{\boldsymbol{\tau}}}\right) \cdot \hat{\mathbf{n}} \right] \, \mathrm{d}\mathcal{V} \\
& + \iiint_{\text{DCVE}} \left[2 (\psi_{\text{i}} - \psi) \mathbf{q} \cdot \nabla p - 2 (\psi_{\text{i}} - \psi) \mathbf{q} \cdot \left(\nabla \cdot \bar{\bar{\boldsymbol{\tau}}}\right) \right] \, \mathrm{d}\mathcal{V}
\end{aligned} \quad \text{(A.50)}$$

The terms on the right-hand side of (A.37) are transformed separately as follows.

$$\iiint_{\mathrm{DCVE}} \frac{\partial}{\partial t}\left[(\psi_\mathrm{i}-\psi)\,\rho q^2\right]\mathrm{d}\mathcal{V} = \iint_{\widetilde{\mathrm{DCVE}}} \frac{\partial}{\partial t}\left\{\int\left[(\psi_\mathrm{i}-\psi)\,\rho q^2\right]\mathrm{d}n\right\}\mathrm{d}\mathcal{A} = \iint_{\widetilde{\mathrm{DCVE}}} \frac{\partial k^\circ}{\partial t}\mathrm{d}\mathcal{A} \tag{A.51}$$

$$\begin{aligned}&\iiint_{\mathrm{DCVE}} \left(\rho_\mathrm{i}\,q_\mathrm{i}^2-\rho\,q^2\right)\frac{\partial \psi_\mathrm{i}}{\partial t}\,\mathrm{d}\mathcal{V} = \iint_{\widetilde{\mathrm{DCVE}}}\left[\int\left(\rho_\mathrm{i}\,q_\mathrm{i}^2-\rho\,q^2\right)\mathrm{d}n\right]\frac{\partial \psi_\mathrm{i}}{\partial t}\,\mathrm{d}\mathcal{A}\\ =&\iint_{\widetilde{\mathrm{DCVE}}} e\frac{\partial \psi_\mathrm{i}}{\partial t}\,\mathrm{d}\mathcal{A} = \iint_{\widetilde{\mathrm{DCVE}}}\frac{e}{q_\mathrm{i}^2}\mathbf{q}_\mathrm{i}\times\frac{\partial \mathbf{q}_\mathrm{i}}{\partial t}\cdot\hat{\mathbf{n}}\,\mathrm{d}\mathcal{A}\end{aligned} \tag{A.52}$$

$$\iiint_{\mathrm{DCVE}} \nabla\cdot\left[(\psi_\mathrm{i}-\psi)\rho q^2\mathbf{q}\right]\mathrm{d}\mathcal{V} = \iint_{\widetilde{\mathrm{DCVE}}}\left[\widetilde{\nabla}\cdot\mathbf{K}^\circ + \cancel{(\ldots)_\mathrm{e}} + \cancel{(\ldots)_\mathrm{w}}\right]\mathrm{d}\mathcal{A} \tag{A.53}$$

$$\iiint_{\mathrm{DCVE}} \left(\rho_\mathrm{i} q_\mathrm{i}^2\mathbf{q}_\mathrm{i}-\rho q^2\mathbf{q}\right)\cdot\nabla\psi_\mathrm{i}\,\mathrm{d}\mathcal{V} = \iint_{\widetilde{\mathrm{DCVE}}}\mathbf{E}\cdot\widetilde{\nabla}\psi_\mathrm{i}\,\mathrm{d}\mathcal{A} = \iint_{\widetilde{\mathrm{DCVE}}}\frac{1}{q_\mathrm{i}^2}\left[\mathbf{q}_\mathrm{i}\times\left(\mathbf{E}\cdot\widetilde{\nabla}\mathbf{q}_\mathrm{i}\right)\cdot\hat{\mathbf{n}}\right]\mathrm{d}\mathcal{A} \tag{A.54}$$

$$\begin{aligned}&\iiint_{\mathrm{DCVE}}\left[(\mathbf{q}_\mathrm{i}\times\nabla p_\mathrm{i})\cdot\hat{\mathbf{n}}-(\mathbf{q}\times\nabla p)\cdot\hat{\mathbf{n}}\right]\mathrm{d}\mathcal{V}\\ =&\iiint_{\mathrm{DCVE}}\left\{\left[(\mathbf{q}_\mathrm{i}-\mathbf{q})\times\nabla p_\mathrm{i}+\mathbf{q}\times\nabla\cancel{(p_\mathrm{i}-p)}\right]\right\}\cdot\hat{\mathbf{n}}\,\mathrm{d}\mathcal{V}\\ =&\iint_{\widetilde{\mathrm{DCVE}}}\left(\mathbf{Q}\times\widetilde{\nabla}p_\mathrm{i}\right)\cdot\hat{\mathbf{n}}\,\mathrm{d}\mathcal{A} = \iint_{\widetilde{\mathrm{DCVE}}}\left(\mathbf{Q}\times\left(-\frac{\partial \mathbf{q}_\mathrm{i}}{\partial t}-\frac{1}{2}\rho_\mathrm{i}\widetilde{\nabla}q_\mathrm{i}^2\right)\right)\cdot\hat{\mathbf{n}}\,\mathrm{d}\mathcal{A}\end{aligned} \tag{A.55}$$

$$\iiint_{\mathrm{DCVE}} \mathbf{q} \times \left(\nabla \cdot \overline{\overline{\boldsymbol{\tau}}}\right) \cdot \hat{\mathbf{n}} \, \mathrm{d}\mathcal{V} = \iiint_{\mathrm{DCVE}} \left[\nabla \cdot \left(\cancel{\mathbf{q} \times \overline{\overline{\boldsymbol{\tau}}}}\right) + \left(\overline{\overline{\boldsymbol{\tau}}} \cdot \nabla\right) \times \mathbf{q}\right] \cdot \hat{\mathbf{n}} \, \mathrm{d}\mathcal{V} = \iint_{\widetilde{\mathrm{DCVE}}} \mathcal{D}^{\times} \, \mathrm{d}\mathcal{A} \tag{A.56}$$

$$\iiint_{\mathrm{DCVE}} 2(\psi_{\mathrm{i}} - \psi)\mathbf{q} \cdot \nabla p \, \mathrm{d}\mathcal{V} = \iint_{\widetilde{\mathrm{DCVE}}} 2\mathbf{Q}^{\circ} \cdot \widetilde{\nabla} p_{\mathrm{i}} \, \mathrm{d}\mathcal{A} = \iint_{\widetilde{\mathrm{DCVE}}} 2\mathbf{Q}^{\circ} \cdot \left(-\frac{\partial \mathbf{q}_{\mathrm{i}}}{\partial t} - \frac{1}{2}\rho_{\mathrm{i}} \widetilde{\nabla} q_{\mathrm{i}}^2\right) \mathrm{d}\mathcal{A} \tag{A.57}$$

$$\begin{aligned}
&\iiint_{\mathrm{DCVE}} -2(\psi_{\mathrm{i}} - \psi)\mathbf{q} \cdot \left(\nabla \cdot \overline{\overline{\boldsymbol{\tau}}}\right) \mathrm{d}\mathcal{V} \\
&= \iiint_{\mathrm{DCVE}} -2\left\{\nabla \cdot \left[(\psi_{\mathrm{i}} - \psi)\mathbf{q} \cdot \overline{\overline{\boldsymbol{\tau}}}\right] - \nabla\left[(\psi_{\mathrm{i}} - \psi)\mathbf{q}\right] : \overline{\overline{\boldsymbol{\tau}}}\right\} \mathrm{d}\mathcal{V} \\
&= \int_{\partial\widetilde{\mathrm{DCVE}}} \int -2(\psi_{\mathrm{i}} - \psi)\cancel{\mathbf{q} \cdot \overline{\overline{\boldsymbol{\tau}}}} \cdot \hat{\mathbf{t}} \, \mathrm{d}n \, \mathrm{d}\ell + \iint_{\widetilde{\mathrm{DCVE}}} \left[-2(\psi_{\mathrm{i}} - \psi)\mathbf{q} \cdot \cancel{\overline{\overline{\boldsymbol{\tau}}}}\right]_{\mathrm{e}} \cdot \hat{\mathbf{n}}_{\mathrm{e}} \, \mathrm{d}\mathcal{A} \\
&\quad + \iint_{\widetilde{\mathrm{DCVE}}} \left[-2(\psi_{\mathrm{i}} - \psi)\cancel{\mathbf{q}} \cdot \overline{\overline{\boldsymbol{\tau}}}\right]_{\mathrm{w}} \cdot (-\hat{\mathbf{n}}_{\mathrm{w}}) \, \mathrm{d}\mathcal{A} + \int_{\widetilde{\mathrm{DCVE}}} \int 2\widetilde{\nabla}\left[(\psi_{\mathrm{i}} - \psi)\mathbf{q}\right] : \overline{\overline{\boldsymbol{\tau}}} \, \mathrm{d}n \, \mathrm{d}\mathcal{A} \\
&\quad = \iint_{\widetilde{\mathrm{DCVE}}} 2\mathcal{D}^{\circ} \, \mathrm{d}\mathcal{A}
\end{aligned} \tag{A.58}$$

where $\widetilde{\nabla}\left[(\psi_{\mathrm{i}} - \psi)\mathbf{q}\right] : \overline{\overline{\boldsymbol{\tau}}}$ is an alternative notation for the same term $\left(\overline{\overline{\boldsymbol{\tau}}} \cdot \nabla\right) \cdot \left[(\psi_{\mathrm{i}} - \psi)\mathbf{q}\right]$ in the definition (A.9).

Summarizing Equations (A.49) to (A.58) yields the integral form of the 3D IBL lateral curvature equation (2.4) where $\mathbf{q}_{\mathrm{i}}$ is replaced with $\mathbf{q}_{\mathrm{e}}$ following first-order boundary layer approximations.

Appendix B

Closure Details

B.1 Neural Network Training

In training the neural network models, the regression quality is verified by monitoring the model error convergence and the final prediction accuracy. Take the training of the laminar closure relation of H_{22} for example. After the variable selection process, the neural network model in the functional form of $H_{22}(H_1, H_2, H_{12})$ is trained with L_2/L_1 regularization and without sparsity-input regularization as discussed in Section 3.3. The mean square error (MSE) as well as the loss (i.e. the objective function being minimized) evolves over training epochs (i.e. iterations) as shown in Figure B-1. The small gap between the MSE of training and testing data is achieved which indicates reasonable model generalization capability (i.e. less overfitting). Also, the regularization weighting factor is tuned by trial and error to achieve a similar order of magnitude in the loss contributions from the MSE and the regularization (which is the overall loss subtracting the MSE). This is intended to reduce overfitting (if MSE dominates) and over-regularization (if the regularization loss prevails).

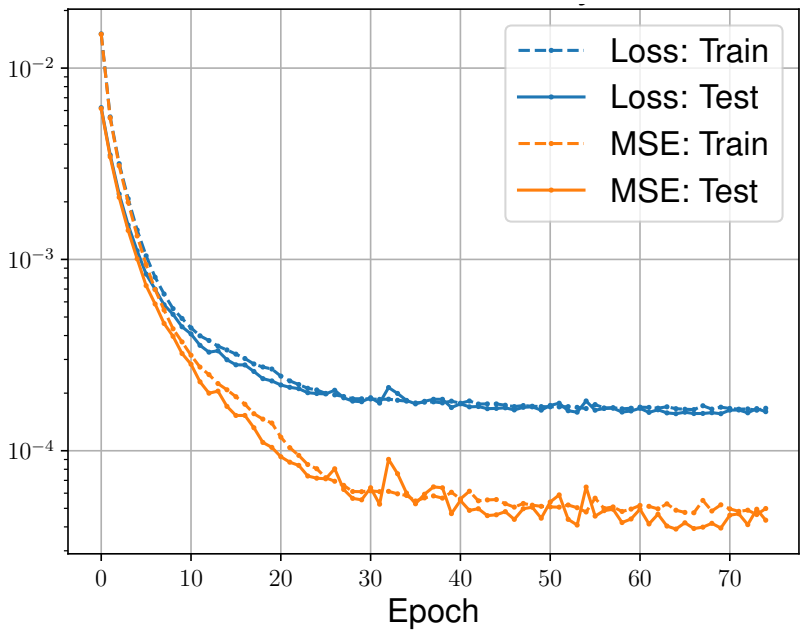

Figure B-1: Sample convergence history of the loss and mean square error (MSE) in the training of the neural network closure for $H_{22}(H_1, H_2, H_{12})$

The quality of fit is also checked by comparing the prediction of the trained model against the data. Figure B-2. Both the prediction and the data have been normalized to a zero-to-one scale based on the range of the data. An exact match would result in all the prediction-data pair to fall on the $y = x$ line and a bigger deviation from that indicates a larger prediction error. The closure models newly trained in this work all result in reasonable quality of fit as measured by the R^2-score.

B.2 Neural Network Closure

The final neural network closure models are documented in this section. Some useful notations are defined first to facilitate the ensuing discussion.

The standard scaler $\mathcal{S}_{\text{std}}$ with the mean $\boldsymbol{\mu}$ and scale $\boldsymbol{\sigma}$ normalizes a d-dimensional

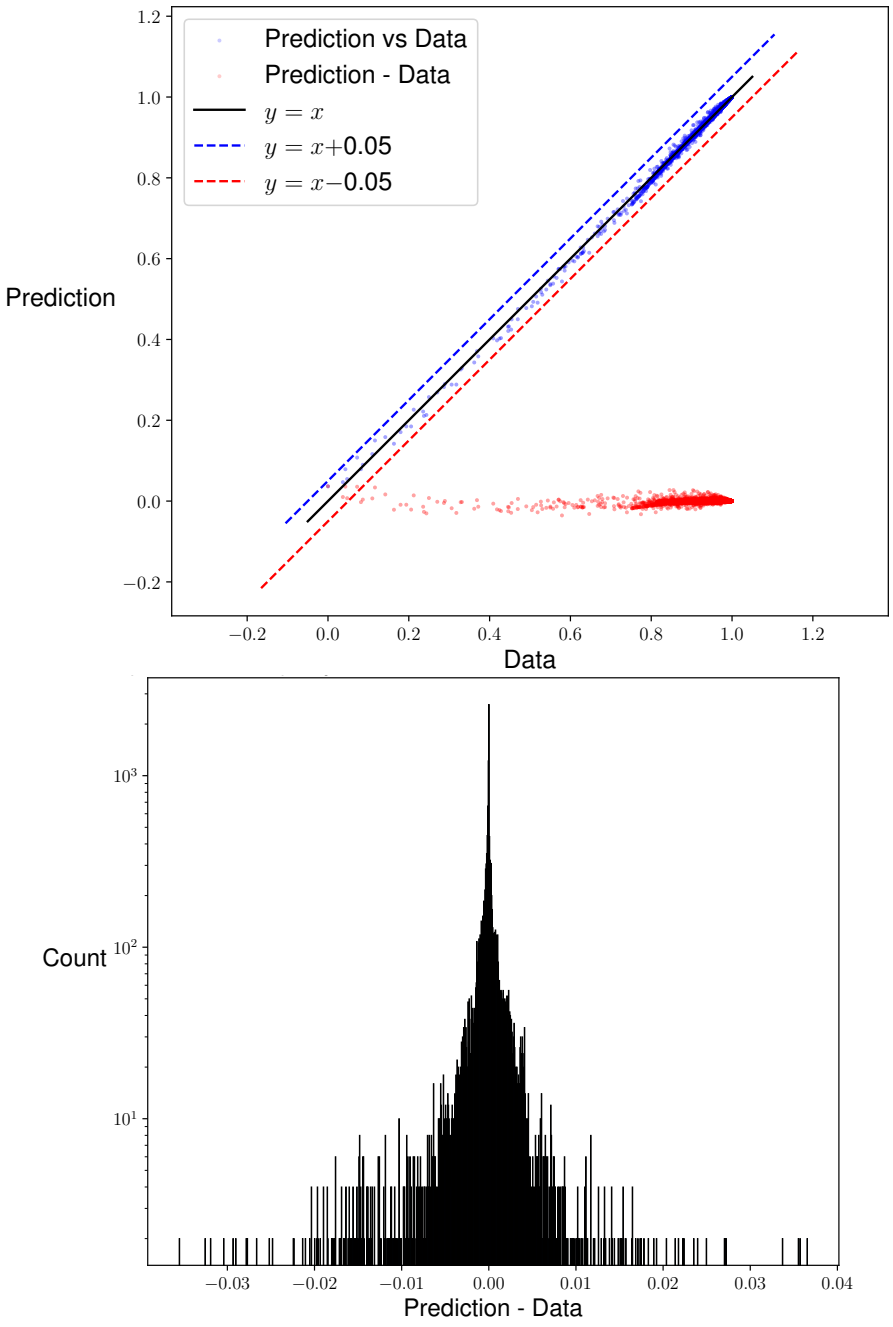

Figure B-2: Top: Prediction versus data for the trained neural network closure $H_{22}(H_1, H_2, H_{12})$ ($R^2 = 0.998$). Bottom: Histogram of prediction error. Numerical values are on a zero-to-one scale resulting from normalization based on the range of H_{22} data.

input array $\boldsymbol{x}$. $\mathcal{S}_{\text{std}}$ and its inverse are given as follows.

$$\mathcal{S}_{\text{std}}(\boldsymbol{x}\,;\,\boldsymbol{\mu},\boldsymbol{\sigma}) \equiv \text{diag}(\boldsymbol{\sigma})^{-1}(\boldsymbol{x}-\boldsymbol{\mu}) \tag{B.1}$$

$$\mathcal{S}_{\text{std}}^{-1}(\tilde{\boldsymbol{x}}\,;\,\boldsymbol{\mu},\boldsymbol{\sigma}) \equiv \text{diag}(\boldsymbol{\sigma})\,\tilde{\boldsymbol{x}}+\boldsymbol{\mu} \qquad \boldsymbol{x},\tilde{\boldsymbol{x}},\boldsymbol{\mu},\boldsymbol{\sigma}\in\mathbb{R}^d \tag{B.2}$$

The minmax scaler $\mathcal{S}_{\text{minmax}}$ with the minimum $x_{\min}$ and maximum $x_{\max}$ scales a scalar input x to the range of $[0,1]$. $\mathcal{S}_{\text{minmax}}$ and its inverse are given as follows.

$$\mathcal{S}_{\text{minmax}}(x;\,x_{\min},x_{\max}) \equiv \frac{x-x_{\min}}{x_{\max}-x_{\min}} \tag{B.3}$$

$$\mathcal{S}_{\text{minmax}}^{-1}(\tilde{x};\,x_{\min},x_{\max}) \equiv (x_{\max}-x_{\min})\,\tilde{x}+x_{\min}$$

$$x,\tilde{x},x_{\min},x_{\max}\in\mathbb{R} \tag{B.4}$$

A fully-connected feed-forward neural network is denoted as $h:\boldsymbol{x}\mapsto h(\boldsymbol{x})$, where the output is scalar and the input $\boldsymbol{x}$ depends on the specific functional form listed in (3.6) and (3.7). A sample neural network configuration is illustrated in Figure B-3. The hidden layer weights and biases are denoted as $\bar{\bar{W}}$ and $\boldsymbol{b}$ respectively with corresponding index subscripts. The output layer weight and bias are $\boldsymbol{w}$ and b respectively.

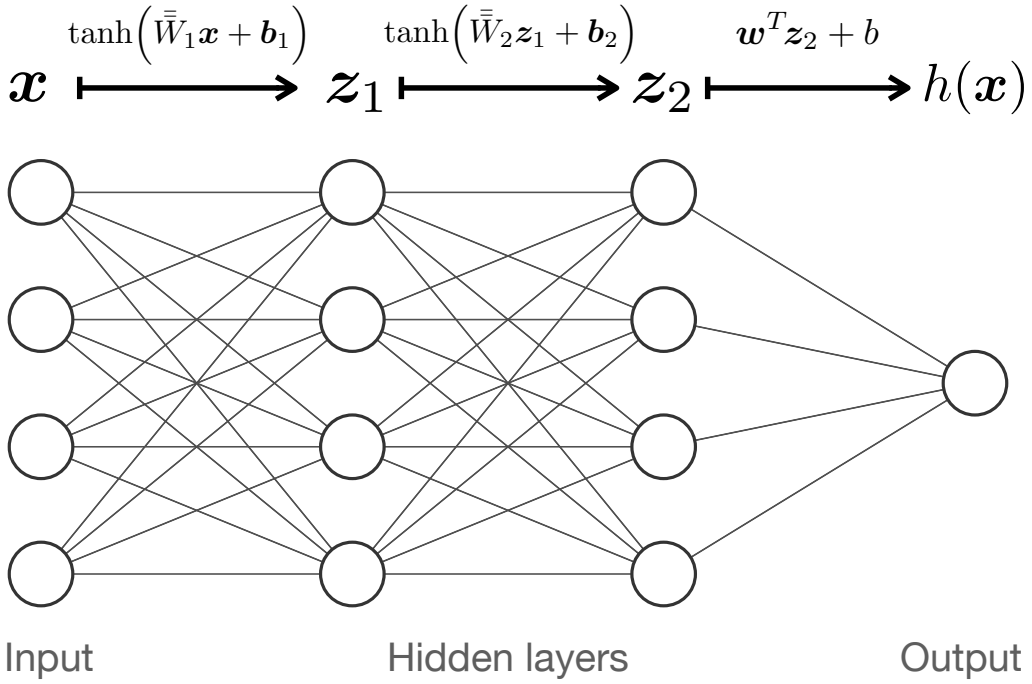

Figure B-3: Sample neural network configuration with two hidden layers of the same width as the input (4-dimensional plotted as an example)

B.2.1 Laminar

$$H_{22}(\boldsymbol{x}) = \mathcal{S}^{-1}_{\text{minmax}}(\tilde{y};\, y_{\min}, y_{\max}), \qquad \tilde{y} = \frac{1}{2}[f(\boldsymbol{x}) + f(\bar{\boldsymbol{x}})] - f(\boldsymbol{x}_{\text{2D}}) + \tilde{y}_{\text{2D}}$$

$$f(\,\cdot\,) \equiv h\left(\mathcal{S}_{\text{std}}(\,\cdot\,;\boldsymbol{\mu},\boldsymbol{\sigma})\right), \quad \boldsymbol{x} = (H_1, H_2, H_{12}), \quad \bar{\boldsymbol{x}} = (H_1, -H_2, -H_{12}), \quad \boldsymbol{x}_{\text{2D}} = (H_1, 0, 0)$$

$$y_{\min} = \text{-3.8921400000000002e-02}, \quad y_{\max} = \ 0\ , \quad \tilde{y}_{\text{2D}} = 1$$

$$\boldsymbol{\mu} = \ (\text{2.7993311559999996e+00},\ 0,\ 0)$$

$$\boldsymbol{\sigma} = \ (\text{8.3775363721826701e-01},\ \text{7.5251785050584066e-02},\ \text{3.7715359296182145e-02})$$

$$\bar{\bar{W}}_1 = \begin{bmatrix} \text{-2.2397816181182861e-01},\ \text{3.7631131708621979e-03},\ \text{-2.5438147783279419e-01} \\ \text{-2.4255822598934174e-01},\ \text{-4.1462838649749756e-02},\ \text{-3.4697806835174561e-01} \\ \text{4.5997455716133118e-01},\ \text{5.7588559389114380e-01},\ \text{3.6220005154609680e-01} \end{bmatrix}$$

$$\boldsymbol{b}_1 = (\text{-1.0779798030853271e+00},\ \text{5.4756022989749908e-02},\ \text{-5.1904648542404175e-01})$$

$$\bar{\bar{W}}_2 = \begin{bmatrix} \text{6.9522500038146973e-01},\ \text{-6.6782337427139282e-01},\ \text{4.8708307743072510e-01} \\ \text{-5.1154631376266479e-01},\ \text{5.1373207569122314e-01},\ \text{-4.2518413066864014e-01} \\ \text{1.4354919195175171e+00},\ \text{-1.1367483139038086e+00},\ \text{6.3172781467437744e-01} \end{bmatrix}$$

$$\boldsymbol{b}_2 = (\text{2.6991438865661621e-01},\ \text{-2.7172306180000305e-01},\ \text{5.3624115884304047e-02})$$

$$\boldsymbol{w} = (\text{-1.7762746810913086e+00},\ \text{2.6439216732978821e-01},\ \text{-2.0124142169952393e+00})$$

$$b = 0$$

It holds that

$$H_{22}(H_1, H_2, H_{12}) \equiv H_{22}(H_1, -H_2, -H_{12}), \qquad H_{22}(H_1, 0, 0) \equiv 0$$

$$H_2^\circ(\boldsymbol{x}) = \mathcal{S}_{\text{minmax}}^{-1}(\tilde{y};\, y_{\min}, y_{\max}), \qquad \tilde{y} = \frac{1}{2}[f(\boldsymbol{x}) + f(\bar{\boldsymbol{x}})] - f(\boldsymbol{x}_{\text{2D}}) + \tilde{y}_{\text{2D}}$$

$$f(\,\cdot\,) \equiv h\left(\mathcal{S}_{\text{std}}(\,\cdot\,;\boldsymbol{\mu},\boldsymbol{\sigma})\right), \quad \boldsymbol{x} = (H_1, H_2, H_{12}), \quad \bar{\boldsymbol{x}} = (H_1, -H_2, -H_{12}), \quad \boldsymbol{x}_{\text{2D}} = (H_1, 0, 0)$$

$$y_{\min} = \text{-1.9278699999999999e-02}, \quad y_{\max} = 0, \quad \tilde{y}_{\text{2D}} = 1$$

$$\boldsymbol{\mu} = (\text{2.7993311559999996e+00},\ 0,\ 0)$$

$$\boldsymbol{\sigma} = (\text{8.3775363721826701e-01},\ \text{7.5251785050584066e-02},\ \text{3.7715359296182145e-02})$$

$$\bar{\bar{W}}_1 = \begin{bmatrix} \text{-2.3375809192657471e-01},\ \text{4.2706140875816345e-01},\ \text{5.4958528280258179e-01} \\ \text{1.1007745265960693e+00},\ \text{-4.5790042728185654e-02},\ \text{6.7091636359691620e-02} \\ \text{5.5829071998596191e-01},\ \text{-6.5840405225753784e-01},\ \text{-4.1475591063499451e-01} \end{bmatrix}$$

$$\boldsymbol{b}_1 = (\text{-7.7356314659118652e-01},\ \text{5.9074974060058594e-01},\ \text{-7.2994935512542725e-01})$$

$$\bar{\bar{W}}_2 = \begin{bmatrix} \text{1.2454129457473755e+00},\ \text{9.0634942054748535e-02},\ \text{2.1943511962890625e+00} \\ \text{-6.9076269865036011e-01},\ \text{-8.8583481311798096e-01},\ \text{-8.1048613786697388e-01} \\ \text{-1.0436104238033295e-01},\ \text{-1.8513680696487427e+00},\ \text{-8.2104790210723877e-01} \end{bmatrix}$$

$$\boldsymbol{b}_2 = (\text{-6.6288971900939941e-01},\ \text{-1.0589946806430817e-01},\ \text{-7.4675244092941284e-01})$$

$$\boldsymbol{w} = (\text{-1.4458167552947998e+00},\ \text{1.9542400836944580e+00},\ \text{5.1080971956253052e-01})$$

$$b = 0$$

It holds that

$$H_2^\circ(H_1, H_2, H_{12}) \equiv H_2^\circ(H_1, -H_2, -H_{12}), \qquad H_2^\circ(H_1, 0, 0) \equiv 0$$

$$H_{d_2}(\boldsymbol{x}) = \mathcal{S}^{-1}_{\text{minmax}}(\tilde{y};\, y_{\min}, y_{\max}), \qquad \tilde{y} = \frac{1}{2}[f(\boldsymbol{x}) + f(\bar{\boldsymbol{x}})] - f(\boldsymbol{x}_{\text{2D}}) + \tilde{y}_{\text{2D}}$$

$$f(\,\cdot\,) \equiv h\left(\mathcal{S}_{\text{std}}(\,\cdot\,;\boldsymbol{\mu},\boldsymbol{\sigma})\right), \quad \boldsymbol{x} = (H_1, H_2, H_{12}), \quad \bar{\boldsymbol{x}} = (H_1, -H_2, -H_{12}), \quad \boldsymbol{x}_{\text{2D}} = (H_1, 0, 0)$$

$$y_{\min} = \text{-1.0628799999999999e-01}, \quad y_{\max} = 0, \quad \tilde{y}_{\text{2D}} = 1$$

$$\boldsymbol{\mu} = (\text{2.7993311559999996e+00},\ 0,\ 0)$$

$$\boldsymbol{\sigma} = (\text{8.3775363721826701e-01},\ \text{7.5251785050584066e-02},\ \text{3.7715359296182145e-02})$$

$$\bar{\bar{W}}_1 = \begin{bmatrix} \text{3.0395579338073730e-01},\ \text{1.0938671231269836e-01},\ \text{3.8796237111091614e-01} \\ \text{1.0371387004852295e+00},\ \text{5.0546383857727051e-01},\ \text{3.6536067724227905e-01} \\ \text{-2.4718590080738068e-01},\ \text{3.7444088608026505e-02},\ \text{3.7491607666015625e-01} \end{bmatrix}$$

$$\boldsymbol{b}_1 = (\text{1.2340452671051025e+00},\ \text{-3.2872813940048218e-01},\ \text{-7.8886389732360840e-01})$$

$$\bar{\bar{W}}_2 = \begin{bmatrix} \text{-6.6305464506149292e-01},\ \text{-8.6312264204025269e-01},\ \text{-1.0593793392181396e+00} \\ \text{2.0099744796752930e+00},\ \text{-4.2855685949325562e-01},\ \text{-6.2193071842193604e-01} \\ \text{-7.0910936594009399e-01},\ \text{1.3168816566467285e+00},\ \text{2.1219766139984131e+00} \end{bmatrix}$$

$$\boldsymbol{b}_2 = (\text{2.5362739339470863e-02},\ \text{4.7407567501068115e-01},\ \text{7.8544534742832184e-02})$$

$$\boldsymbol{w} = (\text{1.3328793048858643e+00},\ \text{1.8945306539535522e+00},\ \text{-1.3435930013656616e+00})$$

$$b = 0$$

It holds that

$$H_{d_2}(H_1, H_2, H_{12}) \equiv H_{d_2}(H_1, -H_2, -H_{12}), \qquad H_{d_2}(H_1, 0, 0) \equiv 0$$

$$Re_{\theta_{11}} c_{f_2}(\boldsymbol{x}) = \mathcal{S}^{-1}_{\text{minmax}}(\tilde{y};\, y_{\min}, y_{\max}), \qquad \tilde{y} = f(\boldsymbol{x}) - f(\bar{\boldsymbol{x}}) + \tilde{y}_{\text{2D}}$$

$$f(\,\cdot\,) \equiv h\left(\mathcal{S}_{\text{std}}(\,\cdot\,;\boldsymbol{\mu},\boldsymbol{\sigma})\right), \quad \boldsymbol{x} = (H_1, H_2, H_{12}), \quad \bar{\boldsymbol{x}} = (H_1, -H_2, -H_{12}), \quad \boldsymbol{x}_{\text{2D}} = (H_1, 0, 0)$$

$$y_{\min} = \text{-3.7137097861999996e-01}, \quad y_{\max} = 3.7137097861999996\text{e-01}, \quad \tilde{y}_{\text{2D}} = 0$$

$$\boldsymbol{\mu} = (2.7993311559999996\text{e+00},\ 0,\ 0)$$

$$\boldsymbol{\sigma} = (8.3775363721826701\text{e-01},\ 7.5251785050584066\text{e-02},\ 3.7715359296182145\text{e-02})$$

$$\bar{\bar{W}}_1 = \begin{bmatrix} 2.8753907680511475\text{e+00},\ \text{-2.1634419262409210e-01},\ \text{-1.1957298219203949e-01} \\ \text{-3.8782262802124023e-01},\ 1.8055701255798340\text{e-01},\ 9.9620986729860306\text{e-03} \\ \text{-1.3161288499832153e+00},\ \text{-9.7712862491607666e-01},\ \text{-1.0744823217391968e+00} \end{bmatrix}$$

$$\boldsymbol{b}_1 = (9.4779312610626221\text{e-01},\ \text{-1.2380976676940918e+00},\ 2.5619685649871826\text{e-01})$$

$$\bar{\bar{W}}_2 = \begin{bmatrix} 1.5801591873168945\text{e+00},\ 7.0788484811782837\text{e-01},\ \text{-6.5934133529663086e-01} \\ \text{-4.6391662955284119e-01},\ 5.7920837402343750\text{e-01},\ 1.6060512065887451\text{e+00} \\ 3.3363944292068481\text{e-01},\ 4.7434797883033752\text{e-01},\ \text{-5.7778567075729370e-01} \end{bmatrix}$$

$$\boldsymbol{b}_2 = (\text{-1.0891193151473999e+00},\ \text{-1.0409305095672607e+00},\ 1.3738555908203125\text{e+00})$$

$$\boldsymbol{w} = (5.6974327564239502\text{e-01},\ \text{-8.0781781673431396e-01},\ \text{-1.3251502513885498e+00})$$

$$b = 0$$

It holds that

$$Re_{\theta_{11}} c_{f_2}(H_1, H_2, H_{12}) \equiv -Re_{\theta_{11}} c_{f_2}(H_1, -H_2, -H_{12}), \qquad Re_{\theta_{11}} c_{f_2}(H_1, 0, 0) \equiv 0$$

$$Re_{\theta_{11}} c_{\mathcal{D}}^{\circ}(\boldsymbol{x}) = \mathcal{S}_{\text{minmax}}^{-1}(\tilde{y};\, y_{\min}, y_{\max}), \qquad \tilde{y} = f(\boldsymbol{x}) - f(\bar{\boldsymbol{x}}) + \tilde{y}_{\text{2D}}$$

$$f(\,\cdot\,) \equiv h\left(\mathcal{S}_{\text{std}}(\,\cdot\,;\boldsymbol{\mu},\boldsymbol{\sigma})\right), \quad \boldsymbol{x} = (H_1, H_2, H_{12}), \quad \bar{\boldsymbol{x}} = (H_1, -H_2, -H_{12}), \quad \boldsymbol{x}_{\text{2D}} = (H_1, 0, 0)$$

$$y_{\min} = \text{-3.6779355709318021e-02}, \quad y_{\max} = 3.6779355709318021\text{e-02}, \quad \tilde{y}_{\text{2D}} = 0$$

$$\boldsymbol{\mu} = (2.7993311559999996\text{e+00},\ 0,\ 0)$$

$$\boldsymbol{\sigma} = (8.3775363721826701\text{e-01},\ 7.5251785050584066\text{e-02},\ 3.7715359296182145\text{e-02})$$

$$\bar{\bar{W}}_1 = \begin{bmatrix} 1.5942254066467285\text{e+00},\ 2.2215312719345093\text{e-01},\ 1.0936068743467331\text{e-01} \\ \text{-5.7833576202392578e-01},\ \text{-7.5626581907272339e-02},\ 4.1446790099143982\text{e-02} \\ 4.3717780709266663\text{e-01},\ \text{-5.1782065629959106e-01},\ \text{-8.1346619129180908e-01} \end{bmatrix}$$

$$\boldsymbol{b}_1 = (7.4972319602966309\text{e-01},\ \text{-1.0875395536422729e+00},\ 5.8123970031738281\text{e-01})$$

$$\bar{\bar{W}}_2 = \begin{bmatrix} 1.1340995877981186\text{e-01},\ 6.9219553470611572\text{e-01},\ \text{-4.0919706225395203e-01} \\ \text{-4.2947837710380554e-01},\ 5.8811587095260620\text{e-01},\ 1.0435531139373779\text{e+00} \\ 5.3446684032678604\text{e-02},\ 1.2964241504669189\text{e+00},\ 6.4232498407363892\text{e-01} \end{bmatrix}$$

$$\boldsymbol{b}_2 = (\text{-3.6477741599082947e-01},\ \text{-3.8031446933746338e-01},\ 6.8510305881500244\text{e-01})$$

$$\boldsymbol{w} = (\text{-1.2021777629852295e+00},\ 5.5657458305358887\text{e-01},\ \text{-1.1782170534133911e+00})$$

$$b = 0$$

It holds that

$$Re_{\theta_{11}} c_{\mathcal{D}}^{\circ}(H_1, H_2, H_{12}) \equiv -Re_{\theta_{11}} c_{\mathcal{D}}^{\circ}(H_1, -H_2, -H_{12}), \qquad Re_{\theta_{11}} c_{\mathcal{D}}^{\circ}(H_1, 0, 0) \equiv 0$$

The closure relations of $\left\{H_1^*, Re_{\theta_{11}} c_{f_1}, Re_{\theta_{11}} c_{\mathcal{D}}\right\}$ follow Ref. [41].

$$H_1^*(H_1) = \begin{cases} 1.528 + 0.0111\dfrac{(H_1 - 4.35)^2}{H_1 + 1} - 0.0278\dfrac{(H_1 - 4.35)^3}{H_1 + 1} - 0.0002(H_1 - 4.35)^2 H_1^2, & H_1 < 4.35 \\ 1.528 + 0.015\dfrac{(H_1 - 4.35)^2}{H_1}, & \text{else} \end{cases}$$

$$Re_{\theta_{11}} c_{f_1}(H_1) = \begin{cases} 0.0727\dfrac{(5.5 - H_1)^3}{H_1 + 1} - 0.07, & H_1 < 5.5 \\ 0.015\left(1 - \dfrac{1}{H_1 - 4.5}\right)^2 - 0.07, & \text{else} \end{cases}$$

$$Re_{\theta_{11}} c_{\mathcal{D}}(H_1) = \begin{cases} \dfrac{H_1^*}{2}\left(0.207 + 0.00205(4 - H_1)^{5.5}\right), & H_1 < 4 \\ \dfrac{H_1^*}{2}\left(0.207 - 0.0016\dfrac{(H_1 - 4)^2}{1 + 0.02(H_1 - 4)^2}\right), & \text{else} \end{cases}$$

The following closure relations are simply linear models because the trained neural network models reveal a linear structure. These simplified models are more interpretable and do not compromise the quality of fit.

$$H_2^*(H_2, H_{12}) = (-0.1568682053359842)H_2 + (1.0698363410623215)H_{12}$$

$$H_0^\circ(H_2, H_{12}) = H_2 + H_{12}$$

$$H_1^\circ(H_2, H_{12}) = (0.8420706610515913)H_2 + (1.0690341593331103)H_{12}$$

$$H_{d_1}(H_2) = (0.9939333095360753)H_2$$

B.2.2 Turbulent

$$H_{22}(\boldsymbol{x}) = \mathcal{S}^{-1}_{\text{minmax}}(\tilde{y};\, y_{\min}, y_{\max}), \qquad \tilde{y} = \frac{1}{2}[f(\boldsymbol{x}) + f(\bar{\boldsymbol{x}})] - f(\boldsymbol{x}_{\text{2D}}) + \tilde{y}_{\text{2D}}$$

$$f(\,\cdot\,) \equiv h\left(\mathcal{S}_{\text{std}}(\,\cdot\,;\boldsymbol{\mu},\boldsymbol{\sigma})\right), \quad \boldsymbol{x} = (H_1, H_2, H_{12}), \quad \bar{\boldsymbol{x}} = (H_1, -H_2, -H_{12}), \quad \boldsymbol{x}_{\text{2D}} = (H_1, 0, 0)$$

$$y_{\min} = \text{-9.3049746071047643e-02}, \quad y_{\max} = \text{-9.8385849483043944e-09}$$

$$\tilde{y}_{\text{2D}} = 1.0000002384185791\text{e+}00$$

$$\boldsymbol{\mu} = (1.4625283402665179\text{e+}00,\ \text{-4.6986082276125218e-02},\ 1.1493733084907835\text{e-}02)$$

$$\boldsymbol{\sigma} = (1.7249160623132892\text{e-}01,\ 1.3436658103367680\text{e-}01,\ 3.4758401714377343\text{e-}02)$$

$$\bar{\bar{W}}_1 = \begin{bmatrix} 3.3790177106857300\text{e-}01,\ 5.5653494596481323\text{e-}01,\ 1.6308912634849548\text{e-}01 \\ 3.9777696132659912\text{e-}02,\ 9.9870637059211731\text{e-}02,\ \text{-1.5895242989063263e-}01 \\ \text{-1.2145277112722397e-}01,\ \text{-2.6856473088264465e-}01,\ 9.6223905682563782\text{e-}02 \end{bmatrix}$$

$$\boldsymbol{b}_1 = (2.2608113288879395\text{e+}00,\ 8.5491049289703369\text{e-}01,\ \text{-1.2569828033447266e+}00)$$

$$\bar{\bar{W}}_2 = \begin{bmatrix} 7.3750913143157959\text{e-}01,\ \text{-8.5242879390716553e-}01,\ 5.3226274251937866\text{e-}01 \\ \text{-2.5905585289001465e-}01,\ \text{-2.2768472135066986e-}01,\ \text{-1.4084454774856567e+}00 \\ 3.0546978116035461\text{e-}01,\ 1.1485596895217896\text{e+}00,\ \text{-5.7742416858673096e-}01 \end{bmatrix}$$

$$\boldsymbol{b}_2 = (3.0809196829795837\text{e-}01,\ 1.4036870002746582\text{e-}01,\ 7.4692380428314209\text{e-}01)$$

$$\boldsymbol{w} = (\text{-1.5466769933700562e+}00,\ 7.9786974191665649\text{e-}01,\ 2.0145027637481689\text{e+}00)$$

$$b = 0$$

It holds that

$$H_{22}(H_1, H_2, H_{12}) \equiv H_{22}(H_1, -H_2, -H_{12}), \qquad H_{22}(H_1, 0, 0) \equiv 0$$

$$H_2^*(\boldsymbol{x}) = \mathcal{S}_{\text{minmax}}^{-1}(\tilde{y};\, y_{\min}, y_{\max}), \qquad \tilde{y} = f(\boldsymbol{x}) - f(\bar{\boldsymbol{x}}) + \tilde{y}_{\text{2D}}$$

$$f(\,\cdot\,) \equiv h\left(\mathcal{S}_{\text{std}}(\,\cdot\,;\boldsymbol{\mu},\boldsymbol{\sigma})\right), \quad \boldsymbol{x} = (H_2, H_{12}), \quad \bar{\boldsymbol{x}} = (-H_2, -H_{12}), \quad \boldsymbol{x}_{\text{2D}} = (0,0)$$

$$y_{\min} = \text{-5.0581008458557442e-01}, \quad y_{\max} = 3.7820926085283441\text{e-01}, \quad \tilde{y}_{\text{2D}} = 1.4434166252613068\text{e-01}$$

$$\boldsymbol{\mu} = (\text{-4.6748604920101237e-02},\ 1.1435641386012645\text{e-02})$$

$$\boldsymbol{\sigma} = (1.3406800245063352\text{e-01},\ 3.4680031486403411\text{e-02})$$

$$\bar{\bar{W}}_1 = \begin{bmatrix} 2.3147594183683395\text{e-02}, & \text{-8.2733199000358582e-02} \\ \text{-7.8917604684829712e-01}, & \text{-6.2849903106689453e-01} \end{bmatrix}$$

$$\boldsymbol{b}_1 = (\text{-4.1462343931198120e-01},\ \text{-8.4058445692062378e-01})$$

$$\bar{\bar{W}}_2 = \begin{bmatrix} 5.1425129175186157\text{e-01}, & 9.9222302436828613\text{e-02} \\ 9.9479562044143677\text{e-01}, & \text{-1.8372111022472382e-01} \end{bmatrix}$$

$$\boldsymbol{b}_2 = (3.6433863639831543\text{e-01},\ \text{-7.4794369935989380e-01})$$

$$\boldsymbol{w} = (\text{-6.9801872968673706e-01},\ \text{-8.0292963981628418e-01})$$

$$b = 0$$

It holds that

$$H_2^*(H_2, H_{12}) \equiv -H_2^*(-H_2, -H_{12}), \qquad H_2^*(0,0) \equiv 0$$

$$H_1^\circ(\boldsymbol{x}) = \mathcal{S}_{\text{minmax}}^{-1}(\tilde{y};\, y_{\min}, y_{\max}), \qquad \tilde{y} = f(\boldsymbol{x}) - f(\bar{\boldsymbol{x}}) + \tilde{y}_{\text{2D}}$$

$$f(\,\cdot\,) \equiv h\left(\mathcal{S}_{\text{std}}(\,\cdot\,;\boldsymbol{\mu},\boldsymbol{\sigma})\right), \quad \boldsymbol{x} = (H_2, H_{12}), \quad \bar{\boldsymbol{x}} = (-H_2, -H_{12}), \quad \boldsymbol{x}_{\text{2D}} = (0,0)$$

$$y_{\min} = \text{-3.4934612138952609e-01}, \quad y_{\max} = 5.8740911115537853\text{e-01},$$

$$\tilde{y}_{\text{2D}} = \text{-2.5413575768470764e-01}$$

$$\boldsymbol{\mu} = (\text{-4.6748604920101237e-02, 1.1435641386012645e-02})$$

$$\boldsymbol{\sigma} = (1.3406800245063352\text{e-01, 3.4680031486403411e-02})$$

$$\bar{\bar{W}}_1 = \begin{bmatrix} \text{-1.5480455756187439e-01, -3.7523645907640457e-02} \\ 3.2359755039215088\text{e-01, 4.4526794552803040e-01} \end{bmatrix}$$

$$\boldsymbol{b}_1 = (\text{-3.9882284402847290e-01, -1.2200978398323059e-01})$$

$$\bar{\bar{W}}_2 = \begin{bmatrix} \text{-9.8874002695083618e-01, 2.2917245328426361e-01} \\ 4.4596487283706665\text{e-01, 1.6396912932395935e-01} \end{bmatrix}$$

$$\boldsymbol{b}_2 = (4.0967342257499695\text{e-01, 2.7685090899467468e-01})$$

$$\boldsymbol{w} = (1.1326305866241455\text{e+00, -6.0041403770446777e-01})$$

$$b = 0$$

It holds that

$$H_1^\circ(H_2, H_{12}) \equiv -H_1^\circ(-H_2, -H_{12}), \qquad H_1^\circ(0,0) \equiv 0$$

$$H_2^{\circ}(\boldsymbol{x}) = \mathcal{S}_{\text{minmax}}^{-1}(\tilde{y};\, y_{\min}, y_{\max}), \qquad \tilde{y} = \frac{1}{2}[f(\boldsymbol{x}) + f(\bar{\boldsymbol{x}})] - f(\boldsymbol{x}_{\text{2D}}) + \tilde{y}_{\text{2D}}$$

$$f(\,\cdot\,) \equiv h\left(\mathcal{S}_{\text{std}}(\,\cdot\,;\boldsymbol{\mu},\boldsymbol{\sigma})\right), \quad \boldsymbol{x} = (H_1, H_2, H_{12}), \quad \bar{\boldsymbol{x}} = (H_1, -H_2, -H_{12}), \quad \boldsymbol{x}_{\text{2D}} = (H_1, 0, 0)$$

$$y_{\min} = \text{-7.2933991904749682e-02}, \quad y_{\max} = \text{-6.5507359790066520e-09}$$

$$\tilde{y}_{\text{2D}} = 1.0000002384185791\text{e+}00$$

$$\boldsymbol{\mu} = (1.4625283402665179\text{e+}00,\ \text{-4.6986082276125218e-02},\ 1.1493733084907835\text{e-}02)$$

$$\boldsymbol{\sigma} = (1.7249160623132892\text{e-}01,\ 1.3436658103367680\text{e-}01,\ 3.4758401714377343\text{e-}02)$$

$$\bar{\bar{W}}_1 = \begin{bmatrix} \text{-2.7821419760584831e-02},\ 7.3168182279914618\text{e-}04,\ 3.4611698985099792\text{e-}01 \\ 5.1606476306915283\text{e-}02,\ \text{-3.0290272831916809e-01},\ 6.9798581302165985\text{e-}02 \\ \text{-1.3965171575546265e-01},\ \text{-5.1536273956298828e-01},\ \text{-2.3399601876735687e-01} \end{bmatrix}$$

$$\boldsymbol{b}_1 = (\text{-4.3508896231651306e-01},\ 1.6390706300735474\text{e+}00,\ \text{-1.1608028411865234e-01})$$

$$\bar{\bar{W}}_2 = \begin{bmatrix} \text{-9.5133669674396515e-05},\ 1.7458312504459172\text{e-}04,\ 2.0578416297212243\text{e-}05 \\ \text{-6.3414293527603149e-01},\ 1.4869534969329834\text{e+}00,\ \text{-5.0587588548660278e-01} \\ \text{-1.1397643902455457e-05},\ 1.9579358195187524\text{e-}05,\ \text{-7.5229101639706641e-05} \end{bmatrix}$$

$$\boldsymbol{b}_2 = (5.4423842811957002\text{e-}05,\ \text{-5.3621006011962891e-01},\ 6.4842897700145841\text{e-}05)$$

$$\boldsymbol{w} = (\text{-1.3170858437661082e-05},\ 1.8760536909103394\text{e+}00,\ \text{-2.4201539417845197e-05})$$

$$b = 0$$

It holds that

$$H_2^{\circ}(H_1, H_2, H_{12}) \equiv H_2^{\circ}(H_1, -H_2, -H_{12}), \qquad H_2^{\circ}(H_1, 0, 0) \equiv 0$$

$$H_{d_1}(\boldsymbol{x}) = \mathcal{S}^{-1}_{\text{minmax}}(\tilde{y};\, y_{\min}, y_{\max}), \qquad \tilde{y} = f(\boldsymbol{x}) - f(\bar{\boldsymbol{x}}) + \tilde{y}_{\text{2D}}$$

$$f(\,\cdot\,) \equiv h\left(\mathcal{S}_{\text{std}}(\,\cdot\,;\boldsymbol{\mu},\boldsymbol{\sigma})\right), \quad \boldsymbol{x} = (H_2, H_{12}), \quad \bar{\boldsymbol{x}} = (-H_2, -H_{12}), \quad \boldsymbol{x}_{\text{2D}} = (0,0)$$

$$y_{\min} = \text{-6.3187603561175576e-01}, \quad y_{\max} = 8.3635235879966041\text{e-01}$$

$$\tilde{y}_{\text{2D}} = \text{-1.3926738500595093e-01}$$

$$\boldsymbol{\mu} = (\text{-4.6748604920101237e-02},\ 1.1435641386012645\text{e-02})$$

$$\boldsymbol{\sigma} = (1.3406800245063352\text{e-01},\ 3.4680031486403411\text{e-02})$$

$$\bar{\bar{W}}_1 = \begin{bmatrix} 9.5667481422424316\text{e-02},\ \text{-3.0010012909770012e-02} \\ 3.6956495046615601\text{e-01},\ 2.0046144723892212\text{e-01} \end{bmatrix}$$

$$\boldsymbol{b}_1 = (2.2887329757213593\text{e-01},\ \text{-3.7224281579256058e-02})$$

$$\bar{\bar{W}}_2 = \begin{bmatrix} \text{-1.6499416828155518e+00},\ 7.7200150489807129\text{e-01} \\ 5.6903165578842163\text{e-01},\ \text{-1.1702221632003784e+00} \end{bmatrix}$$

$$\boldsymbol{b}_2 = (\text{-2.3792868852615356e-01},\ 9.8518204689025879\text{e-01})$$

$$\boldsymbol{w} = (\text{-8.0239075422286987e-01},\ \text{-1.2149887084960938e+00})$$

$$b = 0$$

It holds that

$$H_{d_1}(H_2, H_{12}) \equiv -H_{d_1}(-H_2, -H_{12}), \qquad H_{d_1}(0,0) \equiv 0$$

$$H_{d_2}(\boldsymbol{x}) = \mathcal{S}^{-1}_{\text{minmax}}(\tilde{y};\, y_{\min}, y_{\max}), \qquad \tilde{y} = \frac{1}{2}[f(\boldsymbol{x}) + f(\bar{\boldsymbol{x}})] - f(\boldsymbol{x}_{\text{2D}}) + \tilde{y}_{\text{2D}}$$

$$f(\,\cdot\,) \equiv h\left(\mathcal{S}_{\text{std}}(\,\cdot\,; \boldsymbol{\mu}, \boldsymbol{\sigma})\right), \quad \boldsymbol{x} = (H_2, H_{12}), \quad \bar{\boldsymbol{x}} = (-H_2, -H_{12}), \quad \boldsymbol{x}_{\text{2D}} = (0, 0)$$

$$y_{\min} = \text{-1.9997753472009891e-01}, \quad y_{\max} = 0, \quad \tilde{y}_{\text{2D}} = 1$$

$$\boldsymbol{\mu} = (\text{-4.6907202338243865e-02},\ \text{1.1522592560737078e-02})$$

$$\boldsymbol{\sigma} = (\text{1.3372088954808728e-01},\ \text{3.4262883457906450e-02})$$

$$\bar{\bar{W}}_1 = \begin{bmatrix} \text{8.8955365121364594e-02}, & \text{-1.6376788914203644e-01} \\ \text{-9.4249911606311798e-02}, & \text{1.5356405079364777e-01} \end{bmatrix}$$

$$\boldsymbol{b}_1 = (\text{1.4196012020111084e+00},\ \text{-7.3968642950057983e-01})$$

$$\bar{\bar{W}}_2 = \begin{bmatrix} \text{-1.4153600931167603e+00}, & \text{8.8833039999008179e-01} \\ \text{-8.7160691618919373e-02}, & \text{-1.0940052270889282e+00} \end{bmatrix}$$

$$\boldsymbol{b}_2 = (\text{-2.3703123629093170e-01},\ \text{-9.1944985091686249e-02})$$

$$\boldsymbol{w} = (\text{-1.3416335582733154e+00},\ \text{1.5230376720428467e+00})$$

$$b = 0$$

It holds that

$$H_{d_2}(H_2, H_{12}) \equiv H_{d_2}(-H_2, -H_{12}), \qquad H_{d_2}(0, 0) \equiv 0$$

$$c_{f_1}(\boldsymbol{x}) = \mathcal{S}^{-1}_{\text{minmax}}(\tilde{y};\, y_{\min}, y_{\max}), \qquad \tilde{y} = \frac{1}{2}[f(\boldsymbol{x}) + f(\bar{\boldsymbol{x}})]$$

$$f(\,\cdot\,) \equiv h\left(\mathcal{S}_{\text{std}}(\,\cdot\,;\boldsymbol{\mu},\boldsymbol{\sigma})\right), \quad \boldsymbol{x} = (H_1, H_2, \log_{10}(Re_{\theta_{11}})), \quad \bar{\boldsymbol{x}} = (H_1, -H_2, \log_{10}(Re_{\theta_{11}}))$$

$$y_{\min} = \text{-1.2059803671296990e-03}, \quad y_{\max} = 7.0251658407900893\text{e-}03$$

$$\boldsymbol{\mu} = 1.4625283402665179\text{e+}00,\ \text{-4.6986082276125218e-02},\ 3.4826366550054928\text{e+}00)$$

$$\boldsymbol{\sigma} = (1.7249160623132892\text{e-}01,\ 1.3436658103367680\text{e-}01,\ 4.8793862541703992\text{e-}01)$$

$$\bar{\bar{W}}_1 = \begin{bmatrix} \text{-1.1598546802997589e-01},\ \text{-1.3822902925312519e-02},\ \text{-3.0707776546478271e-01} \\ \text{-2.6456149294972420e-02},\ \text{-6.9740772247314453e-02},\ \text{-5.4342991113662720e-01} \\ \text{-4.4744458794593811e-01},\ 1.2672057747840881\text{e-}01,\ 1.3565671443939209\text{e-}01 \end{bmatrix}$$

$$\boldsymbol{b}_1 = (1.2257097661495209\text{e-}01,\ \text{-1.0792042016983032e+}00,\ 6.1476096510887146\text{e-}02)$$

$$\bar{\bar{W}}_2 = \begin{bmatrix} \text{-4.4434082508087158e-01},\ \text{-9.3711984157562256e-01},\ \text{-4.8265841603279114e-01} \\ 3.1648817658424377\text{e-}01,\ 1.2352051585912704\text{e-}01,\ 1.4785574376583099\text{e-}01 \\ 1.8704571994021535\text{e-}04,\ 1.5679409261792898\text{e-}04,\ 1.2212141882628202\text{e-}05 \end{bmatrix}$$

$$\boldsymbol{b}_2 = (\text{-4.3748643249273300e-02},\ 1.4199081063270569\text{e-}01,\ 2.6742622139863670\text{e-}05)$$

$$\boldsymbol{w} = (\text{-1.0834887027740479e+}00,\ 4.2614325881004333\text{e-}01,\ \text{-4.9808797484729439e-05})$$

$$b = 4.7568202018737793\text{e-}01$$

It holds that

$$c_{f_1}(H_1, H_2, \log_{10}(Re_{\theta_{11}})) \equiv c_{f_1}(H_1, -H_2, \log_{10}(Re_{\theta_{11}}))$$

$$c_{f_2}(\boldsymbol{x}) = \mathcal{S}^{-1}_{\text{minmax}}(\tilde{y};\, y_{\min}, y_{\max}), \qquad \tilde{y} = f(\boldsymbol{x}) - f(\bar{\boldsymbol{x}}) + \tilde{y}_{\text{2D}}$$

$$f(\,\cdot\,) \equiv h\left(\mathcal{S}_{\text{std}}(\,\cdot\,;\boldsymbol{\mu},\boldsymbol{\sigma})\right), \quad \boldsymbol{x} = (H_1, H_{12}, \log_{10}(Re_{\theta_{11}}))$$

$$\bar{\boldsymbol{x}} = (H_1, -H_{12}, \log_{10}(Re_{\theta_{11}})), \quad \boldsymbol{x}_{\text{2D}} = (H_1, 0, \log_{10}(Re_{\theta_{11}}))$$

$$y_{\min} = \text{-1.5967338534111210e-03}, \quad y_{\max} = 7.0708332513952658\text{e-}04$$

$$\tilde{y}_{\text{2D}} = 3.8616368174552917\text{e-}01$$

$$\boldsymbol{\mu} = 1.4625283402665179\text{e+}00,\ 1.1493733084907835\text{e-}02,\ 3.4826366550054928\text{e+}00)$$

$$\boldsymbol{\sigma} = (1.7249160623132892\text{e-}01,\ 3.4758401714377343\text{e-}02,\ 4.8793862541703992\text{e-}01)$$

$$\bar{\bar{W}}_1 = \begin{bmatrix} \text{-7.3524643667042255e-03, -1.2786479294300079e-01, -9.4823521375656128e-01} \\ \text{-1.1777081340551376e-01, -1.3134601712226868e-01, -1.4226184785366058e-01} \\ 3.8980883359909058\text{e-}01,\ \text{-3.6779776215553284e-01},\ 4.9846926331520081\text{e-}01 \end{bmatrix}$$

$$\boldsymbol{b}_1 = (\text{-8.0284768342971802e-01, -3.7892085313796997e-01, -2.0350310206413269e-01})$$

$$\bar{\bar{W}}_2 = \begin{bmatrix} \text{-1.1095912456512451e+00, -3.9693075232207775e-03, -7.3544365167617798e-01} \\ \text{-7.7037864923477173e-01, -4.2854893207550049e-01, -1.2486571073532104e-01} \\ 2.9022341966629028\text{e-}01,\ 5.0248736143112183\text{e-}01,\ 3.1924769282341003\text{e-}01 \end{bmatrix}$$

$$\boldsymbol{b}_2 = (\text{-6.1456892639398575e-02},\ 4.2218580842018127\text{e-}01,\ \text{-3.4334599971771240e-01})$$

$$\boldsymbol{w} = (\text{-4.4391679763793945e-01},\ 8.2045823335647583\text{e-}01,\ \text{-1.0598660707473755e+00})$$

$$b = 0$$

It holds that

$$c_{f_2}(H_1, H_{12}, \log_{10}(Re_{\theta_{11}})) \equiv -c_{f_2}(H_1, -H_{12}, \log_{10}(Re_{\theta_{11}})), \qquad c_{f_2}(H_1, 0, \log_{10}(Re_{\theta_{11}})) \equiv 0$$

$$c_{\mathcal{D}}^{\circ}(\boldsymbol{x}) = \mathcal{S}_{\text{minmax}}^{-1}(\tilde{y};\, y_{\min}, y_{\max}), \qquad \tilde{y} = f(\boldsymbol{x}) - f(\bar{\boldsymbol{x}}) + \tilde{y}_{\text{2D}}$$

$$f(\,\cdot\,) \equiv h\left(\mathcal{S}_{\text{std}}(\,\cdot\,;\boldsymbol{\mu},\boldsymbol{\sigma})\right), \quad \boldsymbol{x} = (H_2, H_{12}, \log_{10}(Re_{\theta_{11}}), c_{\mathcal{D}})$$

$$\bar{\boldsymbol{x}} = (-H_2, -H_{12}, \log_{10}(Re_{\theta_{11}}), c_{\mathcal{D}}), \quad \boldsymbol{x}_{\text{2D}} = (0, 0, \log_{10}(Re_{\theta_{11}}), c_{\mathcal{D}})$$

$$y_{\min} = \text{-9.9981307800507362e-05}, \quad y_{\max} = 9.9776783353772638\text{e-}05$$

$$\tilde{y}_{\text{2D}} = 1.0238606482744217\text{e-}03$$

$\boldsymbol{\mu} =$ (-5.3735705353315691e-02, 1.2670559325955785e-02, 3.4881628016305797e+00, 1.4775314624231183e-03)

$\boldsymbol{\sigma} =$ (1.1645807755189665e-01, 3.0781281614935620e-02, 4.8205941597420482e-01, 2.9058393442407850e-04)

$$\bar{\bar{W}}_1 = \begin{bmatrix} \text{-7.9647445678710938e-01, -7.7597087621688843e-01, -1.7566627264022827e-01, -3.3038653433322906e-02} \\ \text{-6.5163150429725647e-03, 5.6284911930561066e-02, 5.2329522371292114e-01, -5.1631187088787556e-03} \\ \text{-1.9391560554504395e-01, -5.1117247343063354e-01, 2.1224832534790039e-01, -5.3156320005655289e-02} \\ \text{2.2672533988952637e-01, -1.0588613338768482e-02, 6.0577827692031860e-01, 5.1828873157501221e-01} \end{bmatrix}$$

$\boldsymbol{b}_1 =$ (-8.5662975907325745e-03, 1.5119668096303940e-03, 1.0300333499908447e+00, -7.0270246267318726e-01)

$$\bar{\bar{W}}_2 = \begin{bmatrix} \text{7.5300049502402544e-05, 5.7488705351715907e-06, 7.5533942435868084e-05, -1.6259378753602505e-05} \\ \text{-5.9861737489700317e-01, 2.7848154306411743e-01, 9.0827649831771851e-01, -6.8334120512008667e-01} \\ \text{2.4564220802858472e-04, 1.8624850781634450e-06, -5.1653558330144733e-05, -1.3583124382421374e-04} \\ \text{-5.0936633348464966e-01, -2.2990398108959198e-01, 4.0485945343971252e-01, -1.6076691448688507e-01} \end{bmatrix}$$

$\boldsymbol{b}_2 =$ (-2.1583786292467266e-04, 6.5153330564498901e-02, 6.6714754211716354e-05, 4.5869951136410236e-03)

$\boldsymbol{w} =$ (5.6621971452841535e-05, -1.3285604715347290e+00, -5.1922743296017870e-05, -6.4092695713043213e-01)

$$b = 0$$

It holds that

$$c_{\mathcal{D}}^{\circ}(H_2, H_{12}, \log_{10}(Re_{\theta_{11}}), c_{\mathcal{D}}) \equiv -c_{\mathcal{D}}^{\circ}(-H_2, -H_{12}, \log_{10}(Re_{\theta_{11}}), c_{\mathcal{D}})$$

$$\beta(\boldsymbol{x}) = \mathcal{S}^{-1}_{\text{minmax}}(\tilde{y};\, y_{\min}, y_{\max}), \qquad \tilde{y} = h\left(\mathcal{S}_{\text{std}}(\,\boldsymbol{x}\,;\boldsymbol{\mu},\boldsymbol{\sigma})\right)$$

$$\boldsymbol{x} = (H_1, \log_{10}(Re_{\theta_{11}}), c_\tau)$$

$$y_{\min} = 4.9464609478663973\text{e-}01, \quad y_{\max} = 1.3150223139703396\text{e+}00$$

$$\boldsymbol{\mu} = 1.5590171974852978\text{e+}00,\ 2.8153980366079807\text{e+}00,\ 1.7397550470856706\text{e-}03)$$

$$\boldsymbol{\sigma} = (1.5539093693660683\text{e-}01,\ 3.1170402711802825\text{e-}01,\ 5.1421510856559352\text{e-}04)$$

$$\bar{\bar{W}}_1 = \begin{bmatrix} -7.4844497442245483\text{e-}01,\ 3.9487469196319580\text{e-}01,\ 9.1911308467388153\text{e-}02 \\ -1.9887601956725121\text{e-}03,\ 4.9568200111389160\text{e-}01,\ -5.7626700401306152\text{e-}01 \\ 8.9828798081725836\text{e-}05,\ -6.5513677895069122\text{e-}02,\ 1.5470439195632935\text{e-}01 \\ -5.7760206982493401\text{e-}04,\ -2.4711549282073975\text{e-}01,\ 1.5355776250362396\text{e-}01 \\ 4.5609226799570024\text{e-}04,\ -2.4322293698787689\text{e-}02,\ 1.5303683280944824\text{e-}01 \end{bmatrix}$$

$$\boldsymbol{b}_1 = \begin{pmatrix} -5.8381187915802002\text{e-}01,\ -3.6139875650405884\text{e-}01,\ 4.4912524754181504\text{e-}04,\ -1.4575174450874329\text{e-}01,\ 5.2102282643318176\text{e-}04 \end{pmatrix}$$

$$\bar{\bar{W}}_2 = \begin{bmatrix} -4.5112858060747385\text{e-}05,\ 1.5337005606852472\text{e-}04,\ -9.3188078608363867\text{e-}05,\ 8.8895598310045898\text{e-}05,\ -1.7704005585983396\text{e-}05 \\ 1.7013751494232565\text{e-}04,\ 8.1610894203186035\text{e-}01,\ -9.5176079776138067\text{e-}04,\ -1.3498802483081818\text{e-}01,\ 6.2196864746510983\text{e-}04 \\ -1.6927043907344341\text{e-}04,\ -5.9477766626514494\text{e-}05,\ 1.2795464135706425\text{e-}04,\ -1.8978866137331352\text{e-}05,\ -1.0964431567117572\text{e-}04 \\ -7.8898787498474121\text{e-}01,\ 5.4303783923387527\text{e-}02,\ -3.0626797676086426\text{e-}01,\ -6.4862078428268433\text{e-}01,\ -2.3815728724002838\text{e-}01 \\ -1.6690832853782922\text{e-}04,\ -5.7666162319947034\text{e-}05,\ 8.0914476711768657\text{e-}05,\ -1.6989328287309036\text{e-}05,\ 3.3248765248572454\text{e-}05 \end{bmatrix}$$

$$\boldsymbol{b}_2 = \begin{pmatrix} 8.2617421867325902\text{e-}05,\ -7.9635647125542164\text{e-}05,\ 1.4603341696783900\text{e-}05,\ -1.3285605609416962\text{e-}01,\ -1.7533259233459830\text{e-}04 \end{pmatrix}$$

$$\boldsymbol{w} = \begin{pmatrix} 1.3621192192658782\text{e-}04,\ 7.6168119907379150\text{e-}01,\ 6.5017840825021267\text{e-}05,\ 1.3732773065567017\text{e+}00,\ -1.2890323705505580\text{e-}04 \end{pmatrix}$$

$$b = 5.5532885016873479\text{e-}04$$

where the neural network model has two hidden layers with a width of 5.

The closure relations of H_1^* follows Ref. [41].

$$H_1^*(H_1, Re_{\theta_{11}}) = \begin{cases} 1.5 + \dfrac{4}{R_z} + \left(0.5 - \dfrac{4}{R_z}\right) \dfrac{1.5}{H_1 + 0.5} \left(\dfrac{H_0 - H_1}{H_0 - 1}\right)^2, & H_1 < H_0 \\ 1.5 + \dfrac{4}{R_z} + (H_1 - H_0)^2 \left(\dfrac{0.007 \ln(R_z)}{(H_1 - H_0 + 4/\ln(R_z))^2} + \dfrac{0.015}{H_1}\right), & \text{else} \end{cases}$$

$$\text{where} \qquad H_0 = \begin{cases} 4, & Re_{\theta_{11}} < 400 \\ 3 + \dfrac{400}{Re_{\theta_{11}}}, & \text{else} \end{cases}, \qquad R_z = \max(200, Re_{\theta_{11}})$$

The closure relation of H_0° is simply a linear model because the trained neural network model reveals a linear structure. These simplified model is more interpretable and does not compromise the quality of fit.

$$H_0^\circ(H_2, H_{12}) = H_2 + H_{12}$$

B.3 Turbulent Boundary Layer Data

This section describes the setup of RANS cases for generating 3D turbulent boundary layer data. These cases are set up to mimic the laminar cases of flat plate boundary flow under a torpedo or sphere as in Sections 3.5.2 and 5.4.3.

The computational domain is the box of $(x, y, z) \in [-0.2, 1.2] \times [0, 0.2] \times [0, 0.5]$, as illustrated in Figure B-4. The RANS equations with an SA-negative turbulent model are solved to model the boundary layer that develops on the flat plate on the $y = 0$ plane in the interval of $x \in [0, 1]$. The presence of a torpedo or sphere body over the flat plate drives the 3D boundary layer behavior and is modeled by a constant freestream velocity and a point source or doublet respectively (along

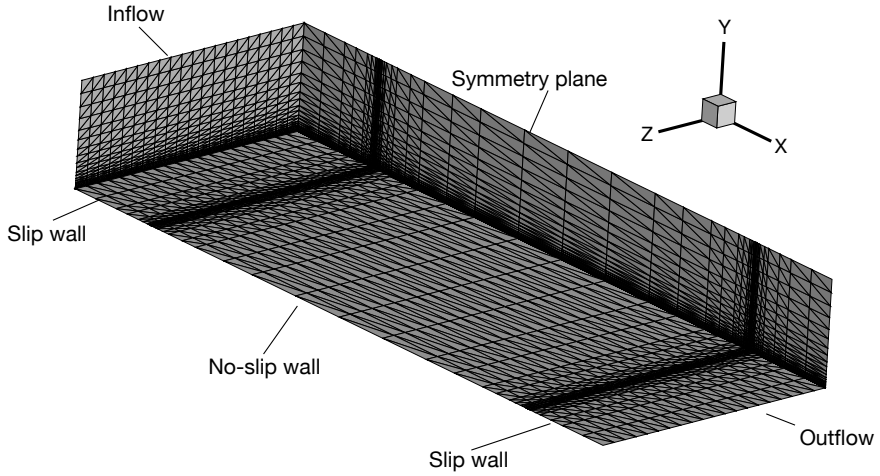

Figure B-4: Isometric view of the box computational domain for RANS turbulent cases . For clarify, only $x = 0$, $y = 0$ and $z = 0$ planes are shown. A sample medium-resolution structured tetrahedral mesh is shown to illustrate grid clustering along y near the $z = 0$ plane and along x near the leading and trailing edges of the no-slip flat plate.

with its associated mirrored image about the $y = 0$ plane). The effect of such point singularities is imposed by prescribing Dirichlet data of flow velocity and static pressure at the inflow ($x = -0.2$), outflow ($x = 1.2$), top ($y = 0.2$) and side ($z = 0.5$) boundaries. A symmetry condition is imposed for the $z = 0$ boundary. The flat plate is a no-slip and adiabatic wall, while the remaining portion of the $y = 0$ plane is a slip wall. The freestream Mach number is 0.05. The Prandtl number is 0.72. A constant molecular viscosity is used. The following list enumerates the various cases for generating the 3D turbulent boundary layer data, with adjusted parameters including Reynolds number (based on freestream velocity and unit plate length) and singularity strength (doublet μ or source Σ) and location (x_c, y_c, z_c).

- $Re = 5 \times 10^6, \quad (x_c, y_c, z_c) = (0.5, 1, 0), \quad \Sigma/q_\infty = 4$

- $Re = 5 \times 10^6, \quad (x_c, y_c, z_c) = (0.5, 1, 0), \quad \Sigma/q_\infty = 5$
- $Re = 5 \times 10^6, \quad (x_c, y_c, z_c) = (0.5, 1, 0), \quad \Sigma/q_\infty = 6$
- $Re = 5 \times 10^6, \quad (x_c, y_c, z_c) = (-0.25, 1, 0), \quad \Sigma/q_\infty = -3$
- $Re = 5 \times 10^6, \quad (x_c, y_c, z_c) = (0, 1, 0), \quad \Sigma/q_\infty = -3$
- $Re = 5 \times 10^6, \quad (x_c, y_c, z_c) = (0.25, 1, 0), \quad \Sigma/q_\infty = -3$
- $Re = 5 \times 10^6, \quad (x_c, y_c, z_c) = (0.5, 1, 0), \quad \Sigma/q_\infty = -3$
- $Re = 5 \times 10^6, \quad (x_c, y_c, z_c) = (0.75, 1, 0), \quad \Sigma/q_\infty = -3$
- $Re = 5 \times 10^6, \quad (x_c, y_c, z_c) = (1, 1, 0), \quad \Sigma/q_\infty = -3$
- $Re = 5 \times 10^6, \quad (x_c, y_c, z_c) = (0.6, 1, 0), \quad \Sigma/q_\infty = -6$
- $Re = 5 \times 10^6, \quad (x_c, y_c, z_c) = (-0.5, 1, 0), \quad \Sigma/q_\infty = 3$
- $Re = 5 \times 10^6, \quad (x_c, y_c, z_c) = (1.5, 1, 0), \quad \Sigma/q_\infty = 3$
- $Re = 5 \times 10^6, \quad (x_c, y_c, z_c) = (-0.6, 1, 0), \quad \Sigma/q_\infty = 10$
- $Re = 5 \times 10^6, \quad (x_c, y_c, z_c) = (-0.25, 1, 0), \quad \Sigma/q_\infty = 10$
- $Re = 5 \times 10^6, \quad (x_c, y_c, z_c) = (0, 1, 0), \quad \Sigma/q_\infty = 10$
- $Re = 5 \times 10^6, \quad (x_c, y_c, z_c) = (0.5, 1, 0), \quad \Sigma/q_\infty = 10$
- $Re = 5 \times 10^6, \quad (x_c, y_c, z_c) = (-0.5, 0.75, 0), \quad \Sigma/q_\infty = 10$
- $Re = 5 \times 10^6, \quad (x_c, y_c, z_c) = (-0.4, 0.5, 0), \quad \Sigma/q_\infty = 5$
- $Re = 5 \times 10^6, \quad (x_c, y_c, z_c) = (1, 3, 0), \quad \Sigma/q_\infty = -150$

- $Re = 10^6, \quad (x_c, y_c, z_c) = (-0.25, 1, 0), \quad \Sigma/q_\infty = 10$
- $Re = 10^6, \quad (x_c, y_c, z_c) = (-0.25, 1, 0), \quad \Sigma/q_\infty = 20$
- $Re = 10^6, \quad (x_c, y_c, z_c) = (-0.25, 1, 0), \quad \Sigma/q_\infty = 30$
- $Re = 10^6, \quad (x_c, y_c, z_c) = (0, 1, 0), \quad \Sigma/q_\infty = 10$
- $Re = 10^6, \quad (x_c, y_c, z_c) = (0.5, 1, 0), \quad \Sigma/q_\infty = 10$
- $Re = 10^6, \quad (x_c, y_c, z_c) = (1, 1, 0), \quad \Sigma/q_\infty = 10$
- $Re = 10^6, \quad (x_c, y_c, z_c) = (1.3, 1, 0), \quad \Sigma/q_\infty = 10$
- $Re = 10^6, \quad (x_c, y_c, z_c) = (1.75, 1, 0), \quad \Sigma/q_\infty = 10$
- $Re = 10^6, \quad (x_c, y_c, z_c) = (0.25, 1, 0), \quad \mu/q_\infty = 0.5$
- $Re = 5 \times 10^6, \quad (x_c, y_c, z_c) = (0.5, 0.75, 0), \quad \mu/q_\infty = 2$
- $Re = 10^6, \quad (x_c, y_c, z_c) = (0.5, 0.75, 0), \quad \mu/q_\infty = 2$
- $Re = 5 \times 10^6, \quad (x_c, y_c, z_c) = (0.5, 0.75, 0), \quad \mu/q_\infty = 3$
- $Re = 5 \times 10^6, \quad (x_c, y_c, z_c) = (0.25, 0.75, 0), \quad \mu/q_\infty = 2$
- $Re = 5 \times 10^6, \quad (x_c, y_c, z_c) = (0.25, 0.75, 0), \quad \mu/q_\infty = 2$
- $Re = 5 \times 10^6, \quad (x_c, y_c, z_c) = (0.5, 1, 0), \quad \mu/q_\infty = 5$
- $Re = 5 \times 10^6, \quad (x_c, y_c, z_c) = (0.5, 1, 0), \quad \mu/q_\infty = 7.5$
- $Re = 10^6, \quad (x_c, y_c, z_c) = (0.5, 1, 0), \quad \mu/q_\infty = 7.5$
- $Re = 5 \times 10^6, \quad (x_c, y_c, z_c) = (0.25, 1, 0), \quad \mu/q_\infty = 5$

- $Re = 10^6, \quad (x_c, y_c, z_c) = (0.25, 1, 0), \quad \mu/q_\infty = 5$
- $Re = 10^6, \quad (x_c, y_c, z_c) = (0.75, 1, 0), \quad \mu/q_\infty = 5$
- $Re = 5 \times 10^6, \quad (x_c, y_c, z_c) = (0.3, 2, 0), \quad \mu/q_\infty = 50$
- $Re = 10^6, \quad (x_c, y_c, z_c) = (0.1, 2, 0), \quad \mu/q_\infty = 75$
- $Re = 10^6, \quad (x_c, y_c, z_c) = (0.1, 2, 0), \quad \mu/q_\infty = 100$
- $Re = 10^6, \quad (x_c, y_c, z_c) = (0.1, 2, 0), \quad \mu/q_\infty = 125$
- $Re = 10^6, \quad (x_c, y_c, z_c) = (0.5, 2, 0), \quad \mu/q_\infty = 100$

B.4 e^N Envelope Method Closure

The amplification factor growth rate function f_{TS} in Equation (5.1) is given by the following expression owing to Ref. [41] and previously documented in Ref. [4].

$$f_{\text{TS}}(H_1; Re_{\theta_{11}}) = R\,\frac{\mathrm{d}\tilde{n}}{\mathrm{d}Re_{\theta_{11}}}\,\theta_{11}\frac{\mathrm{d}Re_{\theta_{11}}}{\mathrm{d}s} \qquad \text{(laminar)} \tag{B.5}$$

$$\text{where} \qquad R = \frac{1}{2} + \frac{1}{2}\tanh\left[10\left(\ln Re_{\theta_{11}} - \ln Re_{\theta_{11,0}}\right)\right] \tag{B.6}$$

$$\ln Re_{\theta_{11,0}} = \frac{5.738}{(H_1-1)^{0.43}} + 1.612\left[\tanh\left(\frac{14}{H_1-1} - 9.24\right) + 1\right] \tag{B.7}$$

$$\frac{\mathrm{d}\tilde{n}}{\mathrm{d}Re_{\theta_{11}}} = 0.028(H_1-1) - 0.0345\exp\left[-\left(\frac{3.87}{H_1-1} - 2.52\right)^2\right] \tag{B.8}$$

$$\theta_{11}\frac{\mathrm{d}Re_{\theta_{11}}}{\mathrm{d}s} = -0.05 + \frac{2.7}{H_1-1} - \frac{5.5}{(H_1-1)^2} + \frac{3.0}{(H_1-1)^3} + 0.1\exp\left(\frac{-20}{H_1-1}\right) \tag{B.9}$$

The correlations (B.7), (B.8), and (B.9) are obtained by fitting the e^N envelope growth rates computed based on the Orr-Sommerfeld equation for self-similar flows [70]. The ramp function R given by the expression (B.6) is introduced to smoothly model the onset of TS wave growth (i.e. at the first neutrally stable locality); that is, R is effectively zero and one, respectively, before and after the instability onset.

The aforementioned closure relations are formulated for laminar flows and are extended to the turbulent regime by introducing the following definitions,

$$f_{\mathrm{TS}} = K_N \left(\tilde{n}_{\mathrm{crit}} - \tilde{n}_0\right) \frac{\theta}{\ell_{\mathrm{ref}}}, \qquad R = 1 \qquad \text{(turbulent)} \tag{B.10}$$

where K_N is a non-dimensional parameter (with $K_N = 4$ being a practical value) and ℓ_{ref} is a characteristic length scale over which the shear layer develops. The same ℓ_{ref} is used for defining the Reynolds number, for example, the chord length for an airfoil or the streamwise length for a flat plate. The turbulent f_{TS} is intended to maintain the growth of $\tilde{n}$ in the turbulent flows and thereby facilitate the numerical treatment of transition in both the fitting and capturing approaches discussed in Chapter 5. Re-laminarization is not considered at present although it can potentially be modeled by modifying the turbulent function f_{TS}.

B.5 Lag Equation Closure

The lag equation (3.16) is completed with the following closure relations for the laminar regime.

$$\widetilde{\delta} = \theta_{11} \min\left\{12,\ \left(3.15 + \frac{1.72}{H_1 - 1}\right) + \frac{\delta_1^*}{\theta_{11}}\right\}, \tag{B.11}$$

$$K_{\mathrm{dl}} = \begin{cases} 1.0, & \text{boundary layer} \\ 0.9, & \text{wake} \end{cases} \tag{B.12}$$

$$(c_\tau)_{\mathrm{eq}} = \frac{H^*}{2}\frac{1}{1 - U_S} G_A^2 G_B, \qquad U_S = \frac{H^*}{2}\left(1 - \frac{H-1}{H\, B_{\mathrm{eq}}}\right) \tag{B.13}$$

$$G_A \equiv \frac{H-1}{A_{\mathrm{eq}} H}, \qquad G_B \equiv \frac{H-1}{B_{\mathrm{eq}} H} \tag{B.14}$$

$$A_{\mathrm{eq}} \approx 6.7, \qquad B_{\mathrm{eq}} \approx 0.75 \tag{B.15}$$

The shear stress magnitude from the outset of turbulent viscous layer, corresponding to $q'_{\mathrm{T,\ init}}$ as shown in Fig. 5-1, is specified as follows,

$$c_\tau = (c_\tau)_{\mathrm{T,\ init}} = \left(1.8 \exp\left(-\frac{3.3}{H-1}\right)\right)^2 (c_\tau)_{\mathrm{eq}} \qquad \text{(turbulent outset)} \tag{B.16}$$

This turbulent initial condition needs to be enforced at the transition front. In the transition fitting treatment of Section 5.2, this condition is imposed as a boundary condition at the inlet of the turbulent sub-element. For the transition capturing treatment of Section 5.3, the lag equation is extended to the laminar regime as follows [47],

$$\frac{\partial \mathcal{G}}{\partial t} + \mathbf{q}_{\mathrm{e}} \cdot \widetilde{\nabla}\mathcal{G} - K' K_G \left(\mathcal{G}_{\mathrm{T,\ init}} - \mathcal{G}\right) \frac{1}{t_{\mathrm{ref}}} = 0 \qquad \text{(laminar)} \tag{B.17}$$

where the non-dimensional parameter K_G is chosen to be positive and large so that $\mathcal{G}$ follows $\mathcal{G}_{\mathrm{T,\ init}}$ closely as they both evolve. For example, $K_G = 10$ is a practical choice. The non-dimensional parameter K' is defined as,

$$K' = \min\left\{1, \exp\left(\frac{\mathcal{G}_{\mathrm{T,\ init}} - \mathcal{G}}{\mathcal{G}_{\mathrm{ref}}}\right)\right\}, \qquad \mathcal{G}_{\mathrm{ref}} = 0.05 \tag{B.18}$$

so that $\mathcal{G}$ will not decrease excessively after it surpasses $\mathcal{G}_{\mathrm{T,\ init}}$ from below. With the laminar extension given by Eq. (B.17), the value of $\mathcal{G}$ is driven to approximately reach $\mathcal{G}_{\mathrm{T,\ init}}$ at transition and thus satisfies the turbulent initial condition (B.16).

Appendix C

Characteristic Analysis

The characteristic analysis of the IBL equations would provide useful insights for the formulation of boundary conditions (see Section 2.2) and numerical stabilization (see Section 4.3). However, this work reveals several challenges with it.

Conservation laws are a system of equations often defined in the following generic differential form

$$\frac{\partial \mathbf{U}}{\partial t} + \widetilde{\nabla} \cdot \mathbf{F} = 0 \tag{C.1}$$

where $\mathbf{U}$ and $\mathbf{F}$ refer to the conservative states and fluxes respectively. The characteristic analysis seeks the eigen-decomposition of the Jacobian of the flux along the direction $\hat{\mathbf{t}}$, defined and evaluated as follows.

$$\frac{\partial(\mathbf{F} \cdot \hat{\mathbf{t}})}{\partial \mathbf{U}} = \frac{\partial(\mathbf{F} \cdot \hat{\mathbf{t}})}{\partial \mathcal{Q}} \left(\frac{\partial \mathbf{U}}{\partial \mathcal{Q}} \right)^{-1} \tag{C.2}$$

where $\mathcal{Q}$ denotes the solution variables and may differ from the conservative states. The resulting eigenvalues and eigenvectors characterize, respectively, the speed and contents of the underlying information propagation, which are then useful for formu-

lating boundary conditions and numerical stabilization schemes.

However, the 3D IBL equations are not strictly conservation laws in the sense of Equation (C.1). Instead, as derived in Section A.4, they are obtained by algebraically manipulating and combining the mass and momentum conservation laws. Hence, the definition of conservative states and fluxes is ambiguous in the characteristic analysis of the IBL equations. Take Equations (2.2) to (2.4) for example, restated as follows.

$$\frac{\partial(\mathbf{M}-m\,\mathbf{q}_\mathrm{e})}{\partial t}+m\frac{\partial \mathbf{q}_\mathrm{e}}{\partial t}+\widetilde{\nabla}\cdot\overline{\overline{\mathbf{P}}}+\mathbf{M}\cdot\widetilde{\nabla}\mathbf{q}_\mathrm{e}-\boldsymbol{\tau}_\mathrm{w}=\mathbf{0}$$

$$\frac{\partial e}{\partial t}-\rho_\mathrm{e}\mathbf{Q}\cdot\frac{\partial \mathbf{q}_\mathrm{e}}{\partial t}-q_\mathrm{e}^2\frac{\partial m}{\partial t}+\widetilde{\nabla}\cdot\mathbf{K}+\mathbf{D}\cdot\widetilde{\nabla}\left(q_\mathrm{e}^2\right)-2\,\mathcal{D}=0$$

$$\begin{aligned}&\frac{\partial k^\circ}{\partial t}+\frac{e}{q_\mathrm{e}^2}\left(\mathbf{q}_\mathrm{e}\times\frac{\partial \mathbf{q}_\mathrm{e}}{\partial t}\right)\cdot\hat{\mathbf{n}}-\rho_\mathrm{e}\mathbf{Q}\times\frac{\partial \mathbf{q}_\mathrm{e}}{\partial t}\cdot\hat{\mathbf{n}}-2\rho_\mathrm{e}\mathbf{Q}^\circ\cdot\frac{\partial \mathbf{q}_\mathrm{e}}{\partial t}+\widetilde{\nabla}\cdot\mathbf{K}^\circ\\&+\frac{\mathbf{E}}{q_\mathrm{e}^2}\cdot\left(\mathbf{q}_\mathrm{e}\times\widetilde{\nabla}\mathbf{q}_\mathrm{e}\right)\cdot\hat{\mathbf{n}}-\frac{1}{2}\rho_\mathrm{e}\mathbf{Q}\times\widetilde{\nabla}(q_\mathrm{e}^2)\cdot\hat{\mathbf{n}}-\rho_\mathrm{e}\mathbf{Q}^\circ\cdot\widetilde{\nabla}(q_\mathrm{e}^2)+\mathcal{D}^\times+2\mathcal{D}^\circ=0\end{aligned}$$

To match the conventional form as in Equation (C.1), the quantities colored in red and blue are identified as the conservative states $\mathbf{U}$ and fluxes $\mathbf{F}$ respectively, listed as follows.

$$\mathbf{U}\equiv\left[\hat{\mathbf{e}}_1\cdot(\mathbf{M}-m\,\mathbf{q}_\mathrm{e}),\ \hat{\mathbf{e}}_2\cdot(\mathbf{M}-m\,\mathbf{q}_\mathrm{e}),\ e,\ k^\circ\right]^T \tag{C.3}$$

$$\mathbf{F}\equiv\left[\hat{\mathbf{e}}_1\cdot\overline{\overline{\mathbf{P}}},\ \hat{\mathbf{e}}_2\cdot\overline{\overline{\mathbf{P}}},\ \mathbf{K},\ \mathbf{K}^\circ\right]^T \tag{C.4}$$

Note that $\mathbf{q}_\mathrm{e}$ is governed by the EIF model and hence considered to be independent of the IBL solution for the sake of standalone analysis of the IBL equations.

An alternative form of the equations as follows can be obtained by algebraic

manipulation,

$$\frac{\partial(\mathbf{M}-m\,\mathbf{q}_\mathrm{e})}{\partial t}+m\frac{\partial \mathbf{q}_\mathrm{e}}{\partial t}+\widetilde{\nabla}\cdot\left(\overline{\overline{\mathbf{P}}}+\mathbf{q}_\mathrm{e}\otimes\mathbf{M}\right)+\mathbf{q}_\mathrm{e}(\widetilde{\nabla}\cdot\mathbf{M})-\boldsymbol{\tau}_\mathrm{w}=\mathbf{0}$$

$$\frac{\partial e}{\partial t}-\rho_\mathrm{e}\mathbf{Q}\cdot\frac{\partial \mathbf{q}_\mathrm{e}}{\partial t}-q_\mathrm{e}^2\frac{\partial m}{\partial t}+\widetilde{\nabla}\cdot\left(\mathbf{K}+q_\mathrm{e}^2\,\mathbf{M}\right)-q_\mathrm{e}^2(\widetilde{\nabla}\cdot\mathbf{M})-\rho_\mathrm{e}\mathbf{Q}\cdot\widetilde{\nabla}\left(q_\mathrm{e}^2\right)-2\,\mathcal{D}=0$$

$$\begin{aligned}&\frac{\partial k^\circ}{\partial t}+\frac{e}{q_\mathrm{e}^2}\left(\mathbf{q}_\mathrm{e}\times\frac{\partial \mathbf{q}_\mathrm{e}}{\partial t}\right)\cdot\hat{\mathbf{n}}-\rho_\mathrm{e}\mathbf{Q}\times\frac{\partial \mathbf{q}_\mathrm{e}}{\partial t}\cdot\hat{\mathbf{n}}-2\rho_\mathrm{e}\mathbf{Q}^\circ\cdot\frac{\partial \mathbf{q}_\mathrm{e}}{\partial t}+\widetilde{\nabla}\cdot\mathbf{K}^\circ\\&+\frac{\mathbf{E}}{q_\mathrm{e}^2}\cdot\left(\mathbf{q}_\mathrm{e}\times\widetilde{\nabla}\mathbf{q}_\mathrm{e}\right)\cdot\hat{\mathbf{n}}-\frac{1}{2}\rho_\mathrm{e}\mathbf{Q}\times\widetilde{\nabla}(q_\mathrm{e}^2)\cdot\hat{\mathbf{n}}-\rho_\mathrm{e}\mathbf{Q}^\circ\cdot\widetilde{\nabla}(q_\mathrm{e}^2)+\mathcal{D}^\times+2\mathcal{D}^\circ=0\end{aligned}$$

However, this form suggests the following flux definition

$$\mathbf{F}\equiv\left[\hat{\mathbf{e}}_1\cdot\left(\overline{\overline{\mathbf{P}}}+\mathbf{q}_\mathrm{e}\otimes\mathbf{M}\right),\ \hat{\mathbf{e}}_2\cdot\left(\overline{\overline{\mathbf{P}}}+\mathbf{q}_\mathrm{e}\otimes\mathbf{M}\right),\ \mathbf{K}+q_\mathrm{e}^2\,\mathbf{M},\ \mathbf{K}^\circ\right]^T \tag{C.5}$$

which differs from Equation (C.4) and results in a different set of eigenvalues and eigenvectors for the flux Jacobian in Equation (C.2). Hence, such characteristic analysis of the IBL equations does not provide unambiguous insights on the underlying information propagation.

On the other hand, even if the IBL characteristic problem is well-defined, it has no analytic solution. Calculation of the derivatives in Equation (C.2) requires differentiating the complicated IBL closure models. Consequently, it is infeasible to obtain analytic solution to this eigenvalue problem, in contrast to classic problems such as Euler equations and shallow water equations where eigenvalues and eigenvectors are known analytically.

The IBL equations are conventionally considered to be hyperbolic [22, 23]. One qualitative justification is that, if the IBL closure that characterizes the boundary layer reasonably accurately, the information propagation behavior of the IBL equa-

tions is expected to be similar to the hyperbolic in-plane character of the differential boundary layer equations. However, it is difficult (if possible at all) to design a set of closure while maintaining the hyperbolicity of the governing equations.

Moreover, the notion of characteristics gets more complicated or even ambiguous when it comes to the viscous-inviscid interaction formulation. Even if the IBL equations are strictly hyperbolic, the inviscid formulation may not be so simultaneously. For example, the incompressible potential flow is governed by an elliptic PDE. For all the aforementioned challenges, the characteristic analysis has not informed the formulation of boundary conditions and numerical stabilization in this work.

Appendix D

Slip Sidewall Boundary Condition

This appendix examines the slip sidewall boundary condition and provides evidence regarding why it is well-defined for Navier-Stokes equations but ill-posed for the differential boundary layer equations and, by extension, the IBL equations.

Let us consider, in cylindrical coordinates (r, θ, z), a boundary layer developing on the $z = 0$ plane. The sidewall is defined to be part of the $r = R$ perimeter surface for some radius $R \in \mathbb{R}$. This definition applies to any curved sidewalls locally. The steady-state incompressible Navier-Stokes equations in cylindrical coordinates [71] are

$$\mathbf{q} \cdot \nabla q_r - \frac{q_\theta^2}{r} = -\frac{1}{\rho}\frac{\partial p}{\partial r} + \nu\Big(\overbrace{\frac{1}{r^2}\frac{\partial^2 q_r}{\partial \theta^2} + \frac{1}{r}\frac{\partial}{\partial r}\left(r\frac{\partial q_r}{\partial r}\right) + \frac{\partial^2 q_r}{\partial z^2}}^{\nabla^2 q_r} - \frac{q_r}{r^2} - \frac{2}{r^2}\frac{\partial q_\theta}{\partial \theta}\Big) \tag{D.1}$$

$$\mathbf{q} \cdot \nabla q_\theta - \frac{q_\theta\, q_r}{r} = -\frac{1}{\rho\, r}\frac{\partial p}{\partial \theta} + \nu\left(\frac{1}{r^2}\frac{\partial^2 q_\theta}{\partial \theta^2} + \frac{1}{r}\frac{\partial}{\partial r}\left(r\frac{\partial q_\theta}{\partial r}\right) + \frac{\partial^2 q_\theta}{\partial z^2} + \frac{2}{r^2}\frac{\partial q_r}{\partial \theta} - \frac{q_\theta}{r^2}\right) \tag{D.2}$$

$$\mathbf{q} \cdot \nabla q_z = -\frac{1}{\rho}\frac{\partial p}{\partial z} + \nu\left(\frac{1}{r^2}\frac{\partial^2 q_z}{\partial \theta^2} + \frac{1}{r}\frac{\partial}{\partial r}\left(r\frac{\partial q_z}{\partial r}\right) + \frac{\partial^2 q_z}{\partial z^2}\right) \tag{D.3}$$

where the velocity in cylindrical components is $\mathbf{q} = (q_r, q_\theta, q_z)$. The following boundary conditions are prescribed.

$$\text{slip sidewall} \quad q_r = 0 \quad \text{for} \quad r = R, \forall\theta \in [0, 2\pi), z > 0 \tag{D.4}$$

$$\text{no-slip wall} \quad \mathbf{q} = \mathbf{0} \quad \text{for} \quad z = 0, \forall r \in [0, R], \theta \in [0, 2\pi) \tag{D.5}$$

At the corner of walls in the limit of $r \to R$ and $z \to 0$, both the governing equations and the boundary conditions should hold. Then, the Navier-Stokes equations at the juncture of the no-slip wall and slip sidewall reduce to

$$0 = -\frac{1}{\rho}\frac{\partial p}{\partial r} \tag{D.6}$$

$$0 = -\frac{1}{\rho\, r}\frac{\partial p}{\partial \theta} + \nu\frac{\partial^2 q_\theta}{\partial z^2} \tag{D.7}$$

$$0 = -\frac{1}{\rho}\frac{\partial p}{\partial z} + \nu\frac{\partial^2 q_z}{\partial z^2} \tag{D.8}$$

In comparison, the differential boundary layer equations (after applying thin shear layer approximations) are

$$\mathbf{q}\cdot\nabla q_r - \frac{q_\theta^2}{r} = -\frac{1}{\rho}\frac{\partial p}{\partial r} + \nu\frac{\partial^2 q_r}{\partial z^2} \tag{D.9}$$

$$\mathbf{q}\cdot\nabla q_\theta - \frac{q_\theta\, q_r}{r} = -\frac{1}{\rho\, r}\frac{\partial p}{\partial \theta} + \nu\frac{\partial^2 q_\theta}{\partial z^2} \tag{D.10}$$

$$0 = -\frac{1}{\rho}\frac{\partial p}{\partial z} \tag{D.11}$$

which, combined with the boundary conditions in Equations (D.4) and (D.5), reduce

to the following relations at the wall juncture.

$$0 = -\frac{1}{\rho}\frac{\partial p}{\partial r} \tag{D.12}$$

$$0 = -\frac{1}{\rho\, r}\frac{\partial p}{\partial \theta} + \nu\frac{\partial^2 q_\theta}{\partial z^2} \tag{D.13}$$

$$0 = -\frac{1}{\rho}\frac{\partial p}{\partial z} \tag{D.14}$$

Based on the thin shear layer approximations, the pressure p is assumed to be constant across the thickness of the boundary layer. Hence, Equation (D.6) leads to

$$0 = -\frac{1}{\rho}\frac{\partial p}{\partial r} = -\frac{1}{\rho}\frac{\partial p_\mathrm{e}}{\partial r} \tag{D.15}$$

which indicates that the differential boundary layer equations only admit solution with zero wall-normal pressure gradient $\partial p_\mathrm{e}/\partial r$. However, any curvature of the sidewall would induce some nonzero $\partial p_\mathrm{e}/\partial r$ value driven by the external inviscid flow (i.e. EIF). Hence, the general curved slip sidewall boundary condition may not be admissible for the differential boundary layer equations, which could be a reason that ill-posedness was empirically observed for 3D IBL with such boundary condition as discussed in Section 2.2.3.

Appendix E

Juncture Flow Modeling and IBL

This appendix describes the modeling of juncture flow (for example, at the wing-fuselage joint) in the IBL context, both in terms of physical modeling and numerical treatment.

Let us consider a duct geometry as in Figure E-1. The boundary layer develops on the four sides of the duct's inner wall (i.e. on the $z = 0$, $z = 1$, $y = 0$ and $y = 1$ planes). Juncture flow appears at the 90-degree corners between adjacent walls.

From a physical modeling perspective, the thin shear layer approximations underlying the IBL model break down at the juncture. Take the corner between the $y = 0$ and $z = 0$ planes for example. Near that corner, the assumption that in-plane diffusion is negligible compared to that in the wall-normal direction breaks down because viscous effects have comparable magnitude in both the y and z directions. Hence, the IBL model is not expected to produce genuinely physical characterization of the juncture flow behavior, which, if possible, requires additional physical modeling at the corner and can potentially examined more closely in the future.

The corner geometry also raises numerical issues. In a viscous-inviscid interaction

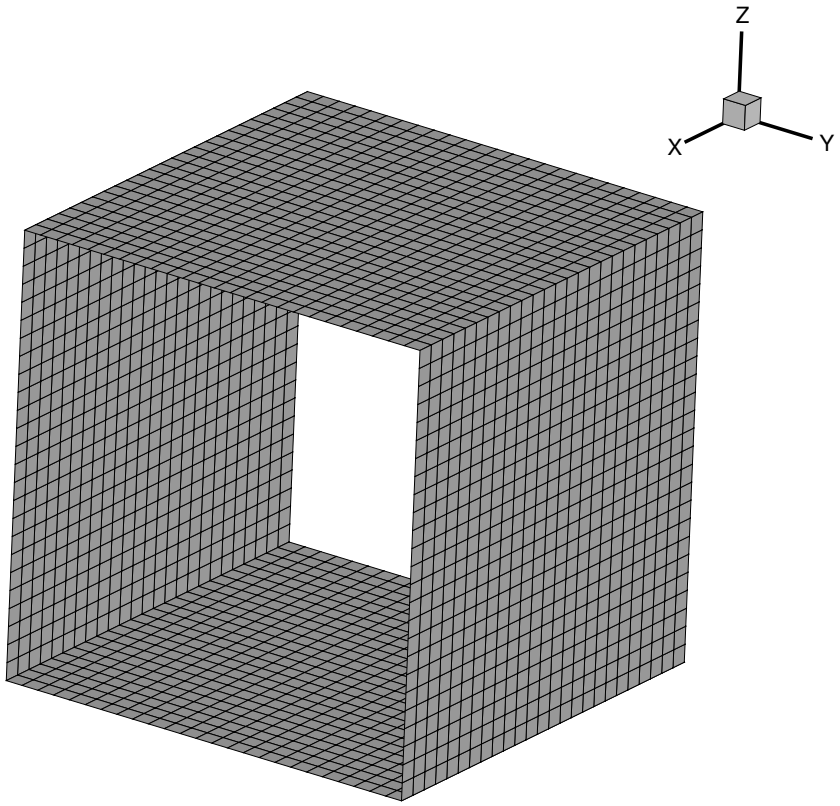

Figure E-1: Sample duct geometry quadrilateral surface grid. The walls are formed by extruding the perimeter bounding the square of $[0, 1] \times [0, 1]$ in the yz-plane from $x = 0$ to $x = 1$.

problem, the viscous effects lead to a generally nonzero wall-normal mass flux as in Equation (2.10). Hence, $\mathbf{q}_e$ at the $y = z = 0$ corner may have both y and z components that are positive. On the other hand, the IBL momentum equation is resolved into the respective planes (with corresponding surface normal vector $\hat{\mathbf{n}}$) while discarding the wall-normal component. In this work, $\hat{\mathbf{n}}$ is chosen to coincide with the wall-normal vector $\hat{\mathbf{n}}_w$ and hence changes discontinuously across the corner. This results in discontinuity in the IBL equations and hence oscillation in the numerical solution as shown in Figure E-2, whereas the solution is expected vary predominantly

only in the x direction in this quasi-2D problem. One practical workaround is to add geometric fairing to the sharp corner as in Figure E-3, which produces more regularized solution. The fairing can be made small as long as it can be resolved with sufficient grid resolution. Alternatively, the fairing effect can be imitated by constructing $\hat{\mathbf{n}}$ that changes smoothly across the corner. In this case, the surface-tangent basis vectors $\{\hat{\mathbf{e}}_1, \hat{\mathbf{e}}_2\}$ need to be constructed differently from the current approach in Equation (4.1).

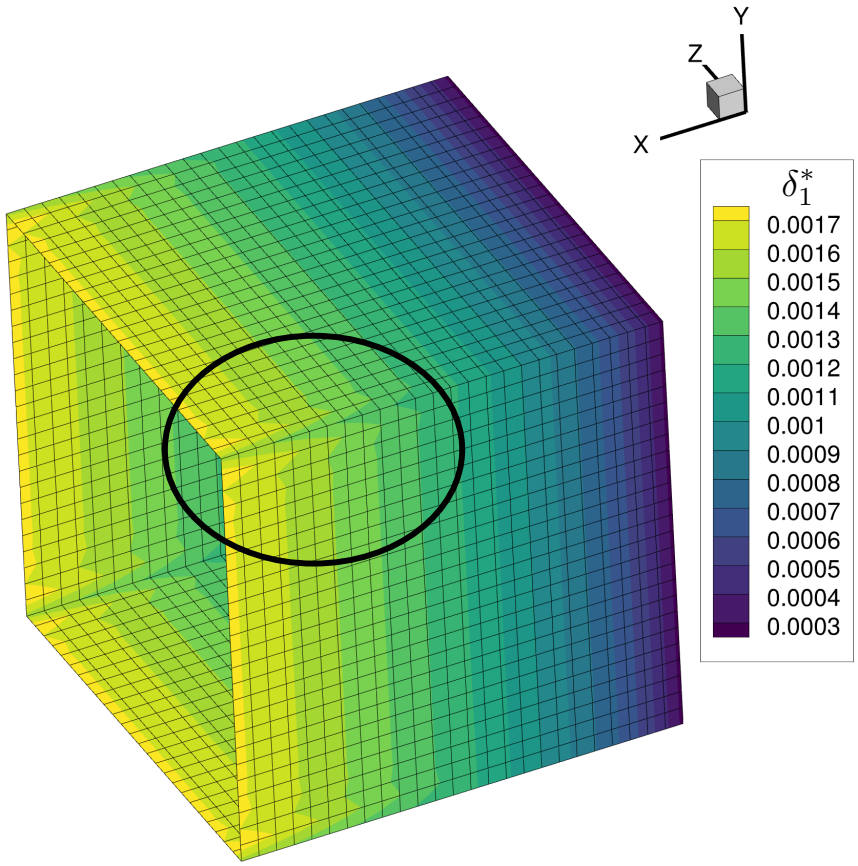

Figure E-2: Viscous-inviscid coupled IBL solution δ_1^* with oscillatory behavior (such as the circled variation along the y and z directions) near sharp corners between walls.

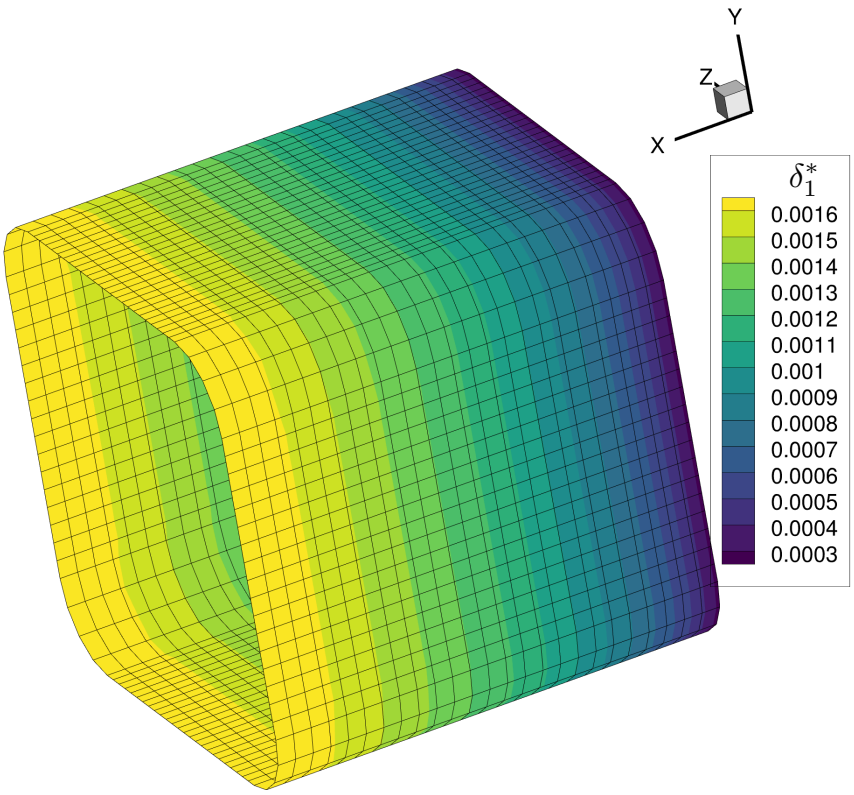

Figure E-3: Viscous-inviscid coupled IBL solution δ_1^* with regularized behavior across rounded corners.

Bibliography

[1] Nicolai, L. M. and Carichner, G. E., *Fundamentals of Aircraft and Airship Design*, American Institute of Aeronautics and Astronautics, Reston ,VA, Jan. 2010.

[2] Roskam, J., *Airplane Design*, Roskam Aviation and Engineering Corporation, Ottawa, Kansas, 1985.

[3] Drela, M., "Three-Dimensional Integral Boundary Layer Formulation for General Configurations," *21st AIAA Computational Fluid Dynamics Conference*, American Institute of Aeronautics and Astronautics, San Diego, CA, Jun. 2013.

[4] Zhang, S., Drela, M., Allmaras, S. R., Galbraith, M. C., and Darmofal, D. L., "A Strongly-coupled Non-parametric Integral Boundary Layer Method for Aerodynamic Analysis with Free Transition," *AIAA Scitech 2019 Forum*, American Institute of Aeronautics and Astronautics, San Diego, CA, Jan. 2019.

[5] Chae, M. G., Park, S. H., Lee, J. Y., and Bae, J. S., "Efficient Coupled Time Integration Methods for Transonic Aeroelastic Analysis," *Tenth International Conference on Computational Fluid Dynamics (ICCFD10)*, Barcelona, Spain, 2018, pp. 1–14.

[6] Martins, J. R., "CFD-based Aircraft Design Optimization," 2019.

[7] Wikipedia, "Airbus A350 XWB," .

[8] Bouissiere, F., Cuiller, C., Dereux, P., Kersuzan, S., Polacsek, T., Pralet, C., & Roussel, S., "Co-engineering in Aeronautics? The A320 Forward Section Case Study," *The 9th European Congress Embedded Real Time Software And Systems (ERTS)*, 2018.

[9] Aftosmis, M., Berger, M., and Alonso, J., "Applications of a Cartesian Mesh Boundary-Layer Approach for Complex Configurations," *44th AIAA Aerospace*

Sciences Meeting and Exhibit, American Institute of Aeronautics and Astronautics, Reston, Virigina, Jan. 2006.

[10] Drela, M., "Power Balance in Aerodynamic Flows," *AIAA Journal*, Vol. 47, No. 7, jul 2009, pp. 1761–1771.

[11] Drela, M., "XFOIL: An Analysis and Design System for Low Reynolds Number Airfoils," *Low Reynolds number aerodynamics*, Vol. 54, 1989, pp. 1–12.

[12] Morgado, J., Vizinho, R., Silvestre, M., and Páscoa, J., "XFOIL vs CFD performance predictions for high lift low Reynolds number airfoils," *Aerospace Science and Technology*, Vol. 52, May 2016, pp. 207–214.

[13] Drela, M., *Flight Vehicle Aerodynamics*, The MIT Press, Cambridge, MA, USA, 2014.

[14] Martins, J. R., Kenway, G. K. W., and Brooks, T., "Multidisciplinary Design Optimization of Aircraft Configurations Part 2: High-fidelity Aerostructural Optimization," May 2016, Lecture series, Von Karman Institute for Fluid Dynamics, Sint-Genesius-Rode, Belgium.

[15] Bieterman, M., Melvin, R., Johnson, F., Bussoletti, J., Young, D., Huffman, W., Hilmes, C., and Drela, M., "Boundary Layer Coupling in a General Configuration Full Potential Code," Tech. rep., The Boeing Company, 1994.

[16] Johnson, F. T., Tinoco, E. N., and Yu, N. J., "Thirty Years of Development and Application of CFD at Boeing Commercial Airplanes, Seattle," *Computers & Fluids*, Vol. 34, No. 10, Dec. 2005, pp. 1115–1151.

[17] Young, D. P., Melvin, R. G., Huffman, W. P., Arian, E., Hong, M., and Drela, M., "Implementation of a Separated Flow Capability in TRANAIR," *AIAA Journal*, Vol. 52, No. 8, Aug. 2014, pp. 1699–1716.

[18] Cumpsty, N. A. and Head, M. R., "The Calculation of the Three-Dimensional Turbulent Boundary Layer: Part III. Comparison of Attachment-Line Calculations with Experiment," *Aeronautical Quarterly*, Vol. 20, No. 2, May 1969, pp. 99–113.

[19] Bradshaw, P. and Ferriss, D. H., "Calculation of Boundary-Layer Development Using the Turbulent Energy Equation: Compressible Flow on Adiabatic Walls," *Journal of Fluid Mechanics*, Vol. 46, No. 01, Mar. 1971, pp. 83.

[20] Mclean, J. and Randall, J., "Computer Program To Calculate Three-Dimensional Boundary Layer Flows Over Wings With Wall Mass Transfer," Tech. rep., National Aeronautics and Space Administration, 1979.

[21] Swafford, T. W. and Whitfield, D. L., "Time-dependent Solution of Three-dimensional Compressible Turbulent Integral Boundary-layer Equations," *AIAA Journal*, Vol. 23, No. 7, Jul. 1985, pp. 1005–1013.

[22] Nishida, B. A., *Fully Simultaneous Coupling of the Full Potential Equation and the Integral Boundary Layer Equations in Three Dimensions*, Ph.D. Thesis, Massachusetts Institute of Technology, 1996.

[23] Mughal, B. H., *Integral Methods for Three-Dimensional Boundary Layers*, Ph.D. Thesis, Massachusetts Institute of Technology, 1998.

[24] Lokatt, M. and Eller, D., "Finite-volume scheme for the solution of integral boundary layer equations," *Computers & Fluids*, Vol. 132, Jun. 2016, pp. 62–71.

[25] Lock, R. and Williams, B., "Viscous-Inviscid Interactions in External Aerodynamics," *Progress in Aerospace Sciences*, Vol. 24, No. 2, 1987, pp. 51–171.

[26] Goldstein, S., "On Laminar Boundary Layer Flow Near a Position of Separation," *The Quarterly Journal of Mechanics and Applied Mathematics*, Vol. 1, No. 1, Jan. 1948, pp. 43–69.

[27] Zhang, S., *A Non-parametric Discontinuous Galerkin Formulation of the Integral Boundary Layer Equations with Strong Viscous-Inviscid Coupling*, Master's thesis, Massachusetts Institute of Technology, 2018.

[28] Galbraith, M. C., Allmaras, S. R., and Darmofal, D. L., "SANS RANS solutions for 3D benchmark configurations," *2018 AIAA Aerospace Sciences Meeting*, American Institute of Aeronautics and Astronautics, Reston, Virginia, jan 2018.

[29] Lu, L., Jin, P., Pang, G., Zhang, Z., and Karniadakis, G. E., "Learning nonlinear operators via DeepONet based on the universal approximation theorem of operators," *Nature Machine Intelligence*, Vol. 3, No. 3, Mar. 2021, pp. 218–229.

[30] Pan, S., Brunton, S. L., and Kutz, J. N., "Neural Implicit Flow: a mesh-agnostic dimensionality reduction paradigm of spatio-temporal data," Apr. 2022.

[31] Drela, M. and Giles, M. B., "Viscous-inviscid Analysis of Transonic and Low Reynolds Number Airfoils," *AIAA Journal*, Vol. 25, No. 10, Oct. 1987, pp. 1347–1355.

[32] Drela, M., "DBL3: A Surface-Based Cartesian-Basis Differential 3D Boundary Layer Formulation (Unpublished)," 2019.

[33] Goodfellow, I., Bengio, Y., and Courville, A., *Deep Learning*, MIT Press, 2016.

[34] Abadi, M., Agarwal, A., Barham, P., Brevdo, E., Chen, Z., Citro, C., Corrado, G. S., Davis, A., Dean, J., Devin, M., Ghemawat, S., Goodfellow, I., Harp, A., Irving, G., Isard, M., Jia, Y., Jozefowicz, R., Kaiser, L., Kudlur, M., Levenberg, J., Mané, D., Monga, R., Moore, S., Murray, D., Olah, C., Schuster, M., Shlens, J., Steiner, B., Sutskever, I., Talwar, K., Tucker, P., Vanhoucke, V., Vasudevan, V., Viégas, F., Vinyals, O., Warden, P., Wattenberg, M., Wicke, M., Yu, Y., and Zheng, X., "TensorFlow: Large-Scale Machine Learning on Heterogeneous Systems," 2015, Software available from tensorflow.org.

[35] Guyon, I. and Elisseeff, A., "An introduction to variable and feature selection," *Journal of Machine Learning Research*, Vol. 3, 2003, pp. 1157–1182.

[36] Scardapane, S., Comminiello, D., Hussain, A., and Uncini, A., "Group sparse regularization for deep neural networks," *Neurocomputing*, Vol. 241, Jun. 2017, pp. 81–89.

[37] Feng, J. and Simon, N., "Sparse-Input Neural Networks for High-dimensional Nonparametric Regression and Classification," nov 2017, pp. 1–37.

[38] Ma, L., Resvanis, T., and Vandiver, K., "A Weighted Sparse-Input Neural Network Technique Applied to Identify Important Features for Vortex-Induced Vibration," *Proceedings of the AAAI 2020 Spring Symposium on Combining Artificial Intelligence and Machine Learning with Physical Sciences, Stanford, CA, USA, March 23rd - to - 25th, 2020*, edited by J. Lee, E. F. Darve, P. K. Kitanidis, M. W. Farthing, and T. Hesser, Vol. 2587 of *CEUR Workshop Proceedings*, CEUR-WS.org, 2020.

[39] Karniadakis, G. E., Kevrekidis, I. G., Lu, L., Perdikaris, P., Wang, S., and Yang, L., "Physics-informed machine learning," *Nature Reviews Physics*, Vol. 3, No. 6, Jun. 2021, pp. 422–440.

[40] Mattheakis, M., Protopapas, P., Sondak, D., Di Giovanni, M., and Kaxiras, E., "Physical Symmetries Embedded in Neural Networks," apr 2019.

[41] Drela, M., "XFOIL: Subsonic Airfoil Development System, (version 6.99)," Dec. 23, 2013, Available at http://web.mit.edu/drela/Public/web/xfoil/. Retrieved on December 6, 2017 .

[42] Singh, A. P., Medida, S., and Duraisamy, K., "Machine-Learning-Augmented Predictive Modeling of Turbulent Separated Flows over Airfoils," *AIAA Journal*, Vol. 55, No. 7, jul 2017, pp. 2215–2227.

[43] Yang, M. and Xiao, Z., "Improving the k–ω–γ–A r transition model by the field inversion and machine learning framework," *Physics of Fluids*, Vol. 32, No. 6, Jun. 2020, pp. 064101.

[44] LeVeque, R. J., *Numerical Methods for Conservation Laws*, Birkhäuser Basel, Basel, 1992.

[45] Toro, E. F., *Riemann Solvers and Numerical Methods for Fluid Dynamics*, 2009.

[46] Zhang, S., Galbraith, M., Allmaras, S., Drela, M., and Darmofal, D., "A Non-parametric Discontinuous Galerkin Formulation of the Integral Boundary Layer Equations With Strong Viscous/Inviscid Coupling," *23rd AIAA Computational Fluid Dynamics Conference, 2017 AIAA Aviation and Aeronautics Forum and Exposition*, American Institute of Aeronautics and Astronautics, Denver, Colorado, Jun. 2017.

[47] Zhang, S., Drela, M., Galbraith, M. C., Allmaras, S. R., and Darmofal, D., "An Integral Boundary Layer Method using Discontinuous Galerkin Discretization and Captured Transition Modeling," *AIAA AVIATION 2020 FORUM*, American Institute of Aeronautics and Astronautics, Reston, Virginia, Jun. 2020.

[48] Oliver, T. A. and Darmofal, D. L., "Analysis of Dual Consistency for Discontinuous Galerkin Discretizations of Source Terms," *SIAM Journal on Numerical Analysis*, Vol. 47, No. 5, Jan. 2009, pp. 3507–3525.

[49] Saric, W. S., Reed, H. L., and White, E. B., "Stability and Transition of Three-dimensional Boundary Layers," *Annual Review of Fluid Mechanics*, Vol. 35, No. 1, Jan. 2003, pp. 413–440.

[50] Krumbein, A., "eN transition prediction for 3D wing configurations using database methods and a local, linear stability code," *Aerospace Science and Technology*, Vol. 12, No. 8, 2008, pp. 592–598.

[51] Krimmelbein, N. and Krumbein, A., "Automatic Transition Prediction for Three-Dimensional Configurations with Focus on Industrial Application," *Journal of Aircraft*, Vol. 48, No. 6, Nov. 2011, pp. 1878–1887.

[52] Olichevis Halila, G. L., Fidkowski, K. J., and Martins, J. R. R. A., "Toward Automatic Parabolized Stability Equation-Based Transition-to-Turbulence Prediction for Aerodynamic Flows," *AIAA Journal*, Oct. 2020, pp. 1–12.

[53] Halila, G. L. O., Yildirim, A., Mader, C. A., Fidkowski, K. J., and Martins, J. R. R. A., "Linear Stability-Based Smooth Reynolds-Averaged Navier–Stokes Transition Model for Aerodynamic Flows," *AIAA Journal*, Vol. 60, No. 2, Feb. 2022, pp. 1077–1090.

[54] Langtry, R. B. and Menter, F. R., "Correlation-Based Transition Modeling for Unstructured Parallelized Computational Fluid Dynamics Codes," *AIAA Journal*, Vol. 47, No. 12, Dec. 2009, pp. 2894–2906.

[55] Coder, J. G. and Maughmer, M. D., "Computational Fluid Dynamics Compatible Transition Modeling Using an Amplification Factor Transport Equation," *AIAA Journal*, Vol. 52, No. 11, nov 2014, pp. 2506–2512.

[56] Coder, J. G., "Enhancement of the Amplification Factor Transport Transition Modeling Framework," *55th AIAA Aerospace Sciences Meeting*, American Institute of Aeronautics and Astronautics, Reston, Virginia, Jan. 2017.

[57] Langtry, R., "Extending the Gamma-Rethetat Correlation based Transition Model for Crossflow Effects (Invited)," *45th AIAA Fluid Dynamics Conference*, American Institute of Aeronautics and Astronautics, Reston, Virginia, Jun. 2015.

[58] Grabe, C., Shengyang, N., and Krumbein, A., "Transition Transport Modeling for the Prediction of Crossflow Transition," *34th AIAA Applied Aerodynamics Conference*, American Institute of Aeronautics and Astronautics, Reston, Virginia, Jun 2016.

[59] Choudhari, M. M., "Transition Modeling and CFD Vision 2030," Available at `https://transitionmodeling.larc.nasa.gov/`. Retrieved on June 5, 2022.

[60] Sturdza, P., *An Aerodynamic Design Method for Supersonic Natural Laminar Flow Aircraft*, Ph.D. Thesis, Stanford University, 2003.

[61] Kroo, I. and Sturdza, P., "Design-Oriented Aerodynamic Analysis for Supersonic Laminar Flow Wings," *41st Aerospace Sciences Meeting and Exhibit*, American Institute of Aeronautics and Astronautics, Reston, Virigina, Jan. 2003.

[62] Strang, G., *An analysis of the finite element method*, Wellesley-Cambridge, Wellesley, MA, 2nd ed., 2008.

[63] Modisette, J. M., *An Automated Reliable Method for Two-Dimensional Reynolds-Averaged Navier-Stokes Simulations*, Ph.d. thesis, Massachusetts of Technology, 2011.

[64] Fries, T. P. and Belytschko, T., "The extended/generalized finite element method: An overview of the method and its applications," *International Journal for Numerical Methods in Engineering*, Vol. 84, No. 3, Aug. 2010, pp. 253–304.

[65] Drela, M., "MTFLOW Overview," November 2015.

[66] Huang, A. C.-w., *An Adaptive Variational Multiscale Method with Discontinuous Subscales for Aerodynamic Flows*, Ph.d. thesis, Massachusetts Institute of Technology, 2019.

[67] Galbraith, M. C., Allmaras, S. R., and Haimes, R., "Full Potential Revisited: A Medium Fidelty Aerodynamic Analysis Tool," *55th AIAA Aerospace Sciences Meeting*, American Institute of Aeronautics and Astronautics, Grapevine, Texas, Jan. 2017, pp. 1–26.

[68] Drela, M., Galbraith, M., Haimes, R., Allmaras, S. R., and Darmofal, D., "Hybrid Shell Model for Aeroelastic Modeling," *AIAA Scitech 2019 Forum*, American Institute of Aeronautics and Astronautics, Reston, Virginia, jan 2019.

[69] Drela, M., "IBL3: A Four-Equation 3D Integral Boundary Layer Formulation," (unpublished). March 3, 2017.

[70] Drela, M., *Aerodynamics of Viscous Flows*, (unpublished), 2015.

[71] Batchelor, G. K., *An Introduction to Fluid Dynamics*, Vol. 76, Cambridge University Press, Cambridge, 1973.